UNIVERSITY of CALIFORNIA
Santa Barbara

Charting the Substellar Mass Landscape: Unveiling Precise Dynamical Masses for Exoplanets and Brown Dwarfs Orbiting Nearby Stars

A dissertation submitted in partial satisfaction of the
requirements for the degree of

Doctor of Philosophy

in

Physics

by

Yiting Li

Committee in charge:

Professor Timothy D. Brandt, Chair

Professor Peng Oh

Professor Benjamin Mazin

September 2023

The dissertation of Yiting Li is approved:

Professor Peng Oh

Professor Benjamin Mazin

Professor Timothy D. Brandt, Chair

July 2023

Charting the Substellar Mass Landscape: Unveiling Precise Dynamical Masses for Exoplanets and Brown Dwarfs Orbiting Nearby Stars

by

Yiting Li

Dedicated to my late grandfather, Shunyu Chen.

Acknowledgements

Technical Acknowledgements and Attributions:

The research presented in this thesis benefited from data obtained from the the European Space Agency (ESA) mission Gaia (https://www.cosmos.esa.int/Gaia), processed by the Gaia Data Processing and Analysis Consortium (DPAC, https://www.cosmos.esa.int/web/Gaia/dpac/consortium). The gratitude is extended to the national institutions and the participating organizations of the Gaia Multilateral Agreement for their generous funding and support, without which this work would not have been possible.

I am extremely grateful to Dr. Trent J. Dupuy for sharing his IDL orbit fitting code, which laid the foundation for the development of the orbit code `orvara`. In Chapter 2, I want to thank the dedicated teams responsible for creating and maintaining various RV data banks including the calibrated HIRES (Tal-Or et al., 2018) and HARPS (Trifonov et al., 2020) radial velocity catalogs, which form the basis for selecting and analyzing our RV sample. The analysis in Chapter 3 greatly relies on the work ten years earlier by Dr. Cátia V. Cardoso and Dr. Mark J. McCaughrean, which guided a large part of our re-analysis of the ε Indi B astrometry. Chapter 4 and Chapter 5 utilize data collected by the NIRC2 camera at the W.M. Keck Observatory (WMKO), which is publicly available from the Keck Observatory Archive (KOA) jointly managed by the WMKO and NASA Exoplanet Science Institute (NExScI). I extend my appreciation to the staff at the WMKO as well as to the CHARIS collaboration for their invaluable assistance in facilitating the setup of our observation nights, ensuring the successful acquisition of our data.

The work in this thesis makes extensive use of the following `Python` packages: The NumPy Array (van der Walt et al., 2011), Matplotlib (Hunter, 2007), and SciPy (Virtanen et al., 2020), pandas (McKinney, 2010), `htof` (Brandt et al., 2021b), `orvara` (Brandt et al., 2021f) and VIP (Gomez Gonzalez et al., 2017a).

Personal Acknowledgements:

First and foremost, I wish to thank my advisor, Dr. Timothy Brandt, for being a steadfast source of encouragement and guidance over the past five years. Your mentorship has played a pivotal role in nurturing my intellectual growth and cultivating my passion for exoplanet research. I consider myself fortunate to have had the opportunity to collaborate with you and learn from your expertise. I extend my deep gratitude to the dissertation committee members, and organizers of the Astro Tea, Colloquium, Lunches, and Journal Clubs for facilitating stimulating discussions and provide a platform where we can share the excitement about the latest ground-breaking astrophysics research.

I am grateful to my incredible family for their unconditional love as I pursued my passion for astronomy. From the earliest chapters of my memory where we delved into the pages of astronomy books, to the enchanted moment you presented me with my first telescope, your support have been instrumental in enabling me to pursue higher education.

My sincere thanks to my undergraduate advisors at Penn State and the HPF/NEID team, in particular Dr. Suvrath Mahadevan and Dr. Guðmundur K. Stefánsson. I also want to thank Dr. B.S. Sathyaprakash for his guidance in my undergraduate research. Your mentorship have had lasting impact on me as a researcher, extending into my graduate studies.

I want to thank my exceptional collaborators around the world, whose collective efforts have played an integral role in the realization of this endeavor. In no particular order, I thank Dr. Trent Dupuy, Dr. G. Mirek Brandt, Kyle Franson, Minghan Chen, Rachel Bowens-Rubin, Briley Lewis, Dr. Brendan Bowler, Dr. Rocio Kiman, Dr. Jacqueline Faherty, Dr. Thayne Currie, Dr. Daniella Gagliuffi, Dr. Rebecca Jensen-Clem, Hengyue Zhang, Qier An, and Dr. Daniel Michalik. It is through our collaborative efforts that we have achieved meaningful progress and advancements in our field.

Lastly, I am indebted to my cherished personal friends, be they longstanding companions or those forged during my graduate school tenure. I thank Dr. Curtis Smith, Nicole Huang, Min Lee, Sabrina Zheng, Raya Lin, Don George, Yahya Almumin, Laura Lei, Estefania Gonzalez, Dian Dian Wang, Zhencheng Wang, among many others. I also wish to thank the Pan and Ma family, our dear family friends, for their generosity and warm hospitality that have made California feel like a truly welcoming home.

Curriculum Vitæ

Yiting Li

Education

2023	(Expected) Ph.D., Physics, University of California, Santa Barbara, CA
2021	M.A., Physics, University of California, Santa Barbara, CA
2018	B.S., Physics, Mathematics and Astronomy & Astrophysics, Penn State University, State College, PA

Select Publications

“Keck Discovery of a 20au Companion around HD 63754 Straddling the Substellar-Stellar Boundary”, **Li, Y**, Brandt, T.D., Q. An, Franson K., Dupuy, T. et al., *To be submitted to Monthly Notices of the Royal Astronomical Society (MNRAS) 2023.*

“Surveying Nearby Brown Dwarfs with HGCA: Direct Imaging Discovery of a Faint, High Mass Brown Dwarf Orbiting HD 176535 A”, **Li, Y**, Brandt, T.D., Brandt, G.M., An, Q., Franson K., Dupuy, T., Chen, M. et al., *MNRAS* 522, 4, 5622–5637 (2023).

“Precise Dynamical Masses of ε Indi Ba and Bb: Evidence of Slowed Cooling at the L/T Transition”, **Chen, M. & Li, Y.**, Brandt, T. D., Dupuy, T. J., Cardoso, C. V., McCaughrean, M. J. *The Astronomical Journal*, Volume 163, Number 6. (2022).

“The Formation of the First Quasars. I. The Black Hole Seeds, Accretion and Feedback Models”, Zhu, Q., **Li, Y.**, Li, Y. et al., *MNRAS*, Volume 514, Issue 4, Pages 5583–5606 (2022).

“The Gliese 86 Binary System: A Warm Jupiter Formed in a Disk Truncated at 2 AU”, Zeng, Y., Brandt, T. D., Li, G., Dupuy, T. J., **Li, Y.** et al., *The Astronomical Journal*, vol. 164, no. 5 (2022).

“Precise Masses and Orbits for Nine Radial Velocity Exoplanets”, **Li, Y.** Brandt, T.D., Brandt, G.M., Dupuy, T.J., Michalik, D. et al. *The Astronomical Journal* Vol 162, Pages 266 (2021).

“orvara: An Efficient Code to Fit Orbits Using Radial Velocity, Absolute, and/or Relative Astrometry”, Brandt, T.D., Dupuy, T.J., **Li, Y.**, et al. *The Astronomical Journal* vol. 162, no. 5 (2021).

"Precise Dynamical Masses and Orbital Fits for β Pic b and β Pic c", Brandt, G., Brandt, T., Dupuy, T., **Li, Y.**, Michalik, D., *The Astronomical Journal*, vol. 161, no. 4 (2021).

"Improved Dynamical Masses for Six Brown Dwarf Companions Using Hipparcos and Gaia EDR3", Brandt, G. M., Dupuy, T. J., **Li, Y.**, Chen, M., Brandt, T. D., Long, T., Wong, S., Currie, T., Bowler, B. P., Liu, M. C., et al., *The Astronomical Journal*, Vol. 162, Number 6, Pages 301 (2021).

"14 Her: a likely case of planet-planet scattering", Gagliuffi, D., Faherty, J.K., **Li, Y.** et al., *The Astrophysical Journal Letters*, Vol. 922, L43 (2021).

"htof: A new open-source tool for analyzing Hipparcos, Gaia, and future astrometric missions", Brandt, G. M., Michalik, D., Brandt, T. D., **Li, Y.** et al., *The Astronomical Journal*, Vol. 162, Pages 230 (2021).

"Diffuser-assisted Photometric Follow-up Observations of the Neptune-sized Planets K2-28b and K2-100b", **G. Stefansson & Li, Y.**, S. Mahadevan, J. Wisniewski, L. Hebb, B. Morris, J. Huehnerhoff, and S. Hawley, *The Astronomical Journal*, Vol. 156, Pages 266 (2018).

"Extreme precision photometry from the ground with beam-shaping diffusers for K2, TESS, and beyond", Stefansson, G., Mahadevan S., Wisniewski, J., **Li Y.** et al., *Ground-based and Airborne Instrumentation for Astronomy VII* (2018).

"A candidate transit around Proxima Centauri", **Li, Y.**, Stefansson, G., Robertson, P., Monson, A., Caas, C., Mahadevan, S., *Research Notes of the American Astronomical Society*, vol. 1, no. 1 (2017).

Abstract

Charting the Substellar Mass Landscape: Unveiling Precise Dynamical Masses for Exoplanets and Brown Dwarfs Orbiting Nearby Stars

by

Yiting Li

Extra-solar planets, brown dwarfs, and low-mass stars are distinct astronomical objects that encompass a wide range of masses, occupying the lower end of the mass and temperature spectrum within the vastness of the Universe. These cool objects' peak emission occurs at longer wavelengths in the red and infrared regions. They present abundant avenues for observational and theoretical exploration, facilitating the study of their evolutionary pathways. It is believed that stars are born from gravitational collapse of molecular clouds of gas and dust that are scattered throughout most galaxies over thousands to millions of years. The hot core of the collapsing cloud will form a protostar with fast rotation. Some of these spinning clouds of collapsing gas and dust break up into two or three blobs that each form stars which later become multiple systems. The crucial factor setting these objects apart lies in their initial masses, which provide valuable insights into their formation mechanisms and their post-formation evolution. Stars ($\geq 80 M_{\rm Jup}$), including low-mass stars like M dwarfs, are self-luminuous entities that sustain nuclear fusion in their cores, generating energy through the fusion of hydro-

gen atoms. Brown dwarfs occupy a mass range between that of the heaviest gas giant planets and the lightest stars ($\sim 15 - \sim 80 M_{\mathrm{Jup}}$), they fall short of the mass required for sustained hydrogen burning and do not possess a stable energy-generating mechanism. They briefly undergo deuterium burning during their early formation stages, but this process is not sustainable in the long term. Planets ($< 15 M_{\mathrm{Jup}}$), distinct from stars and brown dwarfs, lack an inherent energy generation process and primarily emit radiation received from their host star and residual internal heat from their formation. Their energy output is primarily determined by the absorbed and reflected light from their parent star. The distinction between these objects is crucial as it helps us classify and study the vast diversity of objects beyond our solar system, providing insights into their formation, evolution, and the conditions that allow for the existence of habitable planets. If one can determine the mass of a detected object empirically and independently, it not only helps confirm the nature of the object but also tests and informs evolutionary models of substellar or sometimes stellar evolution. The work in this thesis expands the sample of planets and brown dwarfs whose dynamical masses and orbits are empirically measured, in order to chart the vast substellar evolutionary landscape spanning the entire range of masses.

Before the Gaia satellite, the detection of directly imaged brown dwarfs and giant planets orbiting main-sequence stars was a rare occurrence. Merely a small collection of approximately thirty such objects had been identified, and only a fraction of them possessed independently measured masses. These masses, determined through the observation of orbital dynamics, are known as dynamical masses and are regarded as the most reliable and independent measurements, as they do not rely on cooling or evolutionary models. The work undertaken in this thesis focuses specifically on attaining precise mass measurements using the synergistic capabilities of the Hipparcos and Gaia astrometric missions. By combining multiple observation data types, namely Radial Velocity (RV), relative astrometry, and absolute astrometry, one can determine the 3D Keplerian orbit and the precise dynamical mass of a potential, presumably faint companion orbiting a star by measuring the reflex motion of the star in the sky as it responds to the gravitational tug exerted by the unseen companion in orbit.

In Chapter 2, we demonstrate the powerful combination of radial velocities, direct imaging, and Hipparcos and Gaia absolute astrometry via the Hipparcos-Gaia Catalog of Accelerations (HGCA) to achieve highly accurate dynamical mass measurements. To accomplish this, we utilize the Markov-Chain-Monte-Carlo code `orvara`, along with the epoch astrometry fitting code `htof`, which enable us to effectively constrain orbits using these three distinct sources of data. By employing `orvara`, we successfully address the inherent degeneracy in determining an exoplanet's mass and inclination encountered in RV-only studies by incorporating absolute astrometry in conjunction with radial velocity. Moving on to Chapter 3, we focus on astrometry-only data, using Gaia EDR3 to calibrate ground-based relative and absolute astrometry from VLT/ESO, to precisely determine the barycentric orbit of ε Indi B, one of the closest and the first discovered binary T dwarf systems. These measurements establish them as the most accurately characterized binary brown dwarfs to date, and enable both a relative and absolute test of currently available substellar cooling models. In Chapter 4 and Chapter 5, we present the detection results from our pilot observation program conducted at the Keck/NIRC2 instrument, aiming to identify and image substellar companions around nearby accelerating stars. By utilizing the valuable precursor information from `orvara` and HGCA, we are able to predict the precise location of the companion a priori, detect the companion with direct imaging, and jointly fit orbits to their data to obtain precise dynamical masses. Our work significantly enhances the success rate of high-contrast imaging surveys, and can serve as a powerful tool for selecting promising follow-up candidates for interferometry and spectroscopic characterizations with instruments like JWST and GRAVITY/KPIC.

Contents

Chapter 1

Introduction

1.1 Planets and Brown Dwarfs

Planets are substellar objects that orbit stars and lack the mass required for sustained nuclear fusion or deuterium burning ($\geq\sim 13\ M_{\rm Jup}$) (Luhman, 2008). They span a wide range of sizes, compositions, and environments. Plants are typically formed through the process of accretion within protoplanetary disks (Chambers, 2010). They can be found in a variety of systems, including single-star systems like our own solar system, as well as multiple-star systems. The diversity of planets is vast, ranging from small rocky worlds like Earth to gas giants like Jupiter and Saturn. They can also exhibit a range of atmospheres and surface conditions, influenced by factors such as their distance from the host star, composition, and presence of an atmosphere (Alibert et al., 2018). For example, rocky planets like Earth have a solid surface and a variety of atmospheric compositions, including nitrogen, oxygen, and trace amounts of other gases (Morley et al., 2017). Gas giants, on the other hand, are composed primarily of hydrogen and helium and possess thick atmospheres with swirling clouds and powerful storms (Helled et al., 2022).

Brown dwarfs (BDs) are substellar objects above the deuterium burning mass limit ($\geq\sim 13\ M_{\mathrm{Jup}}$) (Luhman, 2008) but with insufficient mass ($\leq\sim 75\ M_{\mathrm{Jup}}$) (Spiegel et al., 2011; Dieterich et al., 2014) to achieve the core densities and pressures to sustain stable nuclear fusion of hydrogen to helium (Kumar, 1963; Hayashi & Nakano, 1963). Brown dwarfs may form isolated, in multiple systems or in protostellar disks and envelopes around single stars (Chabrier et al., 2000; Stamatellos et al., 2007). The surface effective temperature of a brown dwarf post formation is in the range of $\sim$2,500 $-$ 3,000 K (Basri, 2000). Brown dwarfs gradually lose energy radiatively and become denser and cooler with time, until electron degeneracy pressure halts gravitational collapse (Stamatellos & Whitworth, 2008). Their surface temperature drops to 50% of its original value by $\sim$500 Myr as the deuterium gets depleted. As they age and cool, they evolve across the M, L, T, and Y spectral types categorizable with infrared spectroscopy. The observed temperatures are as low as $\sim$250 K for late type ultra-cool brown dwarfs with low masses (Luhman, 2008; Phillips et al., 2020a). For example, an L-dwarf ($T_{\mathrm{eff}} =\sim$ 1250-2000 K) spectrum is dominated by metal hydride absorption bands (FeH, CrH, MgH, CaH) and prominent alkali metal lines (Na I, K I, Cs I, Rb I), while the cooler T-dwarfs with surface temperatures of $\sim$500-1250 K have methane-rich atmospheres characterized by absorption lines of H_2O, CO, TiO and CH_4 (Lodders & Fegley, 2006; Delorme et al., 2008; Phillips et al., 2020a). The chemically diverse atmospheres of brown dwarfs disclose crucial information on their appearance, physical processes, evolution, cooling, effective temperature, and luminosity (Madhusudhan et al., 2011).

Over the last two decades, the evolution of brown dwarfs became mainly understood through theoretical modeling (Marley et al., 1996; Saumon & Marley, 2008). In particular, cloud formation in brown dwarf atmospheres is thought to be an important factor in understanding major variations in their thermal spectra and observable properties, especially those on the L-T transition (Cooper & Showman, 2006; Morley et al., 2017). Brown dwarfs cool on a timescale of several million years post-formation, and their cooling follows a mass-luminosity-age relation. Uncertainties in the measurements of mass, age or luminosity, especially in mass and age, present a major challenge for using them to test and calibrate evolutionary and brown dwarf cooling models (Burrows et al., 1989; Dupuy & Liu, 2017a). Therefore, brown dwarfs whose properties are measured independent of evolutionary models serve as important benchmark objects anchoring our understanding of brown dwarf properties and their evolution.

1.2 Dynamical Mass Measurements of Substellar Companions

1.2.1 Precise Masses and Inclinations for RV Planets

The radial velocity (RV) technique is one of the earliest and most commonly used indirect methods in the detection of exoplanets in both nearby and distant solar systems (Hatzes, 2016; Wei, 2018; Wright, 2018). 51 Pegasi b, the first exoplanet around a Sun-like star, was discovered via RV in 1995 (Mayor & Queloz, 1995). Since then, RV instruments have overcome many design and performance challenges to reach extreme m/s precisions, at once revealing the richness and diversity of the population of exoplanets (e.g. Udry et al., 2007; Akeson et al., 2013; Rice, 2014).

The RV method measures the Doppler shift in the spectrum of a star perturbed by one or multiple unseen orbiting companions (Walker, 2012; Plavchan et al., 2015; Fischer et al., 2016; Wright, 2018). The RV semi-amplitude due to a companion scales with the companion's mass, the sine of the orbital inclination ($\sin i$), and the inverse of the square root of the semi-major axis. This means that massive and close-in RV companions are usually more easily and precisely characterized owing to complete orbital coverage. Much like 51 Pegasi b, these are often short-period Jupiter analogs orbiting solar-type stars (Wright et al., 2003).

Thanks to the growing temporal baselines of RV surveys, detection sensitivity is now being extended beyond the ice line ($\gtrsim$ 3 AU) (Ford, 2014; Wittenmyer et al., 2016). In this wider orbital regime, long-period giant planets are frequently being revealed (Perrier et al., 2003; Marmier et al., 2013; Rickman et al., 2019). Small planets or Uranus/Neptune-like ice giants on such wide orbits however are very challenging to detect due to long orbital periods (80-165 years), low transit probability, and the high contrast barrier. Still longer-period companions can induce measurable RV trends or accelerations (Eisner & Kulkarni, 2001; Cumming, 2004; Knutson et al., 2014). Sumi et al. 2016.

Not all stars are accessible to RV searches for planets. RV surveys often target old and inactive main sequence FGK stars and M dwarfs because their lower RV jitter and abundance of narrow absorption lines allow very precise velocity measurements (e.g. Howard et al., 2012; Marchwinski et al., 2014; Gaidos et al., 2016; Hsu et al., 2019; Borgniet et al., 2019; He et al., 2020; Bauer et al., 2020; Jin, 2021). In addition, there are several limitations to using the RV method alone to characterize long period companions. Firstly, orbital phase coverage drives estimations of orbital periods, so the RVs must cover a significant fraction of an orbit which requires long term time commitments from RV-surveys. Secondly, RVs only constrain $M_p \sin i$, providing a minimum mass that is estimated assuming an edge-on system with $\sin i = 1$. This $\sin i$ degeneracy permits only a statistical estimate of a planet's true mass and limits our ability to understand an individual exoplanetary system (e.g., Batalha et al., 2019; Gaudi, 2021).

One way to break the degeneracy in RV-only orbital fits is to combine RVs with precision astrometry. Astrometry measures the sky-projected Keplerian motion of accelerating stars. Together, radial velocity accelerations and astrometric accelerations probe orthogonal components of the 3D acceleration of a star through space, enabling us to map out the complete stellar reflex motion of a star under the influence of any unseen companion(s) (Lindegren & Dravins, 2003).

Efforts to measure the reflex motion of stars astrometrically date back to the Fine Guidance Sensor (FGS) on the Hubble Space Telescope (HST). FGS/HST has achieved sub-milliarcsecond single-star optical astrometry precision (Benedict et al., 2008). Pioneering works incorporated HST/FGS observations in ground-based astrometric and radial velocity fits to derive true masses for exoplanetary systems (e.g., Benedict et al., 2002; Benedict et al., 2006; McArthur et al., 2010). Beyond FGS/HST, the recent advent of Gaia astrometry and long-baseline interferometry open up the possibility of identifying and characterizing accelerating systems more systematically and on a larger scale. In particular, the combination of proper motion data from *Hipparcos* and *Gaia* provides a powerful and unique opportunity to realize this.

Previous works have explored the idea of using *Hipparcos* epoch astrometry in conjunction with RVs or relative astrometry to obtain precise dynamical masses (e.g., Han et al. (2001); Sozzetti & Desidera (2010); Reffert & Quirrenbach (2011); Sahlmann et al. (2011)). More recently, with the release of *Gaia* astrometry, a number of works have achieved improved astrometric/RV mass approximations by combining different data types: RV+relative astrometry (e.g., Brown, 2011; Boffin et al., 2016), RV+absolute astrometry (e.g., Feng et al. (2019); Kervella et al. (2019); Venner et al. (2021)), relative astrometry+absolute astrometry (e.g., Chen & Li et al. (2022)), or RV+relative astrometry+absolute astrometry (e.g., Snellen & Brown (2018); Brandt et al. (2019); Grandjean et al. (2019); Brandt et al. (2020); Nielsen et al. (2020); Brandt et al. (2021a); Kiefer et al. (2021); Brandt et al. (2021b)).

In Chapter 2, we derive orbital solutions for nine RV-detected exoplanet candidates by jointly analyzing RVs and complementary absolute astrometry data from the

HGCA (Gaia EDR3 version): HD 29021, HD 81040, HD 87883, HD 98649, HD 106252, HD 106515 A, HD 171238, HD 196067, and HD 221420. We use the MCMC orbit-fitting package `orvara` (Brandt et al., 2021g) that is capable of fitting one or more Keplerian orbits to any combination of RVs, direct imaging astrometry and absolute astrometry from the HGCA. Because the epoch astrometry from Gaia is not yet available, `orvara` uses the intermediate astrometry fitting package `htof` (Brandt et al., 2021b) to provide a workaround for this. `htof` fetches the intermediate astrometry from Hipparcos and Gaia, and reproduces positions and proper motions from synthetic Hipparcos or Gaia epoch astrometry using five or higher degree parameter fits. We focus our work on systems with known single RV companions. Two host stars in our sample, HD 106515 A and HD 196067, have known wide stellar companions that we solve as 3-body systems with `orvara`.

1.2.2 Revised Orbits for the T-dwarf Binary ε Indi B

ε Indi B, discovered by Scholz et al. (2003), is a distant companion to the high proper motion (∼4.7 arcsec/yr) star ε Indi. It was later resolved to be a binary brown dwarf system by McCaughrean et al. (2004), who estimated the two components of the binary, ε Indi Ba and Bb, to be T dwarfs with spectral types T1 and T6, respectively. It was the first binary T dwarf to be discovered and remains one of the closest binary brown dwarf systems to our solar system; *Gaia* EDR3 measured a distance of 3.638 ± 0.001 pc to ε Indi A (Lindegren et al., 2020). Their proximity makes ε Indi Ba and Bb bright enough and their projected separation wide enough to obtain high quality, spatially resolved images and spectra. And their relatively short orbital period of $\approx$10 yr allows the entire orbit to be traced in a long-term monitoring campaign. Being near the boundary of the L-T transition, ε Indi Ba is especially valuable for understanding the atmospheres of these ultra-cool brown dwarfs (Apai et al., 2010; Goldman et al., 2008; Rajan et al., 2015).

King et al. (2010) carried out a detailed photometric and spectroscopic study of the system, and derived luminosities of $\log_{10} L/L_{\odot} = -4.699 \pm 0.017$ and -5.232 ± 0.020 for Ba and Bb, respectively. They found that neither a cloud-free nor a dusty atmospheric model can sufficiently explain the brown dwarf spectra, and that a model allowing partially settled clouds produced the best match. The relative orbit monitoring was still ongoing at the time, so a preliminary dynamical system mass of $121 \pm 1\, M_{\rm Jup}$ measured by Cardoso (2012) was assumed by the authors to derive mass ranges of 60-73 $M_{\rm Jup}$ and 47-60 $M_{\rm Jup}$ for Ba and Bb based on their photometric and spectroscopic observations.

In this Chapter, we use relative orbit and absolute astrometry monitoring of ε Indi B from 2005 to 2016 acquired with the VLT to measure the individual dynamical masses of ε Indi Ba and Bb. Much of this data set overlaps with that used by Cardoso (2012), but we have the advantage of a few more epochs of data, *Gaia* astrometric references (Lindegren et al., 2020) and a better understanding of the direct imaging system thanks to years of work on the Galactic center (Gillessen et al., 2009; Plewa et al., 2015; Gillessen et al., 2017).

1.2.3 Discovery and characterization of a T-dwarf companion HD 176535 B

Young and/or massive brown dwarfs may be directly imaged with the high-contrast imaging technique, providing measurements of their spectra and luminosities. Furthermore, those with RV curves may also be amenable to dynamical mass measurements. To date, close to 30 brown dwarfs with a range of ages and orbital periods have been directly imaged and characterized. These brown dwarfs have been routinely used as benchmarks for substellar evolutionary models (Crepp et al., 2013; Dupuy & Liu, 2017b; Crepp et al., 2016, 2018a; Brandt et al., 2020; Currie et al., 2020; Brandt et al., 2021d; Bowler et al., 2021; Franson et al., 2022a; Chen & Li et al., 2022; Rickman et al., 2022; Swimmer et al., 2022; Kuzuhara et al., 2022; Currie et al., 2022). The T-type brown dwarfs with spectral types T0-T9 were first observed and classified in 1995 (Oppenheimer et al., 1995), which are cool brown dwarfs exhibiting methane absorption features in the near-infrared wavelengths of 1-2.5μm, distinguishing them from the warmer L dwarfs. Most measured T dwarfs have relatively low masses ($\sim 30-60 M_{\rm Jup}$) given their low temperatures, allowing them to progressively cool through the T dwarf sequence over 1-5 Gyr.

With more and more benchmark T dwarfs being observed and characterized, there emerges a small but alarming list of over-massive and under-luminous T dwarfs that challenge the validity of most substellar cooling models, which predict that such massive objects cannot sufficiently cool to their observed low temperatures within their (approximately) known ages. For example, the first T dwarf Gl 229 B's very high mass

$(71.4 \pm 0.6 M_{\rm Jup})$ and low luminosity does not match with the model predictions even at a very old age (Brandt et al., 2020, 2021d). The late-T dwarf HD 4113 C is another example presenting a severe challenge to evolutionary models because its measured dynamical mass of 66 $M_{\rm Jup}$ is significantly higher than the model prediction of $\sim 40 M_{\rm Jup}$ given its low luminosity of $10^{-6} L$ (Cheetham et al., 2018). The late-T dwarf HD 47127 B is a massive and old (7– 10 Gyr) brown dwarf companion to a white dwarf, and another peculiar case where the models prefer a high mass of $100 M_{\rm Jup}$ that is at odds with the measured mass of $67 - 78 M_{\rm Jup}$ (Bowler et al., 2021).

However, despite the couple of outliers, most benchmark T dwarfs appear to be in agreement with evolutionary models (e.g. Dupuy & Liu (2017b); Brandt et al. (2019); Brandt et al. (2021d)): both T dwarfs of the binary brown dwarf system ε Indi B were previously believed overmassive T dwarf candidates (Dieterich et al., 2018), but the recent re-analysis by Chen & Li et al. (2022) supports the consistency of evolutionary models. One possible resolution to the over-massive T dwarf problem is unresolved multiplicity. In this scenario, nearly all of the light would be due to the observed T dwarf, while a modest fraction of the mass would be hidden in a somewhat lower-mass, but much fainter, companion. Unresolved, lower-mass companions would contribute almost nothing to the overall integrated spectra of the brown dwarfs at older ages. If binarity can be ruled out as the cause of the disagreement, these overmassive brown dwarfs may point to a strong tension with evolutionary models. A larger sample of well-characterized brown dwarfs will be required in order to investigate the T dwarf population.

Astrometry has recently emerged as a way to identify stars being tugged across the sky by massive, unseen companions, a new method to identify hosts of T dwarfs. Satellites such as ESA's Hipparcos and Gaia have provided absolute astrometry for billions of stars across the sky; the Hipparcos-Gaia Catalog of Accelerations (HGCA) (Brandt, 2021a) has cross-calibrated Hipparcos and Gaia astrometry. Here, we report the first results from a pilot Keck AO direct imaging survey with the NIRC2 vortex coronagraph at the Keck Observatory targeting stars with astrometric accelerations in the HGCA. With astrometry, one can identify targets worthy of following up by deriving their orbits from RV and absolute astrometry joint fits. Also using this new technique to pre-identify targets, several groups have carried out similar follow-up imaging surveys (Fontanive et al., 2019; Currie et al., 2021; Bonavita et al., 2022; Franson et al., 2022b) that greatly improved detection rates unparalleled by traditional blind imaging surveys. The T-dwarf companion HD 176535 B presented in this Chapter is among the first companions discovered whose astrometric location was known before imaging. In Chapter 4, we present an `orvara` fit incorporating our new Keck/NIRC2 astrometry data to constrain the mass and 3D orbit of the system.

1.2.4 Imaging Detection and Orbital Characterization of HD 63754 B

The stellar-substellar boundary divides brown dwarfs and low-mass stars based on their physical properties. It is primarily defined by an object's mass ($\sim 0.07 - 0.75M$) and its ability to initiate and sustain hydrogen fusion reactions in its core (Dieterich et al., 2014;

Chabrier & Johansson, 2023). Stars maintain stable nuclear fusion of hydrogen atoms into helium in their cores to withstand the forces of gravitational collapse, whereas brown dwarfs with insufficient masses rely on gravitational contraction and the counteracting pressure exerted by electron degeneracy. The mass of the substellar-stellar boundary is also influenced by other parameters such as formation environment and chemical composition (Leggett et al., 1998; Levine et al., 2006; Allard et al., 2012; Gonzales, 2020). Chabrier & Johansson (2023) incorporates a new Equation Of State (EOS) for dense hydrogen-helium mixtures to model the evolution of brown dwarfs and very low-mass stars, and found improved agreement with observationally determined brown dwarf masses. They report a slight increase in the hydrogen-burning minimum mass to 0.075 M ($78.5M_{\mathrm{Jup}}$). Benchmark objects with well-determined masses, ages and luminosities independent of models can be used to test against various evolutionary models (Dupuy et al., 2009; Dupuy & Liu, 2017a; Franson et al., 2023). Past studies found that transitional brown dwarfs – those at the Y/L or L/T transition – have low-rate unsteady hydrogen fusion in their cores, resulting in a slowed cooling rate compared to degenerate brown dwarfs (Zhang, 2021). Recent studies like Chen et al. (2022) found evidence for slowed cooling and cloud clearing for L/T transitional brown dwarfs like ε Ind Ba.

Direct Imaging has become a powerful technique when combined with other detection methods to yield comprehensive characterization of orbits of companions around accelerating stars (Brandt et al., 2021f,d). Blind direct imaging surveys have traditionally low detection rate, especially companions around solar- and subsolar-mass stars. Detection limits of imaging surveys decrease with increasing separation, making it challenging to detect fainter and smaller exoplanets that have low scattered light. Thus, significant improvements in blind survey yields would require substantial gains in contrast or sensitivity at small or wide separations, respectively. However, despite the technique's bias toward young, wide-orbit companions, the occurrence rate of exoplanets at wider separations is low (Nielsen et al., 2019; Bowler & Nielsen, 2018). Luckily, targeted searches on stars exhibiting reflex motion can improve survey outcomes. Both radial velocity and astrometry probe the reflex motion of stars in orthogonal directions. Radial velocity data have been used to identify direct imaging follow-up companions (Crepp et al., 2014), while astrometry as a target selection method is a novel approach that has been demonstrated to be effective by several surveys (Rickman et al., 2016; Currie et al., 2020; Franson et al., 2023). The Hipparcos-Gaia Catalog of Accelerations (HGCA) (Brandt et al., 2021f) offers absolute astrometry for about 115,000 nearby stars, including those with clear evidence of massive, unseen companions. HGCA-derived accelerations can provide dynamical masses of imaged exoplanets and low-mass brown dwarfs independently of luminosity evolution models and stellar age uncertainties (Brandt et al., 2019; Dupuy et al., 2019). This method is particularly useful for stars where precise radial-velocity measurements are unfeasible due to their activity and spectral type.

In Chapter 5, we report the discovery of a massive companion located $0\farcs48$ from HD 63754, a nearby Sun-like star, which lies near the boundary between substellar and stellar masses. Using NIRC2 L'-band imaging on Keck, we discovered the companion as part of a larger survey targeting substellar companions around accelerating stars. This builds on our previous success in the survey, which yielded the discovery of a massive brown dwarf, HD 176535 B, around a K-type star (Li et al., 2023). We present the dynamical mass determinations and orbital constraints for HD 63754 B using a combination of radial velocity, relative astrometry from direct imaging, and Hipparcos-gaia DR3 accelerations.

Chapter 2

Resolving the Msin(i) Degeneracy in RV Systems

2.1 Methods to Fit Orbits of Exoplanets

In this chapter, we first introduce `orvara` (Orbits from Radial Velocity, Absolute, and/or Relative Astrometry), a powerful software designed to analyze data derived from radial velocity, relative astrometry, and absolute astrometry from the Hipparcos-Gaia Catalog of Accelerations (HGCA) (Brandt, 2018). By harnessing the combined usage of these three data types, `orvara` enables precise mass measurements and determination of orbital parameters, even when observations cover only a fraction of an orbit. We demonstrate that `orvara` calculates such orbits with great speed and precision.

Following its introduction, we showcase the remarkable capability of `orvara` to overcome the degeneracy present in a sample of radial velocity planets by incorporating their stellar absolute astrometry from the HGCA. Through the utilization of `orvara`, we successfully obtain precise measurements of their masses and inclinations, which would be unattainable with radial velocity data alone. This study explores a key aspect of the `orvara` code, showcasing one of its initial applications in disentangling mass from inclination in traditional radial velocity orbit fittings.

The contents of this chapter have been published in Brandt et al. (2021f) for `orvara`, and Li et al. (2021a) under the title “Precise Masses and Orbits for Nine Radial-velocity Exoplanets”.

2.1.1 Keplerian Orbit

A Keplerian orbit, which arises from the two-body problem in Newtonian gravity, can be fully characterized by six orbital elements and the masses of the two components. The goal is to determine posterior probability distributions for these eight parameters using measured positions and velocities. This involves accounting for various nuisance parameters, such as the barycenter position, parallax, velocity, and astrophysical jitter in measured radial velocities.

Here, we present the theoretical equations that relate the measured positions and velocities to time and orbital parameters briefly. The mean anomaly M varies linearly with time as

$$M = \frac{2\pi}{P}\left(t - t_p\right) \tag{2.1}$$

where P is the system period and t_p is the epoch of periastron passage. The position and velocity may be computed using the eccentric anomaly, which is given implicitly by

$$M = E - \varepsilon \sin E \tag{2.2}$$

where ε is the eccentricity. The radial velocity RV is given through the true anomaly ν by

$$\nu = 2\,\mathrm{atan2}\left[\sqrt{1+\varepsilon}\sin\frac{E}{2}, \sqrt{1-\varepsilon}\cos\frac{E}{2}\right] \tag{2.3}$$

$$\mathrm{RV} = k\left(\cos\left[\nu + \omega\right] + \varepsilon\cos\omega\right), \tag{2.4}$$

where ω is the argument of periastron, k is the radial velocity amplitude, and atan2 is the two-argument arctangent. We adopt a convention that the orbital parameters all refer to the companion(s). The orbital parameters for the primary are the same except that $\omega_{\mathrm{pri}} = \omega + \pi$.

2.1.2 Types of Data for Measuring Orbits

Constraints on a system's orbit may come from measurements of the primary star's radial velocity over time, the projected angular offset of the two bodies, and/or the projected motion of either component relative to the system's barycenter in an inertial reference frame. This method works because the absolute stellar astrometric accelerations from HGCA, relative astrometry from direct imaging and RV combined through the following equations

$$a_{rv} = \frac{GM_2}{r_{12}^2} sin\phi \qquad a_{astrometric} = \frac{GM_2}{r_{12}^2} cos\phi \qquad \rho_{projected} = r_{12} cos\phi \tag{2.5}$$

will uniquely determine the companion mass M_2.

Radial Velocity

More accurately, given the eccentric anomaly E, eccentricity ε, and radial velocity amplitude k, the radial velocity can be calculated by Equations 2.3 and 2.4. The relative offsets of the secondary from the primary star in right ascension $\alpha*$ and declination δ (where $\alpha* = \alpha \cos \delta$) are given by Equations (2.14) and (2.15). We typically fit orbits using both absolute and relative astrometry. The displacement of the primary star from the system's barycenter is related to the relative separations of Equations (2.14) and (2.15) by

$$\Delta\delta_\star = \left(\frac{-M_\mathrm{B}}{M_\mathrm{A} + M_\mathrm{B}} \right) \Delta\delta \tag{2.6}$$

$$\Delta\alpha*_\star = \left(\frac{-M_\mathrm{B}}{M_\mathrm{A} + M_\mathrm{B}} \right) \Delta\alpha* \tag{2.7}$$

where M_A is the mass of the primary star and M_B is the mass of its companion.

Relative Astrometry

The projected offset between the two bodies may be computed through the elliptical rectangular coordinates

$$X = \cos E - \varepsilon \tag{2.8}$$

$$Y = (\sin E)\sqrt{1-\varepsilon^2}, \tag{2.9}$$

and the Thiele-Innes constants

$$A = \cos\Omega\cos\omega - \sin\Omega\sin\omega\cos i \tag{2.10}$$

$$B = \sin\Omega\cos\omega + \cos\Omega\sin\omega\cos i \tag{2.11}$$

$$F = -\cos\Omega\sin\omega - \sin\Omega\cos\omega\cos i \tag{2.12}$$

$$G = -\sin\Omega\sin\omega + \cos\Omega\cos\omega\cos i. \tag{2.13}$$

In Equations (2.10)–(2.13), i is the inclination, and Ω is the longitude of the ascending node. The projected offsets of the secondary with respect to the primary star in declination $\Delta\delta$ and right ascension $\Delta\alpha* = \Delta(\alpha\cos\delta)$ are then given by

$$\Delta\delta = a(AX + FY) \tag{2.14}$$

$$\Delta\alpha* = a(BX + GY) \tag{2.15}$$

where a is the semimajor axis in angular units.

Absolute Astrometry

Astrometric missions like *Hipparcos* and *Gaia* measure the position of a star many times and fit an astrometric sky path. We use the Hundred Thousand Orbit Fitter (`htof`) (Brandt et al., 2021b) to compute synthetic *Hipparcos* and *Gaia* catalog positions and proper motions from the offsets given in Equations (2.6) and (2.7). We then compare the `htof` synthetic catalog values to the cross-calibrated absolute astrometry of HGCA (Brandt, 2018). We refer the reader to the source code at https://github.com/gmbrandt/htof for further details.

2.1.3 Likelihood of an Orbit

We compute the likelihood $\mathcal{L}$ of an orbit as

$$-2\ln\mathcal{L} = \chi^2 = \chi^2_{\rm RV} + \chi^2_{\rm rel\,ast} + \chi^2_{\rm abs\,ast}. \tag{2.16}$$

We treat $\chi^2_{\rm RV}$, the radial velocity component, first. We then take the latter two terms together as we marginalize out the barycenter's proper motion and the system's parallax.

For the radial velocity, we take

$$\chi^2_{\rm RV} = \sum_{j=1}^{N_{\rm inst}} \sum_{k=1}^{N_{\rm RV}} \left(\frac{\left({\rm RV}_k + {\rm ZP}_j - {\rm RV}\left[t_k\right]\right)^2}{\sigma^2[{\rm RV}_k] + \sigma^2_{\rm jit}} \right. \\ \left. + \ln\left[\sigma^2[{\rm RV}_k] + \sigma^2_{\rm jit}\right] \right), \tag{2.17}$$

where ZP_j is the instrument-specific radial velocity zero point and $\sigma^2_{\rm jit}$ is a jitter term. We use RV_k to denote the measured RV at epoch t_k, $\mathrm{RV}[t_k]$ for the model-predicted RV and $\sigma^2[\mathrm{RV}_k]$ for its variance.

The χ^2 for relative astrometry consists of two components: the relative separation ρ and the position angle θ measured east of north. The model orbit's relative separation is the product of the projected relative separation ρ in AU and the system's parallax ϖ. In general, the measurements of separation and position angle may be covariant: we take $c_{\rho\theta,k} \in (-1, 1)$ to be the correlation coefficient between the two measurements at epoch k. The contribution to χ^2 is then

$$\begin{aligned}\chi^2_{\rm rel\,ast} = &\sum_{k=1}^{N_{\rm ast}} \frac{\lfloor \theta_k - \theta[t_k] \rfloor^2}{(1-c^2_{\rho\theta,k})\sigma^2[\theta_k]} + \sum_{k=1}^{N_{\rm ast}} \frac{\left(\rho_k - \varpi\rho\,[t_k]\right)^2}{(1-c^2_{\rho\theta,k})\sigma^2[\rho_k]} \\ &- 2\sum_{k=1}^{N_{\rm ast}} \frac{c_{\rho\theta,k}\lfloor \theta_k - \theta[t_k] \rfloor \left(\rho_k - \varpi\rho\,[t_k]\right)}{(1-c^2_{\rho\theta,k})\sigma[\theta_k]\sigma[\rho_k]}.\end{aligned} \tag{2.18}$$

where ρ_k and θ_k are the observed separation and position angle at time t_k, $\rho[t_k]$ and $\theta[t_k]$ are the model-predicted values, and $\lfloor \theta_k - \theta[t_k] \rfloor$ is the difference between the measured and the predicted position angles, reduced to the range $(-\pi, \pi]$.

The absolute astrometry in angular units is similarly proportional to parallax, and also has a velocity zero point. This is the proper motion of the system barycenter in the plane of the sky $\overline{\boldsymbol{\mu}}$, an almost perfect analog of the radial velocity zero point. This component of the likelihood then reads

$$
\begin{aligned}
\chi^2_{HG} = &\left(\boldsymbol{\mu}_{H,\mathrm{o}} - \overline{\boldsymbol{\mu}} - \varpi\boldsymbol{\mu}_H\right)^T \mathbf{C}_H^{-1} \left(\boldsymbol{\mu}_{H,\mathrm{o}} - \overline{\boldsymbol{\mu}} - \varpi\boldsymbol{\mu}_H\right) \\
&+ \left(\boldsymbol{\mu}_{HG,\mathrm{o}} - \overline{\boldsymbol{\mu}} - \varpi\boldsymbol{\mu}_{HG}\right)^T \mathbf{C}_{HG}^{-1} \left(\boldsymbol{\mu}_{HG,\mathrm{o}} - \overline{\boldsymbol{\mu}} - \varpi\boldsymbol{\mu}_{HG}\right) \\
&+ \left(\boldsymbol{\mu}_{G,\mathrm{o}} - \overline{\boldsymbol{\mu}} - \varpi\boldsymbol{\mu}_G\right)^T \mathbf{C}_G^{-1} \left(\boldsymbol{\mu}_{G,\mathrm{o}} - \overline{\boldsymbol{\mu}} - \varpi\boldsymbol{\mu}_G\right) \qquad (2.19)
\end{aligned}
$$

where, e.g., $\boldsymbol{\mu}_{H,\mathrm{o}}$ is the observed *Hipparcos* proper motion and $\boldsymbol{\mu}_H$ is the model orbit's predicted *Hipparcos* proper motion in $\mathrm{AU\,yr^{-1}}$ (which must then be multiplied by the parallax to obtain a proper motion in angular units).

2.1.4 MCMC Orbit Code `orvara`

Inspired by the methodology of Brandt et al. (2019), we adopt a similar approach to simultaneously fit absolute astrometry, relative astrometry, and/or radial velocities of a given star and its companion. Our orbit fitting package `orvara` is such a Python code specifically designed for rapid orbit-fitting and visualization of orbits of Keplerian systems. `orvara` is designed to model orbital elements of a Keplerian orbit within the context of Gaussian uncertainties. To enhance computational efficiency, we have implemented several optimizations, including a more efficient eccentric anomaly solver, marginalization of nuisance parameters in the likelihood function, and the utilization of low-level memory management to minimize Python overhead.

Equations (2.18) and (2.19) are quadratic equations in parallax and the two components of the proper motion of the system's barycenter. We adopt a uniform prior on $\overline{\boldsymbol{\mu}}$, but use a Gaussian prior in parallax to incorporate the measured *Gaia* value. This is equivalent to adding one additional component to the log likelihood,

$$\chi^2_{\varpi} = \frac{\left(\varpi - \varpi_{Gaia}\right)^2}{\sigma^2_{\varpi, Gaia}}. \tag{2.20}$$

With the addition of Equation (2.20), we can write the design matrix of the system and solve for the maximum likelihood values of the parameters and their covariance matrix. Integrating the likelihood over parallax and barycentric proper motion is equivalent to substituting these maximum likelihood values into the expressions for χ^2 and multiplying the likelihood by the square root of the determinant of the covariance matrix. We refer the reader to the paper for more detailed mathematical formulation.

With `orvara`, for the first time, we have the capability to detect faint companions without the need to extensively monitor their radial velocity orbits. This also marks a departure from the era of blind direct imaging searches, the results of which will be discussed in Chapter 4 and Chapter 5. In the following sections of this Chapter, we describe the use of `orvara` for breaking the Msin(i) degeneracy of companions in a sample of nine RV systems, including discussions of individual results.

2.2 Sample Properties

Our sample of targets comprises nine dwarf stars of G and early K spectral types, all of which have long term RV monitoring and precision spectroscopy. These stars have precise RV time series because their stable atmospheres and rich absorption spectra make them ideal targets for RV surveys: G and K stars constitute the majority of the host stars of RV-detected planets (Lineweaver & Grether, 2003). In this Section, we provide a general overview on the photometric and atmospheric properties of the host stars using values from the literature. We then derive our own constraints on the ages and masses of our host stars. We need stellar masses in particular to infer planet masses from RV time series: the RV semi-amplitude is a function of both companion mass and total system mass.

2.2.1 Activity-based Age Analysis

Stellar magnetic activity is a term that encompasses a range of phenomena observed of a star, including flares, star spots, and any chromospheric and coronal activity. Mid-F type and cooler main-sequence stars experience a decline in magnetic activity levels and rotational velocity as they age. The well-accepted explanation for the weaker activity and the slower rotation rates of old stars is the dynamo theory developed by Schatzman (1962, 1990); Parker (1955, 1979): late-type stars develop subsurface convection zones that support a magnetic dynamo. The dynamo provides the energy to heat the stellar chromosphere and corona (Kraft, 1967; Hall, 2008; Testa et al., 2015, and references therein). The chromospheres eject winds in the form of jets or flares. These rotate with the stellar angular velocity out to the Alfvén radius, carrying away angular momentum which in turn causes the star to spin down over time. This effect is known as magnetic braking through the magnetic dynamo process (Noyes et al., 1984). The declining rotational velocity due to magnetic braking results in a reduction in the magnetic field generated by the stellar dynamo which, in turn, diminishes the star's Ca II HK and X-ray emissions. Ca II HK and X-ray emission weaken fastest at young ages, thus age dating for young stars is easier than for their old field star counterparts (Soderblom, 2010).

Ca II HK emission, via the chromospheric activity index R'_{HK}, has been widely used as an age indicator for Solar-type (G and K) stars. Age dating of Sun-like stars with R'_{HK} was first done by Wilson (1968) at the Mount Wilson Observatory. The age-activity relationship has since been developed and calibrated across spectral types later than mid-F (Skumanich, 1972; Noyes et al., 1984; Soderblom et al., 1991; Barnes, 2007; Mamajek & Hillenbrand, 2008; David & Hillenbrand, 2015; Angus et al., 2015; van Saders et al., 2016; Lorenzo-Oliveira et al., 2016). Conventionally, R'_{HK} is calculated from the Ca II HK S-index, a measurement of the strength of the emission. Mamajek & Hillenbrand (2008) calibrated the activity relations to an activity level of $logR'_{\mathrm{HK}} \geq -5.0\,\mathrm{dex}$ or a Rossby number (ratio of rotation period to convective overturn time) of 2.2, roughly corresponding to the Solar activity and rotation.

X-ray activity traces magnetic heating of the stellar corona, providing another indirect probe of rotation (Golub, 1996; Mewe, 1996; Jardine et al., 2002; Güdel, 2004; Zhuleku et al., 2020). Brandt et al. (2014) combine R'_{HK} and X-ray activity to infer a Rossby number and, from this, an age via gyrochronology using the Mamajek & Hillenbrand (2008) calibration. Brandt et al. (2014) further allows for a distribution of times, dependent on spectral type, on the C-sequence where the dynamo is saturated and magnetic braking is inefficient (Barnes, 2003). Their model sets a floor for the Rossby number at > 2.2, inflates the error in the activity and rotation by 0.06 dex to account for systematic uncertainties.

A photometric rotation period provides a more direct measure of the Rossby number and a tighter constraint on the stellar age. For stars that have directly measured rotation periods, Brandt et al. (2014) combine this measurement with the indirect probes of coronal and chromospheric emission to derive an age posterior. We refer the reader to that paper for a more detailed discussion.

We adopt the Bayesian inference model described in Brandt et al. (2014) to estimate stellar ages. We take the Ca II HK S-indices from the catalog of Pace (2013) and references therein and convert them to Mt. Wilson $R'_{\rm HK}$ using the relations described in (Noyes et al., 1984). We extract X-ray activities R_X from the ROSAT all-sky survey bright and faint source catalogs (Voges et al., 1999, 2000). For stars that are not in either ROSAT catalog, we take the nearest detection in the faint source catalog and use five times its uncertainty as our upper limit on X-ray flux.

2.2.2 Stellar Luminosity Analysis

Here, we describe the method we use to estimate the bolometric luminosity for our sample of host stars. We adopt the absolutely calibrated effective temperature scales in Casagrande et al. (2010) for FGK stars across a wide range of metallicities. These authors use the InfraRed Flux Method (IRFM) to derive model independent effective

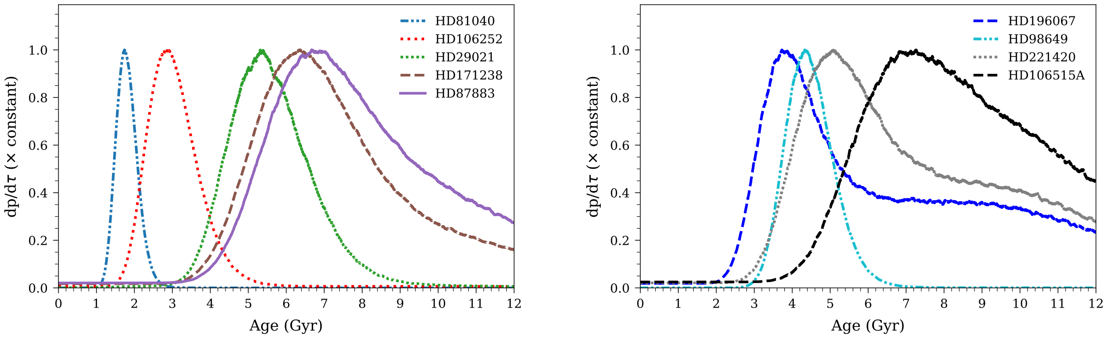

Figure 2.1 Normalized age posteriors for the nine stars presented in this work following the Bayesian technique of Brandt et al. (2014). This method combines the X-ray (R_X) and chromospheric activity ($R'_{\rm HK}$) indicators with an optional rotation period to constrain the Rossby number. It is then transformed into an age diagnostic for a specific star based on the calibration of Mamajek & Hillenbrand (2008).

temperatures $T_{\rm eff}$ in stars with different spectral types and metallicities. The homogeneous, all-sky Tycho-2 (B_T, V_T) optical photometry (Høg et al., 2000a) was combined with the 2MASS infrared photometry in the JHK_s bands (Skrutskie et al., 2006) to calibrate reliable $T_{\rm eff}$ for a sample of solar analogs via IRFM.

All of our stars are late G and K sun-like dwarfs with optical and infrared photometry from Tycho-2 $(BV)_T$ and 2MASS JHK_s, thus we use Table 5 of Casagrande et al. (2010) to derive their bolometric integrated fluxes. In Table 5, the set of Tycho-2 and 2MASS flux calibrations apply to a [Fe/H] range between -2.7 and 0.4, and a color range between 0.19 and 3.29. The standard deviation σ_{ϕ_ξ} in the Tycho-2 and 2MASS flux calibrations is the smallest for the $m_\xi = V_T$ flux calibrations with color indices $V_T - J$ (0.7%) and $V_T - K_s$ (0.9%). We use the $V_T - J$ colors to calibrate V_T magnitudes for our sample of stars with the exception of HD 221420, which has a large uncertainty in its 2MASS J band magnitude due to saturation (4.997 ± 0.252 mag). Therefore, for HD 221420, we

Table 2.1. Adopted stellar parameters for stars investigated in this work.[a]

Star (HD #)	29021	81040	87883	98649	106252
HIP ID	21571	46076	49699	55409	59610
$\bar{\omega}$ (mas)	32.385	29.063	54.668	23.721	26.248
$\sigma[\bar{\omega}]$	0.024	0.041	0.030	0.022	0.027
V_T (mag)	7.842	7.791	7.660	8.066	7.479
$\sigma[V_T]$	0.011	0.012	0.012	0.011	0.011
B_T (mag)	8.612	8.527	8.800	8.793	8.158
$\sigma[B_T]$	0.016	0.017	0.018	0.017	0.017
K_s (mag)	6.082	6.159	5.314	6.419	5.929
$\sigma[K_s]$	0.020	0.021	0.020	0.020	0.026
J (mag)	6.518	6.505	5.839	6.811	6.302
$\sigma[J]$	0.029	0.019	0.020	0.019	0.024
R_X	< -5.14	-5.27	< -5.25	< -4.87	< -5.20
$R'_{\rm HK}$	...	-4.71	-4.98	-4.96	-4.85
$P_{\rm rot}$ (days)	...	15.98	...	26.441	...
[Fe/H](dex)[b]	-0.30 ± 0.10	-0.04 ± 0.05	0.11 ± 0.10	-0.06 ± 0.04	-0.06 ± 0.04
$M_{*,\rm model}(M_\odot)$[c]	0.86 ± 0.02	0.99 ± 0.02	0.80 ± 0.02	0.97 ± 0.02	1.05 ± 0.02
$L_*(L_\odot)$[d]	0.659 ± 0.017	0.838 ± 0.018	0.338 ± 0.008	0.968 ± 0.019	1.328 ± 0.030
Spectral Type	G5	G2/G3	K0	G3/G5 V	G0
Age (Gyr)[e]	$5.5^{+1.2}_{-1.0}$	$1.79^{+0.30}_{-0.26}$	$7.6^{+2.8}_{-1.8}$	$4.44^{+0.68}_{-0.58}$	$3.00^{+0.80}_{-0.60}$

[a] See next Table for Caption.

use the $V_T - K_s$ index instead to calculate the flux calibration in its V_T.

The final bolometric magnitudes can be estimated in terms of the V_T magnitude, the distance d, and the the integrated bolometric fluxes $\mathcal{F}_{\rm Bol}$(Earth):

$$L_{Bol} = 4\pi d^2 10^{-0.4 V_T} \mathcal{F}_{\rm Bol}(\text{Earth}) \tag{2.21}$$

We express $L_{\rm Bol}$ in units of solar luminosity, adopting a value of $L_\odot = 3.828 \times 10^{33}$erg/s. Our parallaxes all have fractional uncertainties $\sim 10^{-3}$; they contribute negligibly to our luminosity uncertainties.

We propagate the errors using standard error propagation techniques. We estimate the final uncertainty in the luminosities as

Table 2.2. Adopted stellar parameters for stars investigated in this work (Cont'd) [a].

Star (HD #)	106515A	106515B *	171238	196067	196068 *	221420
HIP ID	59743A	59743B	91085	102125	102128	116250
$\bar{\omega}$ (mas)	29.315	29.391	22.481	25.033	25.038	32.102
$\sigma[\bar{\omega}]$	0.030	0.029	0.032	0.021	0.017	0.033
V_T (mag)	8.063	8.298	8.737	6.510	7.070	5.884
$\sigma[V_T]$	0.014	0.015	0.020	0.010	0.010	0.009
B_T (mag)	8.994	9.284	9.589	7.193	7.790	6.643
$\sigma[B_T]$	0.021	0.022	0.029	0.015	0.015	0.014
K_s (mag)	6.151	6.267	6.831	5.080	5.713	4.306
$\sigma[K_s]$	0.026	0.017	0.017	0.016	0.018	0.036
J (mag)	6.585	6.746	7.244	5.417	6.061	4.997
$\sigma[J]$	0.024	0.030	0.019	0.021	0.027	0.252
R_X	< -4.84	< -4.77	< -4.83	< -5.08	< -4.87	< -5.55
$R'_{\rm HK}$	-5.10	-5.15	-4.96	-5.06	-5.02	-5.05
$P_{\rm rot}$ (days)	...	...	...	...	...	...
[Fe/H] (dex)[b]	0.03 ± 0.10	0.03 ± 0.10	0.20 ± 0.10	0.23 ± 0.07	0.24 ± 0.10	0.34 ± 0.07
$M_{*,\rm model}(M_\odot)$[c]	0.89 ± 0.03	0.86 ± 0.03	0.92 ± 0.03	1.26 ± 0.07	1.12 ± 0.06	1.28 ± 0.08
$L_*(L_\odot)$[d]	0.686 ± 0.018	0.567 ± 0.017	0.627 ± 0.018	3.435 ± 0.068	2.007 ± 0.045	3.850 ± 0.072
Spectral Type	G5 V	G8 V	G8 V	G5 III	G5 V	G2 V
Age (Gyr)[e]	$8.2^{+2.7}_{-2.1}$	$8.4^{+2.6}_{-2.1}$	$7.0^{+6.0}_{-1.6}$	$5.8^{+4.3}_{-2.2}$	$6.2^{+4.1}_{-2.2}$	$6.6^{+3.7}_{-2.0}$

[*] Secondary stellar companion

[a] **References** – $\bar{\omega}$ from Gaia eDR3 (Gaia Collaboration et al., 2020); V_T and B_T from Tycho-2 (Høg et al., 2000a), K_s from 2MASS (Cutri et al., 2003); R_X from ROSAT (Voges et al., 1999); Rotation period for HD 81040 from Reinhold & Hekker (2020), alternatively 15.2579 days from Oelkers et al. (2018); $R'_{\rm HK}$ from (Pace, 2013); Rotation period for HD 98649 from Oelkers et al. (2018); Spectral types from Wright et al. (2003) and Skiff (2014).

[b] We estimate [Fe/H] from the median of all entries in (Soubiran et al., 2016) with a default uncertainty of 0.1 dex. The references for each star are: **?** for HD 29021; Sousa et al. (2006); Gonzalez et al. (2010); Kang et al. (2011); Luck (2017); Rich et al. (2017); Sousa et al. (2018) for HD 81040; Valenti & Fischer (2005); Kotoneva et al. (2006); Mishenina et al. (2008); Maldonado et al. (2012); Brewer et al. (2016); Luck (2017) for HD 87883; Datson et al. (2012); Santos et al. (2013); Porto de Mello et al. (2014); Ramírez et al. (2014); Rich et al. (2017) for HD 98649; Sadakane et al. (2002); Heiter & Luck (2003); Laws et al. (2003); Santos et al. (2003, 2004, 2005); Huang et al. (2005); Valenti & Fischer (2005); Luck & Heiter (2006); Takeda et al. (2007); Fuhrmann (2008); Gonzalez et al. (2010); Kang et al. (2011); Datson et al. (2015); Spina et al. (2016); Luck (2017); Sousa et al. (2018) for HD 106252; Santos et al. (2013) for HD 106515A and HD 106515B; Brewer et al. (2016) for HD 171238; Valenti & Fischer (2005); Bond et al. (2006); Santos et al. (2013) for HD 196067 and HD 196068; and Valenti & Fischer (2005); Bond et al. (2006); Sousa et al. (2006, 2008); Tsantaki et al. (2013); Jofré et al. (2015); Maldonado & Villaver (2016); Soto & Jenkins (2018a) for HD 221420.

[c] The stellar masses are estimated from PARSEC isochrones (see text).

[d] The stellar luminosities are computed based on the absolute calibration of effective temperature scales performed by (Casagrande et al., 2010) (see text).

[e] The stellar ages and their 1σ error bars are approximated using the Bayesian technique of Brandt et al. (2014).

$$\begin{aligned}\frac{\sigma^2(L_{\mathrm{Bol}})}{L_{\mathrm{Bol}}^2} = &\left(\frac{\sigma(\mathcal{F}_{Bol})}{\mathcal{F}_{Bol}}\right)^2 + \left(\frac{2\sigma(\varpi)}{\varpi}\right)^2 \\ &+ (0.4\ln(10)\sigma(V_T))^2 + (\sigma_{\phi_\xi})^2\end{aligned} \tag{2.22}$$

where the uncertainty in the flux calibration is σ_{ϕ_ξ} is 0.9% for HD 221420 and 0.7% for the rest of the sample. We summarize in Table 2.1 and 2.2 the Tycho-2 $(BV)_T$ and the 2MASS JHK_s photometry and our derived luminosity values for the host stars that we study.

2.2.3 Stellar Masses and Metallicities

We infer masses for the stars using the PARSEC isochrones (Bressan et al., 2012) by matching the observed luminosity at the spectroscopic metallicity and activity-based age. We take spectroscopic metallicities from the PASTEL catalog (Soubiran et al., 2016, and references therein). The PASTEL catalog is a large compilation of high-dispersion spectroscopic measurements from the literature. For the metallicities, we take the median of all entries in the PASTEL catalog. We estimate the uncertainty in the metallicity as the standard deviation of the measurements in the PASTEL catalog, multiplied by $\sqrt{n/(n-1)}$ to correct for the bias in the estimator. Three targets—HD 171238, HD 29021, and HD 106515 A—have only single entries in the PASTEL catalog. For these stars we use the single measurement and assume a conservative uncertainty of 0.1 dex.

Once we have a probability distribution for metallicity, we take a fine grid of stellar models and, for each, compute a likelihood using

$$\mathcal{L} = p(\tau_{\rm model}) \times \exp\left[-\frac{\left(L_\star - L_{\rm model}\right)^2}{2\sigma_L^2} - \frac{\left([{\rm Fe/H}]_\star - [{\rm Fe/H}]_{\rm model}\right)^2}{2\sigma_{[{\rm Fe/H}]}^2}\right]. \qquad (2.23)$$

In Equation (2.23), $p(\tau_{\rm model})$ is our activity-based age posterior at the model age. We then marginalize over metallicity and age to derive a likelihood as a function of stellar mass. We report the mean and standard deviation of this likelihood in Table 2.1 as $M_\star$(model) and adopt it as our (Gaussian) prior for orbital fits. The variances of these distributions are all small; weighting by an initial mass function has a negligible effect.

2.2.4 Results on Individual Stars

Here, we describe the results of the activity-based age analysis and the background for each individual star in our sample. The stellar distances we refer to in this section are inferred from *Gaia* EDR3 parallaxes. The fractional uncertainties on parallax are all $\lesssim$0.1%, so we simply take distance as the inverse of the parallax. The adopted stellar parameters in this paper, including Tycho-2 (Høg et al., 2000a) and 2MASS (Cutri et al., 2003) photometry, $R'_{\rm HK}$, and $R_{\rm X}$, are summarized in Table 2.1 and 2.2.

We combine the chromospheric index $R'_{\rm HK}$, the X-ray activity index R_X, and in some cases a photometric rotation period, to derive an age posterior for each star. Figure 2.1

shows the activity-based age posteriors for the whole sample of stars.

HD 29021 (HIP 21571)

HD 29021 is a G5 star located at a distance of 30.9 pc. Rey et al. (2017) estimated the stellar activity level of the star using high-resolution spectra obtained with the SOPHIE spectrograph at the 1.93 m telescope of the Haute-Provence Observatory, and no significant variability of the star was found from the $H\alpha$ activity indicator. The age of HD 29021 is determined to be ≈6 Gyr from our activity-based analysis, slightly lower than 7.4 Gyr from Winter et al. (2020), the only age reported for this star in the literature. We obtain a luminosity of $0.659 \pm 0.008\, L_{\odot}$, consistent with the luminosity of $\approx 0.7\, L_{\odot}$ from Anderson & Francis (2012); Gaia Collaboration et al. (2018). The mass estimate of the star is between 0.85-1.0 $M_{\odot}$ from multiple sources (Chandler et al., 2016; Mints & Hekker, 2017; Goda & Matsuo, 2019). Combining our luminosity and age with our adopted metallicity, we infer a mass of $0.86 \pm 0.02\, M_{\odot}$.

HD 81040 (HIP 46076)

HD 81040 is a bright, nearby, early G-dwarf star, commonly classified as a very young Galactic disc star (Montes et al., 2001). Sozzetti et al. (2006) used Ca II HK lines in the Keck/HIRES spectra to determine a chromospheric age of 0.73 ± 0.1 Gyr. A significant Lithium (Li) abundance of $\log\epsilon(\mathrm{Li}) = 1.91 \pm 0.07$ also suggests youth (Sozzetti et al., 2006; Gonzalez et al., 2010). Oelkers et al. (2018) and Reinhold & Hekker (2020) measured rotation periods of 15.26 and 15.98 days, respectively, about half the Solar period. Our activity-based analysis produces a narrow age posterior centered just under 2 Gyr, slightly older than the Sozzetti et al. (2006) age. The mass of the star is consistently inferred to be between $0.93\,M_\odot$ and $1.01\,M_\odot$ (Sousa et al., 2006; Butler et al., 2006; Goda & Matsuo, 2019). We obtain a mass of $0.99 \pm 0.02\,M_\odot$ from PARSEC isochrones.

HD 87883 (HIP 49699)

HD 87883 is a K star at a distance of 18.3 pc. Fischer et al. (2009) found modest chromospheric activity with $\log R'_{\mathrm{HK}} = -4.86\,\mathrm{dex}$, a stellar luminosity of $0.318{\pm}0.018\,L_\odot$, and a stellar jitter of $4.5\,\mathrm{m\,s^{-1}}$. We have adopted a slightly lower $\log R'_{\mathrm{HK}}$ value of $-4.98\,\mathrm{dex}$ computed using S-indices from Strassmeier et al. (2000); Gray et al. (2003); Isaacson & Fischer (2010). We derive a slightly higher luminosity of $0.338 \pm 0.004\,L_\odot$. Literature estimates of the stellar mass range from 0.78–0.85 $M_\odot$ (Valenti & Fischer, 2005; Howard et al., 2010; Luck, 2017; Santos et al., 2017; Anders et al., 2019a; Maldonado et al., 2019; Stassun et al., 2019). We find a stellar mass from PARSEC isochrones of $0.80{\pm}0.02\,M_\odot$, in good agreement with previous results. Several studies have constrained the age of this star to ∼5–10 Gyr (Valenti & Fischer, 2005; Takeda et al., 2007; Bonfanti et al., 2015; Brewer et al., 2016; Bonfanti et al., 2016; Yee et al., 2017; Luck, 2017; Winter et al., 2020). Our adopted parameters combined produce an activity-based age peak at ≈7 Gyr which falls within that age range. The combined properties paint a picture of an old aged main-sequence K star with low to modest chromospheric and coronal activity levels.

HD 98649 (HIP 55409)

HD 98649, located at a distance of 42.2 pc from the Sun, is a G3/G5V dwarf. Porto de Mello et al. (2014) label it as a solar analog candidate that closely matches the Sun in colors, absolute magnitude, chromospheric activity as measured from the $H\alpha$ indicator, and atmospheric characteristics. Our luminosity from Tycho-2 and 2MASS photometry yield $L_* = 0.968 \pm 0.012\, L_\odot$. Pace (2013) and Gáspár et al. (2016) have determined the age of the star to be between 4-5 Gyr, in agreement with our activity-based age of $4.436^{+0.677}_{-0.576}$ Gyr.

We adopt an activity index of $R'_{\rm HK} = -4.96$ using S-indices from Arriagada (2011); Jenkins et al. (2011); Pace (2013), consistent with the values published in many sources (Jenkins et al., 2008, 2011; Herrero et al., 2012; Marmier et al., 2013; Gondoin, 2020). The spectroscopic mass of the star is between 0.96-1.03 $M_\odot$ (Allende Prieto & Lambert, 1999; Mortier et al., 2013; Santos et al., 2013; Mints & Hekker, 2017; Goda & Matsuo, 2019). Our PARSEC isochrone fitting provides a value of $0.97 \pm 0.02\, M_\odot$ that is consistent with the literature values. The stellar rotation period is 26.44 days (Oelkers et al., 2018), again a close match to the Solar period. Based on the $\approx$4 Gyr peak from our activity-based analysis, HD 98649 is a chromospherically inactive G dwarf and a close Solar analog.

HD 106252 (HIP 59610)

HD 106252, at a distance of 38.1 pc, is a Sun-like G type star (González Hernández et al., 2010; Datson et al., 2012). Its chromospheric index is comparable with that of the Sun at the minimum of the solar cycle (Lanza et al., 2018). A weak lithium absorption feature (Perrier et al., 2003) and a $R'_{\rm HK} = -4.85$ from Pace (2013) indicate low stellar activity and an old age for HD 106252. Literature values agree on an age of ~4.5 - 7.5 Gyr (Marsakov & Shevelev, 1995; Gonzalez et al., 2010; Casagrande et al., 2011; Gontcharov, 2012; Pace, 2013; Bonfanti et al., 2016; Aguilera-Gómez et al., 2018). Our activity-based age indicators however favor a somewhat younger age, with our distribution peaking at ~3 Gyr; this is driven by a single relatively active measurement by White et al. (2007). The stellar luminosity we infer is higher than that of the Sun. The mass of HD 106252 derived from the PARSEC isochrones model is $1.05 \pm 0.02\,M_{\odot}$, in agreement with independent determinations (Fischer & Valenti, 2005; Butler et al., 2006; Marchi, 2007; Goda & Matsuo, 2019).

HD 106515A (HIP 59743A)

HD 106515 is a high common proper motion binary system consisting of the G-type stars HD 106515 A and B, with $V = 7.96$ and $V = 8.22$ mag, respectively. HD 106515 AB is a gravitationally bound system; the presence of the stellar companion HD 106515 B perturbs the orbit of the planet orbiting around HD 106515 A (Rica et al., 2017). HD 106515 B has an estimated spectroscopic mass of $0.925\,M_{\odot}$ and an effective temperature of 5425 K (Mugrauer, 2019). Dommanget & Nys (2002) list a third visual stellar companion $98\farcs7$ from HD 106515 A with a magnitude of $V = 10.3$ (BD-06 3533, or TYC 4946-202-1). *Gaia* EDR3 places this star at a distance of nearly 1 kpc, conclusively identifying it as a chance alignment.

HD 106515 A has a slow rotational velocity and low levels of chromospheric activity, with $R'_{\mathrm{HK}} = -5.10$ (Schröder et al., 2009; Meunier & Lagrange, 2019), suggesting an old star. Our activity-based age analysis results in a broad posterior peaking at an age just under 8 Gyr. Previous mass measurements of HD 106515 A range between 0.87-0.95 $M_\odot$ (Allende Prieto & Lambert, 1999; Santos et al., 2017; Anders et al., 2019a; Goda & Matsuo, 2019; Queiroz et al., 2020; Gomes da Silva et al., 2021). Our PARSEC isochrone fitting yields a mass of $0.90 \pm 0.03\,M_\odot$. We use the same method to derive a mass of $0.89 \pm 0.03\,M_\odot$ for HD 106515 B.

HD 171238 (HIP 91085)

HD 171238 is a G8 dwarf at a distance of 44.5 pc. With theoretical isochrones, Ségransan et al. (2010) obtain a mass of $M_* = 0.94 \pm 0.03\,M_\odot$ and an age of 4.9 ± 4.1 Gyr. Bonfanti et al. (2016) studied the age consistency between exoplanet hosts and field stars with the PARSEC evolutionary code, and found a stellar age of 4 ± 1.2 Gyr. Our activity-based age analysis yields a broad posterior spread of 3-12 Gyr with a peak at 6 Gyr, in mild tension with above mentioned values. The discrepancies in the ages and a broad posterior suggest that the age of the star is poorly constrained.

HD 196067 (HIP 102125)

HD 196067 is in a bright visual binary gravitationally bound to the G-dwarf star HD 196068 (=HIP 102128) (Gould & Chaname, 2004). The binary pair is located 39.94 pc from the Sun. HD 196067 appears to be slightly evolved on the color-magnitude diagram.

Marmier et al. (2013) derived an age of $3.3 \pm 0.6\,\mathrm{Gyr}$ and a mass $M_* = 1.29 \pm 0.08 M_\odot$, with $[\mathrm{Fe/H}] = 0.34 \pm 0.04$. Our activity-based age for HD 196067 peaks at ≈4 Gyr, consistent with literature findings that most strongly favor an age of about 3 Gyr (Casagrande et al., 2011; Delgado Mena et al., 2015; Winter et al., 2020). These same authors as well as Valenti & Fischer (2005); Mortier et al. (2013); Santos et al. (2017); Goda & Matsuo (2019); Maldonado et al. (2019) infer masses between 1.23-1.32 $M_\odot$. The PARSEC isochrones yield a mass of $1.26 \pm 0.07\,M_\odot$, which agrees well with literature values. We derive a mass of $1.12 \pm 0.06\,M_\odot$ for its companion, HD 196068.

HD 221420 (HIP 116250)

HD 221420 is a slightly evolved G dwarf located 31.2 pc from the Sun. Holmberg et al. (2009) derive a photometric metallicity of $[\mathrm{Fe/H}] = 0.19$ and an age of ∼5 Gyr. Spectroscopic measurements suggest an even higher metallicity (e.g. Valenti & Fischer, 2005; Sousa et al., 2006; Tsantaki et al., 2013). Other authors have inferred ages between 4 and 6 Gyr (Valenti & Fischer, 2005; Baumann et al., 2010; Casagrande et al., 2011; Pace, 2013; Tsantaki et al., 2013; Aguilera-Gómez et al., 2018). Our activity-based age analysis yields an age posterior centered between 4-6 Gyr that closely matches the literature measurements. Unlike most of our other stars, HD 221420 has a luminosity and surface gravity that place it above the main sequence. We therefore verify the activity-based age with an analysis using only the observed luminosity combined with the PARSEC isochrones (Bressan et al., 2012). We derive an age of 3 to 5 Gyr with this approach, consistent with our activity-based age but excluding the tail to old ages.

We derive a mass of $1.28 \pm 0.08\,M_{\odot}$ using an activity-based age prior. This increases slightly to $1.35 \pm 0.09\,M_{\odot}$ if we use a uniform age prior. We adopt $1.28 \pm 0.08\,M_{\odot}$ for our analysis here. Using the higher mass would result in a slightly longer inferred orbital period and higher mass of the substellar companion. In the next section, I discuss the data we used in our `orvara` orbital fits.

2.3 Data Description

2.3.1 Radial Velocity Data

The RV time series for the stars come from decades of monitoring by several long-term RV surveys. Four of the targets, HD 171238 b, HD 98649 b, HD 196067 b and HD 106515 Ab, are long period and massive planets from the CORALIE survey (Marmier et al., 2013). HD 221420 b is a massive companion reported in Kane et al. (2019) with radial velocities from the 3.9-meter Anglo-Australian Telescope (AAT) in the course of the Anglo-Australian Planet Search (AAPS; Diego et al., 1990). It was also observed with the High Accuracy Radial velocity Planet Searcher (HARPS) spectrograph at the ESO 3.6-m telescope in La Silla (Trifonov et al., 2020). The rest of the sample have multi-decade RV data acquired with the HIRES instrument on the Keck I Telescope, the Hamilton spectrograph at Lick Observatory, and the ELODIE and SOPHIE spectrographs at Haute-Provence Observatory. In this section, we briefly summarize the long-term RV history for each star and the data we use for orbital fits.

HD 29021 b

HD 29021 was observed with SOPHIE+ survey for giant planets with 66 RV measurements on a 4.5 yr time baseline (Rey et al., 2017). The resulting orbital solution yielded a mass of $M \sin i = 2.4\,M_{\mathrm{Jup}}$ and an orbital period of 3.7 years, placing the planet just outside the outer limit of its star's habitable zone. The dispersion of the residuals from this fit is within the expected levels for SOPHIE+ and no long term drift was observed by these authors. We use all of the 66 RVs from the SOPHIE search for northern exoplanets.

HD 81040 b

Sozzetti et al. (2006) reported the detection of a massive planetary companion orbiting the young disc star HD 81040 based on five years of precise RV measurements with the HIRES spectrograph on the 10-m Keck telescope and the ELODIE fiber-fed echelle spectrograph on the 1.93 m telescope at the Observatoire de Haute-Provence in France. HIRES/Keck monitored this star for 8.5 months in 1991, obtaining a total of 3 RV measurements, and 23 follow-up RV data were taken with the ELODIE spectrograph from 2002-2005. The orbital fit to all of the data unveiled a massive planet with period $P = 1001.7 \pm 7.0$ days, $e = 0.526 \pm 0.042$ and $M \sin i = 6.86 \pm 0.71\,M_{\mathrm{Jup}}$ (Sozzetti et al., 2006). We utilize the combined data from ELODIE and HIRES/Keck for our orbit analysis.

HD 87883 b

The RV monitoring of HD 87883 began in 1998 December at Lick (Fischer et al., 2013). A total of 44 RV measurements with Lick have a median uncertainty of $5.3\,\mathrm{m\,s^{-1}}$. An additional 25 higher-quality RV measurements with the HIRES instrument in 2009 on the Keck telescope have a median precision of $4.0\,\mathrm{m\,s^{-1}}$ (Fischer et al., 2009). A Keplerian fit to RV data from both Lick and Keck revealed a single long-period RV companion with a period of 7.55 ± 0.24 years, an eccentricity of 0.53 ± 0.12 and a minimum mass of $M \sin i = 1.78 \pm 0.13\,M_{\mathrm{Jup}}$ (Fischer et al., 2009). Butler et al. (2017) has published an additional 46 RVs with a median uncertainty of $1.35\,\mathrm{m\,s^{-1}}$ (Butler et al., 2017) that extends the total time baseline to more than 20 years. We use all of the above measurements in our orbit analysis.

HD 98649 b

For HD 98649, a total of 11 radial velocity measurements were published from CORALIE-98 with a median measurement uncertainty of $4.4\,\mathrm{m\,s^{-1}}$. Then, 37 data were published from CORALIE-07 with a median error of $3.3\,\mathrm{m\,s^{-1}}$. Using the combined data, Marmier et al. (2013) uncovered a companion with $M \sin i = 6.8\,M_{\mathrm{Jup}}$, a period of $13.6^{+1.6}_{-1.3}$ years on an eccentric orbit with $e = 0.85$. CORALIE measured 15 additional RVs in 2014. We make use of all of the 70 RV measurements acquired with the CORALIE spectrograph in the 16-year time span.

HD 106252 b

HD 106252 was observed with the ELODIE high-precision echelle spectrograph at Haute-Provence Observatory as part of the ELODIE survey for northern extra-solar planets (Perrier et al., 2003). A total of 40 high-precision RV measurements with a median uncertainty of 10.5 $\mathrm{m\,s^{-1}}$ were obtained since March 1997 (Perrier et al., 2003). Using these data, Perrier et al. (2003) performed orbit analysis for the companion and found a well-constrained solution with minimum mass of $M \sin i \approx 7.56\,M_{\mathrm{Jup}}$, an eccentricity of 0.471 ± 0.028, and a period of 4.38 ± 0.05 years. Fischer et al. (2002) independently confirmed the planet using 15 RV measurements (median uncertainty of 11 $\mathrm{m\,s^{-1}}$) from Hamilton/Lick, but with poorer constrains due to shorter temporal coverage Perrier et al. (2003). We use both the 40 RVs from ELODIE and 15 measurements from Hamilton.

HD 106252 was observed again with both ELODIE and Hamilton after the initial publications in 2002/2003, providing an additional 15 RVs from ELODIE with a median uncertainty of 11.1 $\mathrm{m\,s^{-1}}$, and 54 RVs from Hamilton with median errors of 10.5 $\mathrm{m\,s^{-1}}$ in 2006 (Butler et al., 2006). We also use the most recent RV measurements in 2009 that include 12 RVs from CDES-TS2 (median uncertainty 10.35 $\mathrm{m\,s^{-1}}$) and 43 RVs (median uncertainty 9.3 $\mathrm{m\,s^{-1}}$) from the High Resolution Spectrograph (HRS) instrument mounted on the 9.2 m Hobby-Eberly Telescope (HET) at the McDonald Observatory (Wittenmyer et al., 2016). Altogether, we use 179 RV data points spanning 12 years.

HD 106515 Ab

In the same CORALIE survey, a massive planet HD 106515 Ab was discovered around one star in the binary system HD 106515 (Marmier et al., 2013). A total of 19 and 24 RV measurements have been collected with CORALIE-98 and CORALIE-07 with median measurement uncertainties of $6.3\,\mathrm{m\,s^{-1}}$ and $4.1\,\mathrm{m\,s^{-1}}$, respectively (Marmier et al., 2013). Its orbital parameters are well constrained, with $M \sin i = 9.61 \pm 0.14\,M_{\mathrm{Jup}}$,

$P = 3630 \pm 12$ days, $e = 0.572 \pm 0.011$, and a semi-major axis of 4.590 ± 0.010 AU. Similar to HD 196067, with the presence of a stellar companion, the Kozai-Lidov pumping mechanism (Kozai, 1962; Lidov, 1962) may be a viable explanation for the high eccentricity. We use all the CORALIE RVs.

HD 171238 b

The RV monitoring of HD 171238 started in October 2002 using the CORALIE spectrograph mounted on the 1.2 Euler Swiss telescope at La Silla Observatory in Chile (Ségransan et al., 2010). Those authors published 32 RV measurements from CORALIE-98 with a median measurement uncertainty of $7.3\,\mathrm{m\,s^{-1}}$. An additional 65 RV measurements from CORALIE-07 show a median measurement error of $3.7\,\mathrm{m\,s^{-1}}$. Using these radial velocities, Ségransan et al. (2010) reported a massive companion with $M \sin i = 2.60\,M_{\mathrm{Jup}}$, a period of 4.17 yrs, a semi-major axis of 2.5 AU, and an eccentricity of $e = 0.40$. They also speculate that the presence of spots on the stellar surface and active chromospheric activity might be the cause of the large RV jitter (10 m s^{-1}) from their single planet Keplerian model fitting. We adopt the 32 RVs from CORALIE-98, 65 RVs from CORALIE-07 and an additional 9 RVs published in 2017 with the HIRES spectrograph on the Keck Telescope (Butler et al., 2017).

HD 196067 b

Like HD 98649 b, HD 196067 b was also discovered in the CORALIE survey for southern exoplanets. A total of 82 Doppler measurements have been obtained since September

1999: 30 were from CORALIE-98 with a median measurement uncertainty of $7.5\,\mathrm{m\,s^{-1}}$ and 52 from CORALIE-07 with a median uncertainty of $5.9\,\mathrm{m\,s^{-1}}$ (Marmier et al., 2013). The data for C98 are sparsely sampled due to poor coverage near periastron (Marmier et al., 2013). With the caveats from this poor coverage, the companion's $M \sin i$ is constrained between $5.8 - 10.8 M_{\mathrm{Jup}}$, the period between 9.5-10.6 yr, and the eccentricity between 0.57-0.84. We use the RVs from both CORALIE-98 and CORALIE-07.

HD 221420 b

The companion to HD 221420 was discovered by Kane et al. (2019) using 18 years of RV data acquired with the Anglo-Australian Telescope (AAT) (AAPS; Diego et al., 1990). The median uncertainty of the 88 measurements is $1.33\,\mathrm{m\,s^{-1}}$. Kane et al. (2019) obtain an orbital period of $61.55^{+11.50}_{-11.23}$ years, a RV semi-amplitude of $54.7^{+4.2}_{-3.6}$, an eccentricity of $0.42^{+0.05}_{-0.07}$, and a $M \sin i$ of $9.7^{+1.1}_{-1.0}\, M_{\mathrm{Jup}}$; they infer a semi-major axis of $18.5 \pm 2.3\,\mathrm{AU}$. The High Accuracy Radial velocity Planet Searcher (HARPS) spectrograph (ESO) also observed the target from 2003-2015, offering 74 higher precision measurements with a median uncertainty of $0.94\,\mathrm{m\,s^{-1}}$. Both AAT+HARPS data are recently utilized by Venner et al. (2021) to derive a precise dynamical mass of $22.9 \pm 2.2 M_{\mathrm{Jup}}$. We include all the RV measurements from AAT and HARPS for this target.

Table 2.3. Summary of Hipparcos and Gaia (EDR3) Astrometry from HGCA.[a]

Star	Data Source	$\mu_{x,\alpha*}$	$\sigma[\mu_{\alpha*}]$	$\mu_{x,\delta}$	$\sigma[\mu_{\delta}]$	Correlation Coefficient	Epoch, α	Epoch, δ	$\Delta\mu_{x-HG,\alpha*}$	$\Delta\mu_{x-HG,\delta}$	Significance
		$\mathrm{mas\,yr^{-1}}$		$\mathrm{mas\,yr^{-1}}$			year		$\mathrm{mas\,yr^{-1}}$		
HD 29021	Hip	60.884	0.674	22.917	0.717	0.160	1991.11	1990.92	-1.004 ± 0.674	-0.261 ± 0.717	
	HG	61.888	0.020	23.178	0.020	0.020					
	Gaia	62.078	0.025	23.430	0.025	0.266	2016.41	2016.09	0.190 ± 0.032	0.252 ± 0.032	8.89σ
HD 81040	Hip	−151.520	0.835	35.954	0.525	−0.320	1991.66	1991.34	-0.369 ± 0.836	0.190 ± 0.525	
	HG	−151.151	0.031	35.764	0.019	−0.265					
	Gaia	−151.265	0.061	35.708	0.049	−0.404	2016.11	2016.32	-0.114 ± 0.068	-0.056 ± 0.053	1.98σ
HD 87883	Hip	−64.197	0.665	−60.478	0.466	−0.006	1991.50	1991.09	-0.391 ± 0.665	0.113 ± 0.466	
	HG	−63.806	0.024	−60.591	0.017	−0.062					
	Gaia	−64.293	0.037	−61.438	0.035	−0.214	2016.13	2016.33	-0.487 ± 0.044	-0.847 ± 0.039	26.57σ
HD 98649	Hip	−199.571	0.663	−177.725	0.575	−0.432	1991.18	1991.51	-0.019 ± 0.663	-0.187 ± 0.575	
	HG	−199.552	0.024	−177.538	0.022	−0.478					
	Gaia	−199.735	0.031	−177.620	0.023	−0.047	2015.81	2015.84	-0.183 ± 0.039	-0.082 ± 0.032	5.68σ
HD 106252	Hip	23.781	0.886	−279.571	0.444	−0.068	1991.28	1991.42	0.179 ± 0.886	0.602 ± 0.444	
	HG	23.602	0.029	−280.173	0.017	−0.144					
	Gaia	23.315	0.044	−279.896	0.028	−0.409	2015.94	2015.49	-0.287 ± 0.053	0.277 ± 0.033	8.65σ
HD 106515A	Hip	−249.256	1.074	−53.466	0.875	−0.372	1991.39	1991.10	1.650 ± 1.075	-1.749 ± 0.876	
	HG	−250.906	0.048	−51.717	0.035	−0.318					
	Gaia	−251.469	0.043	−51.330	0.030	−0.317	2016.10	2016.10	-0.563 ± 0.064	0.387 ± 0.046	10.27σ
HD 171238	Hip	−30.814	1.549	−110.327	1.042	0.069	1991.04	1991.22	-1.776 ± 1.550	-0.713 ± 1.042	
	HG	−29.038	0.043	−109.614	0.030	−0.046					
	Gaia	−29.539	0.046	−109.580	0.038	0.258	2016.25	2016.55	-0.501 ± 0.063	0.034 ± 0.048	7.87σ
HD 196067	Hip	150.240	2.186	−159.708	2.343	−0.477	1991.31	1991.16	-5.894 ± 2.187	1.833 ± 2.344	
	HG	156.134	0.074	−161.541	0.079	−0.277					
	Gaia	156.404	0.026	−162.214	0.031	−0.298	2015.97	2016.24	0.270 ± 0.078	-0.673 ± 0.085	7.76σ
HD 221420	Hip	15.884	0.437	1.648	0.385	0.159	1991.14	1991.30	0.911 ± 0.437	1.193 ± 0.385	
	HG	14.973	0.014	0.455	0.012	0.042					
	Gaia	16.306	0.056	0.736	0.058	0.110	2016.06	2015.98	1.333 ± 0.058	0.281 ± 0.059	23.11σ

[a] from Brandt (2021b)

2.3.2 Absolute Stellar Astrometry Data

Absolute astrometry of each of our host stars provides a constraint orthogonal to that from radial velocities. The ESA satellites *Hipparcos* and *Gaia* each measure a position and proper motion in an inertial reference frame (the International Celestial Reference Frame, or ICRF), but taken 25 years apart. *Hipparcos* detected proper motions near epoch 1991.25 (μ_{Hip}), and *Gaia* near 2016.0 ($\mu_{Gaia,EDR3}$). Differences between the two proper motions probe a star's acceleration. An additional, more accurate tangential proper motion is given by the *Hipparcos*-*Gaia* positional difference divided by the ∼25 year time baseline (μ_{HG}). We reference this scaled positional difference by subtracting it from both *Hipparcos* and *Gaia* proper motions ($\Delta\mu_{Hip-HG}$ or $\Delta\mu_{Gaia-HG}$), and we use them as astrometric constraints for the host stars' orbits. We report these variables in Table 2.3. The proper motion of a star in conjunction with its radial velocity define a three-dimensional vector that traces out the true space velocity of the star.

Table 2.3 summarizes the *Gaia* EDR3 version HGCA catalog astrometry for the host stars in our sample. While *Gaia* and *Hipparcos*'s measurements are independent, a slight covariance results from the use of *Gaia* parallaxes to improve the *Hipparcos* astrometry (Brandt, 2018). We neglect this small covariance in our orbital fits.

All of our stars except for HD 81040 have acceleration χ^2 values greater than 11.8 (i.e., 3σ detections assuming Gaussian errors and two degrees of freedom), indicating significant accelerations between *Hipparcos* and *Gaia*.

2.3.3 Relative Astrometry Data from Gaia

Among the stars in our sample, two systems have gravitationally bound, wide stellar companions measured independently in *Gaia* EDR3. These include HD 196067's stellar companion HD 196068, and HD 106515 A's secondary stellar companion HD 106515 B as discussed in Section 2.2. Table 2.4 lists the single epoch relative astrometry data for both of these systems here. This is obtained using the single epoch measurements of position in R.A. and Dec. (α, δ) from *Gaia* EDR3 at epoch 2016.0 and converting them into position angle east of north (PA) and projected separation (ρ) between the host star and the secondary stellar companion.

We adopt uncertainties of 10 mas in separation and $0\overset{\circ}{.}1$ in PA. These are much larger than the formal *Gaia* uncertainties, but still represent tiny fractional uncertainties. Adopting the actual formal *Gaia* uncertainties gives measurements so precise that it makes the MCMC chains much slower to converge.

Gaia EDR3 also gives proper motions for both stellar companions. We use these proper motions together with the relative astrometry to constrain the orbital fit. Both stellar companions are of similar brightness to the primary stars that we fit. As a result, the magnitude-dependent frame rotation seen by Cantat-Gaudin & Brandt (2021) will be shared by both components and will not affect our analysis.

We impose priors on the masses of the secondary star in both cases. We derive these from the same stellar isochrone fitting described in Section 2.2.2. For HD 106515 B we find a mass of $0.86 \pm 0.03\,M$. This value is slightly lower than $0.925 \pm 0.05\,M$ from

Table 2.4. Adopted single epoch relative astrometry derived from Gaia EDR3.

Companion	HD 196068	HD 106515 B
Epoch	2016.0	2016.0
ρ ($''$)	16.62	6.86
σ_ρ ($''$)[a]	0.01	0.01
PA ($^\circ$)	19.3	85.9
$\sigma_{\rm PA}$ ($^\circ$)[a]	0.1	0.1
$\mu_{{\rm Gaia},\alpha*}$ (mas yr^{-1})	163.531	-244.603
$\sigma[\mu_{{\rm Gaia},\alpha*}]$ (mas yr^{-1})	0.016	0.031
$\mu_{{\rm Gaia},\delta}$ (mas yr^{-1})	-171.346	-67.744
$\sigma[\mu_{{\rm Gaia},\delta}]$ (mas yr^{-1})	0.018	0.021
Corr Coefficient	-0.156	-0.650
$\Delta\mu_{{\rm comp-host},\alpha*}$ (mas yr^{-1})	7.127	6.866
$\sigma[\Delta\mu_{{\rm comp-host},\alpha*}]$ (mas yr^{-1})	0.031	0.053
$\Delta\mu_{{\rm comp-host},\delta}$ (mas yr^{-1})	-9.132	-16.414
$\sigma[\Delta\mu_{{\rm comp-host},\delta}]$ (mas yr^{-1})	0.036	0.037

[a] Adopted errors are much larger than *Gaia* EDR3 values to aid MCMC convergence.

Mugrauer (2019). For HD 196068, we adopt a prior of $1.18 \pm 0.06\,M$.

2.4 Orbital Fit Methods

Precise masses and inclinations become possible for RV planets because RV and astrometry measure orthogonal components of the motion in inertial frames. We perform full orbital analyses for our sample of RV planets using the orbit fitting package `orvara` (Brandt et al., 2021g). `orvara` fits Keplerian orbits to an arbitrary combination of radial velocity, relative and/or absolute astrometry data. None of the RV-detected companions in our sample have previous relative astrometry data from direct imaging. Three of these systems, HD 87883, HD 106252 and HD 106515 AB, were previously observed with AO imaging that did not show signs of companions in the systems. HD 87883 was observed with the Calar Alto 2.2-m telescope with the lucky imaging camera AstraLux in (Ginski et al., 2012; Luck, 2017). HD 106252 was imaged with Palomar/Keck as part of the AO survey of young solar analogs in June, 2004 (Metchev & Hillenbrand, 2009). Finally, the HD 106515 AB system was imaged with AdoPT@TNG (Desidera et al., 2012). For the present analysis, we use published RV data from the literature described in Section 3 and absolute astrometry data from the HGCA described in Section 4.

`orvara` uses the intermediate astrometry fitting package `htof` (Brandt et al., 2021b). `htof` parses the intermediate *Hipparcos* astrometric data by accounting for the scan angles and uncertainties to construct covariance matrices to solve for best-fit positions and proper motion relative to the barycenter. The *Gaia* epoch astrometry is currently unavailable, so `htof` uses an approach to forward model *Gaia* observations using the predicted scan angles and observation times, and fits a five-parameter astrometric model to these synthetic data. The *Gaia* EDR3 predicted observation times and scan angles are publicly accessible via the *Gaia* Observation Forecast Tool [1]. `orvara` then compares the resulting positions and proper motions to the values provided in the HGCA.

`orvara` adopts the parallel-tempering Markov Chain Monte Carlo (MCMC) sampler with `ptemcee` (Foreman-Mackey et al., 2013; Vousden et al., 2016a) to explore the 9-dimensional parameter space comprised of the host star and companion masses M_* and $M_{\rm sec}$, RV jitter, semi-major axis a, inclination i, PA of the ascending node Ω, mean longitude at a particular reference epoch of 2455197.5 JD (λ_{ref}), the eccentricity e and the argument of periastron (ω) fitted as $\sqrt{e}\sin\omega$ and $\sqrt{e}\cos\omega$. For our three-body systems, there are six more orbital elements plus another mass; these become 16-parameter fits.

In addition to the nine free parameters that we fit (sixteen for three-body systems), `orvara` marginalizes out several nuisance parameters to reduce computational costs. These include the systemic RV zero point (one per instrument), the parallax, and the barycenter proper motion. We assume the *Gaia* EDR3 parallax as our parallax prior, and use flat priors for the RV zero point(s) and barycenter proper motion. `orvara` thus produces posterior distributions for all of these parameters as well.

We perform orbital fits for each RV companion in our sample with `orvara`. We chose informative priors on the host stars' masses according to stellar masses derived in Section 2 and listed in Table 2.1. These are Gaussian with the means and standard deviations

---

[1] `https://gaia.esac.esa.int/gost/index.jsp`

Table 2.5. Adopted Priors.

Parameter	Prior
RV Jitter $\sigma_{\rm jit}$	$1/\sigma_{\rm jit}$ (log-flat)
Primary Mass M_*	$1/M$ (Gaussian)
Secondary Mass $M_{\rm sec}$	$1/M$ (log-flat)
Semimajor axis a	$1/a$ (log-flat)
$\sqrt{\varepsilon}\sin\omega$	uniform
$\sqrt{\varepsilon}\cos\omega$	uniform
Inclination i	$\sin(i)$, $0^\circ < i < 180^\circ$ (geometric)
Mean longitude at 2010.0 $\lambda_{\rm ref}$	uniform
Ascending node Ω	uniform
Parallax ϖ	$\exp\left[-\frac{1}{2}(\varpi - \varpi_{\rm EDR3})^2/\sigma_{\varpi}^2\right]$

given in Table 2.1. We assume uninformative priors for our other fitted parameters: either log-uniform, uniform, or geometric (see Table 2.5), except for parallax, which we have marginalized out from the fit. For each target, we use `ptemcee` to fit for the nine parameters, employing 30 temperatures and 100 walkers over 5×10^5 steps per walker. In each case, the MCMC chains converge after no more than 15,000 steps, we thus discard the first 20,000 steps as burn-in and use the rest for inference. We post-process the MCMC chains with `orvara`, and we discuss the results for each individual system in the following Section.

2.5 Revised Orbits and Masses

Table 2.6. Posteriors of single RV companions in our sample from orvara MCMC analysis.

Companion	HD 29021 b	HD 81040 b	HD 87883 b	HD 98649 b	HD 106252 b	HD 106515 Ab	HD 106515 B*	HD 171238 b	HD 196067 b	HD 221420 b
					Fitted parameters					
RV Jitter σ ($\mathrm{m\,s^{-1}}$)	$3.66^{+0.60}_{-0.58}$	$4.14^{+0.69}_{-4.1}$	$4.92^{+0.06}_{-0.12}$	$4.74^{+0.19}_{-0.34}$	$2.9^{+1.7}_{-2.9}$	$7.6^{+1.3}_{-1.3}$	$7.6^{+1.3}_{-1.3}$	$4.96^{+0.03}_{-0.06}$	$7.7^{+1.2}_{-1.1}$	$3.75^{+0.25}_{-0.23}$
Primary Mass ($\mathrm{M_\odot}$)	0.86 ± 0.02	0.97 ± 0.02	0.80 ± 0.02	0.97 ± 0.02	1.05 ± 0.02	0.90 ± 0.03	0.90 ± 0.03	0.92 ± 0.03	1.34 ± 0.06	1.30 ± 0.08
Secondary Mass ($\mathrm{M_{Jup}}$)	$4.47^{+0.67}_{-0.65}$	$7.24^{+1.0}_{-0.37}$	$6.31^{+0.31}_{-0.32}$	$9.7^{+2.3}_{-1.9}$	$10.00^{+0.78}_{-0.73}$	$18.9^{+1.5}_{-1.4}$	904^{+31}_{-31}	$8.8^{+3.6}_{-1.3}$	$12.5^{+2.5}_{-1.8}$	$20.6^{+2.0}_{-1.6}$
Semimajor axis a (AU)	$2.294^{+0.019}_{-0.019}$	$1.946^{+0.014}_{-0.014}$	$3.77^{+0.12}_{-0.094}$	$5.97^{+0.24}_{-0.21}$	$2.655^{+0.017}_{-0.017}$	$4.48^{+0.050}_{-0.050}$	335^{+96}_{-42}	$2.518^{+0.032}_{-0.033}$	$5.10^{+0.22}_{-0.17}$	$9.99^{+0.74}_{-0.70}$
$\sqrt{e}\,\sin\omega$	$-0.007^{+0.038}_{-0.039}$	$0.714^{+0.018}_{-0.020}$	$-0.831^{+0.019}_{-0.019}$	$-0.865^{+0.023}_{-0.012}$	$-0.645^{+0.010}_{-0.010}$	$0.625^{+0.019}_{-0.020}$	$0.39^{+0.16}_{-0.28}$	$0.437^{+0.024}_{-0.024}$	$0.426^{+0.056}_{-0.066}$	$-0.254^{+0.062}_{-0.063}$
$\sqrt{e}\,\cos\omega$	$-0.672^{+0.010}_{-0.010}$	$0.114^{+0.041}_{-0.041}$	$0.178^{+0.055}_{-0.055}$	$-0.312^{+0.051}_{-0.10}$	$0.253^{+0.016}_{-0.017}$	$-0.424^{+0.029}_{-0.029}$	$-0.54^{+0.41}_{-0.12}$	$0.408^{+0.038}_{-0.040}$	$-0.702^{+0.080}_{-0.13}$	$-0.312^{+0.10}_{-0.071}$
Inclination ($i < 90^\circ$) ($^\circ$) [a]	$33.7^{+6.8}_{-4.9}$	73^{+12}_{-16}	$16.8^{+1.7}_{-1.4}$	$43.7^{+13}_{-8.1}$	$46.0^{+4.9}_{-4.1}$	$29.2^{+2.4}_{-2.2}$	$18.8^{+7.8}_{-8.3}$	$19.1^{+7.9}_{-8.5}$	$41.2^{+28}_{-9.1}$	$17.8^{+2.9}_{-2.8}$
Inclination ($i > 90^\circ$) ($^\circ$) [a]	$146.3^{+4.9}_{-6.8}$	107^{+16}_{-12}	$163.2^{+1.4}_{-1.7}$	$136.3^{+8.1}_{-13}$	$134.0^{+4.1}_{-4.9}$	$150.8^{+2.2}_{-2.4}$	–	$162.9^{+5.0}_{-3.1}$	$138.8^{+9.1}_{-28}$	$162.2^{+2.8}_{-2.9}$
Ascending node Ω ($^\circ$)	$40.8^{+7.1}_{-9.1}$	77^{+27}_{-23}	$109.9^{+4.0}_{-4.1}$	54^{+44}_{-26}	$105.3^{+10}_{-6.1}$	$59.9^{+4.6}_{-4.1}$	62^{+45}_{-37}	71^{+47}_{-13}	101^{+59}_{-82}	$66.6^{+5.4}_{-3.1}$
Mean longitude at λ_{ref} ($^\circ$)	$15.2^{+2.7}_{-2.7}$	$148.3^{+3.7}_{-3.8}$	$73.7^{+13}_{-7.4}$	$75.8^{+4.1}_{-7.6}$	$174.6^{+1.5}_{-1.6}$	$100.5^{+1.8}_{-1.8}$	128^{+37}_{-110}	$59.0^{+3.0}_{-3.0}$	150^{+13}_{-15}	$170.5^{+2.3}_{-2.2}$
					Derived parameters					
Period (years)	$3.737^{+0.018}_{-0.018}$	$2.7452^{+0.011}_{-0.0093}$	$8.23^{+0.32}_{-0.34}$	$14.74^{+0.88}_{-0.75}$	$4.202^{+0.011}_{-0.010}$	$9.927^{+0.030}_{-0.032}$	4630^{+2150}_{-850}	$4.148^{+0.045}_{-0.046}$	$9.88^{+0.63}_{-0.43}$	$27.7^{+3.0}_{-2.5}$
Argument of periastron ω ($^\circ$)	$180.6^{+3.4}_{-3.2}$	$81.0^{+3.3}_{-3.3}$	$282.1^{+3.7}_{-3.7}$	$250.2^{+3.2}_{-6.3}$	$291.4^{+1.5}_{-1.5}$	$124.1^{+2.6}_{-2.5}$	144^{+26}_{-42}	$46.9^{+3.9}_{-3.7}$	$148.6^{+7.6}_{-5.5}$	219^{+17}_{-12}
Eccentricity e	$0.453^{+0.014}_{-0.013}$	$0.525^{+0.024}_{-0.026}$	$0.720^{+0.038}_{-0.027}$	$0.852^{+0.033}_{-0.022}$	$0.480^{+0.010}_{-0.010}$	$0.571^{+0.012}_{-0.012}$	$0.399^{+0.12}_{-0.064}$	$0.358^{+0.028}_{-0.026}$	$0.70^{+0.14}_{-0.12}$	$0.162^{+0.035}_{-0.030}$
Semimajor axis (mas)	$74.29^{+0.61}_{-0.62}$	$56.55^{+0.41}_{-0.41}$	$206.4^{+6.7}_{-5.2}$	$141.6^{+5.7}_{-4.9}$	$69.68^{+0.45}_{-0.46}$	$131.2^{+1.5}_{-1.5}$	9813^{+2815}_{-1227}	$56.63^{+0.73}_{-0.74}$	$127.6^{+5.5}_{-4.2}$	321^{+24}_{-23}
Periastron time (JD − 2450000)	$5824.8^{+9.4}_{-9.0}$	$5511.1^{+10}_{-8.7}$	6913^{+17}_{-16}	10500^{+330}_{-280}	$6463.0^{+8.4}_{-8.6}$	$5435.8^{+8.7}_{-8.5}$	$1570000^{+810000}_{-330000}$	5905^{+20}_{-20}	6560^{+350}_{-270}	6580^{+430}_{-280}
$M_p \sin i$ (M_{Jup}) (this work)	$2.483^{+0.070}_{-0.068}$	$6.87^{+0.19}_{-0.19}$	$1.82^{+0.12}_{-0.10}$	$6.64^{+0.45}_{-0.23}$	$7.20^{+0.13}_{-0.13}$	$9.25^{+0.25}_{-0.25}$	–	$2.599^{+0.090}_{-0.088}$	$7.9^{+4.7}_{-1.5}$	$6.24^{+0.65}_{-0.59}$
$M_p \sin i$ (M_{Jup}) (literature)	$2.4^{+0.2}_{-0.2}$	$6.86^{+0.71}_{-0.71}$	$1.54^{+0.26}_{-0.26}$	$7.27^{+0.98}_{-0.98}$	$6.93^{+0.27}_{-0.27}$	$9.08^{+0.20}_{-0.20}$	–	$2.72^{+0.49}_{-0.49}$	$6.9^{+3.9}_{-1.1}$	$6.31^{+0.60}_{-0.61}$
Literature mass reference[b]	R17	S06 S17	S17 F09	R19 M13	S17 W09 L14	S19 M13	–	M18 S10	M13	V21 K19
Difference in $M_p \sin i$ (%)	3.3%	0.1%	15.4%	9.5%	3.8%	1.8%	–	4.7%	12.7%	1.1%
Difference in $M_p \sin i$ (σ)	0.39σ	0.01σ	1.01σ	0.63σ	0.90σ	0.53σ	–	0.24σ	0.54σ	0.08σ

*Secondary stellar companion. Their `orvara` masses in solar masses are $0.86 \pm 0.03\,M$ for HD 106515 B and $1.18 \pm 0.06\,M$ for HD 106515 B.

[a] The inclination distributions are usually bimodal, so we separately report the values for prograde and retrograde orbits.

[b] References abbreviated as S06 (Sozzetti et al., 2006); F09 (Fischer et al., 2009); W09 (Wittenmyer et al., 2009); S10 (Ségransan et al., 2010); M13 (Marmier et al., 2013); L14 (Liu et al., 2014); R17 (Rey et al., 2017); S17 (Stassun et al., 2017); M18 (Ment et al., 2018); V21 (Venner et al., 2021); K19 (Kane et al., 2019); R19 (Rickman et al., 2019); S19 (Saffe et al., 2019). Tabulated masses are from the first reference for each star. The other measurements are 1.78 ± 0.34 (F09) for HD 87883 b; 7.61 ± 0.39 (W09) and 6.92 ± 0.16 (L14) for HD 106252b; 2.60 ± 0.15 (S10) for HD 171238b; 7.27 ± 0.98 (S17) for HD 81040b; 6.8 ± 0.5 (M13) for HD 98649b; and $9.61^{+0.14}_{-0.14}$ (M13) for 106515 Ab.

In this section, we summarize the results of our orbital fits to each target. The `orvara` radial velocity fits and relative astrometric orbits are shown in Figure Set A1, and the corner plots and covariances of our orbital posteriors are showcased in Figure Set A10, both are presented in Appendix A. Table 2.6 lists the nine basic Keplerian orbital elements `orvara` fit, and the inferred parameters computed using the fitted parameters, as well as the $M \sin i$ values from the literature. We obtain tight constraints on the masses of companions except for HD 171238. Aside from HD 221420 b, whose precise mass was measured by Venner et al. (2021), we present the first precise dynamical mass and orbital inclination measurements for the RV companions in our sample. Our derived $M \sin i$ values agree with the RV-only literature values to within 1σ.

For the inclinations (or equivalently the position angle of the ascending node Ω) derived in this paper, there are two complementary values whose absolute values wrap around 180°. This is unsurprising since the orbital inclination is dependent on whether the planet is in prograde ($0 \geq i_1 \leq 90$) or retrograde ($i_2 = 180° - i_1$) motion (Kervella et al., 2020), and there are limited ways to determine which orbit the companion is on without high contrast imaging. Unfortunately, besides the long-period brown dwarfs in our sample, none of the other companions are accessible to imaging in the near term.

The relative astrometric orbits of every RV companion with respect to its host star are demonstrated in Fig. 2.2. As a result of bimodal inclinations, the prograde and retrograde orbits are clearly evident from the two families of orbits shown in the plots.

The orbital fits to the RVs and absolute astrometry from HGCA are presented in

Figure Set A1. The host stars' astrometric reflex motions over the 25-year time baseline between Hipparcos and Gaia are clearly seen. These figures show that the astrometric reflex motion of a star oscillates with a fixed period over 25 years, short period companions induce more cycles of oscillation. One of our companions, HD 221420 b, is a possible target for direct imaging. Figure 12 shows its predicted locations at four future dates. Finally, for each system, we show corner plots in Figure Set A10 of five astrophysically interesting parameters, including the primary and companion masses M_{pri} and M_{sec}, semi-major axis a, eccentricity e and inclination i, and their covariances.

HD 29021 b

Figure Set A10 shows the fitted posterior distributions for the orbital elements of HD 29021 b. All are Gaussian apart from the inclination, which is bi-modal with equal likelihoods for prograde and retrograde orbits: either $33^{\circ}\!.7^{+6.8}_{-4.9}$ or $146^{\circ}\!.3^{+4.9}_{-6.8}$. Although the RV data only cover one and a half periods, the RV orbit of HD 29021 b is well-constrained. For HD 29021 b, we obtain a dynamical mass of $4.47^{+0.67}_{-0.65} M_{\mathrm{Jup}}$, an eccentricity of $0.453^{+0.014}_{-0.013}$, and a semi-major axis of $74.29^{+0.61}_{-0.62}$ AU. The $M \sin i$ inferred from our fit is $2.483^{+0.070}_{-0.068} M_{\mathrm{Jup}}$. We compare our orbital solution with the only orbital fit for this system published by Rey et al. (2017) where $M \sin i = 2.4 \pm 0.2 M_{\mathrm{Jup}}$, $e = 0.459 \pm 0.008$, $a = 2.28^{+0.07}_{-0.08}$, and $P = 3.732^{+0.013}_{-0.012}$ years; all of our parameters are consistent with this orbital solution.

HD 81040 b

HD 81040 b has the shortest period in our sample; the RV orbit is well-constrained by the joint HIRES and ELODIE RV data (see Figure Set A1). The posterior distributions of selected parameters for HD 81040 are displayed in Figure Set A10. Our orbital inclination indicates that it presents itself as an edge-on system with an orbital inclination of either $73^{\circ}{}^{+12}_{-16}$ or $107^{\circ}{}^{+16}_{-12}$. Our solution reveals that the true mass of HD 81040 b is $7.24^{+1.0}_{-0.37}\,M_{\mathrm{Jup}}$, slightly higher than these previous RV-only $M \sin i$ values. Out of the two $M \sin i$ values reported for this system, our inferred $M \sin i = 6.87 \pm 0.19\,M_{\mathrm{Jup}}$ agrees better with a value of $6.86 \pm 0.71\,M_{\mathrm{Jup}}$ from Sozzetti et al. (2006) than a value of 7.27 ± 0.98 from Stassun et al. (2017). The orbit of HD 81040 b is consistent with being edge-on: we find a 0.9% probability that the planet will transit. If it does transit, we predict transit times of 2021-11-11 and 2024-10-08, each with an unfortunately large uncertainty of about 25 days.

HD 87883 b

The posterior probability distributions of selected parameters and their covariances for HD 87883 b are shown in Figure Set A10. The posterior for the semi-major axis is bimodal, peaking at 3.7 AU and 3.9 AU, respectively. Both the prograde and retrograde orbital inclinations are relatively face-on with values of $16\overset{\circ}{.}8^{+1.7}_{-1.4}$ and $163\overset{\circ}{.}1^{+1.4}_{-1.7}$. Figure Set A1 shows the HIRES and Hamilton RVs, and the corresponding best-fit Keplerian models and the residuals. Two families of orbits are possible; current RV data are insufficient to completely constrain the planet's semi-major axis and eccentricity.

HD 87883 was assessed by Fischer et al. (2009) prior to the 2007 publication of the HIRES/Keck RVs. Their eccentricity was poorly constrained ($e \geq 0.4$) due to the incomplete coverage of the orbital phase approaching periastron. Using the extra RV data, we find consistent orbital parameters with Fischer et al. (2009) and Stassun et al. (2017) except for $M \sin i$ where we find a higher value. HD 87883's orbit is face-on and eccentric from our analysis. Our most likely orbit yields $M = 6.31^{+0.31}_{-0.32}\,M_{\rm Jup}$, a=$3.77^{+0.12}_{-0.094}$ AU, P=$8.23^{+0.32}_{-0.34}$ years, and $e = 0.720^{+0.038}_{-0.027}$. Still, further RV monitoring of target will be required to fully constrain its orbit.

HD 98649 b

The posterior distributions for HD 98649 b are depicted in Figure Set A10, and the fits to the RVs and astrometric accelerations are shown in Figure Set A1. Our solution shows that HD 98649 b is a highly eccentric and massive planet with an eccentricity of $0.852^{+0.033}_{-0.022}$ and a true planetary mass of $9.7^{+2.3}_{-1.9}\,M_{\rm Jup}$. There are two possible inclinations: either $136.^{\circ}3^{+8.1}_{-13}$ or $43.^{\circ}7^{+13}_{-8.1}$. The orbit of HD 98649 b was studied in Rickman et al. (2019) and Marmier et al. (2013). Both studies agree on a $M \sin i$ value of around $6.8 \pm 0.5\,M_{\rm Jup}$, and an eccentricity $e = 0.85 \pm 0.05$ but digress on the semi-major axis and the period of the system. We obtain a value of $a = 5.97^{+0.24}_{-0.21}$ AU, which agrees with a value of $a = 5.6 \pm 0.4$ AU found by Marmier et al. (2013), and marginally with the value of $6.57^{+0.31}_{-0.23}$ AU derived by Rickman et al. (2019).

HD 106252 b

The posterior probabilities for HD 106252 b are illustrated in Figure Set A10. The posterior probabilities follow nearly Gaussian distributions, except for the orbital inclination. The inclination is slightly bimodal, depending on whether the companion is in retrograde or prograde orbital motion. Figure Set A1 demonstrates the agreement between the calibrated *Hipparcos-Gaia* proper motions from the HGCA. As shown in Figure Set A1, the RV orbit of HD 106252 b is well-constrained thanks to full orbital phase coverage from 12 years of RV data. We obtain relatively tight constraints on the dynamical mass of the system, with $M = 10.0^{+0.78}_{-0.73}\,M_{\rm Jup}$, and an orbital inclination of $46\overset{\circ}{.}0^{+4.9}_{-4.1}$ (or $134\overset{\circ}{.}0^{-4.9}_{+4.1}$). Our derived $M \sin i$ of $7.20 \pm 0.13\,M_{\rm Jup}$ corroborates the dynamical analyses of Wittenmyer et al. (2009), Stassun et al. (2017) and Liu et al. (2014) within 5%. Other orbital parameters such as semi-major axis, period, and eccentricity are also in perfect agreement with results obtained by these authors.

HD 106515 Ab

The orbits of both HD 106515 Ab and HD 106515 B in the three-body system HD 106515 Ab are fully constrained (see Figure Set A1). The induced astrometric acceleration by HD 106515 Ab on HD 106515 A is the most significant in our list. The posterior distributions for HD 106515 Ab and HD 106515 B are shown in Figure Set A10. Our 3-body fit reveals a brown dwarf companion to HD 106515 A with a precise dynamical mass of $18.9^{+1.5}_{-1.4}\,M_{\rm Jup}$ on a ≈10-year period. Our $M \sin i$ value of $9.25 \pm 0.25\,M_{\rm Jup}$ agrees with the

$9.08 \pm 0.14\, M_{\rm Jup}$ from Saffe et al. (2019)'s analysis within 2%. All other fitted parameters are also in agreement with Saffe et al. (2019) and Marmier et al. (2013).

Our three-body fit yields a semi-major axis of 335^{+96}_{-42} AU for the HD 106515 A/B binary. This is consistent with a 201 AU projected separation given in *Gaia* EDR3 (see Table 2.4) and a 329 AU semi-major axis value provided in Marmier et al. (2013) based on the positions given by Gould & Chaname (2004). Rica et al. (2017) also found a semi-major axis of 345 AU and an eccentricity of about 0.42 that agrees with ours.

HD 171238 b

Our best-fit orbit for HD 171238 b reveals a dynamical mass of $8.8^{+3.6}_{-1.3}\, M_{\rm Jup}$, an $M \sin i = 2.599^{+0.090}_{-0.088}\, M_{\rm Jup}$, a semi-major axis of $a = 2.519^{+0.032}_{-0.033}$ AU and an eccentricity $e = 0.358^{+0.028}_{-0.026}$, all with tight 1σ errors. The MCMC posterior (Figure Set A10) for the mass of HD 171238 b shows a secondary peak around $15\, M_{\rm Jup}$. The RV orbit presented in Figure Set A1 is constrained by three RV instruments. The inclination ($17\overset{\circ}{.}1^{+3.1}_{-5.0}$ or $162\overset{\circ}{.}9^{+5.0}_{-3.1}$) from our solution indicates a relatively face-on orbit for HD 171238 b. The $M \sin i$, eccentricity and semi-major axis are more consistent with the orbit analysis of Ségransan et al. (2010) ($M \sin i = 2.60 \pm 0.15 M_{\rm Jup}$, $a = 2.54 \pm 0.06$ AU and $e = 0.400^{+0.061}_{-0.065}$) than that of Ment et al. (2018). HD 171238 b's mass is bimodal, possibly either $\approx 9 M_{\rm Jup}$ or $\approx 15 M_{\rm Jup}$. Future *Gaia* data releases will confirm the planet's orbit and mass.

HD 196067 b

HD 196067 b is in a 3-body system with HD 196067 and HD 196068, HD 196067 being the host star and HD 196068 being the stellar companion to HD 196067. The wide orbit stellar companion HD 196068 does accelerate HD 196067, though the >1000 AU separation results in a minimal contribution to the astrometric acceleration from HD 196068. Our MCMC posteriors from the 3-body fit with `orvara` are shown in Figure Set A10 for the inner and outer companions, respectively.

The RV orbit of HD 196067 b (see Figure Set A1) is not perfectly constrained. CORALIE-98 data did not sufficiently sample the sharp turnaround region near periastron. This lack of data results in a bimodal distribution for the eccentricity in the MCMC posteriors, one near $e = 0.6$ and the other near $e = 0.85$ (see Figure Set A10). For HD 196067 b, our 3-body solution favors a dynamical mass of $12.5^{+2.5}_{-1.8}\,M_{\rm Jup}$, a semi-major axis of $5.10^{+0.22}_{-0.17}$, and an orbital period of $9.88^{+0.63}_{-0.43}$ years. The orbital period is consistent with the minimum period of 9.5 years found by Marmier et al. (2013) who have studied the system using the same data as us. They also found an eccentricity of $e = 0.66^{+0.18}_{-0.09}$, which is more consistent with the lower peak (e$\approx$ 0.60) than the higher one in our bi-modal eccentricity posteriors. The inclination distribution is again, bi-modal: either $41^\circ2\,^{+28}_{-9.1}$ or $138^\circ8\,^{+9.1}_{-28}$. We find that its true mass was underestimated by RV-only works. Our estimate of its true dynamical mass of $12.8^{+2.6}_{-1.8}\,M_{\rm Jup}$ is nearly twice as much as the minimum mass found by Marmier et al. (2013). HD 196067 b is interesting as it lies extremely close to the deuterium burning limit (Spiegel et al., 2011) that divides planets and brown dwarfs. We expect that further RV data near the periastron passage of the companion will enable us to finalize its full orbit and confirm the dynamical nature of this companion.

The posterior distributions for HD 196068 are shown in Figure Set A10. The inclination of the stellar companion HD 196068, instead of being bi-modal, has a single value of $10.^{\circ}6^{+6.1}_{-5.2}$, suggesting a nearly face-on orbit. This is because the single relative astrometric measurement from *Gaia* at epoch 2016.0 described in Section 2.3.3 successfully differentiated prograde from retrograde orbits of HD 196068. Our 3-body solution leads to a projected binary semi-major axis of 1631^{+208}_{-213} AU, significantly higher than a value of 932 AU in (Marmier et al., 2013). This can be explained by the stellar companion being near apastron in an eccentric orbit where $e = 0.731^{+0.026}_{-0.031}$.

HD 221420 b

The posterior distributions for selected parameters for HD 221420 b from the joint orbit fit are illustrated in Figure Set A10. The RV orbits and astrometric proper motions are displayed in Figure Set A1. The best fit curves agree with both the RV data and proper motions from the HGCA.

The orbital solution for HD 221420 b was first derived by Kane et al. (2019) using only the AAT RVs. This orbital solution presents a period of $61.55^{+11.50}_{-11.23}$ years, an eccentricity of $0.42^{+0.05}_{-0.07}$, a semi-major axis of $18.5^{+2.3}_{-2.3}$ AU, and a minimum mass of $9.7^{+1.1}_{-1.0}M_{\rm Jup}$. This minimum mass is 36.5% discrepant with ours. This companion has recently been revisited by Venner et al. (2021) who use AAT and HARPS RVs, and Hipparcos-Gaia (DR2) astrometry to constrain the precise dynamical mass. They find an orbital inclination of $164.^{\circ}0^{+1.9}_{-2.6}$, a precise dynamical mass of $22.9 \pm 2.2\, M_{\mathrm{Jup}}$, a semi-major axis of $10.15^{+0.59}_{-0.38}$ AU, and a period of $27.62^{+2.45}_{-1.54}$ years. Using the AAT and HARPS RVs, and absolute astrometry from *Hipparcos* and *Gaia* EDR3, we obtain a companion mass of $20.6^{+2.0}_{-1.6} M_{\mathrm{Jup}}$, an eccentricity of $0.162^{+0.035}_{-0.030}$, a semi-major axis of $9.99^{+0.74}_{-0.70}\, AU$, and a period of $27.7^{+3.0}_{-2.5}$. Our EDR3 solution agrees well with that of Venner et al. (2021), with one distinction being our inclination is again bimodal with equal maximum likelihood: $\mathrm{i} = 178^{\circ}5^{+2.9}_{-2.8}$ or $162.^{\circ}2^{+2.8}_{-2.9}$. We validate the findings by Venner et al. (2021) that the companion is near the $25 M_{\mathrm{Jup}}$ upper limit for core accretion and disk instability to be considered plausible formation channels. Venner et al. (2021) also identify a M-dwarf stellar companion HD 221420 B that may be bound to HD 221420 A, but at a separation of more than 20,000 AU, it contributes negligibly to HD 221420's acceleration. HD 221420 b has the longest period and highest companion mass among the RV companions we sample. As a result, it is also the most accessible of our substellar companions for future direct imaging.

Direct imaging can probe the outer architecture of a system (Chauvin et al., 2005; Lafrenière et al., 2008; Ireland et al., 2010; Rameau et al., 2013; Lagrange, 2014; Bowler, 2016). However, only about a dozen wide-orbit giant planets have been discovered at separations of ~10-150 AU of their host stars (e.g. Chauvin et al., 2018; Marois et al., 2008). These surveys have mostly been blind. HD 221420b represents a rare case of a substellar companion whose mass and position we can determine before imaging.

We use our orbital fit to predict the position of HD 221420 b at future epochs. In

Fig. 2.3, we show the predicted locations of HD 221420 b at epochs 2022.0 and 2023.0, 2024.0, and 2025.0. Despite the fact that HD 221420 b has never been imaged, our 68% confidence interval places it within a box of about 100×200 mas, almost sufficient to locate a fiber for the GRAVITY interferometer (Gravity Collaboration et al., 2017). For the next couple of years the brown dwarf will be offset about 0″.4 west of its host star in a slow orbit. Unfortunately, we lack the data to establish whether this orbit is clockwise or counter-clockwise on the sky.

HD 221420 b is an unusually promising accelerating system for high-contrast imaging follow-up. It consists of a relatively low-mass brown dwarf orbiting a bright ($V = 5.8$) and nearby ($d = 31.2$ pc) host star. Depending on the system age (Section 2.2.4), the ATMO2020 evolutionary models (Phillips et al., 2020b) predict an effective temperature of 400-600 K for HD 221420 b. These low temperatures correspond to a late-T or early-Y spectral type. The H-band contrast predicted from ATMO2020 ranges from 16 to 20 magnitudes depending on the brown dwarf's mass and the system age, while the predicted L' contrast ranges from 13 to 15 magnitudes. These exceed the typical performance of SPHERE (Beuzit et al., 2008) but may be achievable with long integrations and, as Figure 2.3 shows, with the knowledge of where to look.

2.6 Discussion and Conclusion

We have presented orvara, a new software tool designed to facilitate data analysis and visualization in the field of astrophysics. With its user-friendly interface and powerful fea-

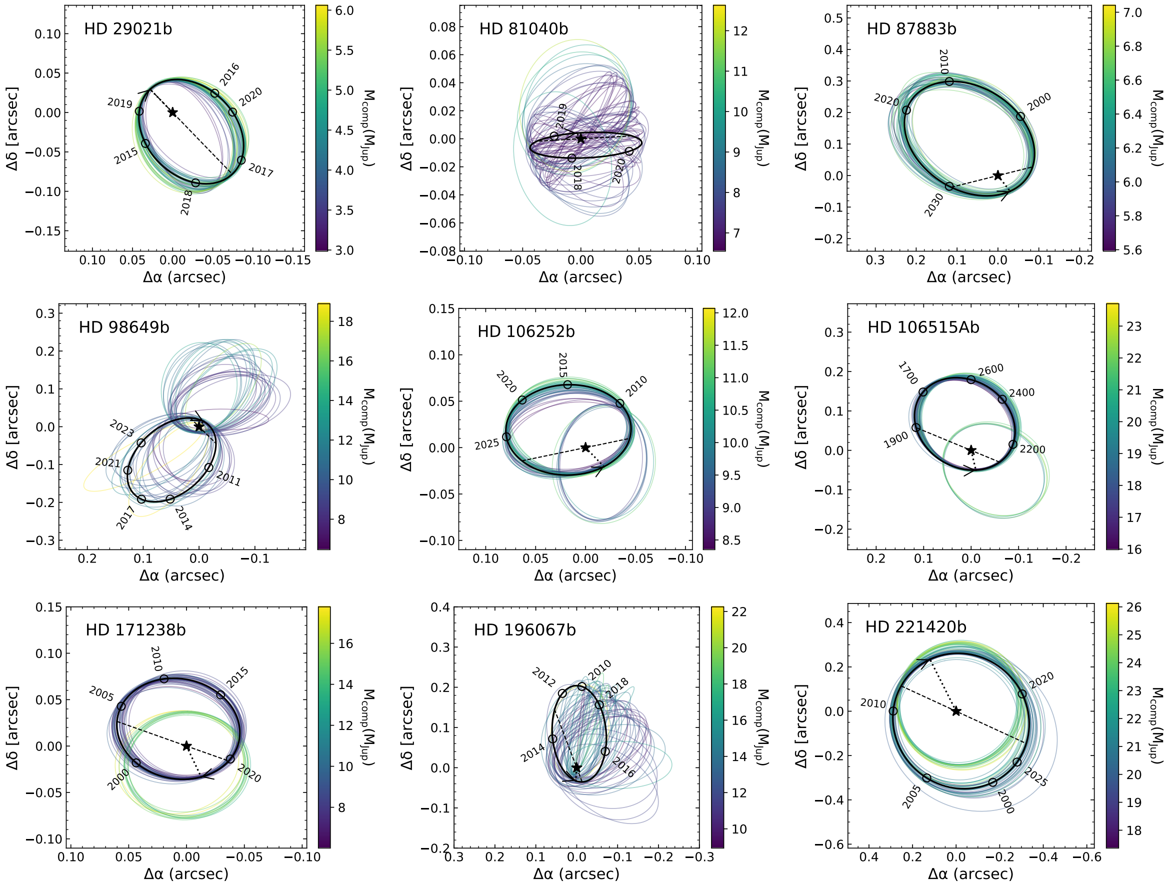

Figure 2.2 Relative astrometric orbits of the nine companions studied in this paper. The thick black lines indicate the best-fit orbit and the colorful thin lines are 50 orbits drawn randomly from corresponding posterior distribution, color-coded by the mass of the secondary companion from purple (low mass) to yellow (high mass). The dashed lines are the line of nodes connecting the host star to the companion's periastron passage. The arrows on the best-fit orbit indicate the direction of motion of the companion revolving around the host star. The hollow circled points label selected epochs along the orbit.

tures, orvara offers astronomers a comprehensive platform for exploring and interpreting observational data.

In this paper, we have refined orbital solutions for nine single RV companions orbiting G and K-type stars using the orbit-fitting package `orvara`. For every target, we have obtained 1σ error bars on the dynamical masses, and we find bi-modal orbital inclinations. Apart from HD 221420 b recently assessed by Venner et al. (2021), no past dynamical mass measurements were available for the RV companions we study. This motivates us to compare our $M \sin i$ with previous RV-only $M \sin i$ values. Our $M \sin i$ values agree with the literature reports within 1σ. Fig. 2.4 compares the minimum mass and true mass of each companion from our orbital fits. The RV-only minimum companion masses were underestimated due to uncertain inclinations by at least ≈ 5 percent and at most ≈ 250 percent. The mass increase is greater for more face-on orbits such as that of HD 87883 b, HD 171238 b, and HD 221420 b, and less so for edge-on orbits like that of HD 81040b.

Several of our companions have periods comparable to the 33-month *Gaia* EDR3 baseline: HD 29021 b ($3.737^{+0.018}_{-0.018}$ years), HD 81040 b ($2.7452^{+0.011}_{-0.0093}$ years), HD 106252 b ($4.202^{+0.011}_{-0.010}$ years), and HD 171238 b ($4.148^{+0.045}_{-0.046}$ years), with the shortest being HD 81040 b. The other five – HD 87883 b, HD 98649 b, HD 106515 Ab, HD 196067 b, HD 221420 b – have long periods ≥ 8 years. The Renormalised Unit Weight Error (RUWE) of the short-period planet HD 81040 b (=1.598) is slightly higher than the usual good astrometry solution *Gaia* recommends of <1.4 (Gaia Collaboration et al., 2018). Since there is no evidence of its binarity in the literature, the anomaly in RUWE may be attributed to the

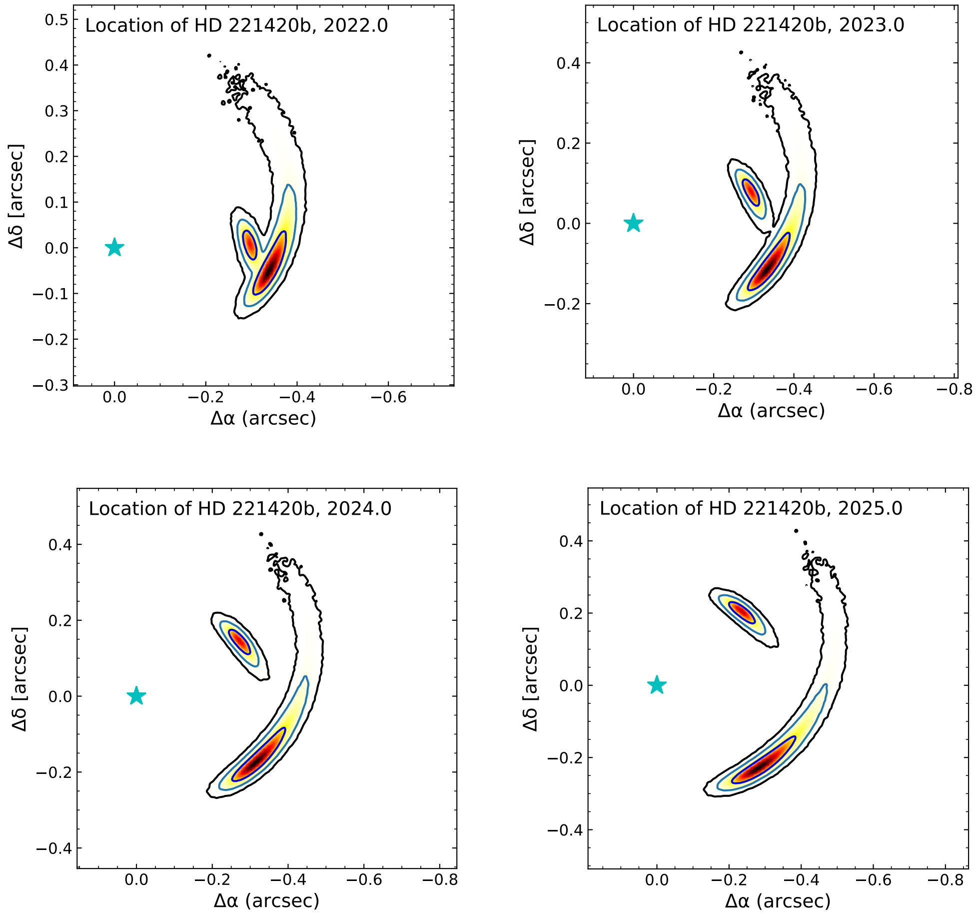

Figure 2.3 Predicted positions of HD 221420 b in epoch 2022, 2023, 2024, and 2025. The light blue stars denote the host star HD 221420. The contours indicate the predicted relative coordinates of the brown dwarf companion HD 221420 b with respect to the location of the host star. The contour lines enclose the 1σ, 2σ and 3σ probabilities with descending normalized likelihood from inner to outer contours (black to red to light yellow). Two possible sets of contours correspond to prograde or retrograde orbits. If the companion can be resolved via high-contrast imaging, it will eventually tell the two orbital motions apart.

perturbation effects from HD 81040 b, its $7.24^{+1.0}_{-0.37}\,M_{\mathrm{Jup}}$ planetary companion. Furthermore, given that its orbital period is comparable to the 33-month baseline of *Gaia* EDR3, it is challenging to constrain its astrometric orbital motion without the *Gaia* intermediate astrometric data. In their absence, all epoch astrometry data are forward-modeled by `htof`. Brandt et al. (2021a) has tested the fidelity of `htof` on data integration against the `REBOUND` code for a 3-body `orvara` fit to the short period planet β Pictoris c, and found that `htof` and `orvara` recover the `REBOUND` fit. Future *Gaia* data releases will include non-single star fits and epoch astrometry, enabling precise orbital fits to these shorter-period systems.

Interestingly, once masses and inclinations are separately constrained, the true dynamical masses of some of these companions are revealed to be much higher than the literature RV-only minimum masses. HD 196067 b, with a true mass of $12.5^{+2.5}_{-1.8}\,M_{\mathrm{Jup}}$, lies on the transition between giant planets and brown dwarfs according to the $13\,M_{\mathrm{Jup}}$ upper mass limit for the ignition of deuterium Boss (2008); Spiegel et al. (2011). HD 106515 Ab and HD 221420 b are rare long period and low-mass brown dwarfs ($\approx 20\,M_{\mathrm{Jup}}$) according to this deuterium-burning mass limit. HD 87883 b, HD 171238 b, and HD 221420 b have almost face-on orbits and, as a result, high masses. This places them in the population suggested by Schlaufman (2018) to be uncorrelated with host star metallicity, though spectroscopic measurements find each of these stars to be of super-Solar metallicity. Our finding of several companions with relatively face-on inclinations may be a selection effect: we have fit stars with signficant astrometric accelerations in the HGCA. Many of our inclinations have bimodal posteriors; these will be resolved with future *Gaia* data releases.

Eccentricities of planets provide insights into their dynamical history and formation mechanisms. Bowler et al. (2020) conducted a population-level study of the eccentricity distributions of directly imaged companions. They found that the eccentricity distribution peaks around $e = 0.23$ for single long-period giant planets, around $e = 0.5$ for brown dwarf on closer orbits (5-30 AU), and around $e = 0.6$ for low-mass companions within 10 AU.

Three of our wide orbit companions—HD 87883 b, HD 98649 b, and HD 196067 b—have high eccentricities >0.7. HD 81040 b and HD 106515 Ab also have moderately high eccentricities of between 0.5 and 0.6. HD 221420 b has a surprisingly low eccentricity of $0.162^{+0.035}_{-0.030}$, much lower than the mean eccentricity of $e = 0.5$ found by Bowler et al. (2020) for short-period brown dwarfs. HD 98649 b, with $e = 0.822^{+0.030}_{-0.024}$ is the most eccentric planet known with a period longer than 600 days and one of the more eccentric planetary orbits ever discovered.

HD 106515 Ab and HD 196067 b have outer stellar companions, raising the possibility that Kozai-Lidov (Kozai, 1962; Lidov, 1962) oscillations brought them onto highly eccentric orbits (Marmier et al., 2013). For HD 106515 Ab and HD 196067 b, the relative inclination angles between the orbital planes of the planet and the stellar companion are $10\overset{\circ}{.}4^{+8.2}_{-8.6}$ and $30\overset{\circ}{.}6^{+28.7}_{-10.5}$, respectively. The Lidov–Kozai interactions Kozai (1962); Lidov (1962) require a relative inclination angle of 39° in order to be invoked. This does not

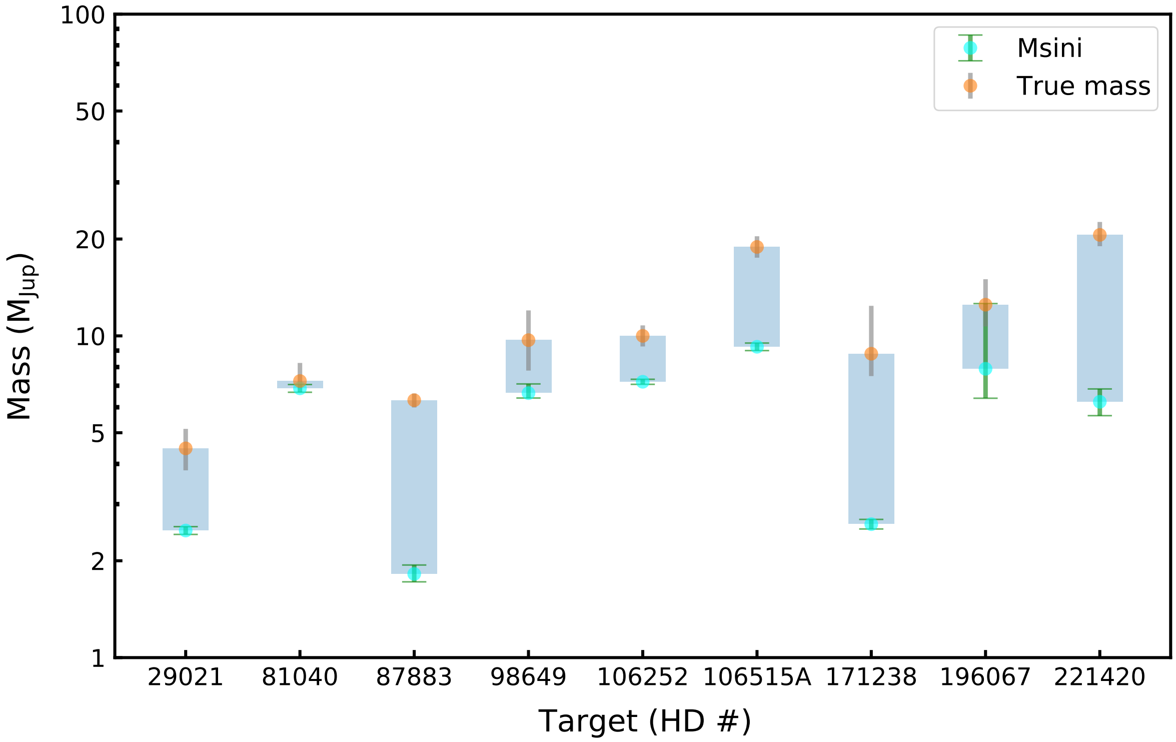

Figure 2.4 A summary of the differences in the final mass and Msini estimations for the nine RV companions studied in this work. The values for each companion are listed in Table 2.6. The orange points and grey error bars are the true dynamical masses derived by this work, and the cyan dots plus green error bars are the Msini values inferred from the orbital parameters in this work. The blue regions highlight how much the true dynamical masses can be underestimated by RV-only fits as a consequence of uncertain inclinations.

apply to HD 106515 Ab, but does apply to HD 196067 b whose relative inclination is subject to large uncertainties. The high orbital eccentricities of HD 87883 b and HD 98649 b may also be explained by the Kozi mechanism, but there's a lack of evidence of the existence of a third body in their systems. Precise *Hipparcos* and *Gaia* astrometry over a 25-year baseline limits the parameter space in which additional, outer companions could be hiding.

HD 29021, HD 81040, and HD 106252 are rare examples of stars with giant planetary companions but with subsolar metallicity. This may support the finding by Adibekyan et al. (2013) that metal-poor stars host planets with longer periods than metal-rich stars. HD 81040 and HD 106252 seem to fall in the high-mass category suggested by Schlaufman (2018) to be uncorrelated with stellar metallicity. Our dynamical masses and orbits, including our substantial corrections to $M \sin i$ for several of our planets, will enable stronger comparisons between the masses of planets around metal-poor and metal-rich stars.

From our RV fits, four of the targets HD 87883 b, HD 171238 b, HD 98649 b and HD 196067 b need at least one more period of RV monitoring in order to completely constrain their orbital solutions. Our companions have typical separations of $\lesssim 0.2''$ and distances within 50 pc. The high contrasts needed to image these planets are on the order of a few 10^{-7} for HD 221420 b in the thermal near-infrared, and slightly worse for HD 106515 Ab. The remainder would have contrasts of $\sim 10^{-9}$ in reflected light depending on orbital phase and albedo. The current generation of high contrast imagers like SPHERE for VLT (Beuzit et al., 2008) and GPI for Gemini (Chilcote et al., 2018) may marginally resolve HD 221420 b. Most of our stars are old and their companions are very cold, so the companions are light-reflecting planets/low-mass brown dwarfs with little thermal emission. These companions will provide comparisons to thermal spectra of outer Solar system planets and very old field brown dwarfs. The systems we study are not the most favorable for the Coronagraph Instrument (CGI) on the Nancy Grace Roman Space Telescope (Kasdin et al., 2020): their $\sim 0\farcs2$ angular separations are too close. However, HD 106515 Ab and HD 221420 b are excellent targets for the Giant Magellan Telescope (GMT), the European Extremely Large Telescope (ESO ELT) , and the Thirty Meter Telescope (TMT).

Absolute astrometry can break the mass-inclination degeneracy inherent in RV work, and can enable the prediction of a planet's location on the sky. We have derived precise dynamical masses of nine planets in this work. Many still have an uncertain orientation on the sky, with existing astrometry unable to distinguish prograde from retrograde orbits. This will change conclusively with future *Gaia* data releases, as *Gaia* achieves the temporal coverage needed to map out orbits on its own. The synergy between RV and absolute astrometry will then enable precise mass and orbit measurements for all of the nearby giant exoplanets.

Chapter 3

Precise Orbits and Masses of the ε Indi B system

3.1 The Necessity for a Re-analysis of the System Orbits

We will adopt the software `orvara`, which we introduced in Chapter 2, to fit orbits of one of the closest binary T dwarfs ε Indi Ba and Bb system, using long-term relative astrometry and absolute astrometry. The motivation behind this re-analysis is fueled by the different literature values obtained for the masses of the companions by different studies.

Cardoso (2012) and Dieterich et al. (2018) both used a combination of absolute and relative astrometry to obtain individual dynamical masses of ε Indi Ba and Bb. Cardoso

(2012) used NACO (Lenzen et al., 2003; Rousset et al., 2003) and FORS2 (Appenzeller et al., 1998; Avila et al., 1997) imaging to measure $77.8 \pm 0.3\,M_{\rm Jup}$ and $61.9 \pm 0.3\,M_{\rm Jup}$ for ε Indi Ba and Bb, respectively, with a parallax of 263.3 ± 0.3 mas. This parallax disagreed strongly with the *Hipparcos* parallax of ε Indi A (ESA, 1997; van Leeuwen, 2007). Fixing parallax to the *Hipparcos* 2007 value of 276.1 ± 0.3 mas, Cardoso (2012) instead obtained masses of $68.0 \pm 0.9\,M_{\rm Jup}$ and $53.1 \pm 0.3\,M_{\rm Jup}$. Dieterich et al. (2018) used a different data set to measure individual masses of $75.0 \pm 0.8\,M_{\rm Jup}$ and $70.1 \pm 0.7\,M_{\rm Jup}$ with a parallax of 276.9 ± 0.8 mas, consistent with the *Hipparcos* distance. The three dynamical mass measurements—two from Cardoso (2012) and one from Dieterich et al. (2018)—disagree strongly with one another. The highest masses of $\gtrsim 75\,M_{\rm Jup}$ are in tension with the predictions of substellar cooling models even at very old ages (Dieterich et al., 2014).

In this Chapter, we use relative orbit and absolute astrometry monitoring of ε Indi B from 2005 to 2016 acquired with the VLT to measure the individual dynamical masses of ε Indi Ba and Bb. Much of this data set overlaps with that used by Cardoso (2012), but we have the advantage of a few more epochs of data, *Gaia* astrometric references (Lindegren et al., 2020) and a better understanding of the direct imaging system thanks to years of work on the Galactic center (Gillessen et al., 2009; Plewa et al., 2015; Gillessen et al., 2017).

3.2 Properties of ε Indi B

The ε Indi B system is bound to ε Indi A (=HIP 108870, HD 209100, HR 8387), a bright K4V or K5V star (Adams et al., 1935; Evans et al., 1957; Gray et al., 2006). ε Indi A has a $2.7^{+2.2}_{-0.4}\,M_{\mathrm{Jup}}$ planet on a low eccentricity and wide orbit (Endl et al., 2002; Zechmeister et al., 2013; Feng et al., 2019). The star appears to be slightly metal poor. Apart from a measurement of [Fe/H] = -0.6 dex (Soto & Jenkins, 2018b), literature spectroscopic measurements range from [Fe/H] = -0.23 dex (Abia et al., 1988) to $+0.04$ dex (Kollatschny, 1980), with a median of -0.17 dex (Soubiran et al., 2016).

Several studies have constrained the age of the ε Indi system via various methods such as evolutionary models, Ca II HK age dating techniques, and kinematics. Using a dynamical system mass of $121 \pm 1 M_{\mathrm{Jup}}$ and evolutionary models, Cardoso (2012) predicted a system age of 3.7-4.3 Gyr. This age is older than the age of 0.8-2.0 Gyr derived from stellar rotation of ε Indi A and the age of 1-2.7 Gyr from the Ca II activity of ε Indi A, reported in Lachaume et al. (1999) assuming a stellar rotation of ∼20 days, but is younger than the kinematic estimate of >7.4 Gyr quoted in the same study. Feng et al. (2019) inferred a longer rotation period of ∼35 days derived from a relatively large data set of high precision RVs and multiple activity indicators for ε Indi A, and found an age of ∼4 Gyr. To date, the age of the star still remains a major source of uncertainty in the evolutionary and atmospheric modeling of the system.

We perform our own analysis on the age of ε Indi using a Bayesian activity-based age dating tool devised by Brandt et al. (2014) and applied in Li et al. (2021b). To do this, we adopt a Ca II chromospheric index of $\log R'_{\rm HK} = -4.72$ from Pace (2013), an X-ray activity index of $R_X = -5.62$ from the ROSAT all-sky survey bright source catalog (Voges et al., 1999), and Tycho $B_T V_T$ photometry ($B_T = 6.048 \pm 0.014$ mag, $V_T = 4.826 \pm 0.009$ mag) from the Tycho-2 catalog (Høg et al., 2000b). The star lacks a published photometric rotation period. Figure 3.1 shows our resulting posterior probability distribution, with an age of $3.48^{+0.78}_{-1.03}$ Gyr. This age is somewhat older than the young ages most literature measurements suggest, but is similar to the system age of 3.7-4.3 Gyr used by Cardoso (2012) for their analysis based on the preliminary system mass for ε Indi Ba+Bb compared to evolutionary models and to the ~4 Gyr age more recently inferred by Feng et al. (2019). We use our Bayesian age posterior when analyzing the consistency with our dynamical masses with brown dwarf models (Section 3.7).

3.3 Astrometry Data

3.3.1 Relative Astrometry

We measure the relative positions of ε Indi Ba and Bb using nine years of monitoring by the Nasmyth Adaptive Optics System (NAOS) + Near-Infrared Imager and Spectrograph (CONICA), NACO for short (Lenzen et al., 2003; Rousset et al., 2003). We use images taken by the S13 Camera on NACO in the J, H and K_s passbands. Our images come from Program IDs 072.C-0689(F), 073.C-0582(A), 074.C-0088(A), 075.C-0376(A), 076.C-0472(A), 077.C-0798(A), 078.C-0308(A), 079.C-0461(A), 380.C-0449(A), 381.C-0417(A),

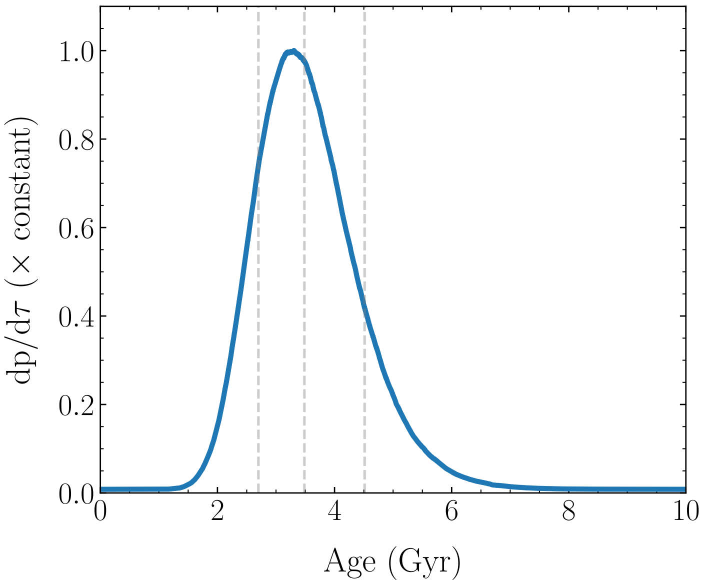

Figure 3.1 Age posterior of ε Indi A based on the Bayesian activity-age method of Brandt et al. (2014). Our analysis does not use a directly measured rotation period for ε Indi. The median and 1σ uncertainties are shown by the grey dotted lines; they correspond to $3.48^{+0.78}_{-1.03}$ Gyr.

382.C-0483(A), 383.C-0895(A), 384.C-0657(A), 385.C-0994(A), 386.C-0376(A), 087.C-0532(A), 088.C-0525(A), 089.C-0807(A), and 091.C-0899(A), all PI McCaughrean, and 381.C-0860(A), PI Kasper.

The S13 camera on NACO has a field of view (FOV) of $14'' \times 14''$ and a plate scale of $\approx$13.2 mas pix^{-1}. Most observing sequences consisted of $\approx$5 dithered images in each filter. The binary system HD 208371/2 was usually observed on the same nights and in the same mode to serve as an astrometric calibrator. We use a total of 939 images of ε Indi Ba and Bb, taken over 56 nights of observations from 2004 to 2013 for which we have contemporaneous imaging of HD 208371/2.

We perform basic calibrations on all of these images. For each night, we use contemporaneous dark images to identify bad pixels and to remove static backgrounds. We construct and use a single, master flat field for all images. We mask pixels for which the flatfield correction deviates by more than 20% from its median or for which the standard deviation of the dark frames is more than five times its median standard deviation. We then subtract the median dark image and divide by the flatfield image.

The data quality varies depending on the observing conditions and the performance of the adaptive optics (AO) system. Therefore, we apply a selection criterion to exclude poor quality data. We first extract the sources in the images using the DAOPHOT program as implemented in the `photutils` python package (Stetson, 1987; Bradley et al., 2021). We obtain estimates of the following parameters for ε Indi Ba and Bb: centroid, sharpness (a DAOPHOT parameter that characterizes the width of the source), roundness (a DAOPHOT parameter that characterizes the symmetry of the source), and signal to noise ratio (SNR). We discard images where one or both of the two targets fall outside the field of view, and for the remaining images we apply the following cut-offs in DAOPHOT detection parameters to exclude highly extended, highly elongated and low signal to noise images: sharpness $\geqslant 0.3$, $-0.5 \leqslant$ roundness $\leqslant 0.5$ and SNR $\geqslant 25$. We then visually inspect the remaining images to remove ones with bad pixels (cosmic rays or optical defects) landing on or near the target objects, and ones with AO correction artifacts that survived our DAOPHOT cut. Table 3.1 summarizes the final data set selected for relative astrometry measurements.

Table 3.1. Relative astrometry data summary

Date	Filter(s)	# Frames	Total integration (s)
2004-09-24	J, H, K_s	15	150
2004-11-14	J, H, K_s	14	840
2004-11-15	J	5	270
2004-12-15	J, H	11	220
2005-06-04	J, H, K_s	13	780
2005-07-06	K_s	6	310
2005-08-06	J, H, K_s	13	780
2005-12-17	J, K_s	7	210
2005-12-30	J, H, K_s	14	840
2005-12-31	J, H, K_s	13	780
2006-07-19	H, K_s	8	80
2006-08-06	J, H	10	100
2006-09-22	J, H, K_s	15	150
2006-10-03	J, H	7	420
2006-10-20	J, H	5	300
2006-11-12	J	5	300
2007-06-18	J, H, K_s	12	720
2007-09-09	J, H	10	450
2007-09-29	J, H	15	900
2007-11-07	J, H	10	600
2008-06-05	J, H	10	600
2008-06-10	J, H	7	70
2008-06-21	J, H	10	100
2008-08-25	J, H	9	540
2008-12-01	J, H	12	720
2009-06-17	J, H, K_s	12	720
2010-08-01	J, H	7	105
2010-11-07	J, H	10	300
2011-07-18	J, H, K_s	13	390
2012-07-18	J, H	9	540
2012-09-14	J, H	9	540
2013-06-07	J, H	10	600

3.3.2 Absolute Astrometry

The long term absolute position of ε Indi B was monitored with the FOcal Reducer and low dispersion Spectrograph (FORS, Appenzeller et al., 1998) installed on ESO's UT1 telescope at the Very Large Telescope (VLT). The FORS system consists of twin imagers and spectrographs FORS1 and FORS2, collectively covering the visual and near UV wavelength. The absolute astrometry monitoring was done with the FORS2 imager coupled with two mosaic MIT CCDs; the camera has a pixel scale of $0\farcs126$/pixel in its unbinned mode and a field of view (FOV) of $\approx 8\farcm6 \times 8\farcm6$.

The FORS2 monitoring of ε Indi B covers a long temporal baseline beginning in 2005 and ending in 2016. Our images come from Program IDs 072.C-0689(D), 075.C-0376(B), 076.C-0472(B), 077.C-0798(B), 078.C-0308(B), 079.C-0461(B), 380.C-0449(B), 381.C-0417(B), 382.C-0483(B), 383.C-0895(B), 384.C-0657(B), 385.C-0994(B), 386.C-0376(B), 087.C-0532(B), 088.C-0525(B), 089.C-0807(B), and 091.C-0899(B), all PI McCaughrean. The FORS-2 focal plane consists of two CCDs, chip1 and chip2. We only consider the data taken with the chip1 CCD. Over the 12 years of absolute position monitoring, 940 images were taken with chip1 over 88 epochs. For the majority of the epochs, 10 dithered images in I_{BESSEL} filter were obtained, with a 20 second exposure time for each image. We exclude 36 blank image frames over 4 epochs between 2009-8-21 and 2009-11-3, resulting in a final total of 904 image frames for our analysis. A summary of the FORS2 data is given in Table 3.2. These 904 science frames are bias-corrected and flat-fielded using the normalized master values generated from median combination of the flat and

Table 3.2. Absolute astrometry data from FORS2[a]

Date	# Frames	Band	Total integration (s)
2005-05-06	10	I_{Bess}	200
2005-05-12	10	I_{Bess}	200
2005-06-08	10	I_{Bess}	200
2005-07-06	10	I_{Bess}	200

[a] The full observing log is available as an online table; only the first four rows are shown here for reference.

bias frames obtained in the same set of observing programs.

3.4 Relative and Absolute Positions

3.4.1 Point Spread Function (PSF) Fitting

To measure the relative separations of the two brown dwarfs in the NACO data, we need to fit their PSFs. Cardoso (2012) has demonstrated that Moffat is the best analytical profile for the NACO data compared to Lorentzian and Gaussian. During the epochs when the projected separations of the two brown dwarfs are small, the two PSFs are only separated by one or two full widths at half maximum (FWHM). As a result, the flux near the center of one source has non-negligible contributions from the wings of the other source. This could introduce significant biases in the measured positions if fitting a PSF profile to each source separately. Therefore, we implement a joint fit of the two PSFs using a sum of two elliptical Moffat profiles:

$$\text{Counts}(x, y) = f_1\psi_1(x, y) + f_2\psi_2(x, y) \tag{3.1}$$

with

$$\psi_i(x, y) = f_i(1 + c_1(x - x_i)^2 + 2c_2(x - x_i)(y - y_i) + c_3(y - y_i)^2)^{-\beta} \tag{3.2}$$

where ψ_i is a general elliptical 2D Moffat profile centered at $\{x_i, y_i\}$ with peak intensity f_i. Our model is the sum of two such profiles with different fluxes at different locations, sharing the same morphology, i.e., the same $\{c_1, c_2, c_3\}$. Instead of fitting for $\{c_1, c_2, c_3\}$ directly, we fit for three equivalent parameters: $\{\text{fwhm}_x, \text{fwhm}_y, \phi\}$, which are the FWHMs of the elliptical Moffat profile along the x and y axes, and the counter-clockwise rotation angle of the PSF, respectively. These physical parameters are related to $\{c_1, c_2, c_3, \beta\}$ through the following equations:

$$c_1 = \frac{\cos^2\phi}{\sigma_x^2} + \frac{\sin^2\phi}{\sigma_y^2} \tag{3.3}$$

$$c_2 = \frac{\sin 2\phi}{2\sigma_x^2} - \frac{\sin 2\phi}{2\sigma_y^2} \tag{3.4}$$

$$c_3 = \frac{\sin^2\phi}{\sigma_x^2} + \frac{\cos^2\phi}{\sigma_y^2} \tag{3.5}$$

$$\text{fwhm}_{x,y} = 2\sigma_{x,y}\sqrt{(2^{1/\beta} - 1)} \tag{3.6}$$

For each background subtracted image, we fit for the sum of two PSFs by minimizing χ^2 over 10 parameters: $\{x_1, y_1, x_2, y_2, f_1, f_2, \mathrm{fwhm}_x, \mathrm{fwhm}_y, \phi, \beta\}$. In this case, χ^2 is defined by:

$$\chi^2 = \sum_i^{n_{pix}} \frac{(D_i - f_1\ \psi_{1,i} - f_2\ \psi_{2,i})^2}{\sigma_i^2} \tag{3.7}$$

We use scipy's non-linear optimization routines (Virtanen et al., 2020) to minimize χ^2 over the 8 non-linear parameters $\{x_1, y_1, x_2, y_2, \mathrm{fwhm}_x, \mathrm{fwhm}_y, \phi, \beta\}$, and for each trial set of non-linear parameters, we solve for the best fit linear parameters $\{f_1, f_2\}$ analytically and marginalize over them.

3.4.2 Calibrations for Relative Astrometry

In order to measure precise relative astrometry, we must measure and correct various instrumental properties and atmospheric effects that can alter the apparent separation and position angle (PA) of ε Indi Ba and Bb. In this section we describe our calibrations for the instrument plate scale and orientation, distortion correction and differential atmospheric refraction.

Plate scale, Orientation, and Distortion Correction

We calibrate the plate scale and the north pointing of the NACO S13 camera using NACO's observations of a nearby wide separation binary, HD 208371/2, observed concurrently with the science data over the ~10-year relative orbit monitoring period. We calibrate the separation and PA of the binary in NACO data against the high precision measurements from Gaia EDR3 for HD 208371/2:

$$\frac{\mathrm{sep}}{\mathrm{arcsec}} = 8.90612 + 0.00011\,(\mathrm{Jyear} - 2016.0) \tag{3.8}$$

$$\frac{\mathrm{PA}}{\mathrm{degree}} = 348.10345 - 0.00040\,(\mathrm{Jyear} - 2016.0) \tag{3.9}$$

The uncertainties on these do depend on the epoch, but with proper motion uncertainties $\lesssim 40\,\mu\mathrm{as\,yr}^{-1}$, positional uncertainties are only $\approx$0.5 mas even extrapolated ten years before Gaia. This represents a fractional uncertainty in separation below 10^{-4} and contributes negligibly to our error budget.

To measure the separation and PA of the calibration binary, we use the Moffat PSF fitting algorithm described in section 3.4.1. Since the binary is widely separated, a joint PSF fit in this case is effectively equivalent to fitting a single 2D Moffat profile for each star separately (albeit with the same structure parameters for each star's Moffat function). The calibration results are shown in Fig.3.2. We measure an overall average plate scale of 13.260 ± 0.001, but we also note that the plate scale seems to increase slightly with time from 2004 to 2010. Both the plate scale and the increasing trend agree with other measurements in the literature, (Chauvin et al., 2010; Cardoso, 2012). In Cardoso (2012), the same calibration binary was used to derive the plate scales but a different reference measurement for the binary was used. Adjusting their results to the more precise Gaia measurement of the binary brings their plate scale into agreement with ours. The PA zero point of the instrument varies from observation to observation, and has a long term trend as well. This is in agreement with the analysis in Plewa (2018).

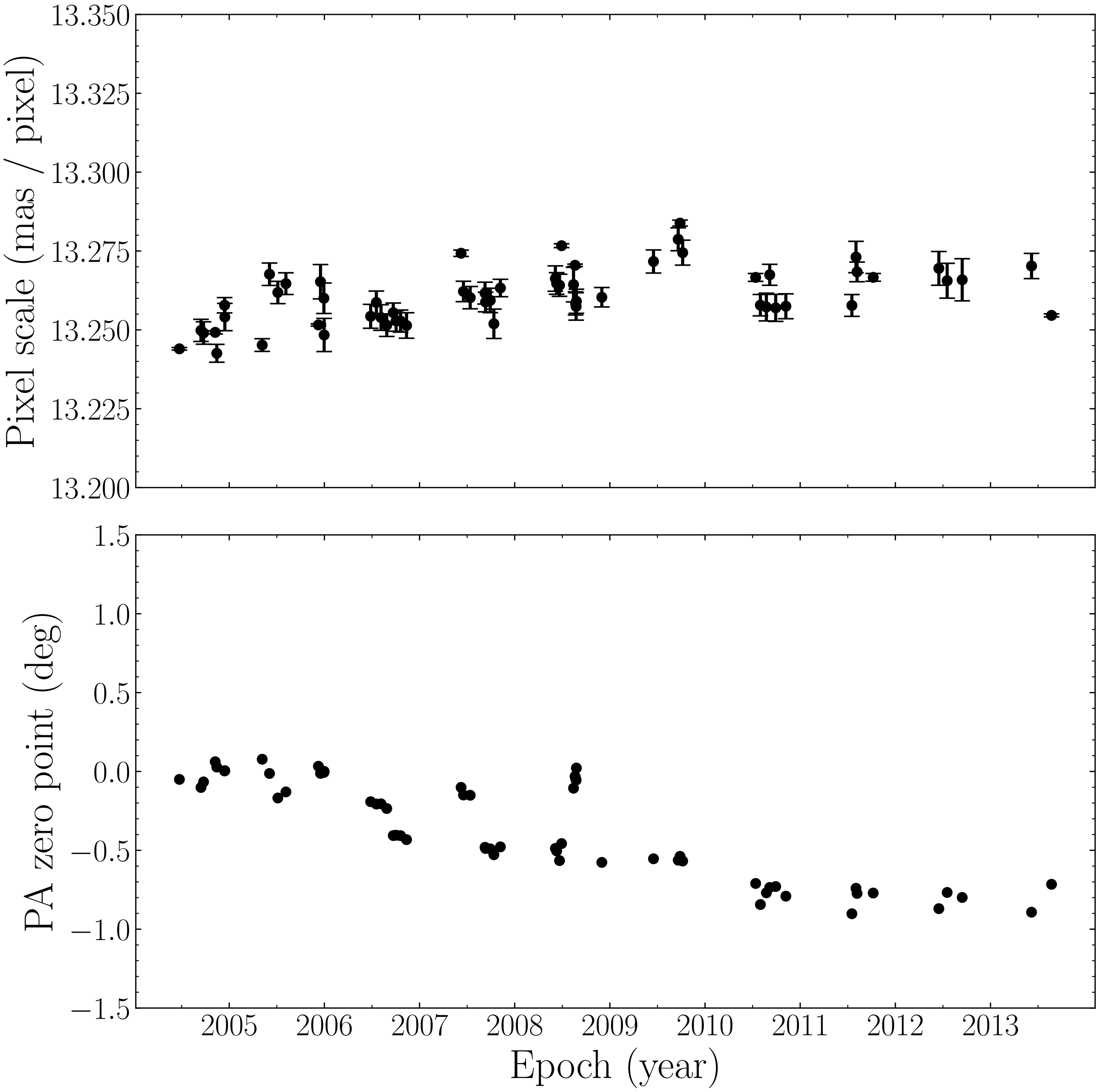

Figure 3.2 Pixel scale and PA zero point calibrations for the NACO S13 camera, derived using the binary HD 208371/2 as measured by Gaia EDR3.

The distortion correction was shown to be of little significance for the NACO S13 camera (Trippe et al., 2008) due to the small field of view. For completeness, we still apply the distortion correction derived by Plewa et al. (2018).

Differential Atmospheric Refraction and Annual Aberration

The dominant atmospheric effect that needs to be corrected for is differential atmospheric refraction (Gubler & Tytler, 1998). When a light ray travels from vacuum into Earth's atmosphere, it is refracted along the zenith direction and changes the observed zenith angle of the source, making the apparent zenith angle, z, deviate from the true zenith angle in the absence of an atmosphere, z_0:

$$z = z_0 + R \tag{3.10}$$

where R is the total refraction angle experienced by the light ray. The amount of this refraction depends on atmospheric conditions, the wavelength of the incoming light, and the zenith angle of the object. Therefore, for two objects at different positions in the sky and with different spectral types, the total refraction angles are different and can alter the apparent separation and PA of the objects. We can write this differential refraction, ΔR, in terms of two components, one due to their difference in color, and one due to the difference of their true zenith angles (Gubler & Tytler, 1998):

$$\Delta R = \Delta R_{\mathrm{color}} + \Delta R_{\Delta z_0} \tag{3.11}$$

For ε Indi Ba and Bb, the second term is much smaller as they are separated by only $< 1''$, and produced negligible effects on the final results compared to the first term. We included both effects for completeness. The total differential refraction can be calculated with:

$$\Delta R = R_2(n_2, z_2) - R_1(n_1, z_1) \tag{3.12}$$

where the n_i's are the effective refractive indices of the Earth's atmosphere for the target sources. n_i depends on the effective central wavelength (λ_i) of the target in the observed passband, and on observing conditions, most commonly pressure (P), temperature (T), humidity (H) and altitude (z). Cardoso (2012) calculated the effective central wavelengths for ε Indi Ba and Bb in the J, H, and K_s bands by integrating high resolution spectra of the two brown dwarfs. To calculate the refractive index, $n_i(\lambda_i, P, T, H, z)$, we use the models in Mathar (2007) covering a wavelength range of 1.3 μm to 24 μm. Then, the total refraction can be approximately expressed as (Smart, 1977):

$$R(n, z) \approx (n - 1)\tan(z) \tag{3.13}$$

A comparison of the separations along the zenith direction of ε Indi Ba and Bb are shown in Figure.3.3. We can clearly see the systematic differences between the J, H, and K_s bands due to differential refraction before the correction. After applying the correction, the three bands are brought to much better agreement as well as having a smaller total scatter around the mean.

Annual aberration is a phenomenon that describes a change in the apparent position of a light source caused by the observer's changing reference frame due to the orbital motion of the Earth (Bradley, 1727; Phipps, 1989). We correct for the differential annual aberration, the difference in aberration between ε Indi Ba and Bb, in relative astrometry

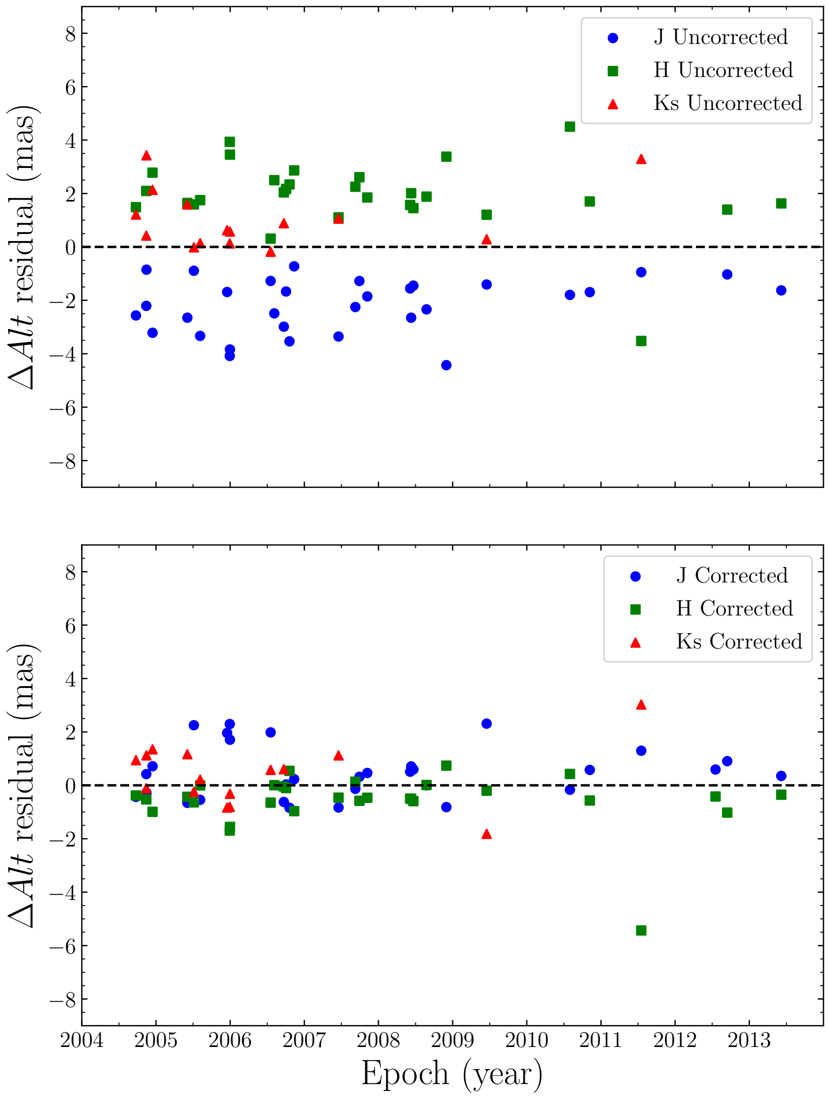

Figure 3.3 Residual altitude separation of ε Indi Ba and Bb in each band compared to the mean of all bands, before (top panel) and after (bottom panel) applying a correction for differential atmospheric refraction.

by transforming the measured positions of ε Indi Ba and Bb to a geocentric reference frame using `astropy`. The effect is generally a small fraction of the relative astrometry error bars and has negligible impact on the relative orbit fit. For absolute astrometry, the aberration is absorbed by the linear component of the distortion correction.

PSF Fitting Performance and Systematics

In order to understand how well our PSF fitting algorithm described in Section 3.4.1 performs, we investigate the systematic errors and potential biases of the algorithm in this section, and adjust the errors of our results accordingly.

To do this, we crop out boxes around the stars in the calibration binary, HD 208371/2, and use them as empirical PSFs. We build a collection of such PSF stamps from the images of the calibration binary based on AO quality and SNR. We use these PSFs stamps and empty background regions of the NACO data to generate mock data sets containing overlapping PSFs. For each such mock image, we randomly select one empirical PSF from the collection and place two copies of this PSF onto the background of an ε Indi B image. We scale the fluxes of the two PSF copies to be similar to those of ε Ba and Bb in a typical image. We then generate a large sample of these mock images at various separations and PAs. Since the calibration binary stars are widely separated, these empirical PSFs are effectively free of nearby star contamination. We then perform the PSF fitting described in Section 3.4.1 on the mock images and compare the measurements to the true, known separations and PAs.

The results for this test are shown in Figure 3.4. Each data point is the root mean

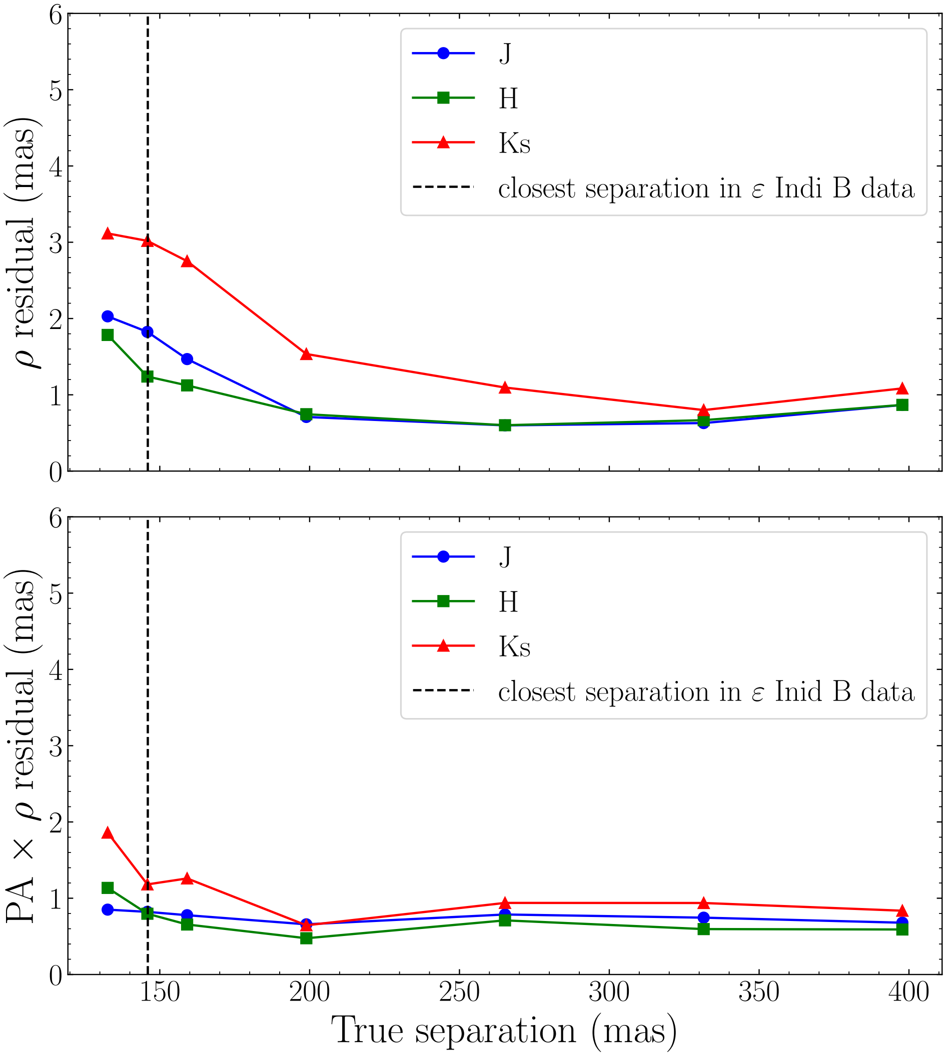

Figure 3.4 Root mean square residuals of the measured separations from the true separations of the PSFs in simulated data. Top panel shows the residuals in the radial direction. Bottom panel shows the residuals in the tangential direction in terms of arclength. Arclength is a better indicator of the fitting algorithm's performance than PA, because we expect arclength residuals to be independent of radial separation, but the PA will go up at smaller separation simply due to geometry.

square residual from fitting 400 mock images at the same separation but with various PAs. The errors we find from these mock data sets are slightly larger but within the same order of magnitude as the scatter in our ε Indi B measurements. We also find that the residuals of these mock data measurements do increase as the PSF overlap becomes significant, but they remain at the milliarcsecond level even at a separation equal to the closest separation in the ε Indi B data set. The performance for the K_s band is slightly worse due to the large flux ratio of the system in K_s. Overall, our joint PSF fitting algorithm has sub-milliarcsec errors across all three bands for widely separated sources, and has within a few milliarcseconds errors for overlapping sources. For our final relative astrometry results for ε Indi B, we add the systematic errors shown in Figure 3.4 to the measurement errors of the relative astrometry in quadrature.

3.4.3 Relative Astrometry Results

The final relative astrometry results are shown in Table 3.3. These are measured by applying the calibrations described in Section 3.4.2 and jointly fitting for the positions of ε Indi Ba and Bb for every selected image, using the PSF fitting method described in Section 3.4.1. We take the mean and the error on the mean for every epoch, and add the systematic errors quadratically to the measurement errors as described in Section 3.4.2. In Figure 3.5, we show a PSF fit for the simple case where the two PSFs are effectively isolated, as well as a PSF fit from the epoch with the closest projected separation and hence maximum PSF overlap. For each case, we take the fit with the median squared

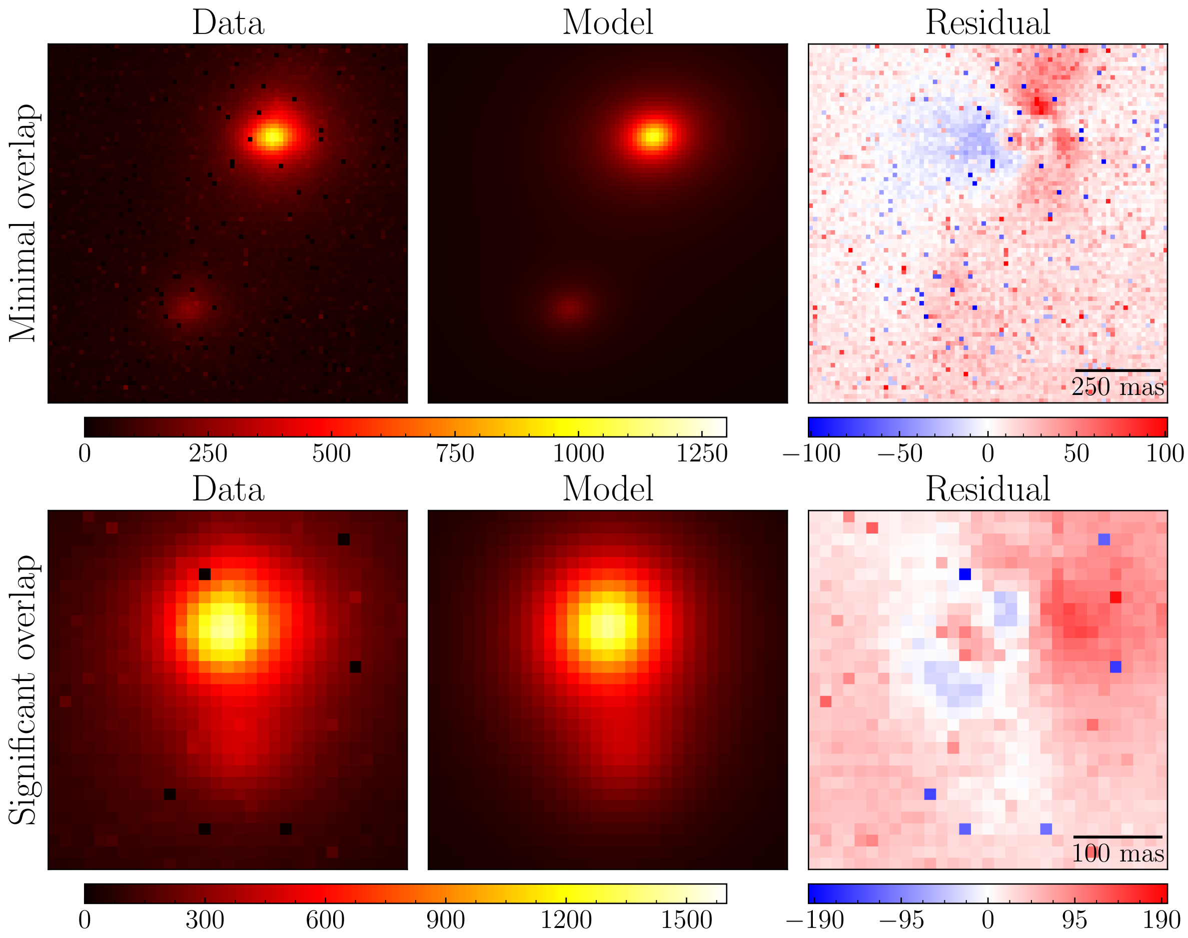

Figure 3.5 Examples of the joint moffat PSF fits to NACO data. Top panel shows an example of negligible PSF overlap. Bottom panel shows an example from the epoch with maximum overlap in NACO data.

residual from that epoch to demonstrate the typical residual level.

3.4.4 Calibrations for Absolute Astrometry

We now seek to measure the position of ε Indi Ba relative to a set of reference stars in the FORS2 images with known absolute astrometry. We approach the problem in stages. First, we fit for the pixel positions of all stars in the frame. We then use Gaia EDR3 astrometry of a subsample of these stars to construct a distortion map. Next, we use our fit to the NACO data (Section 3.6) to fix the relative positions of ε Indi Ba and Bb. Finally, we use the PSFs of nearby reference stars to model the combined PSF of ε Indi Ba and Bb and measure their position in a frame anchored by Gaia EDR3.

We begin by measuring stellar positions in pixel coordinates and using them to derive a conversion between pixel coordinates (x, y) and sky coordinates (α, δ), i.e., a distortion correction. We identify 46 Gaia sources in the field of view of the FORS2 images; these will serve as reference stars to calibrate and derive the distortion corrections.

We fit elliptical Moffat profiles to retrieve each individual reference star's pixel location (x, y) on the detector. These are Gaia sources with known α and δ measurements propagated backwards from Gaia EDR3's single star astrometry in epoch 2016.0. We adopt the same module used for relative astrometry described in Section 3.4.1 to fit for the reference stars' positions. For each star, we fit for three additional parameters: the FWHMs along two directions, and a rotation angle in between.

Table 3.3. Relative astrometry results

Epoch	ρ (arcsec)	σ_ρ(arcsec)	θ (deg)	σ_θ (deg)
2004.730	0.88310	0.00108	140.317	0.047
2004.869	0.89461	0.00110	140.853	0.047
2004.872	0.89560	0.00126	140.814	0.067
2004.954	0.90200	0.00107	141.115	0.051
2005.423	0.93141	0.00112	142.648	0.045
2005.511	0.93351	0.00126	142.888	0.054
2005.595	0.93654	0.00112	143.169	0.044
2005.959	0.94067	0.00118	144.222	0.050
2005.995	0.94079	0.00117	144.352	0.049
2005.997	0.93987	0.00115	144.356	0.050
2006.546	0.92015	0.00111	146.044	0.053
2006.595	0.91721	0.00107	146.230	0.049
2006.724	0.90802	0.00106	146.657	0.047
2006.754	0.90502	0.00110	146.745	0.047
2006.800	0.90222	0.00138	146.984	0.053
2006.863	0.89489	0.00110	147.111	0.054
2007.461	0.81432	0.00109	149.295	0.050
2007.688	0.77183	0.00104	150.250	0.053
2007.743	0.76014	0.00110	150.515	0.055
2007.849	0.73666	0.00109	151.017	0.063
2008.427	0.57619	0.00104	154.647	0.078
2008.441	0.57103	0.00112	154.665	0.106
2008.471	0.56145	0.00110	154.978	0.086
2008.648	0.49830	0.00103	156.664	0.082
2008.915	0.39126	0.00163	160.569	0.148
2009.458	0.14626	0.00273	186.175	0.562
2010.582	0.32838	0.00120	332.295	0.157
2010.849	0.30942	0.00103	339.059	0.134
2011.543	0.17352	0.00243	12.950	0.433
2012.545	0.25518	0.00110	107.165	0.186
2012.703	0.29394	0.00112	112.857	0.164
2013.431	0.47861	0.00104	126.845	0.088

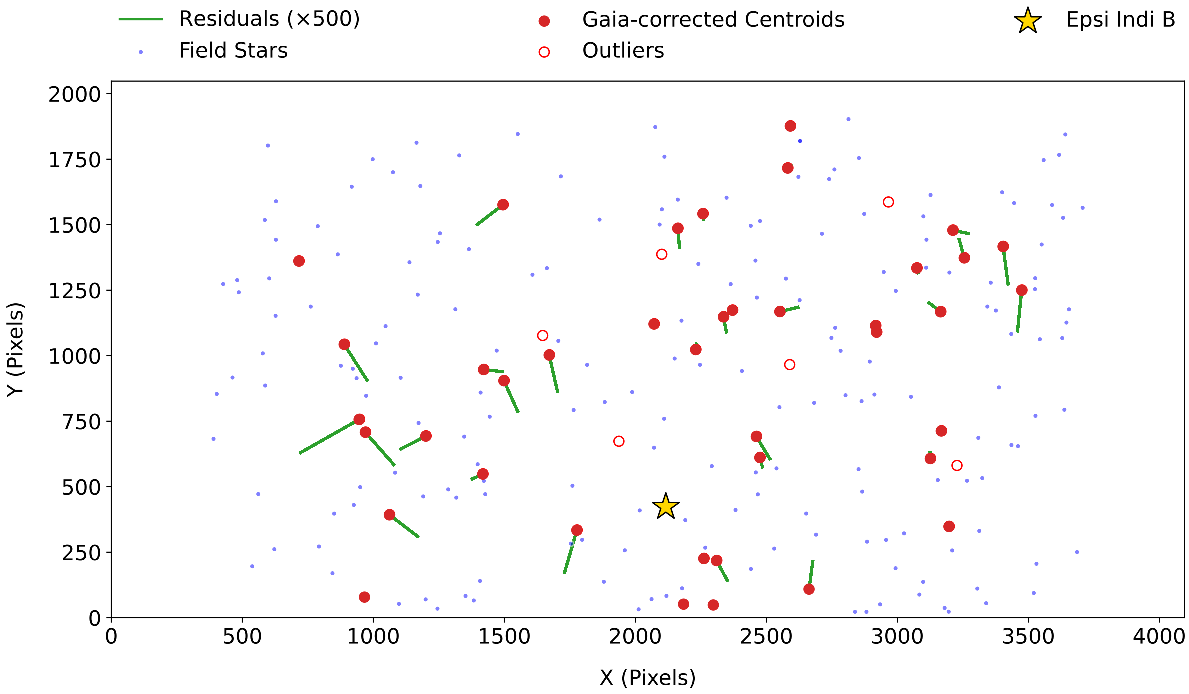

Figure 3.6 Distortion correction to one of the 904 image frames from the FORS2 long term monitoring of ε Indi B's absolute positions. The position of ε Indi B is indicated by the yellow star while the blue dots are field stars. The red points are reference stars in the Gaia EDR3 catalog. The green lines indicate the residuals of the measured centroids from their distortion-corrected predictions based on EDR3 astrometry. Red open circles are Gaia EDR3 stars that we discard as outliers.

We assume a polynomial distortion solution of order N for FORS2:

$$\alpha*_{\rm model} \equiv \alpha \cos\delta = \sum_{i=0}^{N} \sum_{j=0}^{N-i} a_{ij} x^i y^j \tag{3.14}$$

$$\delta_{\rm model} = \sum_{i=0}^{N} \sum_{j=0}^{N-i} b_{ij} x^i y^j. \tag{3.15}$$

minimizing

$$\chi^2 = \sum_{k=1}^{n_{\rm ref}} \left[\left(\frac{\alpha*_k - \alpha*_{{\rm model},k}}{\sigma_{\alpha*,k}} \right)^2 + \left(\frac{\delta_k - \delta_{{\rm model},k}}{\sigma_{\delta_k}} \right)^2 \right]. \tag{3.16}$$

This defines a linear least-squares problem because each of the a_{ij} appears linearly in the data model. To avoid numerical problems, we define $x = y = 0$ at the center of the image and subtract $\alpha_{\rm ref} = 181\overset{\circ}{.}327$, $\delta_{\rm ref} = -56\overset{\circ}{.}789$ from all Gaia coordinates. To determine the best model for distortion correction, we compare 2nd, 3rd and 4th-order polynomial models. We derive distortion corrections excluding one Gaia reference star at a time. We then measure the excluded star's positions, and use the distortion correction built without using this star to derive its absolute astrometry. The consistency of the best-fit astrometric parameters with the Gaia measurements, and the scatter of the individual astrometric measurements about this best-fit sky path, both act as a cross-validation test of the distortion correction. For most stars, a second-order correction outperforms a third-order correction on both metrics. This also holds true dramatically for ε Indi B itself, with a second-order distortion correction providing substantially smaller scatter about the best-fit sky path.

Once we have a list of pixel coordinates (x, y) and sky coordinates $(\alpha_*,\ \delta)$ for all of our reference stars, we derive second order distortion corrections for each image. To avoid having poorly fit stars drive the results, we clip reference stars that are $\geq 10\sigma$ outliers. Figure 3.6 shows an example of an image frame indicating the displacement of the distortion-corrected centroids according to Gaia with respect to their original "uncorrected" centroid locations on the detector. The empty red circles are Gaia stars that were discarded as outliers.

We now seek to measure the position of ε Indi Ba on the distortion-corrected frame defined by the astrometric reference stars. We cannot fit the brown dwarfs' positions in the same way as the reference stars: their light is blended in most images. Instead, we first fix their relative position using an orbital fit to the relative astrometry (Sections 3.4.2 and 3.6). We then model the two-dimensional image around ε Indi Ba and Bb as a linear combination of the interpolated PSFs of the five nearest field stars.

With the relative astrometry fixed, our fit to the image around ε Indi Ba and Bb has nine free parameters: five for the normalization of each reference PSF, one for the background intensity, one for the flux ratio between Ba and Bb, and two for the position of ε Indi Ba. The fit is linear in the first six of these parameters. We solve this linear system for each set of positions and flux ratios, and use nonlinear optimization to find their best-fit values in each image. We then fix the flux ratio to its median best-fit value of 0.195 and perform the fits again, optimizing the position of ε Indi Ba in each FORS2 image.

Figure 3.7 shows two examples of the residuals to this fit. The residual intensity exhibits little structure, whether the two components are strongly blended (bottom panel) or clearly resolved (top panel).

Our fit produces pixel coordinates of ε Indi Ba in each frame. Our use of self-calibration ensures that these pixel coordinates are in the same reference system as the astrometric standard stars. We then apply the distortion correction derived from these reference stars to convert from pixel coordinates to absolute positions in right ascension and declination. Another important calibration for absolute astrometry is the correction for atmospheric dispersion. However, our data were taken with an atmospheric dispersion corrector (ADC) in place, which has not been sufficiently well-characterized to model and remove residual dispersion (Avila et al., 1997). We therefore use only the azimuthal projection of the absolute astrometry in the orbital fit. The effects and implications of the ADC and residual atmospheric dispersion are discussed in Section 3.6.2.

3.5 Photometric Variability

Koen (2005), Koen et al. (2005), and Koen (2013) found potential evidence of variability of the system in the Near-Infrared (I, J, H and K_s) but also stated that the results are inconclusive due to correlation between seeing and variability. With the long-term monitoring data acquired by NACO (J, H, and K_s bands) and FORS2 (I band), we further investigate the photometric variability of ε Indi Ba and Bb in this section.

We apply the generalized Lomb-Scargle method (Zechmeister & Kürster, 2009) and we use the implementation in the `astropy` Python package (Astropy Collaboration et al.,

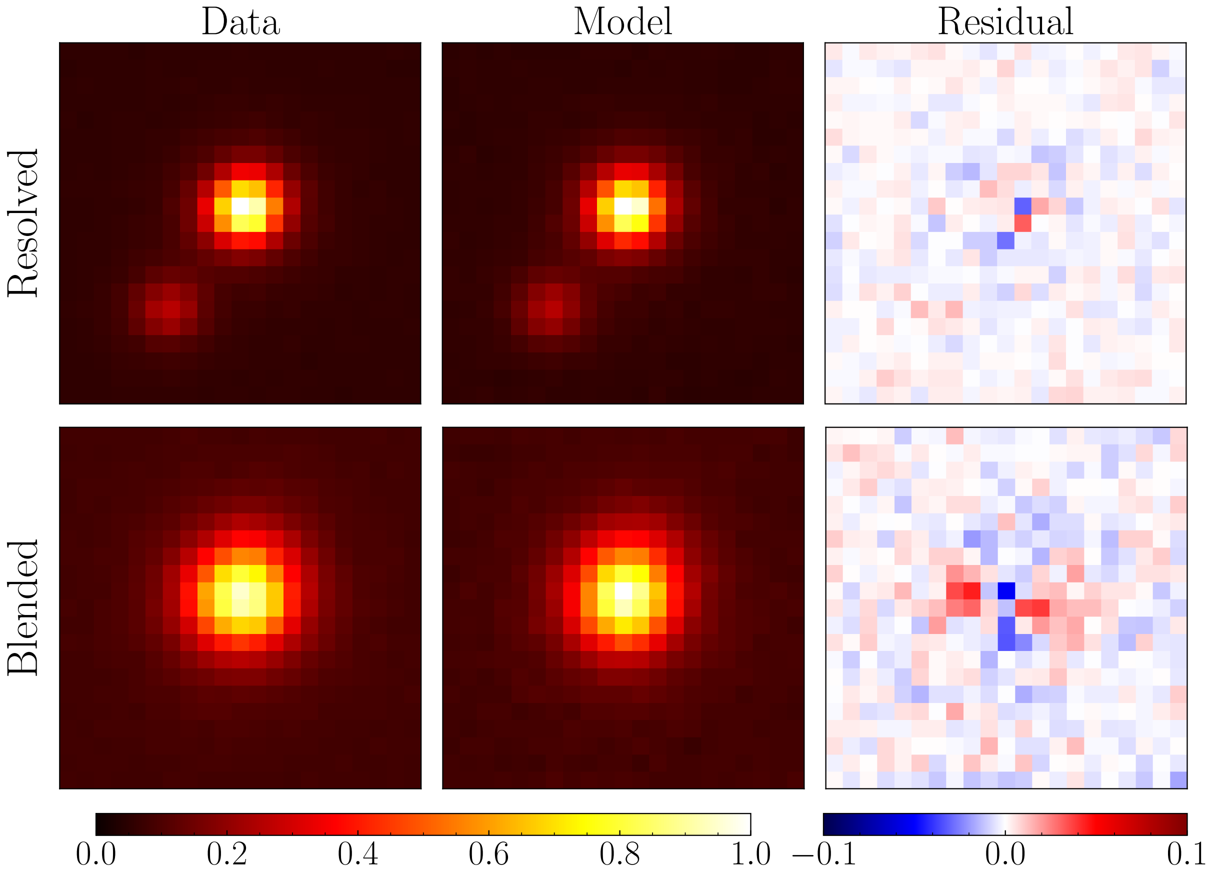

Figure 3.7 Example fits and residuals to FORS2 images when the two components (ε Indi Ba and ε Indi Bb) are completely resolved (top panel) or strongly blended (bottom panel). In each panel, all values are normalized to the peak intensity of the model fits.

2013, 2018) for this work. For NACO data, there are no other field stars within the FOV to calibrate the photometry. Therefore, we take the best fit flux ratios of Ba to Bb from PSF fitting and apply the periodogram on the time series of this flux ratio. For FORS2 data, we use the `photutils` python package to perform differential aperture photometry on the sky-subtracted, flat-fielded and dark-corrected FORS2 images. We first measure the total flux of ε Indi Ba and Bb, and the fluxes of fields stars in the field of view. We then normalize the flux of ε Indi Ba and Bb using the median flux of all the non-variable field stars to obtain the relative flux of the ε Indi system. We apply the periodogram on this relative flux. We choose a minimum frequency of 0 and a maximum frequency of 1 hour^{-1}, which is roughly an upper frequency limit associated with rotational activities if either object were rotating at break-up velocity. We choose a frequency grid size of $\Delta f = 1/n_0 T$, where $n_0 = 10$, $T = 10$ yr to sufficiently sample the peaks (VanderPlas, 2018).

Figure 8 top panel shows the measured flux ratios in both NACO and FORS2 data over all epochs. The bottom panels shows that the ε Indi system has a typical flux scatter for its brightness in FORS2 data. From our simple analysis, we do not see any significant evidence of photometric variability of the system in our periodograms. However, since the observations are not designed for the purpose of investigating variability, the non-uniform and sparsely sampled window function of the observations resulted in very noisy periodograms. Therefore, we also cannot reach any definitive conclusions regarding whether there is any variability of the system with a physical origin.

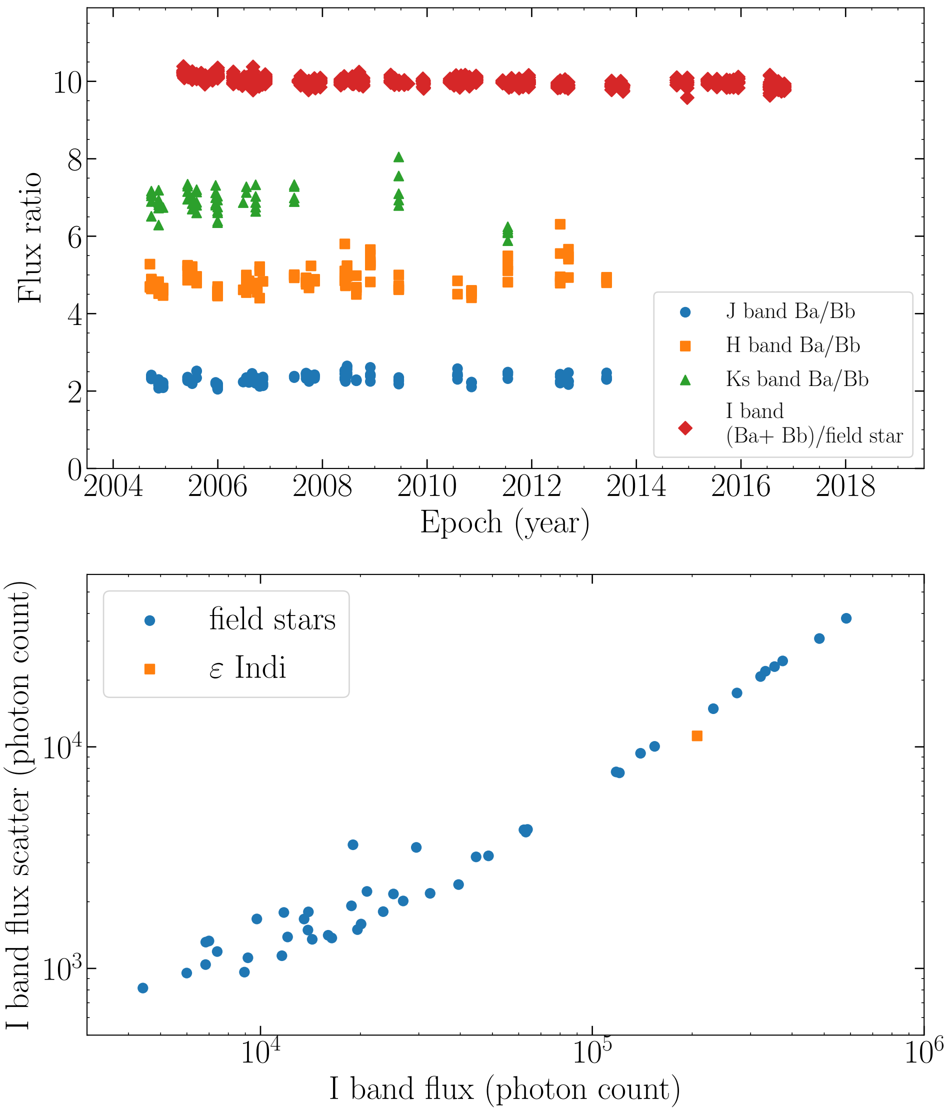

Figure 3.8 Top panel shows the flux ratios of ε Indi Ba over Bb in J, H and Ks bands measured using the joint PSF fitting method, and the flux ratios of Ba + Bb over the average of the field stars measured using aperture photometry. The bottom panel shows the flux scatter of ε Indi compared to the field stars in I band FORS2 data.

3.6 Orbital Fit

3.6.1 Relative Astrometry

We use the relative astrometry measurements summarized in Table 3.3 to fit for a relative orbit and obtain the orbital parameters. For this, we use an adaptation of the open-source orbital fitting python package, `orvara` (Brandt et al., 2021h), and fit for 7 orbital parameters: period, the angular extent of the semi-major axis ($a_{\rm ang}$, hereby referred to as the angular semi-major axis), eccentricity (e), argument of periastron (ω), time of periastron (T_0), longitude of ascending node (Ω), and inclination (i). The corner plot for the MCMC chain is shown in Figure 3.9. The best fit relative orbit is shown in Figure 3.10, and the best fit orbital parameters are summarized in Table. 3.4. The reduced χ^2 is 0.77 which suggests that we may be slightly overestimating the errors, especially for the earlier epochs. This is possibly because the earlier epochs in general have higher quality data, while we used empirical PSFs of a wider range of qualities in order to generate a large enough sample for the error inflation estimate described in section 3.4.2. Nevertheless, we are able to produce an excellent fit and obtain very tight constraints on the orbital parameters thanks to high quality direct imaging data and a long monitoring baseline that almost covers an entire period.

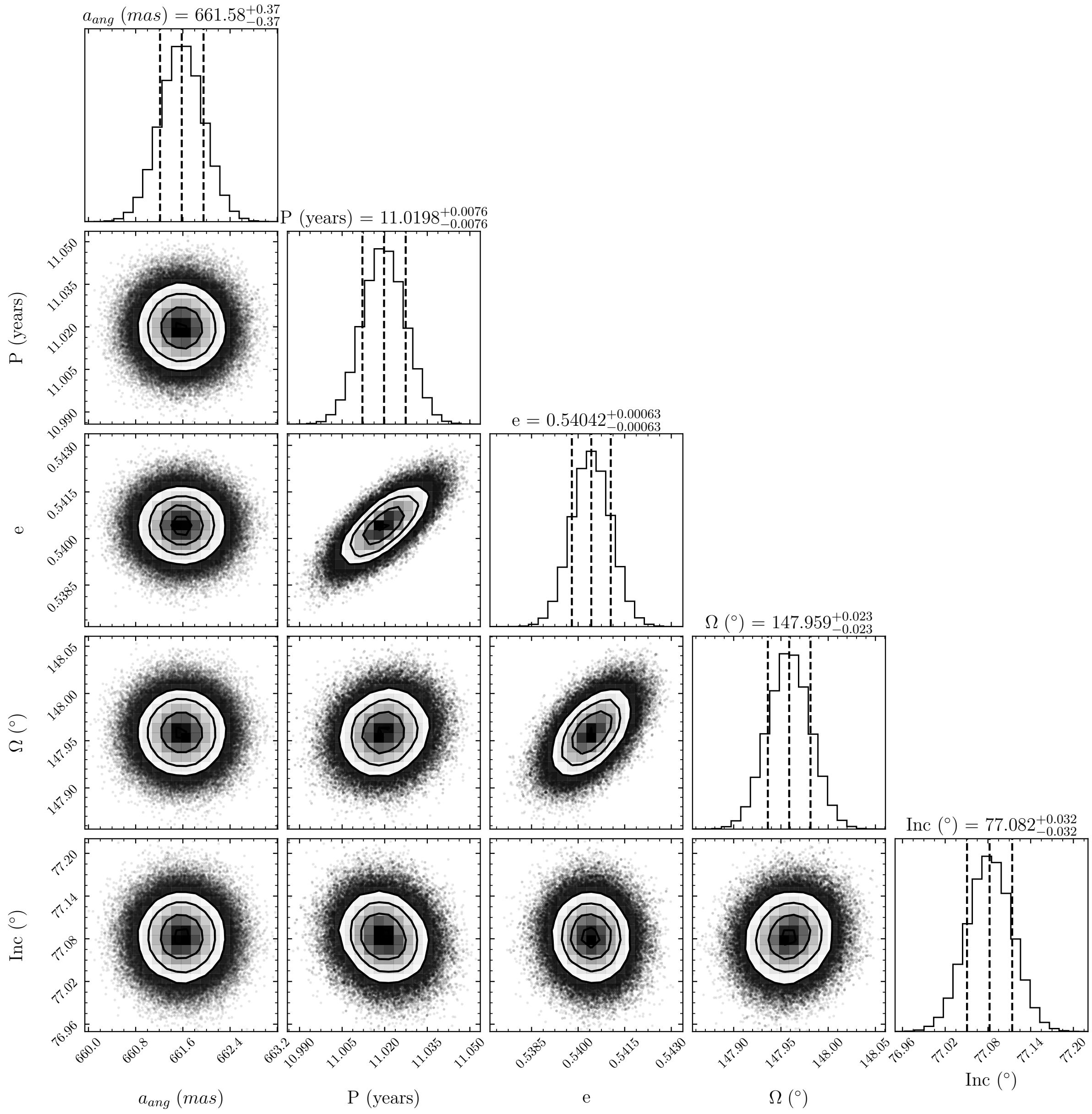

Figure 3.9 Corner plot for the relative orbit fit MCMC chain. The parameters are angular semi-major axis (a_{ang}) in mas, period (P) in years, eccentricity (e), longitude of ascending node (Ω) in degrees and inclination (i) in degrees. The posterior mean is used as the estimator for each parameter, and the errors are one standard deviation from the mean.

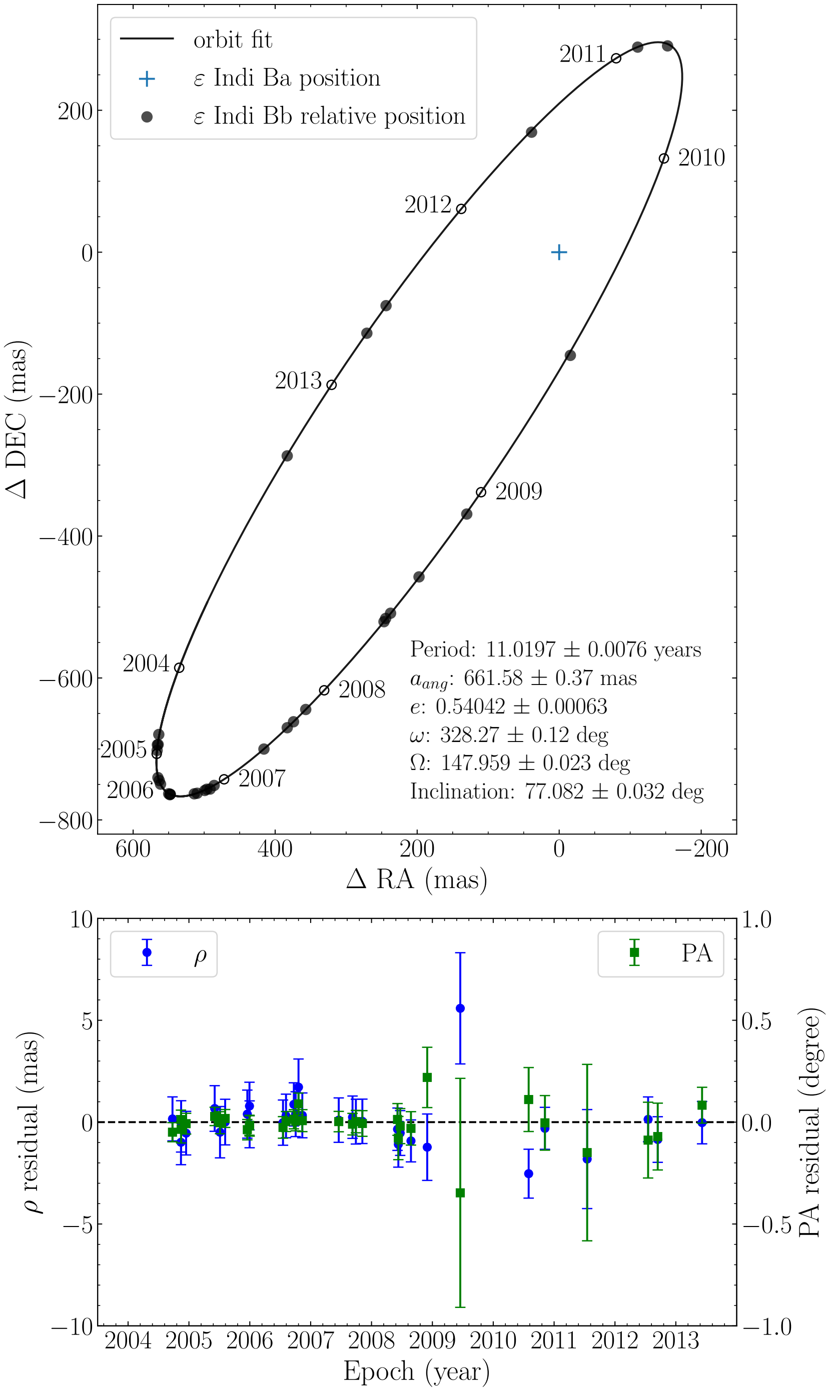

Figure 3.10 Relative orbit fit of ε Indi Ba and Bb. The orbit is plotted as the relative separation of Bb from Ba, where Ba is fixed at the origin. The black dots are the measured relative astrometry, the hollow dots show the beginning of each year, and the solid line is the best fit orbit. The bottom panel shows the residuals of the separation in blue and PA in green.

3.6.2 Absolute Astrometry

We have derived optical geometric distortion corrections for all the FORS2 images in Section 3.4.4. We describe here our approach to fit for astrometric models to the reference stars, field stars, and most importantly the ε Indi B system. We fit standard five-parameter astrometric models, with position, proper motion, and parallax, to the reference stars and field stars in the field of view of the FORS2 images. The results from the fits for reference stars match within 20% from the proper motions and parallaxes Gaia provided. For the binary system ε Indi B, we fit a six-parameter astrometric solution, adding an extra parameter which is the ratio between the semi-major axes of the orbits of the two components. We also review, and ultimately project out, the effects of atmospheric dispersion. The wavelength-dependent index of refraction of air causes an apparent, airmass-dependent displacement between the redder brown dwarfs ε Indi Ba and Bb and the bluer field stars along the zenith direction.

The results from absolute astrometry give proper motions, parallax, and a ratio between the semi-major axes which can then be converted into a mass ratio and individual masses. In conjuction with our previous relative astrometry results, full Keplerian solutions can be derived that completely characterize the orbits of both ε Indi Ba and ε Indi Bb.

Astrometric Solution

The astrometric solution for a single and isolated reference star or background star is a five-parameter linear model in terms of reference pixel coordinates in RA and Declination, proper motions in RA and Declination, and the parallax. A star's instantaneous position $(\alpha*, \delta)$ would be its position $(\alpha*_{\mathrm{ref}}, \delta_{\mathrm{ref}})$ at a reference epoch, plus proper motion $(\mu_{\alpha*}, \mu_\delta)$ multiplied by the time since the reference epoch t_{ref}, and parallax ϖ times the so-called parallax factors $\Delta\pi_{\alpha*}$ and $\Delta\pi_\delta$:

$$\begin{bmatrix} 1 & 0 & t - t_{\mathrm{ref}} & 0 & \Delta\pi_{\alpha*} \\ 0 & 1 & 0 & t - t_{\mathrm{ref}} & \Delta\pi_\delta \end{bmatrix} \begin{bmatrix} \alpha*_{\mathrm{ref}} \\ \delta_{\mathrm{ref}} \\ \mu_{\alpha*} \\ \mu_\delta \\ \varpi \end{bmatrix} = \begin{bmatrix} \alpha* \\ \delta \end{bmatrix}. \tag{3.17}$$

To test the robustness of the distortion corrections in RA and Declination that we have derived for each image, we 'reverse engineer' by excluding a particular reference star from the fit and solve for the astrometric solution of that star based on the discussion above for comparison to the Gaia parameters. In particular, we focus on the reference stars close to ε Indi B.

For the binary system ε Indi B, the astrometric solution demands an additional parameter r_{Ba}: the ratio between the semi-major axis of ε Indi Ba about the barycenter to the total semi-major axis a. The parameter r_{Ba} is related to the binary mass ratio by

$$r_{\mathrm{Ba}} = \frac{M_{\mathrm{Bb}}}{M_{\mathrm{Ba}} + M_{\mathrm{Bb}}}. \tag{3.18}$$

The model becomes

$$\begin{aligned}\begin{bmatrix} 1 & 0 & t-t_{\mathrm{ref}} & 0 & \Delta\pi_{\alpha*} & a_{\alpha*} \\ 0 & 1 & 0 & t-t_{\mathrm{ref}} & \Delta\pi_{\delta} & a_{\delta} \end{bmatrix} \begin{bmatrix} \alpha*_{\mathrm{ref}} \\ \delta_{\mathrm{ref}} \\ \mu_{\alpha*} \\ \mu_{\delta} \\ \varpi \\ r_{\mathrm{Ba}} \end{bmatrix} \\ = \begin{bmatrix} \alpha*_{\mathrm{Ba}} - 0.5\dot{\mu}_{\alpha*}(t-t_{\mathrm{ref}})^2 \\ \delta_{\mathrm{Ba}} - 0.5\dot{\mu}_{\delta}(t-t_{\mathrm{ref}})^2 \end{bmatrix}.\end{aligned} \tag{3.19}$$

We also take into account the perspective acceleration that occurs when a star passes by the observer and its proper motion gets exchanged into radial velocity. This effect is more significant for ε Indi than for remote stars. We employ constant perspective accelerations of $\dot{\mu}_{\alpha*} = 0.165 \ \mathrm{mas\,yr^{-2}}$ in RA and $\dot{\mu}_{\delta} = 0.078 \ \mathrm{mas\,yr^{-2}}$ in Dec for the ε Indi B system based on Gaia EDR3 measurements and assuming the radial velocity measured for ε Indi A. We adopt a reference epoch t_{ref}=2010. With an astrometric baseline of ~10 years, this gives a displacement of $0.5\dot{\mu}(t-t_{\mathrm{ref}})^2 \approx 2\,\mathrm{mas}$ at the edges of the observing window, where $\dot{\mu}$ is the acceleration. The perspective acceleration, because it is known, is included in the right hand side of Equation (3.19).

Residual Atmospheric Dispersion

The FORS2 imaging covers twelve years, with data taken over a wide range of airmasses. This makes it essential to correct for atmospheric dispersion caused by the differential refraction of light of different colors as it passes through the atmosphere. The degree of dispersion is related to the wavelength of light, the filter used, and the airmass, but is always along the zenith direction. Many of the FORS2 images were taken at very high

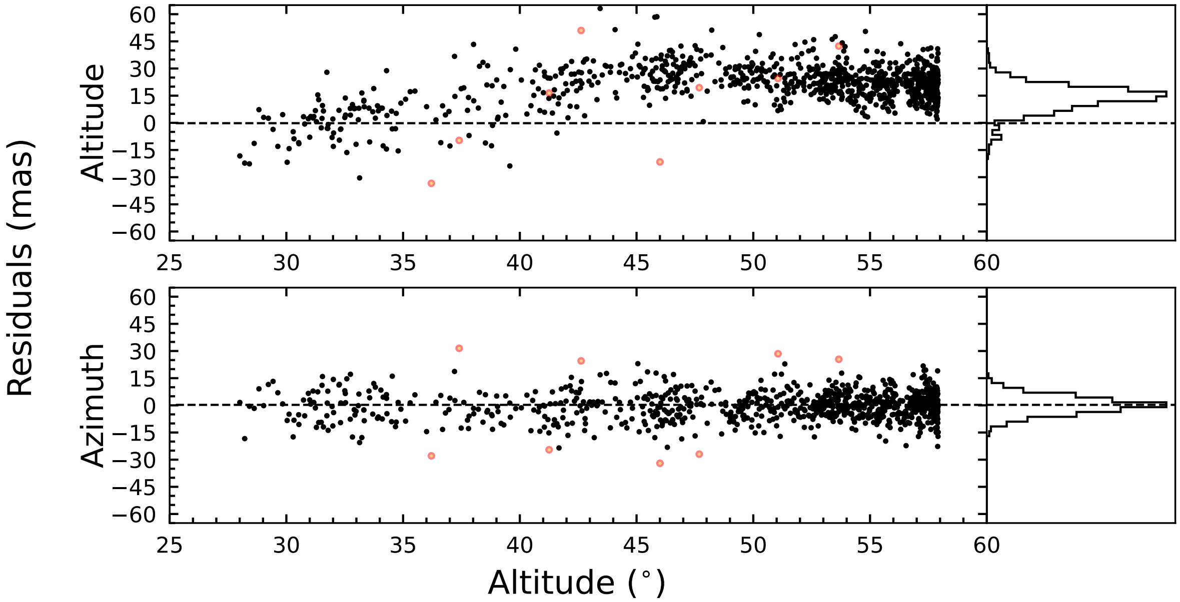

Figure 3.11 Residuals to the best-fit astrometric model for ε Indi Ba. The top panel shows the residuals in altitude, and the bottom panel shows the residuals in azimuth, both plotted as a function of altitude. Empty red circles show the rejected epochs from 3σ clipping of the azimuthal residuals. A histogram of the residuals is shown to the right of each scatter plot. Strong systematics are seen in the altitude residuals but not the azimuth ones, evident from the symmetric, roughly Gaussian distribution for the former and the altitude-dependent nonzero mean for the latter. These systematics are consistent with the magnitude expected for uncorrected ADC residual dispersion (Avila et al., 1997).

airmass. The typical airmass will vary over the course of the year, because the time of observation will vary depending on what part of night the target is up.

All of the FORS2 images were taken with an atmospheric dispersion corrector, or ADC. The residual dispersion depends on filter, airmass, and position on the FOV, but is typically tens of mas (Avila et al., 1997). This is smaller than the system's parallax and angular semi-major axis, but only by a factor of ≈10. Further, the ADC is only intended to provide a full correction to a zenith angle of 50° (Avila et al., 1997). At lower elevations it is parked at its maximum extent; Cardoso (2012) applied an additional correction to these data. Because the residual dispersion is only in the zenith direction, we perform two fits to the absolute astrometry of ε Indi Ba. First, we use our measurements in RA and Decl. directly. Second, we use the parallactic angle θ to take only the component of our measurement along the azimuth direction, which is immune to the effects of differential atmospheric refraction.

We project the data into the altitude-azimuth frame by left-multiplying both sides of Equation (3.19) by the rotation matrix

$$R = \begin{bmatrix} \cos\theta & -\sin\theta \\ \sin\theta & \cos\theta \end{bmatrix}. \tag{3.20}$$

The top row of Equation (3.20) corresponds to the azimuth direction, while the bottom row corresponds to the altitude direction.

Fitting in both the altitude and azimuth directions produces a parallax of 263 mas, in agreement with Cardoso (2012) but much lower than both the Hipparcos and Gaia values for ε Indi A. We then perform a fit only in the azimuth direction: we multiply both sides of Equation (3.19) by the top row of Equation (3.20). We exclude eight 3σ outliers and assume a uniform per-epoch uncertainty of 8.01 mas to give a normalization factor that gives a reduced χ^2 value of 1.00. This procedure results in a parallax of 274.99 ± 0.43 mas, in good agreement with both the Hipparcos and Gaia measurements. We note that the 25-year time baseline between Hipparcos and Gaia causes a small parallax difference. ε Indi A has a radial velocity of 40.5 km/s (Gaia Collaboration et al., 2018), which translates to a fractional change of 3×10^{-4} or a decrease in parallax of about 0.08 mas over 25 years. This difference is much smaller than the uncertainties of any of these parallax measurements.

Figure 3.11 shows the residual to the best-fit model using only azimuthal measurements: the top panel shows the residuals in altitude, while the bottom panel shows the residuals in azimuth. A upward trend and nonzero mean are seen in the altitude component of the parallax as a function of altitude, but no dependence on altitude was seen in the azimuth-based parallax. This confirms that the altitude component of the position measurements is corrupted by residual atmospheric dispersion of a magnitude consistent with expectations (Avila et al., 1997).

The six-parameter azimuth-component-only astrometric solution gives a mass ratio of 0.4431 ± 0.0008 between the binary brown dwarf ε Indi Ba and Bb. This mass ratio is consistent with Cardoso (2012). The only differences in our approaches arise from our usage of Gaia EDR3 to anchor the distortion correction and our account of atmospheric dispersion by only taking the azimuthal projection of the motion of the system. Our parallax of 274.99 ± 0.43 mas agrees with the parallax value from Hipparcos and that of Dieterich et al. (2018).

3.6.3 Individual Dynamical Masses

The relative astrometry orbital fit provides a precise period and angular semi-major axis. With a parallax from absolute astrometry, we convert the angular semi-major axis to distance units: $2.4058 \pm 0.0040\,\mathrm{au}$. We then use Kepler's third law to calculate a total system mass of $120.17 \pm 0.62\,M_{\mathrm{Jup}}$. Finally, the mass ratio derived from absolute astrometry provides individual dynamical masses of 66.92 ± 0.36 and $53.25 \pm 0.29\,M_{\mathrm{Jup}}$ for ε Indi Ba and Bb, respectively. Table 3.4 shows the results of each component of the orbital fit, with the final individual mass measurements in the bottom panel. The uncertainty on these masses is dominated by uncertainty in the parallax: the mass ratio is constrained significantly better than the total mass. In the following section, we use both our individual mass constraints and our measurement of the mass ratio to test models of substellar evolution.

3.7 Testing Models of Substellar Evolution

The evolution of substellar objects is characterized by continuously-changing observable properties over their entire lifetimes. Therefore, the most powerful tests to benchmark evolutionary models utilize dynamical mass measurements of brown dwarfs of known age (usually, from an age-dated stellar companion) or of binary brown dwarfs that can

Table 3.4. Orbital Fit of the ε Indi B system

Fitted Parameters	Posterior mean $\pm 1\sigma$
Period (yr)	11.0197 ± 0.0076
Angular semi-major axis (mas)	661.58 ± 0.37
Eccentricity	0.54042 ± 0.00063
ω (deg)	328.27 ± 0.12
Ω (deg)	147.959 ± 0.023
Inclination (deg)	77.082 ± 0.032
$\mu_{\alpha *}$ ($\mathrm{mas\,yr^{-1}}$)	3987.41 ± 0.12
μ_{δ} ($\mathrm{mas\,yr^{-1}}$)	-2505.35 ± 0.10
$\left(\frac{M_{\mathrm{Bb}}}{M_{\mathrm{Ba}}+M_{\mathrm{Bb}}}\right)$	0.4431 ± 0.0008
ϖ (mas)	274.99 ± 0.43
reduced χ^2	1.00
Derived Parameters	**Posterior mean $\pm 1\sigma$**
a (AU)	2.4058 ± 0.0040
System mass (M_{Jup})	120.17 ± 0.62
$\mathrm{Mass}_{\mathrm{Ba}}$ (M_{Jup})	66.92 ± 0.36
$\mathrm{Mass}_{\mathrm{Bb}}$ (M_{Jup})	53.25 ± 0.29

conservatively presumed to be coeval. A single brown dwarf of known age and mass can test evolutionary models in an absolute sense, and the strength of the test is limited by both the accuracy of the age and of the mass. Pairs of brown dwarfs of known masses can test the slopes of evolutionary model isochrones, even without absolute ages, because their age difference is known very precisely to be near zero unless they are very young.

The ε Indi B system is an especially rare case where both of these types of tests are possible. In fact, it is the only such system containing T dwarfs where both the absolute test of substellar cooling with time and coevality test of model isochrones are possible.

In the following, we consider a collection of evolutionary models applicable to ε Indi Ba and Bb covering a range of input physics. The ATMO-2020 grid (Phillips et al., 2020a) represents the most up-to-date cloudless evolutionary models from the "Lyon" lineage that includes DUSTY (Chabrier et al., 2000), COND (Baraffe et al., 2003), and BHAC15 (Baraffe et al., 2015). For models that include the effect of clouds, we use the hybrid tracks of Saumon & Marley (2008, hereinafter SM08), which are cloudy at $T_{\rm eff} > 1400$ K, cloudless at $T_{\rm eff} < 1200$ K, and a hybrid of the two in between 1400 K and 1200 K. These are the most recent models that include cloud opacity from the "Tucson" lineage. We also compare to the earlier cloudless Tucson models (Burrows et al., 1997) given their ubiquity in the literature.

In order to test these models, we chose pairs of observable parameters from among the fundamental properties of mass, age, and luminosity. Using any two parameters, we computed the third from evolutionary models. When the first two parameters were mass and age, we bilinearly interpolated the evolutionary model grid to compute luminosity. When the first two parameters were luminosity and either mass or age, we used a Monte Carlo rejection sampling approach as in our past work (Dupuy & Liu, 2017a; Brandt et al., 2021e). Briefly, we randomly drew values for the observed independent variable, according to the measured mass or age posterior distribution, and then drew values for the other from an uninformed prior distribution (either log-flat in mass or linear-flat in age). We then bilinearly interpolated luminosities from the randomly drawn mass and age distributions. For each interpolated luminosity $L'_{\rm bol}$, we computed $\chi^2 = (L_{\rm bol} - L'_{\rm bol})^2/\sigma^2_{L_{\rm bol}}$. For each trial we drew a random number between zero and one, and we only retained trial sets of mass, age, and luminosity in our output posterior if $e^{-(\chi^2-\chi^2_{\rm min})/2}$ was greater than the random number.

We used the luminosities of ε Indi Ba and Bb from King et al. (2010), accounting for the small difference between the *Hipparcos* parallax of 276.06 mas that they used and our value of 274.99 mas, which resulted in $\log(L_{\rm bol}/L) = -4.691 \pm 0.017$ dex and -5.224 ± 0.020 dex. Their luminosity errors were dominated by their measured photometry of ε Indi Ba and ε Indi Bb and the absolute flux calibration of Vega's spectrum, so our errors are identical to theirs.

Our Monte Carlo approach naturally accounts for the relevant covariances between measured parameters. There are six independently-measured parameters for which we randomly drew Gaussian-distributed values: the orbital period (P), the semi-major axis in angular units (a''), the ratio of the mass of ε Indi Bb to the total mass of ε Indi B

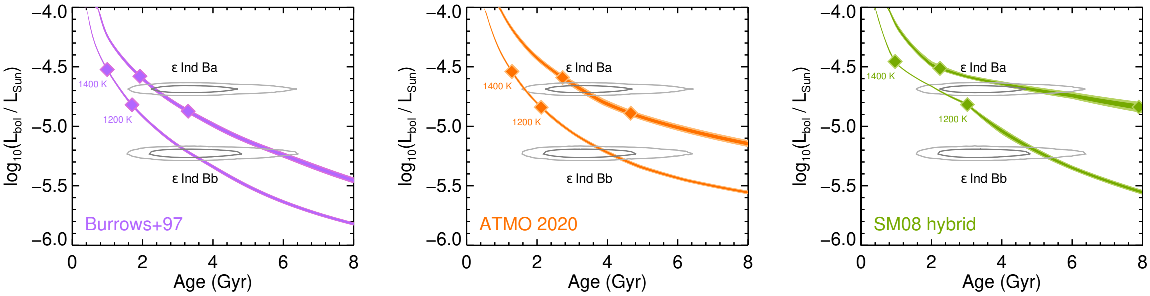

Figure 3.12 Substellar cooling curves derived from three independent evolutionary models given our measured masses. The top curve in each panel corresponds to ε Indi Ba, and the bottom curve corresponds to ε Indi Bb. The darker shaded region of each curve shows the 1σ range in our measured mass, and the lighter shading is the 2σ range. On each curve, the ages corresponding to $T_{\text{eff}} = 1400\,\text{K}$ and $1200\,\text{K}$ are marked, indicating the approximate beginning and ending of the L/T transition. Over-plotted on each panel are the 1σ and 2σ joint uncertainty contours for the age and luminosities of ε Indi Ba and Bb.

$(M_{\text{Bb}}/M_{\text{tot}})$, the parallax in the same angular units as the semi-major axis (ϖ), and the two bolometric fluxes computed from the luminosities and distance in King et al. (2010). From these, we computed the total mass, $M_{\text{tot}} = (a''/\varpi)^3(P/1\text{yr})^{-2}$, and the individual masses and luminosities.

3.7.1 Absolute test of $L_{\text{bol}}(t)$

In general, tests of substellar luminosity as a function of time are either dominated by the uncertainty in the age or in the mass. In the case of the ε Indi B system, with highly precise masses having 0.5% errors, the uncertainty in the system age ($t = 3.5^{+0.8}_{-1.0}\,\text{Gyr}$) is by far the dominant source of uncertainty.

Figure 3.12 shows the measured joint confidence intervals on luminosities and age of ε Indi Ba and Bb compared to evolutionary model predictions given their measured masses. The measured luminosity-age contours overlap all model predictions to within $\approx 1\sigma$ or less for both components. To quantitatively test models and observations, we compared our model-derived substellar cooling ages for ε Indi Ba and Bb to ε Indi A's age posterior, finding that they are all statistically consistent with the stellar age.

Our results for ε Indi Ba and Bb are comparable to other relatively massive (50–75 $M_{\rm Jup}$) brown dwarfs of intermediate age (1–5 Gyr) that also broadly agree with evolutionary model predictions of luminosity as a function of age (Brandt et al., 2021e). These include objects such as HR 7672 B (Brandt et al., 2019), HD 4747 B (Crepp et al., 2018b), HD 72946 B (Maire et al., 2020), and HD 33632 Ab (Currie et al., 2020).

However, despite agreeing with models in an absolute sense, it is evident in Figure 3.12 that the ATMO-2020 and Burrows et al. (1997) models prefer a younger age for ε Indi Ba than for ε Indi Bb. To examine the statistical significance of this difference in model-derived ages between the two components we now consider only their measured masses and luminosities, excluding the rather uncertain stellar age.

3.7.2 Isochrone test of M–$L_{\rm bol}$ relation for T dwarfs

Evolutionary models of brown dwarfs, from some of the earliest theoretical calculations up to modern work (e.g., Phillips et al., 2020a), typically predict a power-law relationship between mass and luminosity with a slope of $\Delta \log L / \Delta \log M = 2.5$–$3.0$. This general agreement between models with very different assumptions—and that vary greatly in other predictions such as the mass of the hydrogen-fusion boundary—can be seen in the

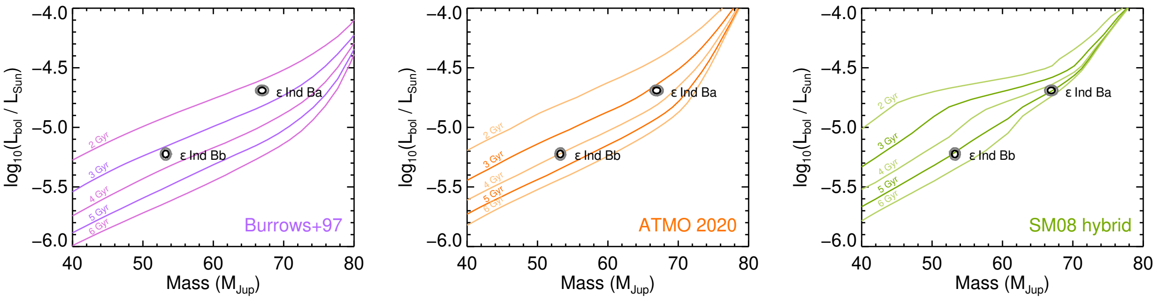

Figure 3.13 Isochrones from three different evolutionary models, ranging from 2 Gyr to 6 Gyr. Black and gray contours show the joint 1σ and 2σ confidence intervals of the masses and luminosities of ε Indi Ba and Bb. Because these two brown dwarfs must be coeval they should lie along a single model isochrone. The only models that pass this test are the Saumon & Marley (2008) hybrid models that predict a distinctly different mass–luminosity relation for brown dwarfs. These models have a much shallower dependence of luminosity on mass as objects cool through the L/T transition over $T_{\rm eff} = 1400$ K to 1200 K, changing from cloudy to cloud-free atmosphere boundary conditions.

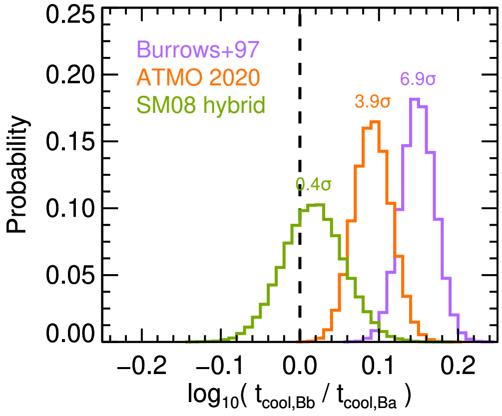

Figure 3.14 Probability distributions of the difference between the model-derived substellar cooling ages ($t_{\rm cool}$) of ε Indi Ba and Bb. The dashed line shows the expectation that $t_{\rm cool,Bb} = t_{\rm cool,Ba}$. Only the Saumon & Marley (2008) hybrid models predict consistent, coeval ages. This is the highest-precision coevality test of brown dwarf binaries to date, and it supports previous results from brown dwarf binaries with mass errors of ≈5% (Dupuy et al., 2015; Dupuy & Liu, 2017a).

slopes of isochrones for 40–60 $M_{\rm Jup}$ brown dwarfs in Figure 3.13.

One set of models, from Saumon & Marley (2008), that substantially alters the atmospheric boundary condition as objects cool from $T_{\rm eff} = 1400\,{\rm K}$ to 1200 K predicts a much shallower slope from the M–L relation during that phase of evolution (Figure 3.13). These so-called hybrid models provide the best match to the M–L relation as measured in binaries composed of late-L dwarf primaries ($T_{\rm eff} \approx 1400\,{\rm K}$) and early-T dwarf secondaries ($T_{\rm eff} \approx 1200\,{\rm K}$), objects that straddle this evolutionary phase (Dupuy et al., 2015; Dupuy & Liu, 2017a). A fundamental prediction of these models is that during the L/T transition, objects of similar luminosity can have wider-ranging masses than in other models. The other chief prediction is that luminosity fades more slowly during the L/T transition, so that the brown dwarfs emerging from this phase are more luminous than in other models.

ε Indi B is the only example of a binary with precise individual masses where one component is an L/T transition brown dwarf and the other is a cooler T dwarf. This provides a unique test of the M–L relation, where the cooler brown dwarf is well past the L/T transition and the other is in the middle of it. According to hybrid models, the brown dwarf within the L/T transition will be experiencing slower cooling, so it would be more luminous than in other models. On the other hand, with the immediate removal of cloud opacity in hybrid models below 1200 K, a brown dwarf will cool even faster than predicted by other, non-hybrid models. These two effects predict that a system like ε Indi B will, in fact, have an especially steep M–L relation.

Our measured masses give a particularly steep slope for the mass-luminosity (M–L) relation of $\Delta \log L / \Delta \log M = 5.37 \pm 0.08$ between the L/T-transition primary ε Indi Ba and the cooler secondary ε Indi Bb. The only evolutionary models that predict such a steep slope are the hybrid models of Saumon & Marley (2008).

To quantitatively test models, we compared the model-derived cooling ages of ε Indi Ba and Bb, given their measured masses and luminosities (Figure 3.14). Models like ATMO-2020 that assume a single, cloud-free atmospheric boundary condition are 3.9σ inconsistent with our measurements. At 6.9σ, models from Burrows et al. (1997) are even more inconsistent because the bunching up of isochrones around the end of the main sequence, which has a similar effect as the bunching up of isochrones due to slowed cooling in the hybrid models, occurs at higher masses than in ATMO-2020.

The ε Indi B system therefore provides further validation of hybrid evolutionary models, where the atmosphere boundary condition is changed drastically over the narrow range of $T_{\rm eff}$ corresponding to late-L and early-T dwarfs. No longer just within the L/T transition, but affirming the consequences of slowed cooling during the L/T transition to cooler brown dwarfs ($T_{\rm eff} < 1000\,{\rm K}$).

3.7.3 Testing Model Atmospheres: $T_{\rm eff}$ and $\log(g)$

Brown dwarfs that have both directly measured masses and individually measured spectra have long been used in another type of benchmark test that tests for consistency between evolutionary models and the atmosphere models that they use as their surface boundary condition. Comparison of model atmospheres to observed spectra allows for determinations of $T_{\rm eff}$, $\log(g)$, and metallicity. Evolutionary models predict brown dwarf radii as a function of mass, age, and metallicity. Combining these radii with empirically determined luminosities produce mostly independent estimates of $T_{\rm eff} = (L_{\rm bol}/4\pi R^2 \sigma_{\rm SB})^{1/4}$, and with masses gives estimates of $\log(g) = \log(GM/R^2)$. (Evolutionary model radii have a small dependence on the model atmospheres and thus estimates of $T_{\rm eff}$ and $\log(g)$ from their radii are not strictly, completely independent.) There are many examples of such benchmark tests, ranging from late-M dwarfs (e.g., Kenworthy et al., 2001; Zapatero Osorio et al., 2004; Dupuy et al., 2010), L dwarfs (e.g., Bouy et al., 2004; Dupuy et al., 2009; Konopacky et al., 2010), and T dwarfs (e.g., Liu et al., 2008; Dupuy & Liu, 2017a).

From King et al. (2010), ε Indi Ba and Bb have perhaps the most extensive and detailed spectroscopic observations (0.6–5.1 μm at up to $R \sim 5000$) of any brown dwarfs with dynamical mass measurements. They found that BT-Settl atmosphere models (Allard et al., 2012) with parameters of $T_{\rm eff}$ = 1300–1340 K and $\log(g) = 5.50$ dex best matched ε Indi Ba. For ε Indi Bb, they found $T_{\rm eff}$ = 880–940 K and $\log(g) = 5.25$ dex.

We computed evolutionary model-derived values for $T_{\rm eff}$ and $\log(g)$ to compare to the model atmosphere results of King et al. (2010). The most precise estimates result from using the mass and luminosity to derive a substellar cooling age and then interpolating $T_{\rm eff}$ and $\log(g)$ from the same evolutionary model grid using the measured mass and the cooling age. The SM08 hybrid models gave $T_{\rm eff} = 1312 \pm 13$ K and 972 ± 13 K for ε Indi Ba and Bb, respectively, and $\log(g) = 5.365 \pm 0.006$ dex and 5.288 ± 0.003 dex. These evolutionary model-derived values agree remarkably well with the model atmosphere results, which were based on an atmosphere grid with discrete steps of 20 K in T_{eff} and 0.25 dex in $\log(g)$.

ATMO-2020 models are only strictly appropriate for ε Indi Bb, and they give $T_{\mathrm{eff}} = 992 \pm 13$ K and $\log(g) = 5.311 \pm 0.003$ dex. This effective temperature is $\approx 4\sigma$ higher than the BT-Settl model atmosphere temperature. ATMO-2020 models are actually based on this family of model atmospheres (BT-Cond and BT-Settl should be effectively equivalent at this T_{eff}), so this suggests a genuine $\approx$50 K discrepancy between atmosphere model-derived T_{eff} (too low) and evolutionary model-derived T_{eff} (too high). If so, this could be due a to a combination of systematics in atmosphere models (e.g., non-equilibrium chemistry, inaccurate opacities) and/or ATMO-2020 evolutionary model radii (10–20% too high).

3.8 Conclusions

In this Chapter we use ~12 years of VLT data to infer dynamical masses of $66.92 \pm 0.36\, M_{\mathrm{Jup}}$ and $53.25 \pm 0.29\, M_{\mathrm{Jup}}$ for the brown dwarfs ε Indi Ba and Bb, respectively. These masses put the the two objects firmly below the hydrogen burning limit. Our system mass agrees with that in Cardoso et al. (2009), who estimated a system mass of $121 \pm 1\ M_{\mathrm{Jup}}$. With extra data from the completed relative and absolute astrometry monitoring campaign, we are able to derive precise individual masses and improve upon their previous analysis on several fronts. Using Gaia EDR3, we provide a much more precise calibration of both relative and absolute astrometry. In addition, we have shown that our joint PSF fitting method accounts for the effect of overlapping halos reasonably well and adjusted our final errors for the relative astrometry according to our systematics analysis. Lastly, we have investigated and corrected for the systematics due to differential atmospheric refraction and residual atmospheric dispersion. As a result, we are able to obtain very tight constraints on the orbital parameters and final masses, and measure a parallax consistent with both the Hipparcos and Gaia values.

Our results disagree with Dieterich et al. (2018), who used the photocenter's orbit together with three NACO epochs to derive a mass of 75.0 ± 0.82 M_{Jup} for Ba, and a mass of 70.1 ± 0.68 M_{Jup} for Bb. These masses are at the boundaries of the hydrogen burning limit, challenging theories of substellar structure and evolution. We cannot conclusively say why Dieterich et al. (2018) derive much higher masses. However, we are able to reproduce their results, and find that rotating their measurements into an azimuth-only frame produces a mass closer to ours. We speculate that highly asymmetric uncertainties in RA/Decl. for a few of their measurements had a disproportionate effect on the results.

We also provide a Fourier analysis of ε Indi B's fluxes to investigate its potential variability. We find no definitive evidence of variability with a frequency less than 1 hr^{-1}.

Our newly precise masses and mass ratios enable new tests of substellar evolutionary models. We find that ε Indi Ba and Bb are generally consistent with cooling models at the activity age of $3.5^{+0.8}_{-1.0}$ Gyr we derive for ε Indi A. However, the two brown dwarfs are consistent with coevality only under hybrid models like those of Saumon & Marley (2008), with a transition to cloud-free atmospheres near the L/T transition.

Our masses for ε Indi Ba and Bb, precise to ≈0.5%, and our mass ratio, precise to ≈0.2%, establish the ε Indi B binary brown dwarf as a definitive benchmark for substellar evolutionary models. As one of the nearest brown dwarf binaries, it is also exceptionally well-suited to detailed characterization with future telescopes and instruments including JWST. ε Indi B, with its two components straddling the L/T transition, now provides some of the most definitive evidence for cloud clearing and slowed cooling in these brown dwarfs.

Chapter 4

Keck Discovery of the Brown Dwarf HD 176535 B

In this Chapter, we will present our L' band imaging survey targeting nearby brown dwarfs on the Keck/NIRC2. In the preceding chapters, the significance of the `orvara` software becomes evident as it assumes a pivotal role in the current analysis. This software enables us to determine accurate orbits of our imaged substellar companions by effectively incorporating their combined radial velocity and astrometry data. Leveraging this information as a precursor, we successfully anticipate the locations of these companions prior to their imaging. Our research endeavors have led to significant discoveries, and we here present two notable companions: HD 176535 B (HIP 93398 B) and HIP 38216 B in the next Chapter 5. These findings represent a fraction of the remarkable results that have emerged from our program.

The T-dwarf companion HD 176535 B presented in this paper is among the first companions discovered whose astrometric location was known before imaging. In this paper, we present an `orvara` fit incorporating our new Keck/NIRC2 astrometry data to constrain the mass and 3D orbit of the system.

The contents of this chapter include works that have been published in Li et al. (2023), under the title "Surveying nearby brown dwarfs with HGCA: direct imaging discovery of a faint, high-mass brown dwarf orbiting HD 176535 A".

4.1 Stellar properties of HD 176535 B

HD 176535 is a main sequence K3.5 V (Gondoin, 2020) star located at a distance of 36.99 ± 0.03 pc based on Gaia EDR3 (Gaia Collaboration, 2020). HD 176535's stellar properties are similar to those of the Sun in terms of age, metallicity, kinematics, and atmospheric chemical abundances; it has a history of being identified as a solar sibling candidate that may share a common birth cluster with the Sun (Batista et al., 2014; Adibekyan et al., 2018). HD 176535 has an effective temperature of 4727 ± 104 K (Sousa et al., 2011) and surface gravity of 4.63 ± 0.05 dex (Gaia Collaboration, 2022). HD 176535 is slightly metal-poor with an iron abundance of $[\mathrm{Fe/H}] \approx -0.15\,\mathrm{dex}$ (Sousa et al., 2011; Adibekyan et al., 2012; Mortier et al., 2013; Gáspár et al., 2016; Suárez-Andrés et al., 2017; Gondoin, 2020). The chromospheric index of $\log_{10} R'_{\mathrm{HK}} \approx -4.732\,\mathrm{dex}$ (Gondoin, 2020) indicates that HD 176535 is an old and relatively inactive star.

HD 176535's age was determined on several accounts. While analyzing a sample of

Table 4.1 Properties of the HD 176535 AB system.

Property	**Value**	**Refs**
Host Star		
ϖ (mas)	27.033 ± 0.018	1
Distance (pc)	36.99 ± 0.03	1
SpT	K3.5V	2,3
Mass (M)	0.72 ± 0.02	4,5
Age (Gyr)	5.04 ± 1.45	12
$\mathrm{T_{eff}}$ (K)	4727 ± 104	6
[Fe/H] (dex)	-0.15 ± 0.07	7
$\log(\mathrm{R}'_{\mathrm{HK}})$ (dex)	-4.85	8
R'_{X} (dex)	< -4.28	9
Gaia RUWE	1.019	1
Luminosity ($L_{\odot}$)	0.208 ± 0.007	12
Gaia G (mag)	9.374 ± 0.003	1
B_T (mag)	11.195 ± 0.066	10
V_T (mag)	9.923 ± 0.035	10
J (mag)	7.804 ± 0.027	11
H (mag)	7.313 ± 0.033	11
K_s (mag)	7.175 ± 0.020	11
Companion		
Mass (M_{Jup})	$65.9^{+2.0}_{-1.7}$	12
L' apparent (mag)	16.31 ± 0.07	12
L' absolute (mag)	13.47 ± 0.07	12
Semi-Major Axis (AU)	$11.05^{+0.64}_{-0.56}$	12
Inclination (°)	$49.8^{+3.4}_{-3.7}$	12
Period (yr)	$40.6^{+3.9}_{-3.5}$	12
Eccentricity	$0.496^{+0.022}_{-0.020}$	12

NOTE: References abbreviated as (1) Gaia Collaboration (2020); (2) Gray et al. (2006); (3) Bourgés et al. (2014); (4) Reiners & Zechmeister (2020); (5) Delgado Mena et al. (2019); (6) Sousa et al. (2011); (7) Gáspár et al. (2016); (8) Pace (2013); (9) Voges et al. (1999); (10) Høg et al. (2000a); (11) Cutri et al. (2003); (12) This work

HARPS FGK stars using Gaia DR2 parallax and PARSEC isochrones (Bressan et al., 2012), Delgado Mena et al. (2019) derive an age of $5.21 \pm 4.68\,\mathrm{Gyr}$ for HD 176535. Besides, Gaia Collaboration (2022) gives an age of 3.34 Gyr using the FLAME model with 1-σ lower and upper confidence levels of 0.61 Gyr and 6.97 Gyr, respectively. Gomes da Silva et al. (2021) found a chromospheric index of $\log_{10} R'_{\mathrm{HK}} = -4.5695 \pm 0.0069\,\mathrm{dex}$ by measuring the Ca II HK emission lines in the star's HARPS spectra, and thus found HD 176535 A to be a relatively old star with a weakly constrained age of $5.57 \pm 4.84\,\mathrm{Gyr}$. Delgado Mena et al. (2019) analyzed the same HARPS spectra as did Gomes da Silva et al. (2021), but found a different S-index of 0.43 rather than Delgado Mena et al. (2019)'s value of 0.63. We perform our own independent analysis to constrain the age of HD 176535 A using a Bayesian-based age-dating method developed by Brandt et al. (2014). We get an age of $5.02^{+1.11}_{-1.39}$ Gyr if adopting only the S-index of 0.43 from Pace, and a value of $2.57^{+0.67}_{-0.89}$ Gyr if adopting the S-index of 0.63 from Gomes. If otherwise adopting both S-indices as lower and upper limits of $\log_{10} R'_{\mathrm{HK}}$, we retrieve a somewhat young age of $3.59^{+0.87}_{-1.15}$ Gyr for HD 176535 A. Although our age estimates are broadly consistent with literature measures, none of the ages were well-established and the age of the system remain largely ambiguous. The rotation period of the star has neither been reported in the literature nor observed in any TESS sector. Future light curves from TESS, when observed, would enable retrieval of a rotation period and thus increase the confidence in the system's age.

The mass of the star is estimated to be between $0.69\,M$ and $0.76\,M$ via several litera-

Table 4.2 HGCA absolute astrometry for HD 176535 A.

Parameter	Hipparcos	Hipparcos-Gaia	Gaia EDR3
$\mu_{\alpha*}$ ($\mathrm{mas\,yr^{-1}}$)	-21.9 ± 1.3	-22.016 ± 0.048	-24.927 ± 0.025
μ_{δ} ($\mathrm{mas\,yr^{-1}}$)	-32.1 ± 1.0	-32.295 ± 0.030	-29.707 ± 0.022
$\mathrm{corr}(\mu_{\alpha*}, \mu_{\delta})$	0.13	-0.02	0.21
t_{α} (Jyr)	1991.27		2016.27
t_{δ} (Jyr)	1991.41		2016.36

Note: The χ^2 value for a model of constant proper motion (Hipparcos-Gaia and Gaia proper motions are equal) is 8215 with two degrees of freedom.

ture sources including the Gaia DR3 catalog (Pinheiro et al., 2014; Chandler et al., 2016; Delgado Mena et al., 2019; Anders et al., 2019a; Stassun et al., 2019; Gomes da Silva et al., 2021; Gaia Collaboration, 2022). In the same way as described in Li et al. (2021a), we obtain an isochronal mass of $0.72 \pm 0.02M$ using the PARSEC model. For this work, we adopt our estimated age of $3.59^{+0.87}_{-1.15}$ Gyr and our estimated mass of $0.72 \pm 0.02M$ for the host star HD 176535.

4.2 Data and Observations

4.2.1 Archival RV data

RVs of HD 176535 come from the High Accuracy Radial velocity Planet Searcher (HARPS) spectrograph mounted at the ESO 3.6m telescope in La Silla. HARPS is a state-of-the-art fiber-fed high-resolution ($R \sim 115000$) optical echelle spectrograph that achieves sub-m/s RV precision (Mayor et al., 2003). We retrieve 18 RVs for HD 176535 from the HARPS public radial velocity database, which has been corrected for common RV systematic errors by Trifonov et al. (2020). These RVs were taken between 2004 and 2015 with a median uncertainty of 1.46 m/s. All were taken prior to the 2015 HARPS fiber upgrade. HD 176535 A is a K star with relatively low level of stellar activity, allowing a high degree of RV precision.

4.2.2 Hipparcos-Gaia Accelerations

Hipparcos and Gaia absolute astrometry have enabled precise dynamical mass measurements of both RV-discovered and directly imaged companions (Brandt et al., 2021f; Brandt et al., 2019; Li et al., 2021a; Bowler et al., 2021; Currie et al., 2020; Franson et al., 2022a; Kuzuhara et al., 2022; Currie et al., 2022). Absolute astrometry provides the tangential component of the host star's acceleration, complementing both stellar radial velocities and relative astrometry that constrains the orbital motion of the companion. The proper motions measured by Hipparcos and Gaia, along with the scaled positional difference over the 25-year baseline between these two proper motions, allow precise constraints on a companion's 3D orbit. Changes in these proper motions indicate acceleration of the host star in an inertial reference frame. In order to compare the proper motions from Hipparcos and Gaia, Brandt (2018) and Brandt (2021a) carried out a cross-calibration between the two catalogs by establishing a common reference frame and correcting for error inflation; this is presented in the Hipparcos-Gaia catalog of accelerations (HGCA).

HD 176535 A is cataloged in the HGCA as a high-proper-motion star observed by both Hipparcos and Gaia. Gaia EDR3 itself provides the most precise proper motion measurement. The long-term proper motion—the difference in position between Hipparcos and Gaia scaled by their time baseline—is almost as precise. These two proper motions differ, demonstrating a significant acceleration of $\sim 90\sigma$ between the long-term Hipparcos-Gaia proper motion and Gaia (EDR3). A summary of the absolute astrometry from the HGCA for HD 176535 A is given in Table 5.3. HD 176535 has a renormalized unit weight error, or RUWE, of 1.019 in Gaia EDR3. This is close to 1, and significantly less than 1.4, indicating that a five-parameter astrometric model (with position, proper motion, and parallax) provides a good fit to the data (Stassun & Torres, 2021; Gaia Collaboration, 2020). The low RUWE strongly disfavors a close, massive companion with a period close to the 33-month baseline of Gaia EDR3.

We perform a preliminary orbital analysis using the existing HARPS RVs and Hipparcos-Gaia absolute astrometry. This enables evaluation of the detectability of the companion, as well as predictions for the location of the companion prior to any on-sky observation. We use the MCMC orbit code `orvara` (Brandt et al., 2021i) to jointly fit the HARPS RVs and HGCA stellar astrometry. Our RV and absolute astrometry-only fit reveals the existence of a $\approx 63\,M_{\rm Jup}$ companion at a distance of $\approx$14 AU in orbit around HD 176535A. However, for RV-systems, even with the addition of complementary HGCA absolute astrometry data, the orbital inclination of the system may still not be precisely determined due to the uncertain direction of motion of the companions (Li et al., 2021a). For such systems, their orbits can be resolved either by future Gaia data releases or by high-contrast imaging.

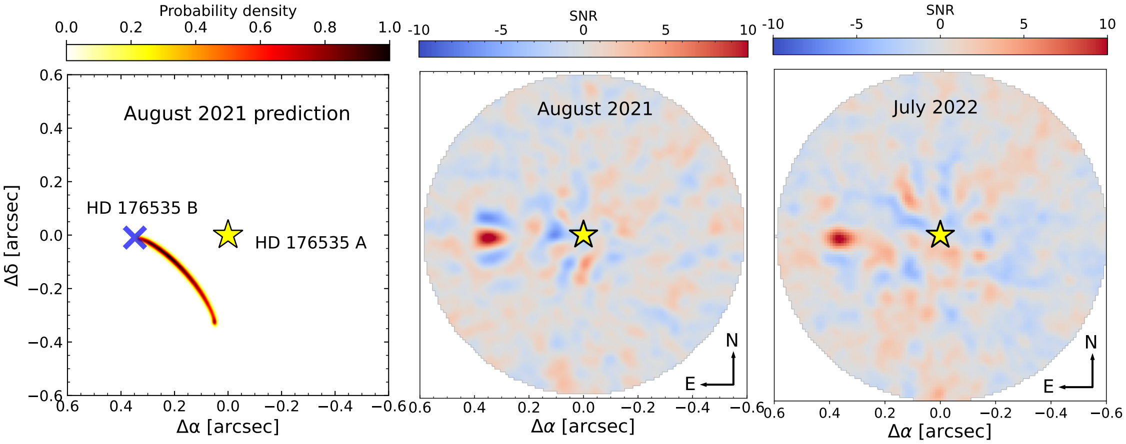

Figure 4.1 (Left) Predicted location of HD 176535 B is shown by the 3-σ probability contour before its first imaging in August 2021. The blue cross is the true location of the companion where it was imaged on August 26th, 2021. (Middle and Right) PSF-subtracted images of HD 176535 B for the August 2021 and July 2022 detections. The yellow star in the center is the host star's location, and the companion was detected both times to the east of the host star. The images are smoothed with a Gaussian filter with a window function of the form $e^{-(x^2+y^2)}$.

`orvara` is capable of generating 3-σ likelihood contours for the coordinates of the companion with respect to its host star at an arbitrary epoch. Our preliminary fit shows that HD 176535 AB is an excellent system for imaging follow-up. The broad inclination posterior distributions gives out a range of possibilities for the location of the companion with respect to the host star. More detailed use of `orvara` will be discussed in Section 4.3. We display the predicted contours that trace out the possible locations of the companion in the left panel of Figure 4.1 for our first observation of the system in August 2021.

4.2.3 Keck/NIRC2 AO Imaging

Our high-contrast imaging observations of HD 176535 took place on both UT 2021 August 26 and UT 2022 July 7 in the L'-band (3.426–4.126 μm) using the NIRC2 camera in pupil-tracking mode at the W.M. Keck Observatory with the Vector Vortex Coronagraph (VVC; Serabyn et al. (2017)). The observations were carried out with natural guide star adaptive optics (Wizinowich, 2013) and the visible-light Pyramid Wavefront Sensor (WFS) (Bond et al., 2020). The observations were set to track the telescope pupil, allowing the sky to rotate during the observation. We use the standard set up for vertical angle mode to track the rotating pupil images when carrying out Angular Differential Imaging (ADI; Marois et al. (2006)). The ADI images of the HD 176535AB system were taken in sequences of 30 science frames using the Quadrant Analysis of Coronagraphic Images for Tip-tilt Sensing (QACITS) algorithm, which centers the star behind the vortex phase mask via small tip-tilt corrections after each exposure (Huby et al., 2015). Each QACITS sequence includes off-axis unsaturated images for flux calibration and optimization, and sky background frames for the science and calibration images. For both of our nights, we observed with 60 coadded integrations and 0.5 s integration time per coadd. We obtain a total of 90 ADI images for the August 2021 observation with a total integration time of 45 minutes, and 79 images for the July 2022 night with a total integration time of 39.5 minutes. In addition, for each of the two nights, dark and twilight flat frames were taken at the end of the night for image reduction.

We employ the Vortex Image Processing (`VIP`) package (Gomez Gonzalez et al., 2017b) for postprocessing. We stack the images for HD 176535AB into three-dimensional ADI sequences and reduce the 3D data cube with the following procedure. First, cosmic rays are removed using the `lacosmic` Python package (van Dokkum, 2001) and geometric correction was performed on each ADI cube with the solutions found by Service et al. (2016) for the narrow-field mode of the NIRC2 camera. We perform sky subtraction for the science and the off-axis flux calibration frames using the `AstroDrizzle` sky-subtraction function from Avila et al. (2015). We then subtract the dark frames and flat-field all the images, and correct for bad pixels. The centering and alignment of the raw ADI images at sub-pixel accuracy is a crucial pre-processing step that directly affects the quality of data reduction. Thus, we use to perform re-centering, rotation and re-alignment of the images by fitting negative 2D Gaussian profiles to the vortex core in each time slice.

After image re-centering is complete, we use to perform stellar PSF subtraction. The stellar PSF is obtained by subtracting the sky frame from the PSF frame with the star off the vortex. Through fitting 2D Gaussians to the host-star's PSF, we measure a FWHM of 7.80 pixels ($0\farcs078$) for both epochs. provides several ADI-based algorithms to handle model PSF subtraction, including Median Combination of Images, the Locally Optimized Combination of Images (LOCI; Lafrenière et al. (2007)), annular and full-frame Principal Component Analysis (PCA), PCA in a single annulus, annular and full-frame Non-negative matrix factorization (NMF) low-rank approximation (Gomez Gonzalez et al., 2017b; Ren et al., 2018), and Local Low-rank plus Sparse plus Gaussian-noise decomposition (LLSG) (Gomez Gonzalez et al., 2016). We choose PCA-based algorithms (Amara & Quanz, 2012; Soummer et al., 2012) for the best performance in speed and efficiency. In ADI data cubes, any putative planet would rotate throughout the images with time, while the stellar halo and speckle pattern stays quasi-static. A reference PSF must be constructed for subtraction to create a residual cube. In PCA-based algorithms, this reference PSF is constructed from the projection of each image on a subset of the principle components. Too few components result in incomplete removal of the stellar PSF, while too many lead to oversubtraction of the companion, with the companion increasingly present in the principal components. The principle components are computed through singular value decomposition of the 2D matrix (time × flattened image array) of the images. The residual cube is then derotated to align the field-of-view and coadded to create a final image.

We apply annular PCA from to do the PSF-subtraction, which uses the PCA low-rank approximation annulus-wise to capture the background and speckle noise for a given concentric annulus (Gomez Gonzalez et al., 2016). In annular PCA, a frame-rejection criterion (Absil et al., 2013) can be applied based on a parallactic angle (PA) threshold. By keeping only the frames where the planet has rotated by this threshold, we can prevent the planetary signal from being captured by the low-rank approximation and thus subtracted from the science images. We tune the amount of rotation gap used with a PA threshold from $0.1 \times FWHM$ to $1 \times FWHM$, and determined a minimum parallactic angle rotation between images of $\delta_{rot} = 0.3 \times FWHM$ at the companion's location that maximizes the SNR in the final frame. We optimize the SNR for each individual companion at the same time by adjusting the number of principle components (PCs). We run PSF subtraction for the pre-processed images varying the number of components from 0 to 40, each time measuring the signal-to-noise Ratio (SNR) at the location of the companion. For each number of PCs used, the signal and noise levels are calculated with relative photometry using FWHM-radius circular apertures. The relative astrometry of the companion each time is determined by fitting a simple 2D Gaussian to a 15 × 15 pixel subimage. The SNR is computed as the ratio of the companion flux and the standard deviation of the flux within the noise estimation apertures via the method outlined by (Mawet et al., 2014). Figure 4.2 shows the SNR as a function of the number of principle components used in annular PCA analysis for both epochs. The optimal number of principal components (PCs) that maximize SNR is 6 for the 2021 epoch with a SNR of 11.7, and 3 components for the 2022 epoch with a SNR of 10.2. The subtracted images are shown in Figure 4.1 where the companion is clearly visible east of the host star.

In stellar PSF subtraction approaches, a 2D Gaussian fit leads to biased results for the astrometry and photometry of a companion because part of the planetary signal is self-subtracted during the stellar halo removal process. To avoid systematic biases, we adopt the negative fake companion (NEGFC) technique described in Marois et al. (2010); Lagrange et al. (2010); Wertz et al. (2017) for robust extraction of the position and flux of detected point-like sources. This method involves the injection of a negative-amplitude PSF template at the location of the companion. Ideally, the injection of a negative-flux synthetic companion completely removes the signal from the true companion in the final image. The NEGFC method proceeds as follows. First, one obtains an estimate of a ‘first guess’ for the (biased) position and flux of the companion from the first image of the reduced ADI data cube. Then, this measured normalized off-axis PSF is scaled and shifted to remove the first estimate from the input data cube before applying PCA. Finally, one applies PCA in a single (optimal) annulus and iterates on the position and flux of the injected negative PSF template, until the absolute residuals χ^2 in the aperture are minimized (i.e. when the injected negative companion flux and position best match those of the true companion). To do the iteration from the last step, we first use a Nelder-Mead simplex minimization algorithm to get a starting guess for the flux and position of the true companion. We then use the `emcee` affine-invariant Markov Chain Monte Carlo (MCMC) ensemble sampler (Foreman-Mackey et al., 2013) to obtain the companion's flux (flux_c) and angular coordinates (ρ, θ). With MCMC, we can infer the highest likelihood parameter values and uncertainties by sampling the posterior distributions of the parameters (ρ, θ, flux_c). We use 100 walkers for our MCMC chain, and iterate over 10^5 steps until convergence is achieved. We use the autocorrelation time based criterion $N/\tau \geq a_c$ with $a_c = 50$ (Christiaens et al., 2021) to test convergence. We discard 30% of the chain as burn-in.

We measure the L' band contrast for the HD 176535 AB system by separately measuring the photometry for HD 176535 A and the negative fake companion of HD 176535 B from MCMC for both August 2021 and July 2022 NIRC2 datasets. We scale the flux ratio according to exposure times. Ultimately, for July 2021 data, we measure a contrast of $\Delta L' = 9.19 \pm 0.07$ mag. We estimate the star's L' band magnitude from both its

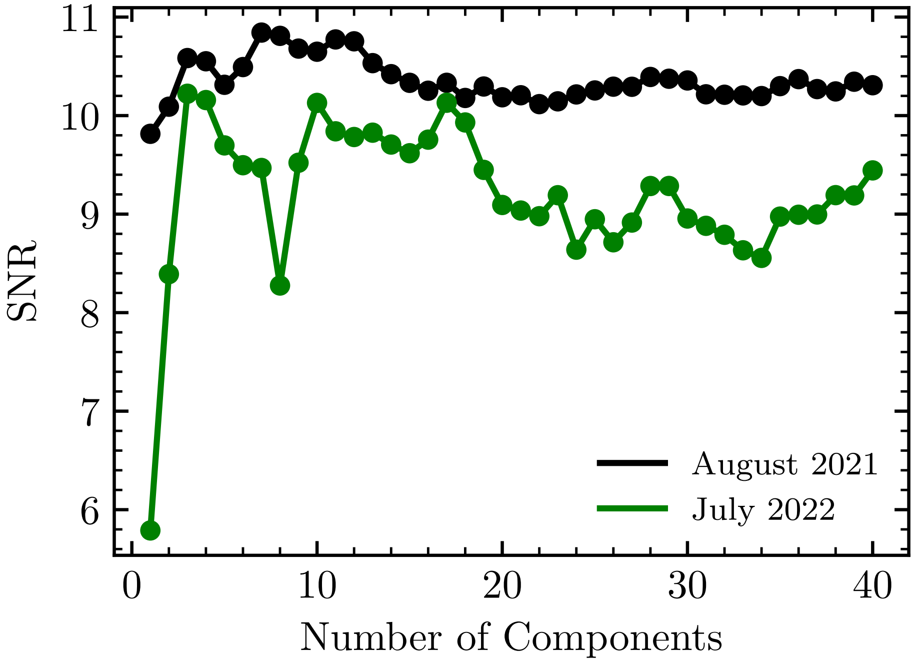

Figure 4.2 The Signal to Noise ratio of HD 176535 B in the PSF-subtracted Keck/NIRC2 images as a function of the number of annular PCA components for both August 2021 and July 2022 images. The optimal number of components that yield the best signal is 6 components for August 2021 with a SNR of 11.7, and 3 components for July 2022 with a SNR of 10.2. We adopt these values to produce our annular PCA PSF subtractions.

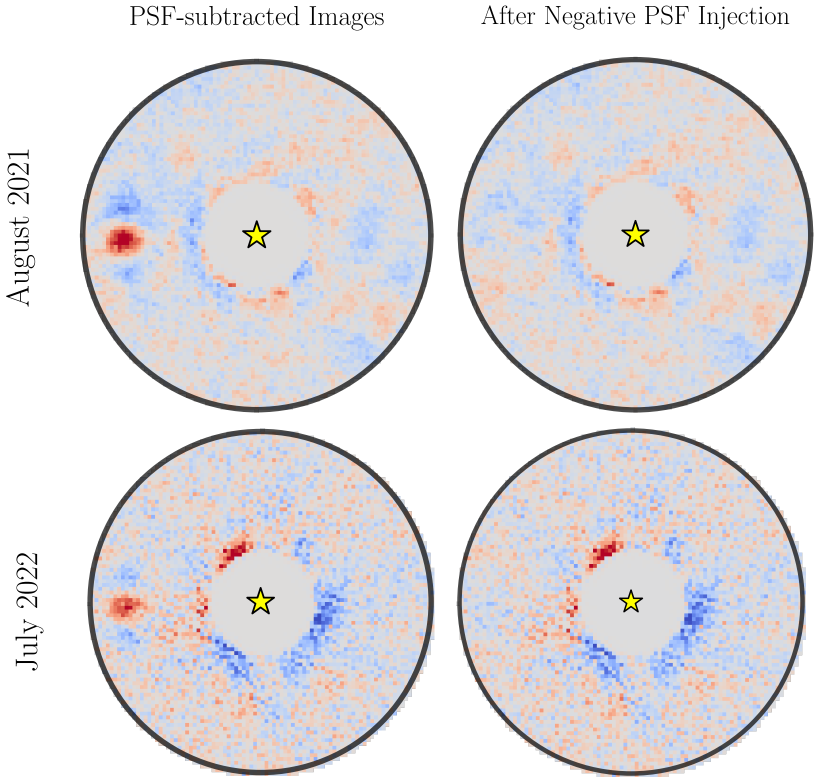

Figure 4.3 The images before (left) and after (right) injecting negative PSF templates with the best-fit separations, position angles, and flux ratios. The left panels show the PSF-subtracted images of HD 176535 B from the August 2021, and July 2022 Keck/NIRC2 datasets. The right panels are the results after negative fake companion injection. The signals of the companions are completely removed after the negative PSF injection. The increase in the noise level near the center is due to proximity to the stellar halo, resulting in poor PSF subtraction.

WISE and from its near-infrared photometry. HD 176535 A has a WISE W1 magnitude of 7.11 ± 0.02 mag (Maldonado et al., 2017). Since the L' band is on HD 176535 A's Rayleigh-Jeans tail and has a central wavelength nearly identical to that of WISE W1, the star's W1 and L' magnitudes are nearly identical. We also transform from 2MASS H (7.313 ± 0.033 mag) (Cutri et al., 2003) to K band, and subsequently to L' using the relations of Bessell & Brett (1988). This approach gives the an L' magnitude of 7.11 ± 0.04, identical to the L' photometry inferred from W1 albeit with a larger uncertainty. We adopt this larger uncertainty for a final L' band magnitude of $L'_* = 7.11 \pm 0.04$ mag. This stellar magnitude and contrast then produces a magnitude of $L'_p = 16.30 \pm 0.07$ for the companion HD 176535 B. Likewise, for the July 2022 NIRC2 dataset, we measure a contrast of $\Delta L' = 9.21 \pm 0.10$, and an L' magnitude of $L'_p = 16.32 \pm 0.10$ for HD 176535 B.

We combine the two epochs to get a final contrast of $\Delta L' = 9.20 \pm 0.06$. We then add the star's magnitude of $L' = 7.11 \pm 0.04$ to obtain an apparent L' magnitude for the companion of 16.31 ± 0.07, or an absolute magnitude of 13.47 ± 0.07.

The uncertainties in our NIRC2 astrometry are dominated by four error terms: the uncertainties in the measurement of the astrometry of the companion from the MCMC posteriors, the distortion correction to the NIRC2 narrow camera individual frames, the NIRC2 plate scale, and the north alignment of the detector. The raw images are corrected for optical geometric distortion using the post-2015 solution from Service et al. (2016) after the Adaptive Optics system and the NIRC2 camera were realigned. They found a post-realignment residual distortion solution through the mean rms scatter in

Table 4.3 New Keck/NIRC2 relative astrometry and L' photometric measurements of the HD 176535 AB brown dwarf-main sequence star system.

HD 176535 AB		
Instrument	Keck/NIRC2	Keck/NIRC2
Filter	L'	L'
Date (UT)	2021-08-26	2022-07-07
Epoch (Jyr)	2021.64875	2022.51510
Relative Astrometry		
Separation (mas)	347 ± 10	362 ± 10
PA (°)	91.55 ± 1.00	94.81 ± 1.00
Photometry		
$\Delta L'$ (mag)	9.19 ± 0.07	9.21 ± 0.10
L'_* Flux (mag)	7.11 ± 0.04	7.11 ± 0.04
L'_p Flux (mag)	16.30 ± 0.07	16.32 ± 0.10

NOTE: We consistently adopt 3% fractional errors in our separation and position angle measurements to aid MCMC convergence. The L' magnitude for the host star is transformed from the H band using Bessell & Brett (1988).

the position measurements of dozens of stars, which is about 1.1 mas in both X and Y. We adopt a post-alignment global plate scale of $9.971 \pm .004 \pm .001$ mas pixel^{-1} for the Keck/NIRC2 (Marois et al., 2008; Bowler et al., 2012; Serabyn et al., 2017; Xuan et al., 2018) AO system in narrow mode (Service et al., 2016). For the position angle, Service et al. (2016) gives an angle of $\theta_{\text{north}} = 0.^\circ262 \pm 0.^\circ020$ to align the images with celestial north. Thus in summary, the position angle of the companion must be corrected from the uncorrected MCMC measurements of the position angle θ_{meas} through the following equation:

$$\theta = \theta_{\text{meas}} - \text{PARANG} - \text{ROTPOSN} + \text{INSTANGL} - \theta_{\text{north}} \tag{4.1}$$

where PARANG is the parallactic angle, ROTPOSN is the rotator position of $4.^\circ43$, and INSTANGL is the NIRC2 position angle zeropoint of $0.^\circ7$. Table 5.2 showcases the dual-epoch relative astrometry and the L' band photometry results from our Keck/NIRC2

Table 4.4 MCMC orbital fit results for HD 176535 AB.

Parameter	**Prior**	**Best Fit**	**68.3% CI**	**95.4% CI**
		Fitted Parameters		
$\sigma_{\rm Jit}\,$(m/s)	$1/\sigma_{Jit}$	3.83	$3.83^{+1.1}_{-0.82}$	(2.40, 6.47)
$\mathrm{M}_*\,(M)$	$N(0.72, 0.02)$	0.728	$0.728^{+0.019}_{-0.019}$	(0.691, 0.766)
$\mathrm{M_p}\,(M)$	$1/M_p$	65.9	$65.9^{+2.0}_{-1.7}$	(62.6, 70.1)
$a\,$(AU)	1/a	11.05	$11.05^{+0.64}_{-0.56}$	(10.03, 12.38)
$\sqrt{e}\sin\omega$	$U(-1,1)$	-0.373	$-0.373^{+0.014}_{-0.012}$	$(-0.398, -0.344)$
$\sqrt{e}\cos\omega$	$U(-1,1)$	0.597	$0.597^{+0.023}_{-0.021}$	(0.557, 0.644)
$i\,(^\circ)$	$\sin i$	49.8	$49.8^{+3.4}_{-3.7}$	(42.4, 56.1)
$\Omega\,(^\circ)$	$U(-180,180)$	129.51	$129.51^{+0.94}_{-1.2}$	(126.8, 131.2)
$\lambda_{\rm ref}\,(^\circ)$	$U(-180,180)$	-176.9	$-176.9^{+356}_{-2.3}$	(-179.885, 179.883)
		Derived Parameters		
$\varpi\,$(mas)	–	27.0326	$27.0326^{+0.0011}_{-0.0011}$	(27.03, 27.035)
$P\,$(yr)	–	41.3	$41.3^{+3.6}_{-3.1}$	(35.7, 48.9)
$\omega\,(^\circ)$	–	328.0	$328.0^{+1.7}_{-1.6}$	(324.8, 331.6)
e	–	0.496	$0.496^{+0.022}_{-0.020}$	(0.459, 0.541)
$a\,$(mas)	–	299	299^{+17}_{-15}	(271, 335)
T_0	–	2468925	2468900^{+1300}_{-1100}	(2466900, 2471700)

NOTE: The reference epoch is 2455197.5 JD.

imaging observations.

4.3 Orbital Fit

We determine the orbit and mass of the HD 176535 AB system by jointly fitting the HARPS RVs, our new Keck/NIRC2 relative astrometry, and the stellar absolute astrometry from the HGCA with the Bayesian orbit fitting code `orvara`(Brandt et al., 2021i). `orvara`fits Keplerian orbits of stars and exoplanets using parallel-tempering Markov Chain Monte Carlo (MCMC) ensemble sampler through `ptemcee` (Foreman-Mackey et al., 2013; Vousden et al., 2016b). `orvara`models nine parameters for the Keplerian orbit: semi-major axis (a), inclination (i), longitude of ascending node (ω), time of periastron passage (T_0), eccentricity and argument of periastron ($\sqrt{e}\sin\omega$ and $\sqrt{e}\cos\omega$), the masses of the two components (M_* and $\mathrm{M}_{\mathrm{comp}}$), and a RV jitter term (σ_{Jit}). We ran our fit using 30 temperatures and 100 walkers over a total of 10^5 steps to sample the nine-dimensional parameter space. We discard the first 200,000 steps as burn-in and save the coldest set of chains for parameter inferences. We adopt log-uniform priors on the companion mass, semi-major axis, and RV jitter. For the mass of the host star, we adopt a Gaussian prior of $0.72 \pm 0.02M$ per our PARSEC isochrone measurement. We also test out a broader prior by inflating the uncertainty. With 3 ($0.72 \pm 0.06M$) and 5 ($0.72 \pm 0.1M$) times the original uncertainty, the mass posterior distributions for the companion changed to $67.9^{+2.9}_{-2.8}M_{\mathrm{Jup}}$ (1.1σ) and $69.3^{+3.4}_{-3.3}M_{\mathrm{Jup}}$ (1.3σ), respectively (see Appendix). We see a slight dependency of the companion mass on the assumed mass of the host star that reflects the covariance between companion and primary mass. There is a slight tension that we found between the observed and expected position. This may be indication that HD 176535 B is a binary, which could potentially account for the extra mass after error inflation and uncertainty in the astrometry. In addition, we use an informative prior on the parallax from Gaia EDR3 and uninformative priors on the remaining parameters.

Figure 4.4 displays our orbital fit for the HD 176535 AB system, including relative astrometry, RVs, and absolute Hipparcos-Gaia astrometry. The black lines highlight the maximum likelihood orbit while the colored lines show 50 random orbits from the MCMC posterior. The best-fitting relative astrometry orbit passes through both our relative astrometry data points.

The companion HD 176535 B has an orbital period of $41.3^{+3.1}_{-3.6}$ years, and the existing HARPS RV data cover around a fourth of the orbital period near its periastron passage. Therefore, as shown in the relative astrometric orbits, the constraints for the periastron part of the orbital arc are much better compared to the apastron part. Future relative astrometry beyond our 2022 data point will better constrain the semimajor axis and, as a result, the dynamical mass of the companion. The proper motions as measured by Hipparcos near 1991.25 and Gaia EDR3 near 2016.0 are the red points with error bars shown in Figure 4.4. The curves reflect the astrometric reflex motion over a 25-year time baseline between the two missions. With the newfound precision of Gaia EDR3, the two stellar astrometric astrometry data provide excellent constraints for this high acceleration system.

The joint posterior distributions for important orbital parameters are showcased in Figure 4.5. The posterior distributions are nearly but not perfectly Gaussian. The companion posterior mass distribution is approximately Gaussian with a value of $65.9^{+2.0}_{-1.7}M_{\rm Jup}$ at the 68.3% confidence interval. The mass is $(62.6,\ 70.1)M_{\rm Jup}$ at the 95.4% credible interval, which puts it definitively in the substellar regime. The HD 176535 system has been recognized as a RV planet hosting system and an infrared excess system based on WISE photometry Maldonado et al. (2017). The brown dwarf itself cannot account for the observed infrared excess: the contrast in L', close to W1, is more than 9 magnitudes. Redder WISE bands lie on the Rayleigh-Jeans tail of both the star's and brown dwarf's spectrum, where the contrast scales as $(R_{\rm bd}^2 T_{\rm bd})/(R_*^2 T_*) \sim 10^{-3}$. The source of the infrared excess remains a mystery.

The only orbital solution of this system is a recent fit by Feng et al. (2022), who found a dynamical mass of $75.5^{+8.6}_{-13.8} M_{\rm Jup}$ for HD 176535 B. Our dynamical mass measurement is in agreement with the lower bound of this result. The orbital fit from Feng et al. (2022) derives a RV semi-amplitude of 509^{+34}_{-123} m/s, a semi-major axis of $a = 9.1^{+1.1}_{-2.8}$ AU, an eccentricity of $0.42^{+0.04}_{-0.13}$, a period of 31^{+5}_{-13} years, and an inclination of $144\overset{\circ}{.}3^{+10.8}_{-8.7}$. The results are broadly consistent with our relative astrometry induced fit. In comparison, our results put the companion on a wider orbit and firmly place the companion in the brown dwarf regime, as opposed to be near the stellar/substellar boundary.

We present the first joint orbit analysis of the system, summarised in Table 5.5. Our best-fit orbit suggests an inclination of $49\overset{\circ}{.}8^{+3.4}_{-3.7}$, a moderate eccentricity of $0.496^{+0.022}_{-0.020}$, and a semi-major axis of $11.05^{+0.64}_{-0.56}$ AU. This corroborates Bowler et al. (2020)'s finding that imaged brown dwarfs form a broad eccentricity posterior distribution with evidence for a dependence on orbital period.

4.4 Discussion

4.4.1 Luminosity of HD 176535B

Here, we describe our approach to derive the luminosity for the brown dwarf HD 176535 B from our L' flux measurements. We calculate the bolometric luminosity of HD 176535 B

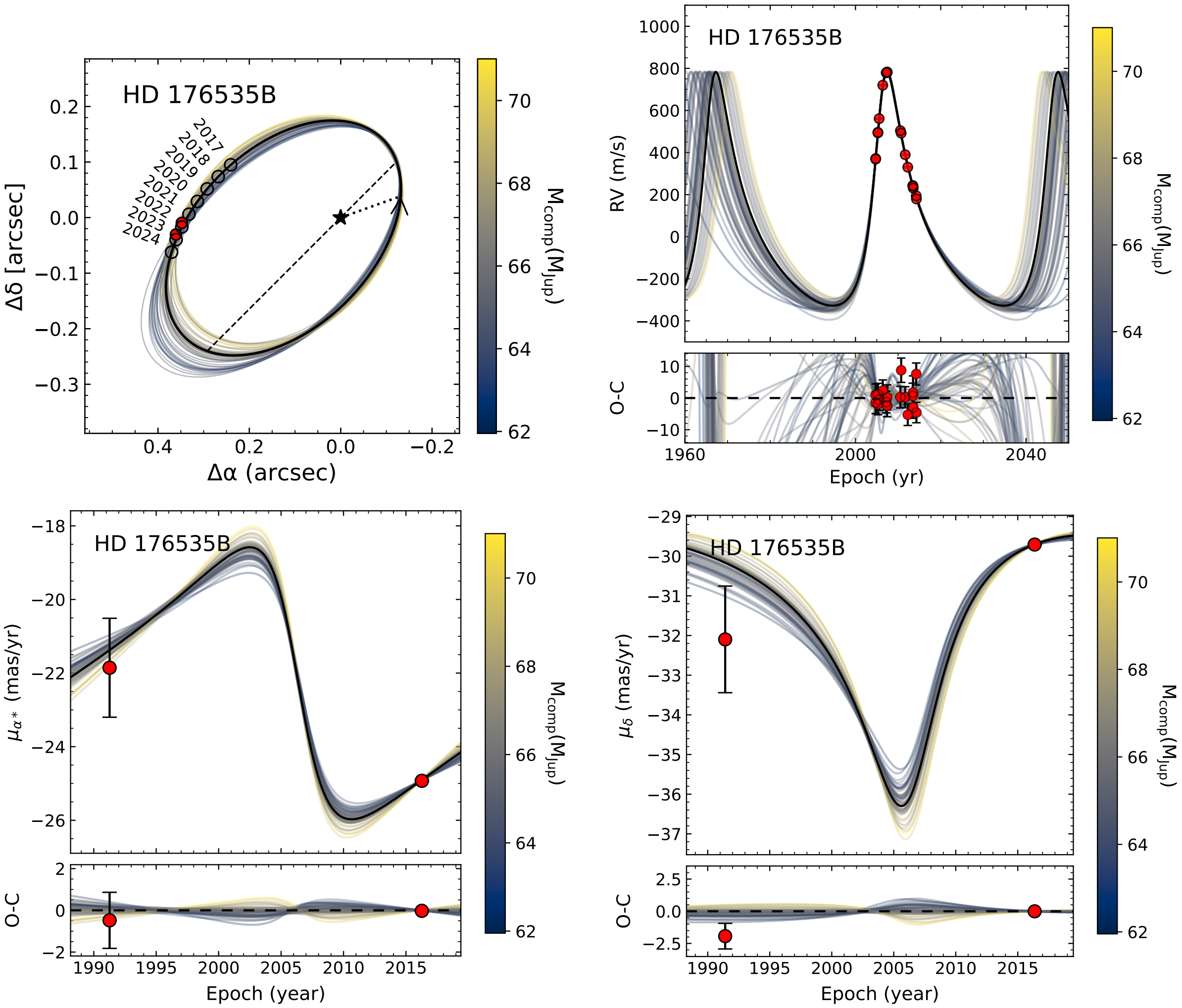

Figure 4.4 (Upper-left panel) Relative astrometry from the July 2021 and August 2022 measurements are represented by the two red points. A random sampling of orbits from the MCMC steps are shown and are color-coded by the mass of the companion (from yellow to dark blue). The black orbit is the best fit orbit; its χ^2 value indicates a formally a good fit. (Upper-right panel) The RV orbit of the companion. The random draws from the MCMC posterior fit tightly to the RVs along with the best fit orbit. The periastron part of the orbit is well-constrained compared to the apastron part of the orbit. (Bottom panels) Proper motions from the model compared to the calibrated Hipparcos and Gaia EDR3 proper motions near 1991.25 and 2016, respectively. Both Hipparcos and Gaia EDR3 proper motions constrain the proper motion of the star well, Gaia EDR3 especially. The integrated proper motion between the Hipparcos and Gaia points is constrained by the long-term HGCA proper motion.

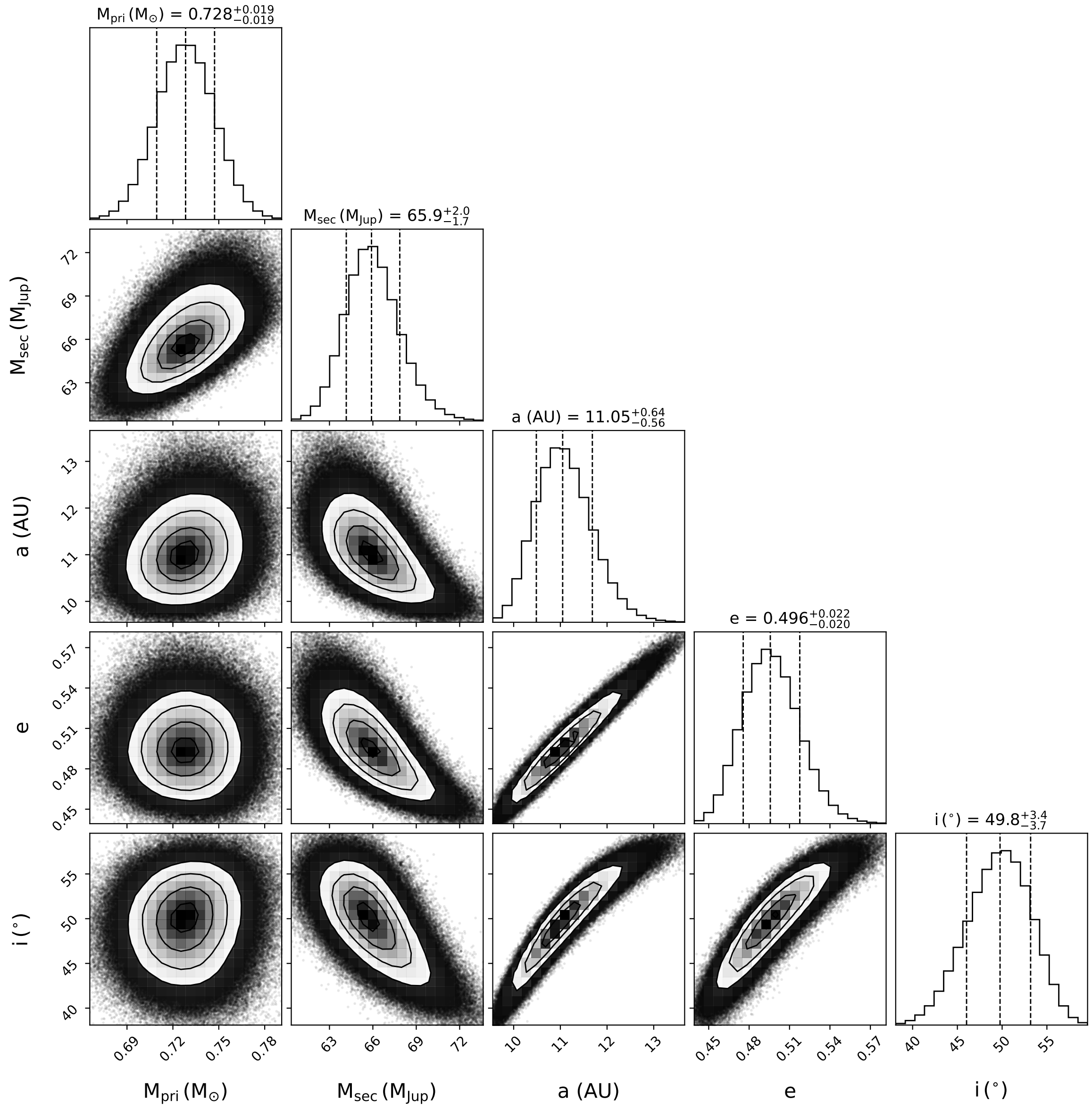

Figure 4.5 Joint posterior distributions for selected parameters for HD 176535 B. The errors are in the 16% and 84% quantiles about the median. The 2d contours give the 1-σ, 2-σ, and 3-σ levels that show the correlations between any two parameters.

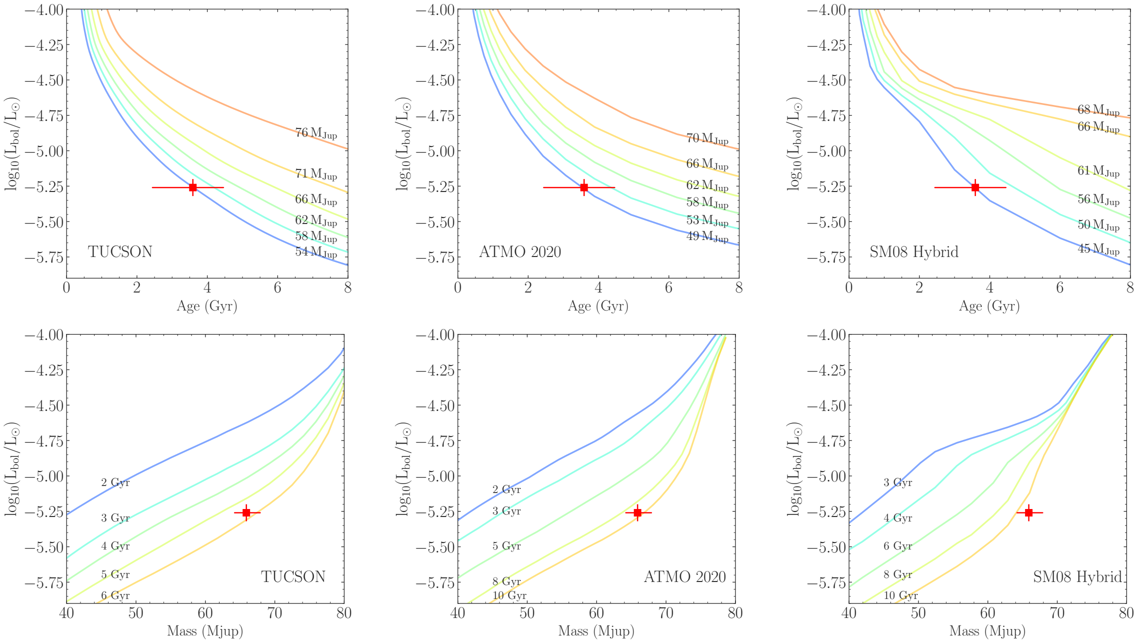

Figure 4.6 Different evolutionary models compared with the astrometric and photometric measurements of the brown dwarf HD 176535 B. Three independent substellar cooling models are considered: TUCSON, ATMO2020, and the SM08 hybrid model. The substellar cooling curves are the iso-mass and iso-age lines derived from each model given the mass and age of HD 176535 B. The top panels show the bolometric luminosity against substellar cooling age, and bottom panels show the bolometric luminosity against the mass of the brown dwarf.

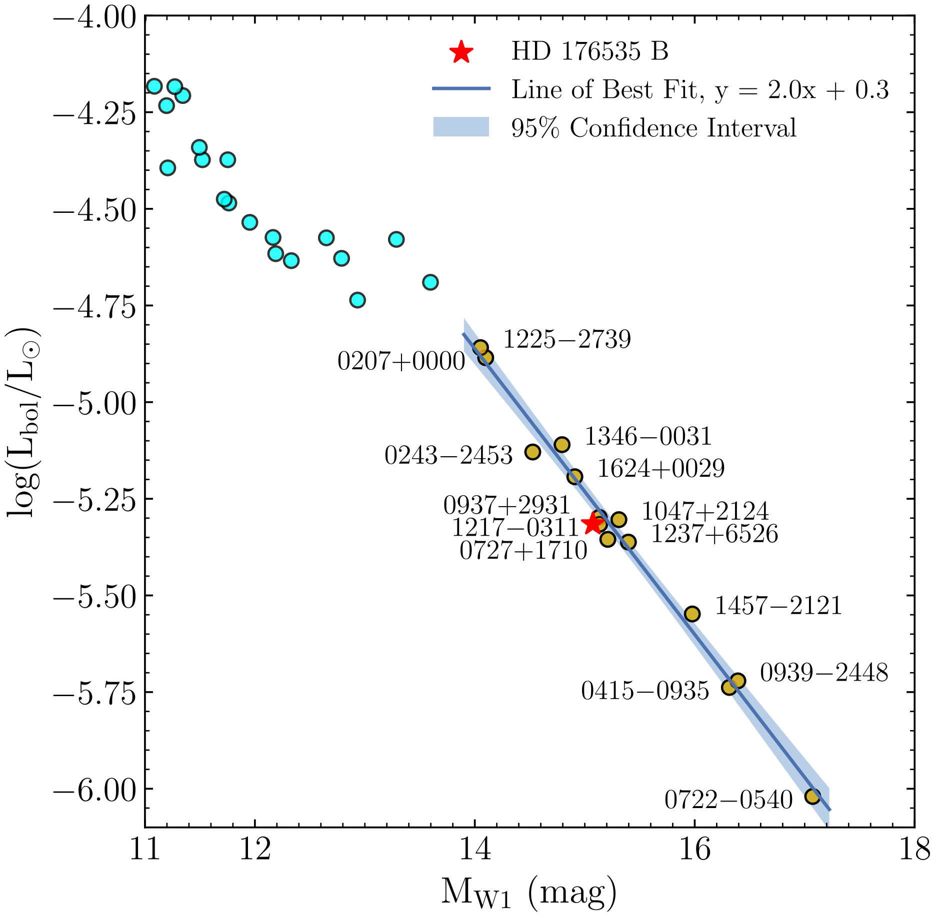

Figure 4.7 W1 as a function of Lbol using the field brown dwarf SED sample from Filippazzo et al. (2015). The cyan dots are L dwarfs, and the orange dots are field T dwarfs that we fit a linear relation to. We derive a relation between the absolute W1 magnitude of the T dwarfs and the log of their luminosity as $\log(L_{\rm bol}/L_{\odot}) = 2.0M_{\rm W1}+0.3$. The red star places HD 176535 B among the T dwarf sequence in the SED sample, and we infer a spectral type of T6 for HD 176535 B.

relying on the measured parameters for field-age (>500Myr) ultracool substellar objects in Filippazzo et al. (2015). As shown in Figure 4.7, we fit a linear relation between the absolute W1 magnitude and the bolometric magnitude estimated from integrating under the absolute flux calibrated SED of 15 field-age T dwarfs. We then employ the 4-th order polynomial relation between the absolute W1 magnitude and L'-W1 derived by Franson et al. (2022b) to convert the L' magnitude of HD 176535 B to a W1 magnitude. In Section 4.2.3, we derived a L'-band contrast of $\Delta L' = 9.20 \pm 0.06$, and an apparent magnitude of $L' = 16.31 \pm 0.07$ for HD 176535 B by combining the two measurements. We assume for the host star a $L'_* = 7.11 \pm 0.04$ as we found through the transformations of (Bessell & Brett, 1988). The transformation in Franson et al. (2022b) gives an absolute W1 magnitude of 15.07 ± 0.15 for HD 176535 B from our estimate of its L' magnitude. The absolute W1 magnitude of HD 176535 B then translates to $\log_{10}(L_{\rm bol}/L_\odot) = -5.26 \pm 0.07$ using our derived linear relation. Here, the errors are estimated by adding the errors from the fit in Franson et al. (2022b) (rms = 0.128), from our measured photometry (0.06 from the measured contrast, 0.04 from the star's L' photometry), and from our L'-$L_{\rm bol}$ fit (rms = 0.035) in quadrature. The bolometric luminosity we derive for HD 176535 B matches most closely with that of Gl 229 B and ϵ Indi Bb, which places it around a spectral class of T6.

Table 4.5 Evolutionary model-derived parameters vs. measured parameters

Property	**TUCSON**	**ATMO2020**	**SM08 Hybrid**	Measurement
Mass (M_{Jup})	$52.9^{+7.1}_{-7.3}\,(2.0\sigma)$	$48.8^{+6.0}_{-5.8}\,(2.9\sigma)$	$44.6^{+5.5}_{-5.7}\,(3.5\sigma)$	$65.9^{+2.0}_{-1.7}$
$\log(L_{\mathrm{bol}}/L_{\odot})$	$-4.95 \pm 0.20\,(1.8\sigma)$	$-4.77 \pm 0.19\,(2.7\sigma)$	$-4.63 \pm 0.11\,(3.3\sigma)$	-5.26 ± 0.07
Age (Gyr)	$5.25^{+0.54}_{-0.61}\,(1.7\sigma)$	$8.03^{+1.42}_{-1.23}\,(2.4\sigma)$	$9.35^{+0.91}_{-0.34}(3.0\sigma)$	$3.59^{+0.87}_{-1.15}$
T_{eff} (K)	982 ± 34	988 ± 35	950 ± 36	–
$\log(g)$ ($\mathrm{cm\,s^{-2}}$)	5.32 ± 0.06	5.30 ± 0.06	5.19 ± 0.06	–
Radius (R_{Jup})	$0.787^{+0.010}_{-0.009}$	$0.776^{+0.012}_{-0.010}$	$0.840^{+0.023}_{-0.024}$	–

NOTE: Masses are computed using the measured $\log(L_{\mathrm{bol}})$ and age; $\log(L_{\mathrm{bol}})$ from measured mass and age; age from measured mass and $\log(L_{\mathrm{bol}})$. Model-derived radii use the measured age and mass; $\mathrm{T_{eff}}$ and log g use model radii and measured mass.

4.4.2 Model Comparison

Brown dwarfs of measured dynamical masses of known ages and luminosities are powerful tools for testing different evolutionary models. Our measurements of HD 176535 B can be directly compared with the predictions from substellar evolutionary models that suggest brown dwarfs follow mass-age-luminosity relationships. The strength of the test correlates with the accuracy in mass, age and luminosity. For instance, the binary T-dwarf system ε Indi B is the most precisely determined dynamical mass system which provided some of the strongest tests of substellar evolutionary models, indicating evidence of slowed cooling in the L/T transition (Chen & Li et al., 2022).

We employ a suite of solar metallicity atmospheric and evolutionary models for cool brown dwarfs and self-luminous giant exoplanets in radiative-convective equilibrium to model the evolution of HD 176535 B. The substellar cooling models are constructed with both an interior structural model and an exterior atmospheric model as a surface boundary condition. The model input physics, equations of states, and atmospheric boundary conditions vary across different evolutionary models for cool T-Y brown dwarfs. We consider the legacy cloudless Tucson models (Burrows et al., 1997) and the most recent

ATMO-2020 models (Phillips et al., 2020a). The Tucson models utilize the cloudless atmospheres of Marley et al. (1996) and the H/He equation of state from Saumon et al. (1995). The ATMO-2020 grid is also a set of cloudless evolutionary models; it is an evolution of the DUSTY, COND, and BHAC15 models (Allard et al., 2001). We adopt a hybrid model from Saumon & Marley (2008) that incorporates the effects of clouds: cloudy at $T_{\rm eff} > 1400\,{\rm K}$, cloudless at $T_{\rm eff} < 1200\,{\rm K}$, and a hybrid of the cloudy and cloudless atmospheres at $T_{\rm eff}$ between 1400 K and 1200 K.

We test these three brown dwarf evolutionary models by coupling any two measured parameters from mass (M), age (A), and luminosity (L), and compute the third from the relevant model. When the chosen parameters are mass and age, we bilinearly interpolate the evolutionary model grids by mapping the log(M)-log(A) two-dimensional coordinates to a corresponding luminosity. When the two parameters are luminosity and mass, we similarly interpolate to get age. This approach can no longer be applied when interpolating mass from an age and luminosity: mass is multiply-valued at certain ages and luminosities. We therefore construct five two-dimensional arrays of mass as a function of age and luminosity, where five is the maximum number of values that mass can take at a given age and luminosity for any of our adopted models. We sample from each of these grids at a given age and luminosity, choosing one of the possible masses with a probability proportional to the inverse of $|dL/dM|$ at the adopted luminosity L and each mass possible mass M. In all cases we draw the two measured parameters from their posterior distributions and draw samples of the third parameter (mass, luminosity, or

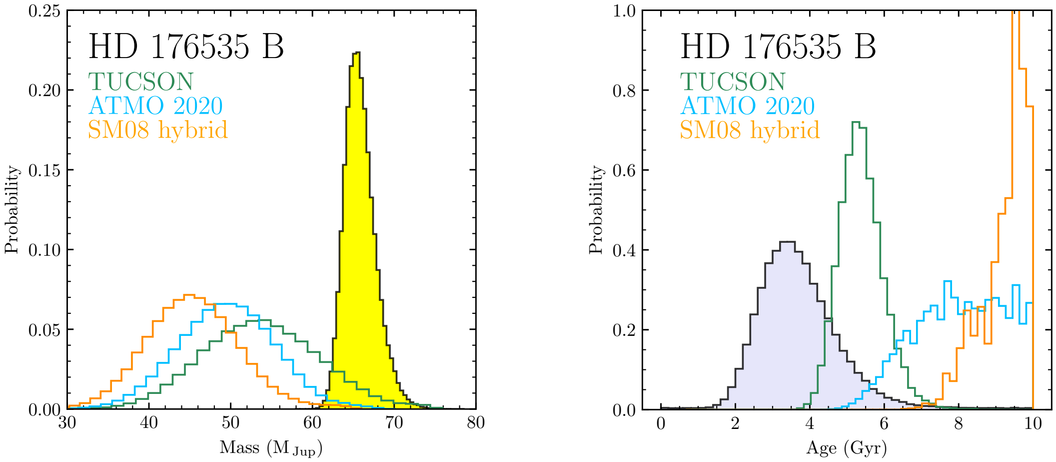

Figure 4.8 (Left) Dynamical mass posterior distribution (filled histogram) compared to the model-derived mass posteriors given L_{bol} and host star ages (step histograms). (Right) host star activity-based age probability distribution (filled histogram) compared to the model-derived age posteriors given L_{bol} and mass. All three models produce model-derived results that are consistent with the measured MCMC mass posteriors and isochronal age distributions.

age) as described above.

Figure 4.6 shows A-L and M-L relations from the three evolutionary models of our choices, as well as our measured benchmark brown dwarf HD 176535 B sitting atop the iso-age and iso-mass evolutionary grids. The TUCSON and ATMO2020 models are consistent with our photometry, age and mass measurements of HD 176535 A within 3-σ uncertainties, while the hybrid model prefer a much older age and/or lower masses for the companion. The discrepancy between the models and our measurement indicate possible tension with evolutionary models.

Figure 4.8 illustrates the inferred mass and age distributions compared to the posterior distributions for HD 176535 B. We compute the discrepancy between our model-derived distributions and model-independent distributions by randomly drawing ages or masses from both distributions to determine what fraction of data is one value larger than the other. We then express this fraction in units of sigma via a percent point function or the inverse of the CDF (cumulative distribution function) of the Gaussian, i.e., probability to the left of the distribution. We find that our dynamical mass distribution is consistent with the TUCSON and ATMO2020 models within 3σ, but slightly disagree with model predictions from the SM08 hybrid model. The model predicted ages deviate from our derived age by 1.7σ (TUSCON model), 2.4σ (ATMO 2020), and 3.0σ (SM08 Hybrid). The model-derived mass distributions deviate from our MCMC posterior masses by 2.0σ (TUCSON), 2.9σ (ATMO 2020), and 3.5σ (SM08 Hybrid), respectively. Both the cloudless TUCSON and ATMO2020 models predict similar, albeit broader mass distributions compared to the MCMC mass posterior distribution. The Saumon & Marley (2008) hybrid model predicted a distribution much lower than our results from MCMC. Our results suggest that substellar evolutionary models may be systematically underestimating luminosity for high-mass T dwarfs, however, improved age estimates will help to better constrain the mass predictions from all models.

Benchmark brown dwarfs with measured spectra may be used to test model atmospheres. Our bolometric luminosity and effective temperature measurements can be used against the evolutionary models to see how well they agree with the models. The brown dwarf radii as a function of mass, age and metallicity predicted by the evolutionary models can be combined with empirically determined luminosity to produce independent estimates of $T_{\text{eff}} = (L_{\text{bol}}/4\pi R^2 \sigma_{\text{SB}})^{1/4}$ and $\log(g) = \log(GM/R^2)$, where σ_{SB} is the

Stefan-Boltzmann constant.

Table 5.4 documents the derived parameters from each model, and our measured values in comparison. Our model-derived temperatures of $\approx$ 1000 K indicate that HD 176535 B is a massive, late T-type brown dwarf compared to the observed SED sample from Filippazzo et al. (2015).

4.4.3 The T-dwarf population

Our measurement for HD 176535 B is comparable to that of several other massive (60-75 M_{Jup}) benchmark T dwarfs of intermediate age (1-6 Gyr) that are slightly inconsistent with evolutionary model predictions of luminosity as a function of dynamical mass. HD 176535 B is over massive given our measurements for its age and luminosity. Here, we discuss the case of HD 176535 B in the context of other well-measured benchmark L/T- or T-dwarf systems (see comprehensive lists in Dupuy & Liu (2017b),Brandt et al. (2021d),Franson et al. (2022a), and discussions within). We plot the luminosities of these systems against their masses, together with the evolutionary grids from the Saumon & Marley (2008) hybrid model in Figure 4.9. All of these T-dwarfs are directly imaged, and have orbits constrained from both RV and Gaia DR2 parallaxes, or newer Gaia EDR3 parallaxes in the cases of Gl 758 B, HD 13724 B, HD 19467 B, HD 33632 Ab, HD 72946 B (Brandt et al., 2021d), and the binary brown dwarfs ε Indi Ba and Bb (Chen & Li et al., 2022).

The benchmark brown dwarfs of T or L/T transition types shown here include

Gl 802 B ($66 \pm 5 M_{\rm Jup}$ aged ≥ 1 Gyr Ireland et al. (2008)), HD 4747 B ($66.2 \pm 2.5 M_{\rm Jup}$ aged 3.6 ± 0.6 Gyr Brandt et al. (2019)), ε Indi Ba (a $66.96 \pm 0.35 M_{\rm Jup}$ L/T transition brown dwarf aged $3.5^{+0.8}_{-1.0}$ Gyr Chen & Li et al. (2022)), HD 72946 B (a massive T dwarf $72.5 \pm 1.3 M_{\rm Jup}$ aged 5.4 ± 1.9 Gyr Brandt et al. (2021d)), and HR 7672 B ($72.7 \pm 0.8 M_{\rm Jup}$ aged 5.4 ± 1.9 Gyr). Although most of these benchmark brown dwarfs are in agreement with the hybrid evolutionary models, there are a couple of outliers that point to a tension in the consistency of evolutionary models. The ones that are consistent with the models within 3σ given their masses and ages include HD 72946 B, HR 7672 B, HD 4747 B, HD 33632 Ab, ε Indi Ba/Bb, and Gl 758 B. Being the only system in this list with two T-dwarfs of the same age, the ε Indi B binary system provided a unique and strong test for evolutionary models (Chen & Li et al., 2022). The very different luminosities of the two brown dwarfs and the moderate mass ratio between the two suggest a steep M-L relationship $L \propto M^{5.47 \pm 0.08}$ that can be explained by a slowed cooling rate in the L/T transition.

However, despite the fact that many T-dwarfs are consistent with the models, there is a nontrivial fraction of over-luminous (under-massive, over-aged) and under-luminous (over-massive, under-aged) brown dwarfs that challenge the substellar evolutionary models' range of validity. The over-luminous brown dwarfs are brighter than models predict given their independent mass and age measurements, e.g. HD 13724 B (older than expected from substellar cooling ages) (Rickman et al., 2020), HD 130948 BC (Geißler et al., 2009), Gl 417 BC (Dupuy et al., 2014), and CWW 89 Ab (Beatty et al., 2018). The under-luminous cases means that the measured luminosities are fainter than model predictions given their masses and ages. These include the first discovered T-dwarf Gl 229 B (Calamari et al., 2022), HD 19467 B (Brandt et al., 2021d), HD 47127 B (Bowler et al., 2021), and HD 4113 C (Cheetham et al., 2018), and our brown dwarf HD 176535 B.

Our measurement of HD 176535 B joins it amongst a growing list of slightly over-massive and under-luminous benchmark brown dwarfs. According to our derivation of HD 176535 B's bolometric luminosity, the most immediate analogs for HD 176535 B are HD 19467 B, Gl 229 B, and ϵ Indi Bb (see Figure 4.9). The closest match is HD 19467 B, a massive ($65 \pm 6 M_{\rm Jup}$) T dwarf (T5.5±0.5) near the substellar mass boundary, and aged 5.4 ± 1.9 Gyr on an eccentric orbit around a G3V star (Brandt et al., 2021d). All of these analogs have spectral types of T6/T7, which indicates that HD 176535 B is likely also a T6 dwarf - it's spectral type can/will further be confirmed and characterized with the CHARIS spectrograph (Lewis et al., In prep). While the analogs of HD 176535 B and itself have similar luminosity, they differ in terms of agreeing/disagreeing with evolutionary models. Namely, ϵ Indi Bb agrees with substellar evolutionary models (Chen & Li et al., 2022), Gl 229 B strongly disagrees with evolutionary models, and both HD 176535 B and HD 19467 B somewhat disagree with the models, but to a lesser extent than Gl 229 B. Gl 229 B, with a mass of $71.4 \pm 0.6 M_{\rm Jup}$ and an age of 5.4 ± 1.9 Gyr, is anomalously over massive and way too faint for its mass at the model predicted substellar cooling ages (Filippazzo et al., 2015; Brandt et al., 2020, 2021d; Calamari et al., 2022). The reason for the different degrees of discrepancy between measurements and models we see in these brown dwarfs may arise from unresolved binarity of the systems. It is plausible that the Gl 229 B system has an unresolved high-mass companion, but HD 176535 B and HD 19467 B also have unresolved, albeit low mass ratio companions. Unfortunately, in all cases, unresolved companion would be too faint to be detected in multi-decade high-resolution spectra (Brandt et al., 2020). Therefore, the origin of HD 176535 B's relatively high mass is ambiguous, but we cannot rule out binarity as an explanation. Other likely explanations include the following: 1) We are substantially underestimating ages of T dwarfs, for example, the ages of HD 176535 B and HD 19467 B are actually closer to 8-10 Gyrs as opposed to 3-5 Gyrs. 2) Missing physics in the brown dwarf cooling models.

In this study, we compared HD 176535 B with three models that are predominately cloud-free given the object's temperature and the hybrid model's degeneracy in cloud treatment. A more accurate estimate of the bolometric correction would require using a range of atmosphere models that account for cloud effects. Unfortunately, no other evolutionary models presently available integrate synthetic spectra with evolutionary tracks, rendering it impracticable to correlate these models with HD 176535 B's mass, luminosity, and age. Thus, we resorted to an empirical correction approach that merely necessitates a single-band measurement in L'.Future multi-wavelength measurements will provide a more precise bolometric correction.

Till now, it is still unclear whether the over-massive T dwarfs are just a handful of unresolved binaries, or a more severe systematic problem for the T dwarf cooling models.

As more L, T, and L/T transition brown dwarfs are being discovered and characterized, a complete picture on the evolution and cooling of brown dwarfs across the L, T, and Y spectra will be better portrayed.

4.4.4 Future follow-ups and Gaia DR4 accelerations

We have carried out direct imaging measurements of HD 176535 B in the L' band with the NIRC2/Keck AO pyramid WFS. HD 176535 B turned out to be a massive, T-type dwarf according to our `orvara` orbital fit. The mass and eccentricity of the system are very well constrained from our orbital fit to less than 3%. Any future high-contrast imaging measurements will not only help refine the mass and orbital parameters, but also determine the spectral type of HD 176535 B. Multi-band near infrared spectra with instruments such as the CHARIS/SCExAO/Subaru, the Keck Planet Imager and Characterizer (KPIC/NIRSPEC), as well as photometry from JWST in the thermal infrared will enable spectroscopic characterizations of HD 176535 B. Further RV monitoring beyond 2024 could also enhance the orbital fit, especially the orbit when the companion is near apastron. In addition to RVs, future Gaia epoch astrometry such as Gaia DR4 and DR5 will slowly resolve HD 176535 B's astrometric orbit as well (see bottom two figures of Figure 5.5).

Given HD 176535 B's current `orvara` orbit presented in this paper, we predict the star HD 176535 A's DR4 accelerations using an adaptation of the epoch astrometry code `htof` (Brandt et al., 2021c). This adaptation parses the intermediate Gaia scanning law

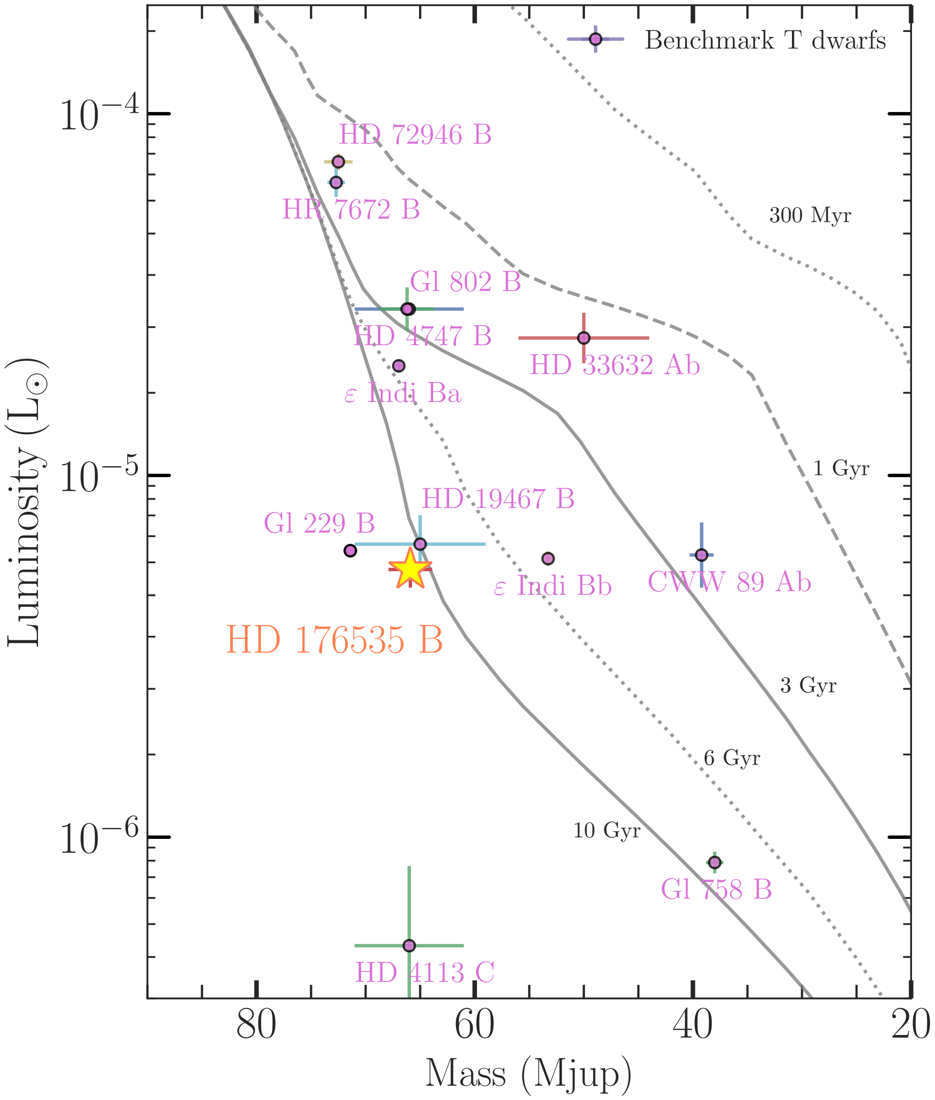

Figure 4.9 Luminosity as a function of mass for literature benchmark T dwarfs (purple), our target HD 176535 B (coral), as well as the hybrid Saumon & Marley (2008) evolutionary models (grey lines). Note that HD 4747 B, CWW 89Ab, ε Indi Ba and HD 33632 Ab are L/T transitioning brown dwarfs. The errorbars on the binary brown dwarfs ε Indi Ba and Bb are the tightest because they have the most precisely measured masses up to date. The literature masses and luminosities are from Dupuy & Liu (2017b); Dupuy et al. (2019); Brandt et al. (2021d); Franson et al. (2022a); Chen & Li et al. (2022).

Table 4.6 Predicted Gaia DR4 accelerations at epoch=2017.5.

Parameter	**Value (mas/yr^2)**
predicted $\dot{\mu}_{\alpha*}$	0.223 ± 0.0323
predicted $\dot{\mu}_{\delta}$	0.059 ± 0.0102

data from GOST from 2014.6403 to 2020.1403 (this covers the 5.5 year baseline for DR4), and densely samples the orbits to fit astrometric solutions to those data. The predicted Gaia DR4 accelerations are summarised in Table 4.6. These accelerations can be directly compared to the DR4 accelerations when they are released. These accelerations provide a unique opportunity, along with more than 100 other predictions in An et al, 2023 in prep., to test the accuracy of Gaia data. These accelerating systems act as "dynamical beacons" that anchor Gaia astrometry for non-single stars.

4.5 Conclusion

In this work, we measured the dynamical mass of the imaged substellar companion HD 176535 B discovered in the first phase of a pilot discovery program targeting accelerating stars using the NIRC2 camera at the W. M. Keck observatory. The companion's on-sky location was predicted in advance of imaging with the orbit-fitting package `orvara` to be a $62 M_{\rm Jup}$ companion on a wide orbit. It was subsequently observed for the first time with Keck/NIRC2 in the L' band in August 2021, and followed up in July 2022. After our observations, we carried out orbital fits with the dual-epoch relative astrometry, RVs from HARPS, and Gaia EDR3 absolute astrometry from the HGCA. Our model-independent dynamical mass measurement of $65.9^{+2.0}_{-1.7} M_{\rm Jup}$ revealed an old ($3.59^{+0.87}_{-1.15}$ Gyr) and massive brown dwarf companion. The thermal spectra of the companion has not been measured yet, but model-dependent measurements of effective temperature and surface gravity places it in the T-dwarf regime. Future astrometric and spectroscopic measurements (e.g. in the H and K bands with CHARIS/SCExAO/Subaru) confirm its T-class spectral type. HD 176535 B joins a growing list of benchmark brown dwarfs that have precisely determined dynamical masses, ages and luminosities. Future data from radial velocities, direct imaging relative astrometry, and/or Gaia epoch astrometry, will place better constraints for its orbit. Finally, multi-band infrared spectroscopy follow-up will be useful to identify its spectra, and to calibrate substellar evolutionary models. The successful imaging of HD 176535 B following its prediction is a proof of the potential for informed direct imaging searches.

Data Availability

This paper includes data collected by the NIRC2 camera at the W. M. Keck Observatory (WMKO), which is publicly available from the Keck Observatory Archive (KOA) jointly managed by the WMKO and NASA Exoplanet Science Institute (NExScI). Funding for this research is provided by the National Aeronautics and Space Administration. All data in this paper are publicly available through the KOA, except for the most recent data for July 2022. The data are analyzed with the `orvara` and open-source packages, which are publicly available at https://github.com/t-brandt/orvara and https://github.com/vortex-exoplanet/VIP, respectively. We acknowledge the use of public

Gaia EDR3 data through the Gaia Archive `https://gea.esac.esa.int/archive/`.

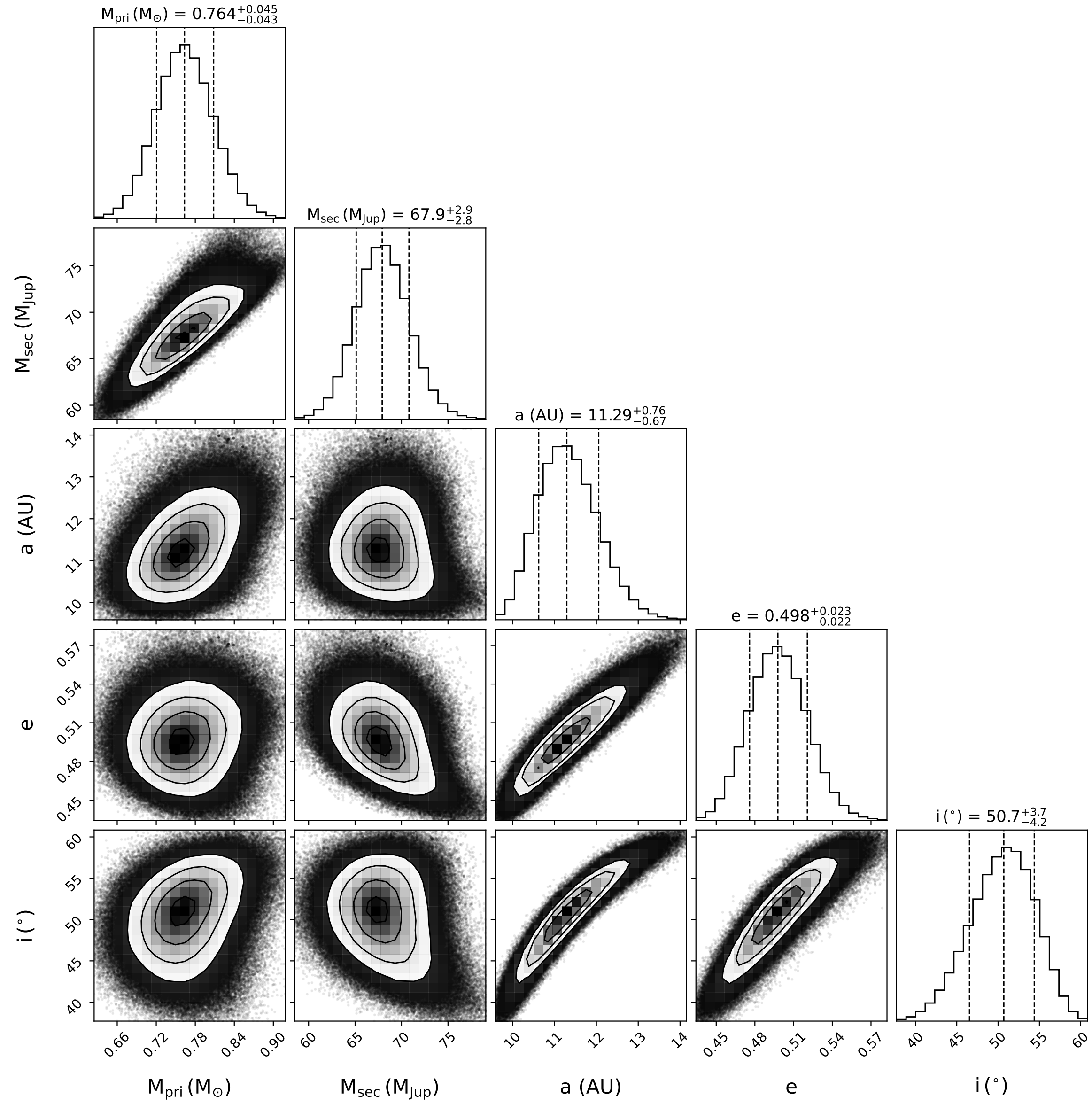

Figure 4.10 Joint posterior distributions for selected parameters for HD 176535 B with a prior of $0.72 \pm 0.06\,M$ on the host star. The errors are in the 16% and 84% quantiles about the median. The 2d contours give the 1-σ, 2-σ, and 3-σ levels that show the correlations between any two parameters.

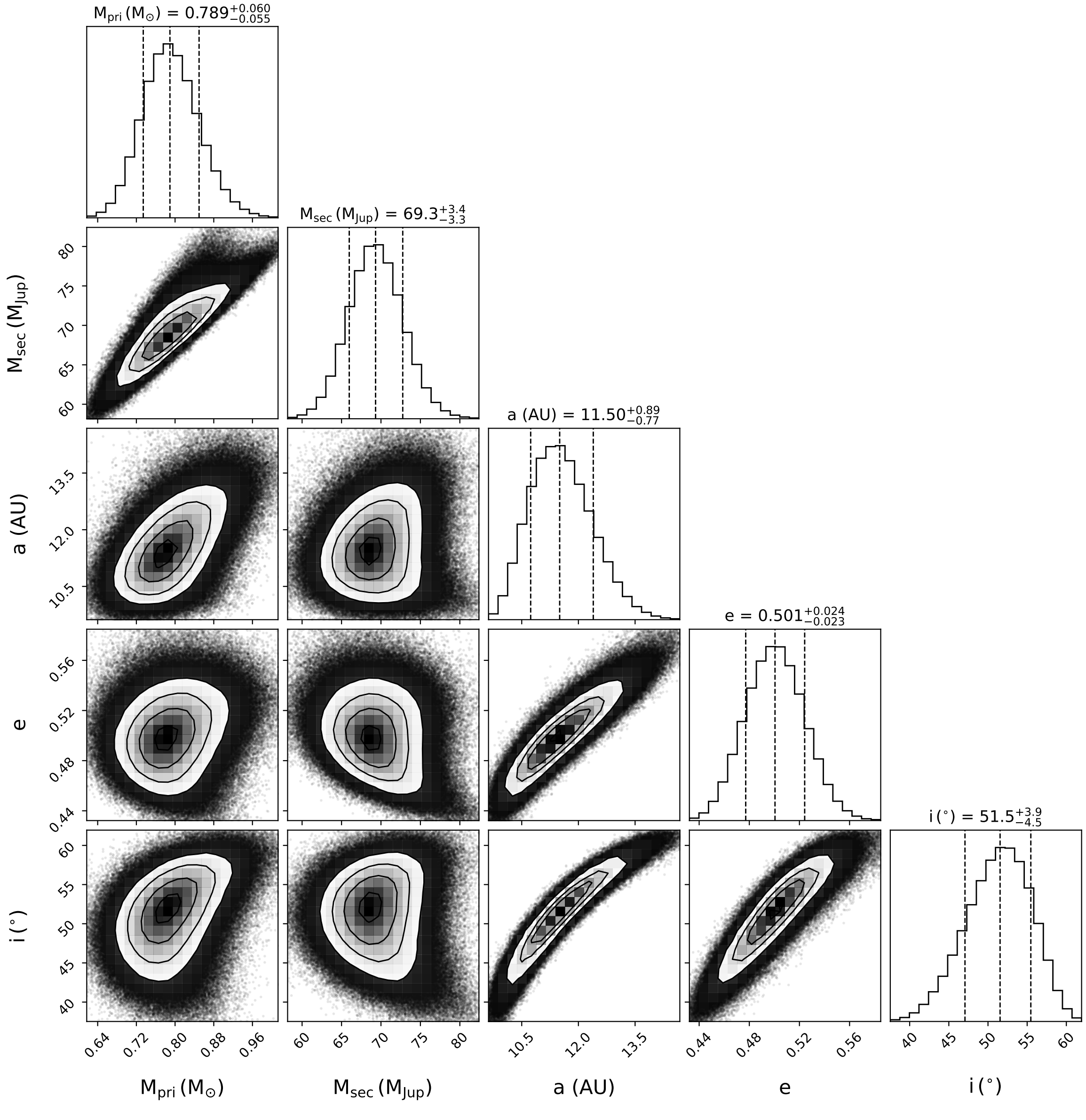

Figure 4.11 Joint posterior distributions for selected parameters for HD 176535 B with a prior of $0.72 \pm 0.1\,M$ on the host star. The errors are in the 16% and 84% quantiles about the median. The 2d contours give the 1-σ, 2-σ, and 3-σ levels that show the correlations between any two parameters.

Chapter 5

Astrometry and Direct Imaging Discovery of HD 63754 B

5.1 System Properties

HD 63754 A (=HIP 38216 A) is a single, bright, main-sequence star of spectral type G0V located at a distance of 50.17±0.051 pc (Gaia Collaboration, 2020). HD 63754 is relatively metal-rich with a metallicity of $[F/H] = 0.20 \pm 0.03$ dex. It also has a slightly lower surface gravity of $\log(g) = 4.04 \pm 0.06$ dex and a slightly hotter temperature of 6088±32 K compared to the Sun, as reported in the PASTEL catalog (Soubiran et al., 2016, 2022).

The chromospheric activity, measured by the S-index, is calculated by determining the ratio of the flux in a narrow bandpass centered on the Ca II H and K lines to the

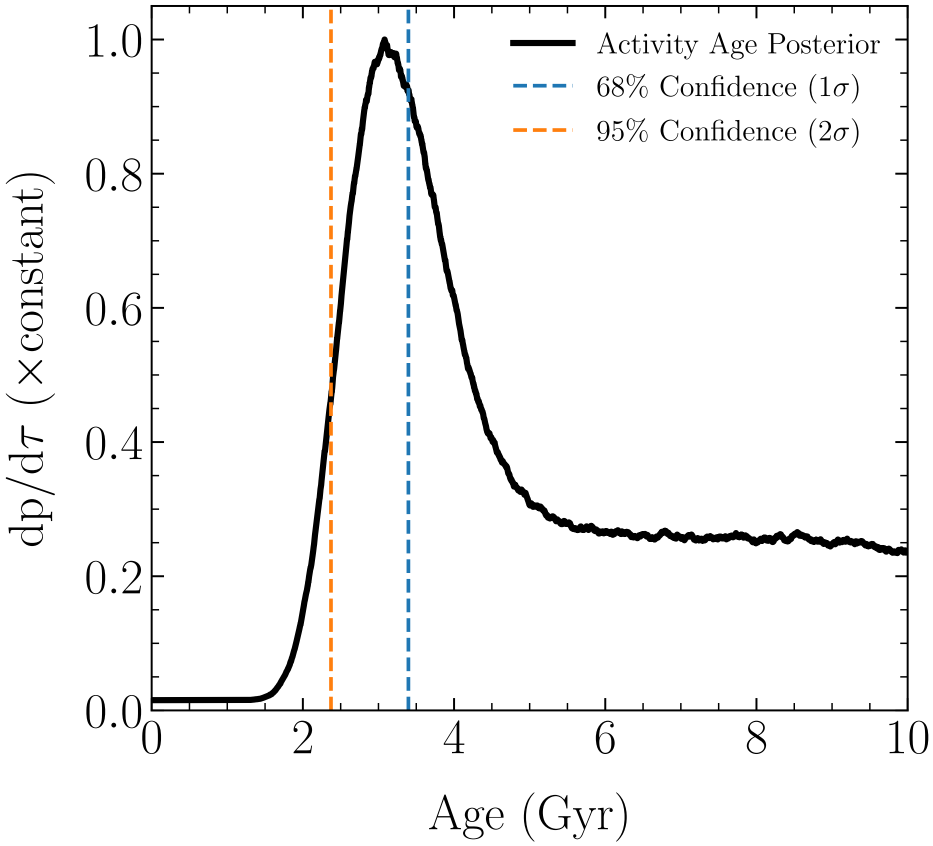

Figure 5.1 The normalized age probability posteriors of HD 63754 A using the Bayesian activity-age dating technique developed by Brandt et al. (2014). This approach incorporates X-ray (R_x) and chromospheric activity (R'_{HK}) indicators, along with the optional inclusion of rotation period, to effectively constrain the Rossby number. the Rossby number is transformed using the calibration provided by Mamajek & Hillenbrand (2008), allowing for the translation of the Rossby number into a reliable age estimate. The upper limit of the age is unconstrained, thus one-sided quantiles were computed by integrating the area under the cumulative density function up to the 68% and 95% confidence levels, corresponding to the 1σ and 2σ confidence intervals, respectively. The age of HD 63754 A is estimated to be greater than 3.4 Gyr at a 68% confidence level (indicated by the blue dashed line), and greater than 2.4 Gyr at a 95% confidence level (orange dashed line).

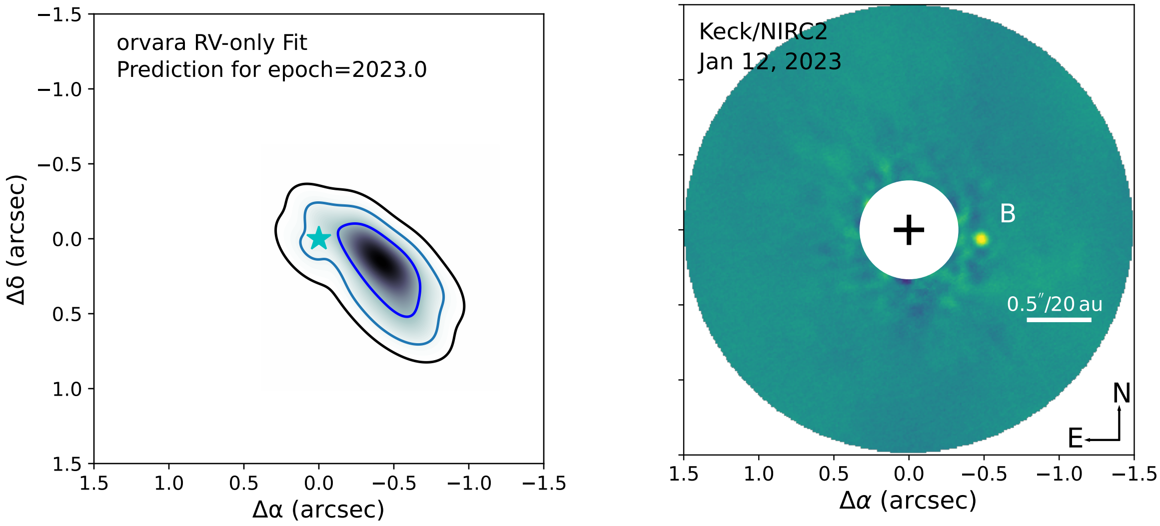

Figure 5.2 (Left) Contour lines depict the predicted astrometry of HD 63754 B relative to the host star (represented by the cyan star) in terms of right ascension and declination. These predictions were obtained using the `orvara` orbit fitting package Brandt et al. (2021f), incorporating pre-existing radial velocities from HAPRS and HIRES. (Right) PSF subtrated image showing the detection of the companion near its predicted position.

Table 5.1 Key Characteristics of the HD 63754 AB system.

Property	**Value**	**Refs**
Host Star		
ϖ (mas)	19.93 ± 0.02	1
Distance (pc)	50.17 ± 0.03	1
SpT	G0V	2
Mass (M)	1.35 ± 0.15	12
Age (Gyr)	> 3.4	12
$\mathrm{T_{eff}}$ (K)	6153 ± 100	3,4
[Fe/H] (dex)	0.20 ± 0.03	3,4
log(g) (dex)	4.04 ± 0.06	3,4
$\log(\mathrm{R}'_{\mathrm{HK}})$ (dex)	-5.12 ± 0.07	5,6,7,8
R'_{X} (dex)	< -4.28	9
Gaia RUWE	1.023	1
Gaia G (mag)	6.413 ± 0.003	1
B_T (mag)	7.235 ± 0.066	10
V_T (mag)	6.597 ± 0.010	10
J (mag)	5.486 ± 0.034	11
H (mag)	5.248 ± 0.047	11
K_s (mag)	5.133 ± 0.023	11
WISE W1 (mag)	5.080 ± 0.201	11

Note: References abbreviated as (1) Gaia Collaboration (2020); (2) Soubiran et al. (2016); (3) Soubiran et al. (2018) (4) Aguilera-Gómez et al. (2018); (5) Wright et al. (2004); (6) Murgas et al. (2013); (7) Brewer et al. (2016); (8) Gomes da Silva et al. (2021); (9) Voges et al. (1999); (10) Høg et al. (2000a); (11) Cutri et al. (2003); (12) This work flux in two nearby continuum bandpasses. This activity serves as an age indicator for the star. HD 63754 has an S-index ranging from 0.127-0.139 based on the Pace (2013) catalog. Literature measurements report $\log(\mathrm{R}'_{\mathrm{HK}})$ values of -5.12±0.07 (Wright et al., 2004; Murgas et al., 2013; Brewer et al., 2016; Gomes da Silva et al., 2021). Literature estimates of the chromospheric activity age consistently favor a young age for the system, ranging from 2.4-3.57 Gyr Marsakov & Shevelev (1995); Valenti & Fischer (2005); Takeda et al. (2007); Holmberg et al. (2009); Delgado Mena et al. (2015); Luck (2017); Yee et al. (2017); Delgado Mena et al. (2019). We carry out independent measurement of the stellar age using the Bayesian age-dating method outlined in Brandt et al. (2014). We use a chromospheric index of $\log(\mathrm{R}'_{\mathrm{HK}}) = -5.12 \pm 0.07$ and an X-ray index of $R_X < -5.32$ from Voges et al. (1999) to derive an activity-based age of $\geq$3.4 Gyr at a 68% confidence level for the HD 63754 AB system in the same way as described in Li et al. (2023) (Figure 5.1). The upper limit of the age remains unconstrained by our approach. However, most literature measurements favor a young age for the star, such as Costa Silva et al. (2020); Delgado Mena et al. (2019); Llorente de Andrés et al. (2021); Palla et al. (2022); Luck (2017). The youth of the system is indicated by the abundance of lithium ([Li/H] = 2.16 dex) in the star's atmosphere (Luck, 2017), its location as a G0V star in the HR diagram, and the star's chromospheric activity level.

Various studies have estimated the mass of HD 63754. Bochanski et al. (2018) used Gaia observations, matched them with data from the 2MASS and Wide-Field Infrared Survey Explorer catalogs, and applied MIST isochrones to derive an estimate of

$1.46 \pm 0.05M$ for HD 63754 among a sample of co-moving stars. Anders et al. (2019b) obtained a mass of $1.27 \pm 0.19M$ by combining photometric and astrometric data from Gaia EDR3 with stellar evolutionary models. Gomes da Silva et al. (2021) analyzed HARPS spectra and determined a mass of $1.426 \pm 0.017M$, while Pägert et al. (2021) utilized Bayesian inference with Gaia parallax data, obtaining a mass of $1.12 \pm 0.15M$ for the TESS input catalog. While the literature currently contains a range of mass estimates, astroseismology with TESS could enable a more accurate determination of the host star's mass.

We conducted an independent estimation of the stellar mass using the method described in Li et al. (2021a), based on the star's chromospheric activity data, resulting in a stellar mass of $1.41 \pm 0.05M$ that falls within the range of literature measurements. We choose a mass prior encompassing the range from 1.12 to $1.5M$, and with a broad uncertainty, yielding a wide prior of $1.35 \pm 0.15M$. We ultimately adopt adopt this prior for our orbital fit.

5.2 The predicted companion

The combination of radial velocity measurements and absolute astrometry holds the potential to identify companions worthy of following up. Initial orbital analysis was conducted using the available HARPS and HIRES RV measurements and Hipparcos-Gaia absolute astrometry. We use the orbit results to assess the detectability of the companion and make predictions of its locations at a given epoch. The joint fitting of

HARPS and HIRES RVs, along with HGCA stellar astrometry was performed using the MCMC orbit code called `orvara` (Brandt et al., 2021f). The initial results from the RV and absolute astrometry fit indicate the presence of a massive companion of $95.36 M_{\rm Jup}$ orbiting HD 63754 A at a distance of around 19 AU.

`orvara` allows for the generation of 3-σ likelihood contours that illustrate the potential coordinates of the companion relative to its host star at any given epoch. Our preliminary analysis identifies HD 63754 A as a promising candidate for follow-up high-contrast imaging. We show the predicted 3-σ contours outlining the potential positions of the companion in the left panel of Figure 5.2. We predicted that the companion's location is predominantly clustered within a confined circle positioned to the west of the star.

5.3 Observation and Data

5.3.1 Relative Astrometry

We observed HD 63754 using the thermal Near-Infrared Camera 2 (NIRC2) on the Keck Observatory in the L'-band (central wavelength 3.8 μm) on UT 2023 Jan 11. We use the narrow camera with a pixel plate scale of 0.009971±0.000004 arcsec/pixel (Service et al., 2016) and a 512×512 pixel field of view. The NIRC2 data were taken behind the Vector Vortex Coronagraph (VVC) (Serabyn et al., 2017) with a vortex phase mask using natural guide star AO and the visible-light Shack-Hartmann wave-front senser. The seeing condition for the night was photometric (<1“) as seen by the differential image motion monitor (DIMM). The observations involve sequences of 20-30 science frames using the Quadrant Analysis of Coronagraphic Images for Tip-Tilt Sensing (QACITS) algorithm. This algorithm applies small tip-tilt corrections to re-center the star after each exposure, achieving sub-milliarcsecond stability (Huby et al., 2017). Each sequence also includes an off-axis unsaturated frame for flux calibration and sky-background frames for both the science images and the point-spread-function (PSF) images. We captured a total of 165 science images, excluding 9 short pointing optimization frames. Each frame consisted of 90 coadds with 0.3s exposures to for optimal readout efficiency. The total integration time lasted 4590s (76.5 minutes) and was accompanied by a parallactic angle shift or frame rotation of 34.61°.

The Angular Differential Imaging (ADI) data cube undergoes a series of pre-processing steps to prepare it for analysis. We utilize the Vortex Image Processing () package (Gomez Gonzalez et al., 2017b), which is specifically designed for processing NIRC2 vortex observations. Initially, we perform flat-fielding and dark subtraction on the science images to correct for pixel sensitivity variations. Then we employ the `lacosmic` Python package to remove cosmic rays (van Dokkum, 2001), and we correct for geometric distortion using the solutions provided by Service et al. (2016) for the narrow-field mode of the NIRC2 camera. To enhance the signal-to-noise (SNR) ratio, we employ to model and subtract the sky background noise in both the science frames and the off-axis flux-calibration frames. Precise centering of the images is crucial in ADI reduction to ensure proper alignment of the vortex with the center of the field of view. For this purpose, we fit a 2D Gaussian to the center halo of the vortex in each image, allowing us to determine the centroid. Subsequently, we extract a subimage measuring 400 by 400 pixels centered around this centroid for each image. This approach automatically aligns the images, enabling us to achieve sub-mas alignment errors between frames.

The package offers PCA-based algorithms (Soummer et al., 2012; Amara & Quanz, 2012) to subtract the point spread function (PSF). The stellar PSF is obtained by subtracting the sky-background frame from the PSF image with the star off the vortex. By fitting 2D Gaussians to the host-star's PSF, we measure a FWHM of 7.89 pixels (0.″079). Here we follow the same procedure adopted in (Li et al., 2023) for PSF subtraction. Unlike simple median combination of ADI, PCA algorithms enhance the subtraction model by modeling the background including leaked starlight, static and quasi-static speckles. This is achieved by projecting each image onto the first n principal components, obtained through singular value decomposition of a 2D matrix created from the observed sequence of images. Applying a PA threshold based on distance, we compute PCA in the entire annulus or separate segments (annular PCA). Our approach estimates the PSF for each image in HD 63754 A's data cube by subtracting principal components from individual annular regions. This effectively removes starlight and remaining static speckles, highlighting fainter and more extended structures like planets or disks. To reduce self-subtraction, we employ a rotation gap/PA threshold and radial scaling criterion (Lafrenière et al., 2007) in annular patches, discarding frames with inadequate rotation.

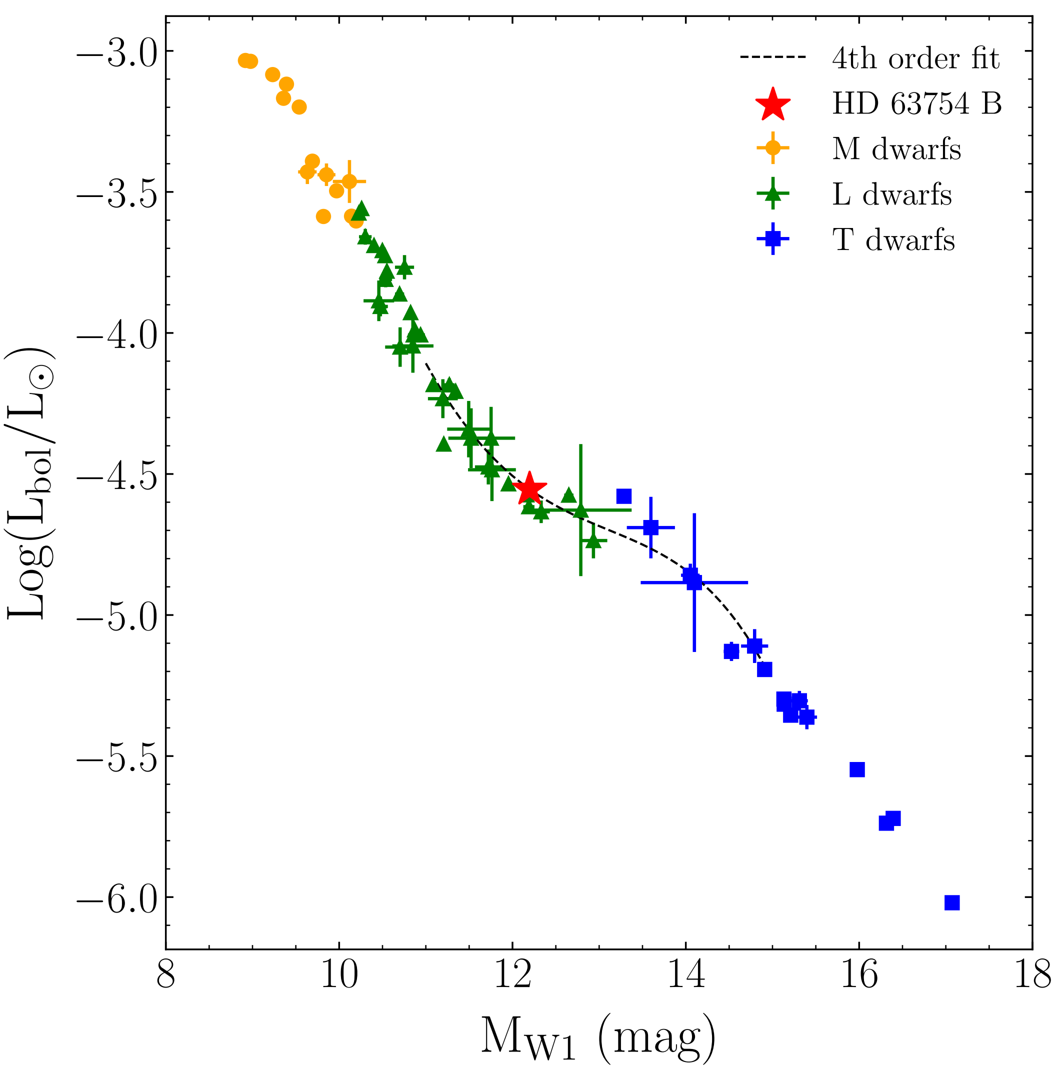

Figure 5.3 The relationship between the bolometric magnitude and the absolute WISE W1 magnitude is shown for field dwarfs, based on the spectral energy distribution (SED) analysis by Filippazzo et al. (2015). A fourth-order polynomial was fitted to the data in the W1 magnitude range of 10.23-15.21, capturing the transitional region between L dwarfs and T dwarfs. The benchmark object HD 63754 B, situated right at the L/T transition, is highlighted by the red star with its corresponding W1 magnitude.

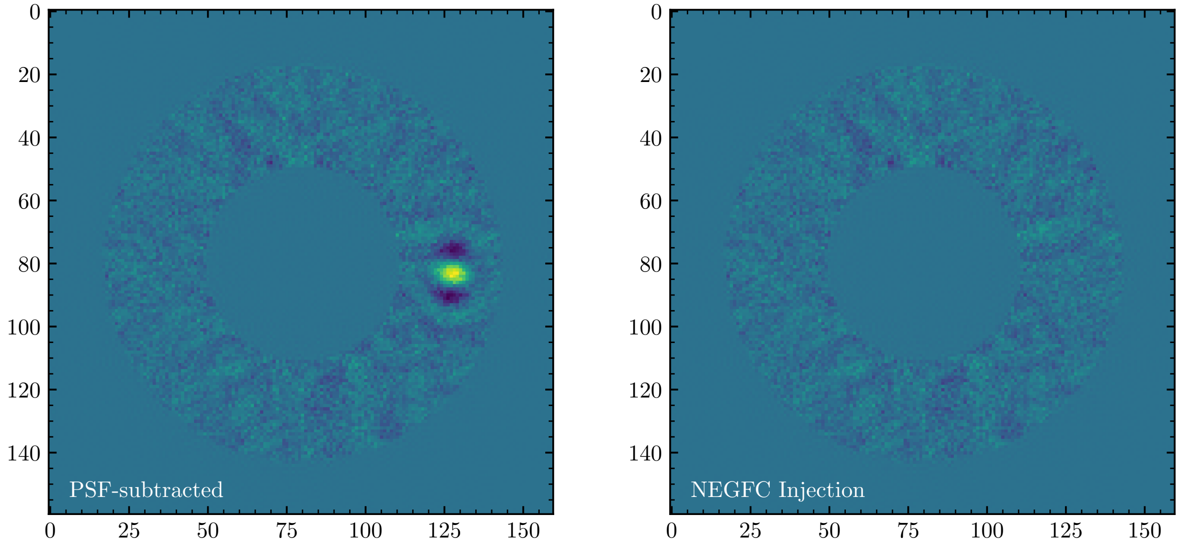

Figure 5.4 PSF-subtracted image (left) and the resulting image after NEGFC injection (right).

Specifically, using , we find that setting a threshold of 0.3 FWHM, or $\delta > 0.3\lambda/D$, where λ is the observing wavelength and D is the diameter of the telescope's primary mirror, best ensure that the companion is not inadvertently subtracted during the image processing. We also tune the optimal number of components that would optimize the SNR by running PSF subtractions from 1 to 30 number of components, measuring the resultant companion SNR each time in the reduced images. SNR is determined using the method outlined in Mawet et al. (2014), which incorporates a penalty for small separations to account for the limited number of resolution elements. We found that the highest SNR is produced by using a number of component of 9. Finally, we achieved a detection of the companion with a signal-to-noise ratios (SNR) of 12.5 using annular PCA reductions. Figure 5.2 shows the detection as a result of Annular PSF-subtraction of a strong point source, which we refer to as HD 63754 B, 47.2 pixel (6.0 FWHM radius) or $0\farcs471$ from the star. We correct for the position angle θ_{meas} through

$$\theta = \theta_{\mathrm{meas}} - \mathrm{PARANG} - \mathrm{ROTPOSN} + \mathrm{INSTANGL} - \theta_{\mathrm{north}} \tag{5.1}$$

where PARANG is the parallactic angle offset, ROTPOSN is the rotator position of $4\overset{\circ}{.}43$, INSTANGL is the NIRC2 position angle zero-point of $0\overset{\circ}{.}7$, and $\theta_{\mathrm{north}} = 0\overset{\circ}{.}262 \pm 0\overset{\circ}{.}020$ (Service et al., 2016) is the angle we applied to rotate the frames counterclockwise in order for them to have a North-up and East-left orientation. We measure a corrected position angle of $97\overset{\circ}{.}89$ south-west from the primary star. HD 63754 B is the only object identified by NIRC2 within $1''$. We visually inspect the Standardized Trajectory Intensity Map (STIM; Pairet et al. (2019)), which did not show any presence of other signals.

The negative fake companion (NEGFC) technique (Marois et al., 2010; Lagrange et al., 2010; Wertz et al., 2017) is often used in conjunction with principal component analysis (PCA) or other PSF subtraction methods to accurately extract the position and flux of point-like sources, particularly for faint companions close to bright stars. The NEGFC technique can be combined with other PSF subtraction techniques to further reduce residual speckle noise or other systematic biases in astrometry. This is because standard PSF subtraction methods like reference star differential imaging (RDI) or ADI can leave behind residual speckles or other systematic artifacts that can bias the extracted photometry of the companion. The NEGFC technique works by injecting a negative-amplitude PSF template at the location of the companion, effectively removing the signal from the true companion in the final image. This allows for a more accurate measurement of the true companion flux and position. NEGFC has been shown to be more effective

Table 5.2 Keck/NIRC2 relative astrometry and L'-band photometric measurements of the HD 63754 AB system

HD 63754 AB	
Instrument	Keck/NIRC2
Filter	L'
Date (UT)	2023-01-11
Epoch (Jyr)	2023.03
Relative Astrometry	
Separation (mas)	471 ± 10
PA (°)	97.9 ± 2.0
Photometry	
$\Delta L'$ (mag)	9.78 ± 0.06
L'_* Flux (mag)	5.11 ± 0.05
L'_p Flux (mag)	14.89 ± 0.06

Note: We chose PA uncertainty to match the smaller uncertainty in separation. The L' magnitude for the host star is transformed from the H band using Bessell & Brett (1988).

for faint companions closer to the primary star, which can be easily affected by residual speckles or other systematic artifacts. We show the PSF-subtracted signal alongside the result after NEGFC injection in Figure 5.4.

Using 's NEGFC, we take the astrometric and photometric measurements form annular PCA to inform the iterative MCMC calculations. First, we utilize the Nelder-Mead simplex optimization algorithm (Nelder & Mead, 1965) to provide the initial guesses that would be used as a starting state in MCMC optimization, which minimizes the sum of the χ^2 residuals within a 1.5 FWHM aperture. Next, we explore the 3D parameter space of the flux within the aperture and polar positions using the emcee affine-invariant Markov Chain Monte Carlo (MCMC) ensemble sampler introduced by Foreman-Mackey et al. (2013). We run 100 walkers, each taking 1000 steps, resulting in a total of 10^5 steps. We use the auto-correlation time based criterion $N/\tau \geq a_c$ with $a_c = 50$ (Christiaens et al.,

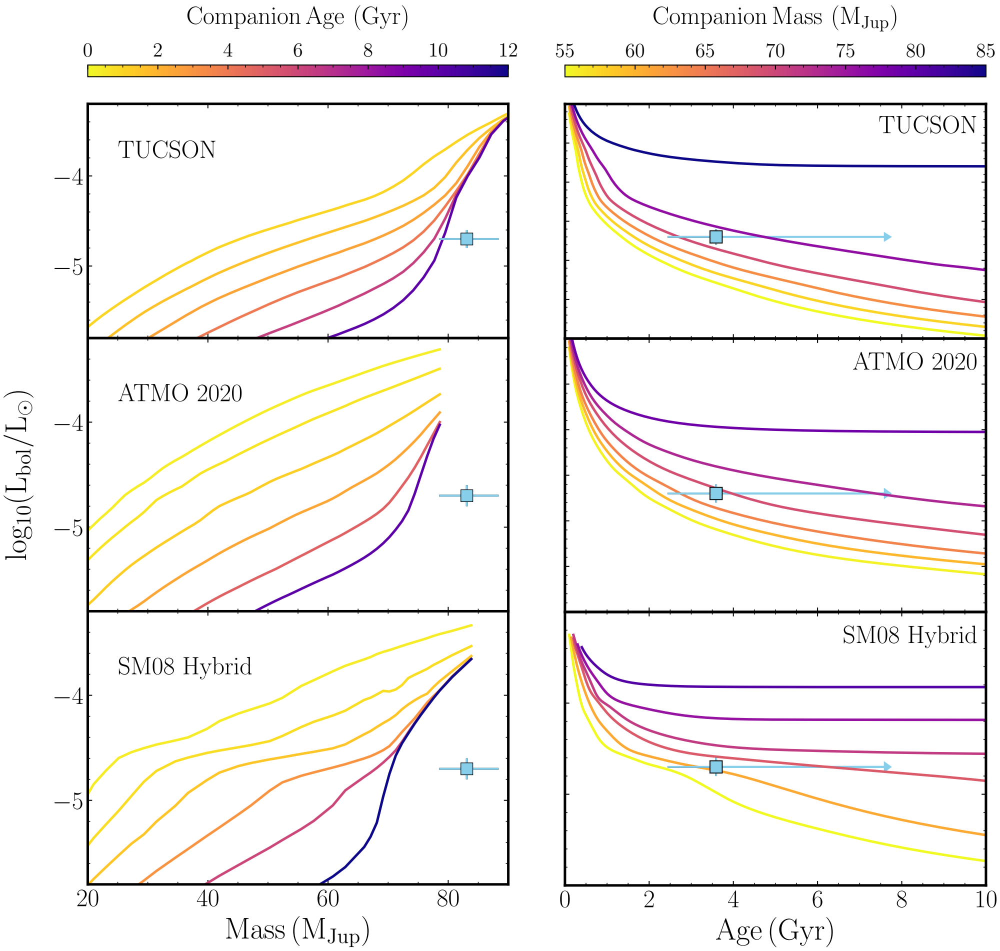

Figure 5.5 Comparison of the dynamical mass, luminosity and age of HD 63754 B with the predicted masses ages from three evolutionary models.

2021) to evaluate convergence. To ensure reliable results, we discard the first 30% of each chain as burn-in. We ran the fit multiple times to ensure consistent and identical astrometry and photometry results for each run, which are listed in Table 5.2. We further correct for throughput and the ratio of exposure times between stellar PSF frames (100 coadds with 0.008 integration time per coadd) and the science frames that contain the companion (90 coadds and 0.3s exposures).

We used a similar method as discussed in Li et al. (2023) to obtain the thermal infrared

L’-band magnitude for HD 63754 B. Since we only have a single measurement and no multi-band data, we are unable to extract a spectrum for the companion. Therefore, our measurement only provides the L’ band flux. The L’ band magnitude can be derived from the WISE W1 band due to a substantial overlap in their central wavelengths. This overlap is significant because both the star and the companion have temperatures that fall within the Rayleigh-Jeans tail. As a consequence, the magnitudes of the star in the W1 and L’ bands are nearly identical. We derive a contrast between the star and the companion in the L’ band of 9.79 ± 0.06 mag. Since the L’ mag of the star is 5.109 mag, the L’ mag for the HD 63754 B is thus L'_p= 14.89 ± 0.06 mag, which corresponds to an absolute brightness of $L'_p = 11.39 \pm 0.06$ mag. This lead to an absolute magnitude in the W1 band of M_{w1}=12.20 ± 0.07 mag according to the relation derived by Franson et al. (2023). To obtain the bolometric absolute magnitude, we convert the absolute magnitude in the W1 band by employing a fitting procedure. Specifically, we fit a fourth order polynomial to a segment of Filippazzo et al. (2015) spectral energy distribution (SED) for field dwarfs spanning the transition from L dwarfs to T dwarfs. Our fitting procedure yielded a reduced χ^2 value of 1, indicating a good fit to the data. By considering the uncertainties from both the fitting procedure and the transformation described in Franson et al. (2023), we calculated the final uncertainty for the bolometric luminosity. Our analysis resulted in a bolometric luminosity of $\log(\mathrm{L}_{\mathrm{bol}}/L) = -4.55 \pm 0.8$ dex. Error propagation was performed to incorporate the uncertainties in both the W1 magnitude and parallax.

Table 5.3 HGCA absolute astrometry for HD 63754 A.

Parameter	Hipparcos	Hipparcos-Gaia	Gaia EDR3
$\mu_{\alpha*}$ ($\mathrm{mas\,yr^{-1}}$)	-35.748 ± 0.492	-33.565 ± 0.016	-33.726 ± 0.025
μ_{δ} ($\mathrm{mas\,yr^{-1}}$)	-129.582 ± 0.386	-127.543 ± 0.013	-125.768 ± 0.025
$\mathrm{corr}(\mu_{\alpha*}, \mu_{\delta})$	0.237	0.177	-0.086
t_α (Jyr)	1991.33	–	2015.87
t_δ (Jyr)	1991.48	–	2015.85

Note: The χ^2 value for a model of constant proper motion (Hipparcos-Gaia and Gaia proper motions are equal) is 4056 with two degrees of freedom.

5.3.2 Absolute Astrometry

The absolute astrometry is taken from the Gaia EDR3 version of the Hipparcos-Gaia Catalog of Accelerations (HGCA, Brandt et al. (2021f)). The HGCA is cross-calibrated between the Hipparcos and Gaia EDR3 catalogues relative to a common reference frame, so that the uncertainties are calibrated. The HGCA compares the discrepancy bewteen the 25-year Hipparcos-Gaia scaled positional difference and Hipparcos proper motion (near 1991.25) and Gaia EDR3 proper motion (near 2016.0), respectively to disentangle the curvature of the reflex motion of stars relative to the star-companion barycenter.

HD 63754 was observed as part of our survey program on Keck/NIRC2 aimed to discover more substellar companions around accelerating stars. The primary star HD 63754 A was selected for the program as it experiences a strongly significant proper-motion differences of 64σ in the HGCA, suggesting a massive companion pulls on the primary star and causes the observed acceleration. Table 5.3 shows HD 63754 A's absolute astrometry from the HGCA, including the Hipparcos proper motion, the Gaia DR3 proper motion, and a joint Hipparcos-Gaia positional difference divided by the temporal baseline between the two missions. The Renormalized Unit Weight Error (RUWE) metric is used to assess

Table 5.4 Inferred parameters from substellar evolutionary models vs. measured parameters for the companion.

Property	**TUCSON**	**ATMO2020**	**SM08 Hybrid**	Measurement
Mass ($M_{\rm Jup}$)	$75.0^{+5.3}_{-3.0}\,(1.5\sigma)$	$69.8^{+5.6}_{-3.3}\,(2.2\sigma)$	$66.1^{+8.1}_{-3.2}\,(2.7\sigma)$	$80.1^{+6.6}_{-6.1}$
Age (Gyr)	$\geq 4.62\,(0.6\sigma)$	$\geq 5.62\,(0.5\sigma)$	$\geq 5.40(0.5\sigma)$	≥ 3.4
$\log(L_{\rm bol}/L_\odot)$	$-4.00^{+0.20}_{-0.08}\,(0.56\sigma)$	$-4.32^{+0.15}_{-0.08}\,(0.92\sigma)$	$-4.55^{+0.07}_{-0.08}\,(0.96\sigma)$	-4.55 ± 0.08
$T_{\rm eff}$ (K)	1381 ± 173	1413 ± 177	1344 ± 71	–
$\log(g)$ (cm s^{-2})	5.30 ± 0.20	5.43 ± 0.20	5.34 ± 0.06	–
Radius ($R_{\rm Jup}$)	0.90 ± 0.21	0.86 ± 0.20	0.95 ± 0.05	–

NOTE: Masses are computed using the measured $\log(L_{\rm bol})$ and age; $\log(L_{\rm bol})$ from measured mass and age; age from measured mass and $\log(L_{\rm bol})$. Model-derived radii use the measured age and mass; $T_{\rm eff}$ and log g use model radii and measured mass.

the quality of astrometric solutions provided by Gaia, with values close to 1 indicating a good fit between the observations and the expected behavior of a single star. The RUWE for HD 63754 in Gaia is 1.02 (Gaia Collaboration, 2020), well below the threshold of 1.4 at which the Gaia pipeline attempts a non-single star solution. This indicates that the Gaia observations for HD 63754 are consistent with a satisfactory single-star solution.

5.3.3 Radial Velocity

The RV of the system is monitored by both HARPS and HIRES. The HARPS and HIRES radial velocity data does not cover the full orbital period, but suggests a shallow trend for HD 63754 A, indicating the subtle presence of a companion. The HIRES RVs are from two separate instruments and jointly have an rms value of 26.32 m/s and a median uncertainty on each individual measurement of 1.87 m/s. The HARPPS RVs have an rms value of 12.97 m/s and a median uncertainty on each individual measurement of 1.459 m/s. We fetch the data from the HAPRS catalog's “DRVmlcnzp" column, which correct for zero-point variations, intra-night RV drift, and an offset in the absolute RV that arose from the upgrade of the HARPS fibers in 2015.

5.4 Orbital Constraints

We utilized the freely available Bayesian orbit fitting code `orvara` (Brandt et al. 2021) to infer the mass and orbital parameters of HD 63754 B. This was accomplished by combining HGCA proper motion anomalies, HIRES and HARPS RVs, and our single-epoch relative astrometry from Keck/NIRC2 L' band imaging. The `orvara` code employs parallel tempering MCMC (PT-MCMC) with the `emcee` ensemble sampler to sample orbital parameter posteriors. PT-MCMC involves running parallel chains at different temperatures, allowing for accurate sampling near the minimum χ^2 and exploration of the entire parameter space. The chains periodically swap positions to exchange information and improve sampling efficiency. Our PT-MCMC process utilized 100 walkers, 30 temperatures, and a total of 10^5 steps. To obtain a representative sample from the posterior distribution for inference, we saved only the coldest chain and discarded the others. The lowest-temperature chain explores the parameter space more thoroughly and converges to the target distribution. `orvara` fits for six orbital elements that fully describe a Keplerian orbit, including three elements that describe the orbital plane: the semi-major axis (a), eccentricity (e), the longitude at the reference epoch of 2010.0 (λ_{ref}), and three elements that describe the orbital plane orientation relative to the sky plane: inclination (i), argument of periastron (ω), and longitude of ascending node (Ω). In addition to the

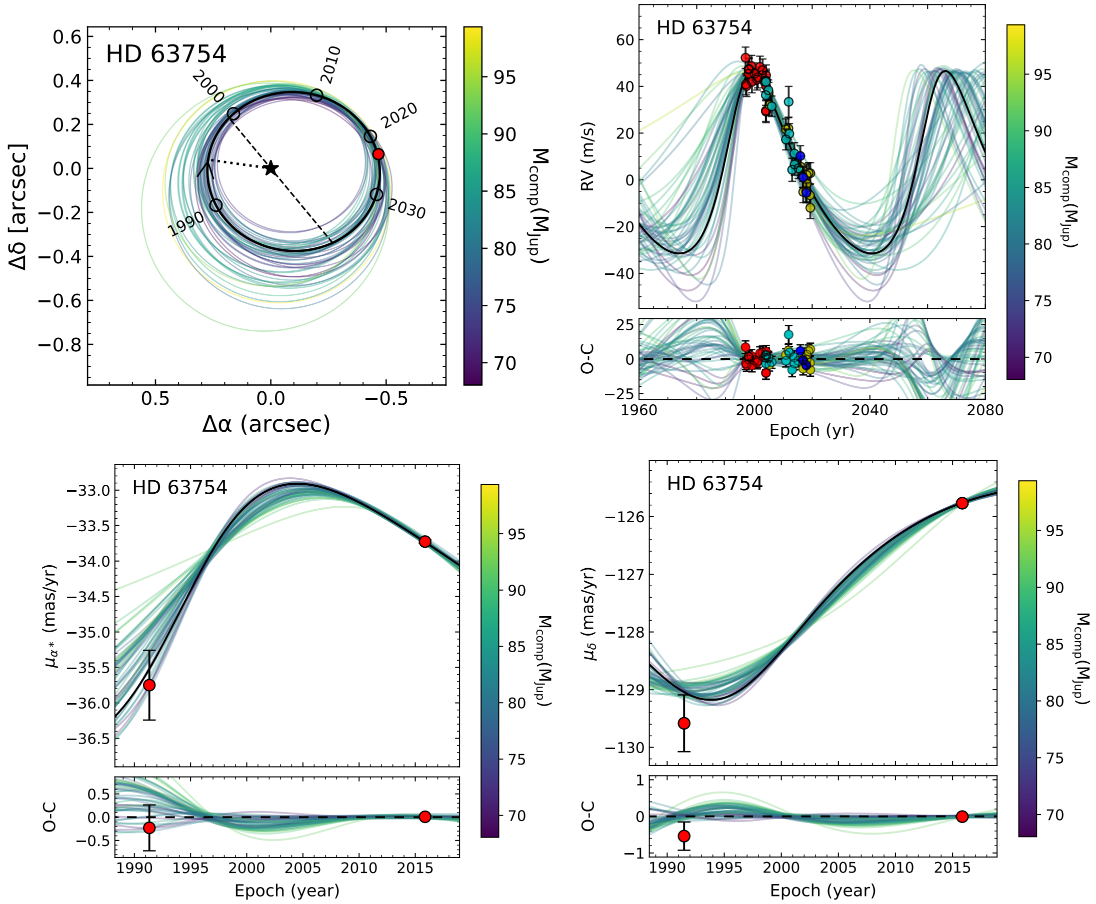

Figure 5.6 Joint orbit fit for HD 63754 B, including sky-projected orbit (top left), radial velocities (top right), and HGCA proper motions (bottom panels). The colorful curves represent 50 randomly drawn orbits from the MCMC chains, while the maximum-likelihood orbit is highlighted in black. The points in the proper motion plots represent the joint proper motion derived form the difference in sky position between Hipparcos and Gaia EDR3. This average proper motion captures the reflex motion over the entire 25-year period between the missions.

six orbital elements, `orvara` incorporates an RV jitter term for all input RV instruments, and estimates the masses of the primary and secondary bodies by leveraging RV and Astrometry data to determine the optimal fitting solution. The code analytically eliminate the influence of several auxiliary parameters like instrumental RV zero-points, parallax and barycenteric proper motion to speed up the fitting process.

We impose an informative broad prior of $1.35 \pm 0.15M$ on the mass of HD 63754 A, covering the range of literature measurements as discussed in Section 5.1. We apply uninformative priors on all other fitted parameters: flat priors on the eccentricity, argument of periastron, mean longitude, and ascending node, and log-flat priors on the mass of the companion, semi-major axis and RV jitter, and geometric priors on the inclination to ensure that each dimension is sampled uniformly. To check convergence, we visually inspect the chains and discard the initial 40% as burn-in. We confirm that further adjustments to the burn-in threshold beyond 40% have negligible impact on the resulting posteriors and consistently produce the same inferred parameters. Using the wide priors, we obtain a dynamical mass of $81.7^{+6.6}_{-6.0}M_{\rm Jup}$, a semi-major axis of $20^{+2.8}_{-1.8}$ AU, an eccentricity of $0.238^{+0.066}_{-0.066}$, and an almost face-on inclination of $175^{\circ}\!.07^{+0.43}_{-0.47}$. Due to the uncertainty associated with the host star's mass, in addition to the broad prior, we also test a narrow prior of $1.35 \pm 0.05M$. With the narrow prior, we measure a dynamical mass of $79.7^{+4.5}_{-3.3}M_{\rm Jup}$, a semi-major axis of $20^{+3.1}_{-1.8}$ AU, an eccentricity of $0.247^{+0.060}_{-0.058}$, and an inclination of $175^{\circ}\!.08^{+0.44}_{-0.46}$. We notice a small positive correlation in the posterior distribution between the mass of the host star and the mass of its companion.

Table 5.5 MCMC orbital fit results for HD 176535 AB.

Parameter	**Prior**	**Best Fit**	**68.3% CI**	**95.4% CI**
Fitted Parameters				
$\sigma_{\mathrm{Jit}}\,(\mathrm{m/s})$	$1/\sigma_{Jit}$	3.83	$0.026^{+7.6}_{-0.026}$	(3.412, 5.801)
$\mathrm{M}_*\,(M)$	$N(0.72, 0.02)$	0.728	$1.25^{+0.52}_{-0.55}$	((1.128, 1.693)
$\mathrm{M}_{\mathrm{p}}\,(M)$	$1/M_p$	65.9	$81.7^{+6.6}_{-6.0}$	(70.163, 95.961)
$a\,(\mathrm{AU})$	1/a	11.05	$20.0^{+2.8}_{-1.8}$	(17.081, 28.067)
$\sqrt{e}\sin\omega$	$U(-1, 1)$	-0.373	$-0.17^{+0.34}_{-0.23}$	(-0.526, 0.48)
$\sqrt{e}\cos\omega$	$U(-1, 1)$	0.597	$0.388^{+0.088}_{-0.12}$	(0.126, 0.543)
$i\,(^\circ)$	$\sin i$	49.8	$175.07^{+0.43}_{-0.47}$	(174.114, 175.918)
$\Omega\,(^\circ)$	$U(-180, 180)$	129.51	$42.7^{+8.1}_{-7.0}$	(29.313, 60.37)
$\lambda_{\mathrm{ref}}\,(^\circ)$	$U(-180, 180)$	-176.9	$45.8^{+11}_{-8.6}$	(30.016, 70.157)
Derived Parameters				
$\varpi\,(\mathrm{mas})$	–	27.0326	$19.9320^{+0.0013}_{-0.0014}$	(19.929, 19.935)
$P\,(\mathrm{yr})$	–	41.3	74^{+17}_{-10}	(57.472, 124.536)
$\omega\,(^\circ)$	–	328.0	312^{+30}_{-286}	(3.372, 356.862)
e	–	0.496	$0.238^{+0.066}_{-0.067}$	(0.106, 0.374)
$a\,(\mathrm{mas})$	–	299	400^{+55}_{-35}	(340.462, 559.407)
T_0	–	2468925	2476916^{+7784}_{-4625}	(2469000, 2497100)

NOTE: The reference epoch is 2455197.5 JD.

Results of our MCMC posteriors from the orbital fit are listed in Table 5.5. We show several visualization plots for different aspects of the orbits in Figure 5.10. The single-epoch relative astrometry, HGCA proper motions, and RVs effectively distinguish between different posterior orbits sampled from the posterior distribution, allowing the best fit solution for the fit to be determined, which is represented by the black curve among the colorful randomly sampled orbits. The Hipparcos and Gaia instantaneous approximate proper motions are both good fits to the astrometric reflex motion of the star, with Gaia providing the more precise measurement of the two. Both the HARPS/HIRES joint RVs and our single-point astrometry only cover a fraction of the orbit near aphelion, making the solution converge better near that part of the orbit. The uncertainty in the orbital fit is caused by a combination of factors, including the long period of the system, limited astrometry data, and the lack of full orbital phase coverage from the radial-velocity sampling. The single astrometric epoch results in a broad range of possible orbits due to the 6% uncertainty in the companion mass. However, continued direct imaging monitoring in the next few decades will provide an ideal opportunity to further narrow down the mass range and the relative orbit of the companion. No previous literature reports were available on the orbit of HD 63754 B. Our independent dynamical mass estimate of $81.7^{+6.6}_{-6.0} M_{\rm Jup}$ at the 68% confidence level cannot definitively classify it as either a brown dwarf or a low-mass star.

5.5 Discussion

5.5.1 Dynamical mass and orbit of HD 63754 B

The Hydrogen-Burning Limit (HBL) is the minimum mass required for nuclear fusion in a star's core and distinguishes brown dwarfs from low-mass stars. The precise value, generally ranging from 70-80 M_{Jup}, depends on several factors such as the equation of state, rotation, composition, and atmospheric properties (Burrows et al., 1997). If adopting $75 M_{\mathrm{Jup}}$ as the HBL, 14.38% of the dynamical mass posterior distribution fall below the HBL, and 85.62% are above this value. If we instead adopt Chabrier & Johansson (2023)'s new estimate for the HBL of $78.5 M_{\mathrm{Jup}}$ which accounts for previously neglected physical effects in its estimation, then 30.57% of the posterior lie within the substellar boundary. Alternatively, using the dynamical mass posterior from the narrow prior, we obtain percentages of 11.41% and 37.92% for HBL of 75 and 78.5 M_{Jup}, respectively.

Our orbit results also suggest that HD 63754 B has an inclination of ~ 180 degrees, which means the orbital orientation of the system is nearly face on. RV and transit methods are biased toward detecting companions with orbits that are edge-on to our line of sight. Systems with face-on inclinations are rare and have orbital planes nearly aligned with our line of sight, resulting in minimal or no detectable RV variations or transits. Consequently, systems with face-on inclinations require alternative techniques, such as direct imaging or astrometry, to be detected and characterized. Face-on orbits are geometrically unlikely, therefore, HD 63754 B is a case where more future direct imaging will be able to accurately determine its real orbit.

5.5.2 Evolutionary Model Comparison

Our empirical determination of the dynamical mass of HD 63754 B, which is independent of any model assumptions, enables us to compare it directly with predicted masses from substellar evolutionary models. We considered several substellar cooling model grids covering a range of ages and luminosities. Specifically, we included the cloudless (Burrows et al., 1997) and ATMO-2020 (Phillips et al., 2020a) models, and the Saumon & Marley (2008) hybrid model with three cloud prescriptions (no clouds, hybrid, and cloudy).

We employ a method outlined in Li et al. (2023) to estimate the inferred masses of the companion based on its luminosity and age for each evolutionary model. We adopt a companion age of $\geq$3.4 Gyr and luminosity of $\log(\mathrm{L}_{\mathrm{bol}}/L)$=-4.67 dex as previously derived in the paper. Briefly, we use an importance sampling approach to calculate inferred masses for each evolutionary model by taking random samples from the distributions of bolometric luminosity and age. Then, we linearly interpolate the model grid to determine the companion's mass corresponding to the given age and luminosity value. We repeat the process to build a model-derived mass distribution from each model. The inferred mass distributions for the three evolutionary grids are depicted in Figure 5.7, along with our measured dynamical mass distribution of HD 63754 B from the orbital fit.

To quantify the difference between the model-independent dynamical mass and model-inferred masses, we utilize the approach described by Li et al. (2023) and Franson et al.

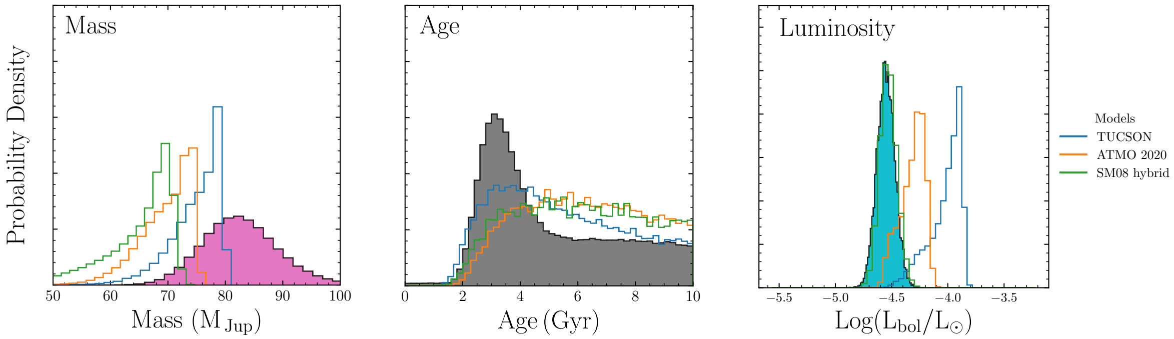

Figure 5.7 Comparison between predicted masses and ages from evolutionary models and the dynamical mass and age of HD 63754 B. (Left) Posterior distribution of dynamical mass (filled magenta histogram) compared to model-derived mass posteriors for specific Lbol and host star ages. Gaussian priors are applied to the mass inferred from MCMC posteriors (magenta histogram). (Right) Posterior distribution of age sampled with evolutionary models. The filled grey distribution represents the posterior from our Bayesian isochrone age-dating model. Considering the uncertainty in the upper bound of our age distribution, we utilize an uninformative flat prior on age to obtain posterior distributions for the evolutionary models (green, orange, and skyblue). Without prior age information, all models converge towards moderate to older ages for the system.

(2023) that involves computing the probability $\mathrm{P}(\mathrm{M}_{\mathrm{model-inferred}} > \mathrm{M}_{\mathrm{empirical}})$, which represents the percentage or likelihood of the inferred mass distribution function being larger than the dynamical mass distribution. This discrepancy in model-dependent and -independent masses can be converted to a one-sided Gaussian-equivalent standard deviation, via the special error function:

$$\sigma = \sqrt{2}\mathrm{erf}^{-1}(1 - 2\mathrm{P}(\mathrm{M}_{\mathrm{model-inferred}} > \mathrm{M}_{\mathrm{empirical}})) \tag{5.2}$$

The model inferred masses and their discrepancy with the measured dynamical mass are $75.0^{+5.3}_{-3.0} M_{\mathrm{Jup}}$ (1.5 σ), $69.8^{+5.6}_{-3.3} M_{\mathrm{Jup}}$ (2.2 σ) and $66.2^{+8.1}_{-3.2} M_{\mathrm{Jup}}$ (2.7 σ) for the TUCSON, the ATMO 2020 and the SM08 hybrid models respectively.

Figure 5.5 showcases this benchmark object against the predicted masses and ages from three evolutionary models. Figure 5.8 shows all the benchmark brown dwarfs dis-

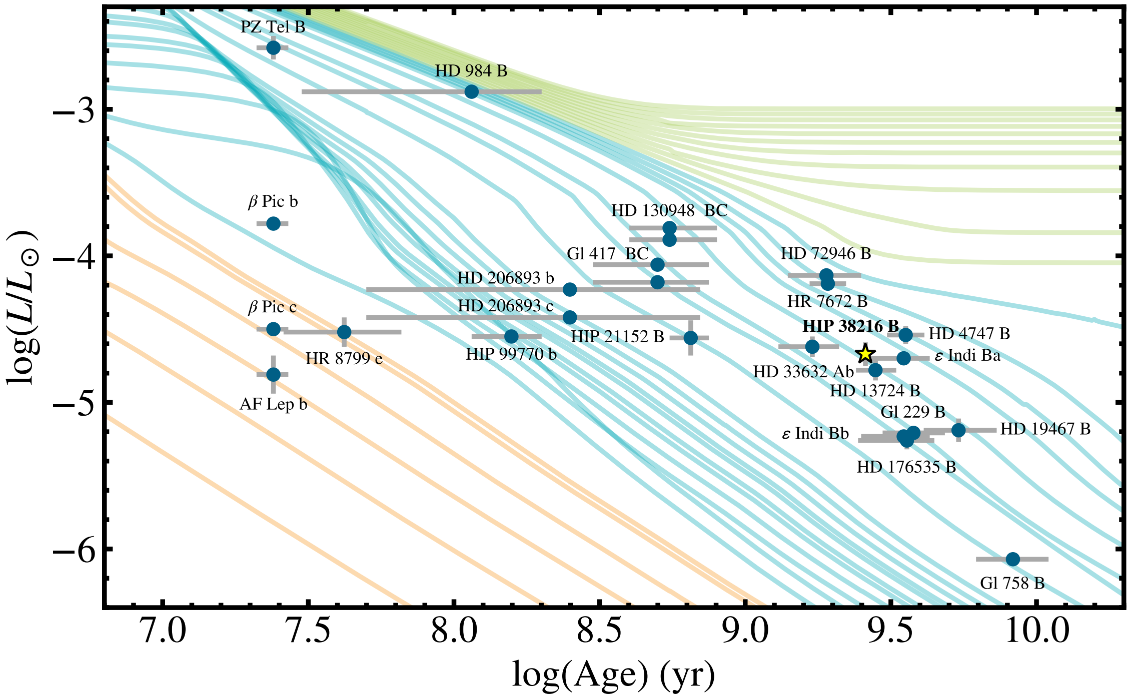

Figure 5.8 The accompanying background models depict the luminosity evolution of planets (orange), brown dwarfs (blue), and low-mass stars (green) across various mass ranges, as elucidated by Burrows et al. (1997). Our benchmark object, HD 63754 B (highlighted by the yellow star), occupies a position at the boundary between substellar and stellar objects, representing one of the few objects found in this particular regime. Luminosity and age data for the majority of systems are derived from the meticulous study conducted by Franson & Bowler (2023).

covered so far. Among the various models considered, we find that the dynamical mass of the object is consistent within 3 σ with all three models. The TUCSON model demonstrates the closest agreement with the true mass of the companion, with the inferred mass falling within 1.5 standard deviations. All three models consistently indicate lower masses compared to our measured value for HD 63754 B, suggesting that the companion is over-massive given its age and luminosity. This discrepancy highlights the need for further investigation to understand the underlying nature of this object. We can also explore the ages predicted by evolutionary models based on the companion's luminosity and dynamical mass, and compare the model-inferred ages with our isochrone age for the system. Considering HD 63754 B's dynamical mass of $80.1^{+6.6}_{-6.1} M_{\mathrm{Jup}}$, all three models consistently agree with the age of the system within 1σ.

The high-mass origin of the companion currently remains uncertain until additional data is obtained. We offer three possibilities to explain this uncertainty. One possibility is that the data itself is inaccurate, leading to an inaccurate determination of the companion's mass. For instance, it is conceivable that the Gaia data may not be adequately modeled by `orvara`, introducing potential discrepancies. Another possibility is that the evolutionary models used to interpret the data are biased in the fundamental physics, which would be highly unexpected. A third possibility is that the companion itself is a binary system, with a companion of planetary mass. This scenario suggests the presence of an additional object in the system, contributing to the observed characteristics. To test these possibilities, we can compare the `orvara` results with future Gaia data releases to better understand the systematics in the `orvara` modeling approaches. If the substellar cooling models are indeed flawed, this might involve exploring alternative modeling approaches to accurately explain the observed data. Finally, in the case of a companion binary system, we can investigate for signs of binarity using various techniques, such as high-resolution imaging or spectroscopic observations, to detect potential companions orbiting the primary companion.

5.5.3 Future Work and Gaia DR4 Predictions

`orvara`'s approximation of the proper motions is robust. However, it does have certain limitations when dealing with massive companions that exhibit significant differences in proper motion within the HGCA, such as HD 63754 B. While the scaled positional difference or proper motion between Hipparcos and Gaia proves effective in separating the curvature of the stellar reflex motion caused by massive companions, there is a potential bias in the fit convergence due to the exceptionally precise Gaia DR3 data point at 2016.0, particularly considering the high uncertainty in the Hipparcos proper motion. In such cases, relying on a single Gaia data point is insufficient, and the comprehensive astrometry data from Gaia DR4, encompassing multiple epochs and a longer temporal baseline, becomes necessary to accurately constrain the astrometric stellar reflex motion.

The epoch astrometry fitting code `htof` (Brandt et al., 2021d) is an open-source code to fit arbitrary high-order astrometric solutions to the underlying perturbation of absolute astrometry. `htof` fits the Hipparcos intermediate data and Gaia GOST-predicted

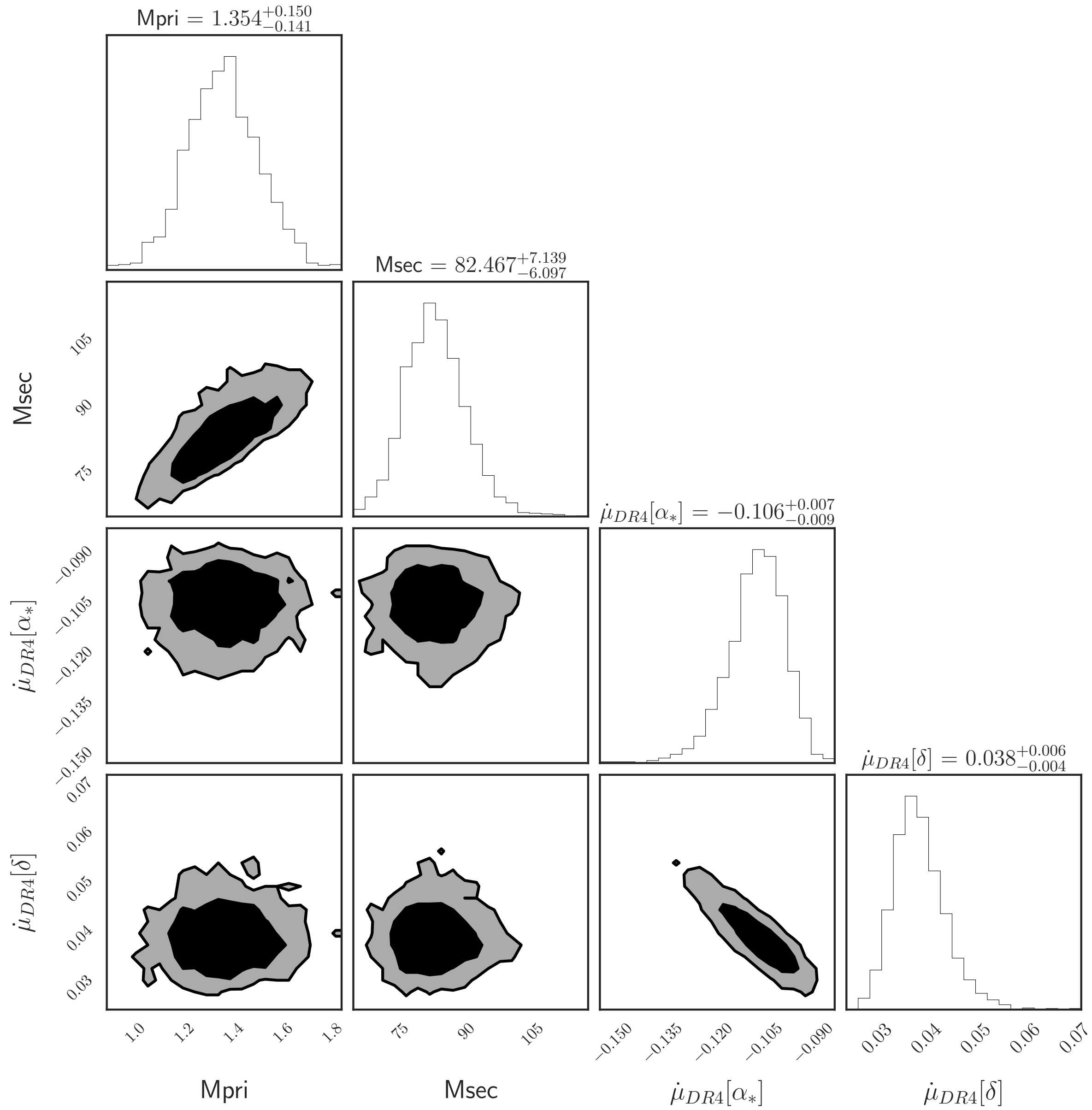

Figure 5.9 The corner plot showcases the mass distribution of the HD 63754 AB system and the predicted accelerations at the Gaia DR4 epoch.

scanning laws to recover the effects of unseen companions on the host star's single star five-parameter solution. `htof` is fully integrated in `orvara` to calculate Keplerian orbits of companions around stars by fitting epoch astrometry and forward models the astrometry within `orvara` to compare with the HGCA catalog values. We observed a very slight discrepancy in the mass of the companion when incorporating `htof`'s forward modeling, suggesting a possible divergence between `orvara`'s approximations of proper motions and a hypothetical fit to Gaia's future DR4 full epoch astrometry.

Here, we utilize a modified version of the Gaia epoch astrometry code, $htof$, to calculate the anticipated accelerations for HD 63754 B at the epoch corresponding to Gaia Data Release 4 (DR4). This adaptation allows us to estimate the expected accelerations of the companion based on the available astrometric data from the Gaia mission. From these predictions, we gain valuable insights into the motion and dynamics of HD 63754 B within the context of the Gaia DR4 epoch. We a corner plot to visualize the masses of the HD 63754 AB system along with the predicted accelerations at the Gaia DR4 epoch. The corner plot allows us to explore the joint distribution of these parameters and understand any correlations or relationships between them. The correlations between the accelerations and the masses are minimal, indicating Gaia DR4 may be only a limited help in refining HD 63754 B's mass and validating our measurement. Future data releases from Gaia, with extended temporal baselines, will extend the existing orbital coverage and provide more precise measurements of the companion's orbit.

5.6 Conclusion

In this study, we present an independent discovery of a companion located near the boundary between substellar and stellar objects. Our investigation includes a comprehensive analysis of its orbital dynamics and evolutionary characteristics. HD 63754 was specifically targeted in our ongoing program, called "Imaging Substellar Companions around Accelerating Stars," conducted at the Keck Observatory. This selection was driven by the significant acceleration exhibited by HD 63754, indicating the presence of an intriguing companion.

we conducted imaging observations on January 12th, 2023, utilizing the Keck Near-Infrared Camera 2 (NIRC2) equipped with a vector vortex coronagraph. By performing a joint orbital fit using the newly acquired single-epoch Keck/NIRC2 astrometry in combination with radial velocity measurements from HIRES and HARPS, we derived a dynamical mass for the companion, yielding a value of $79.7^{+4.5}_{-3.3} M_{\rm Jup}$. This dynamical mass significantly exceeds the model-inferred masses from substellar evolutionary models. This finding highlights the need for further investigations and refinements in our understanding of substellar objects and the comparison to observations. HD 63754 can also be a case of unresolved binary with a planetary mass companion. Future direct imaging, spectroscopic and epoch astrometry data will shed lights on its high-mass origin.

By examining the object's photometry, we determine that it resides on the L/T transition. By investigating its properties, we contribute to the broader understanding of the substellar-stellar boundary and shed light on the diverse nature of objects in this transitional regime. HGCA-based imaging surveys across the sky are revolutionary, and will continue to discover more faint companions with significant accelerations until the orbits for all the nearby brown dwarfs and giant exoplanets are fully characterized.

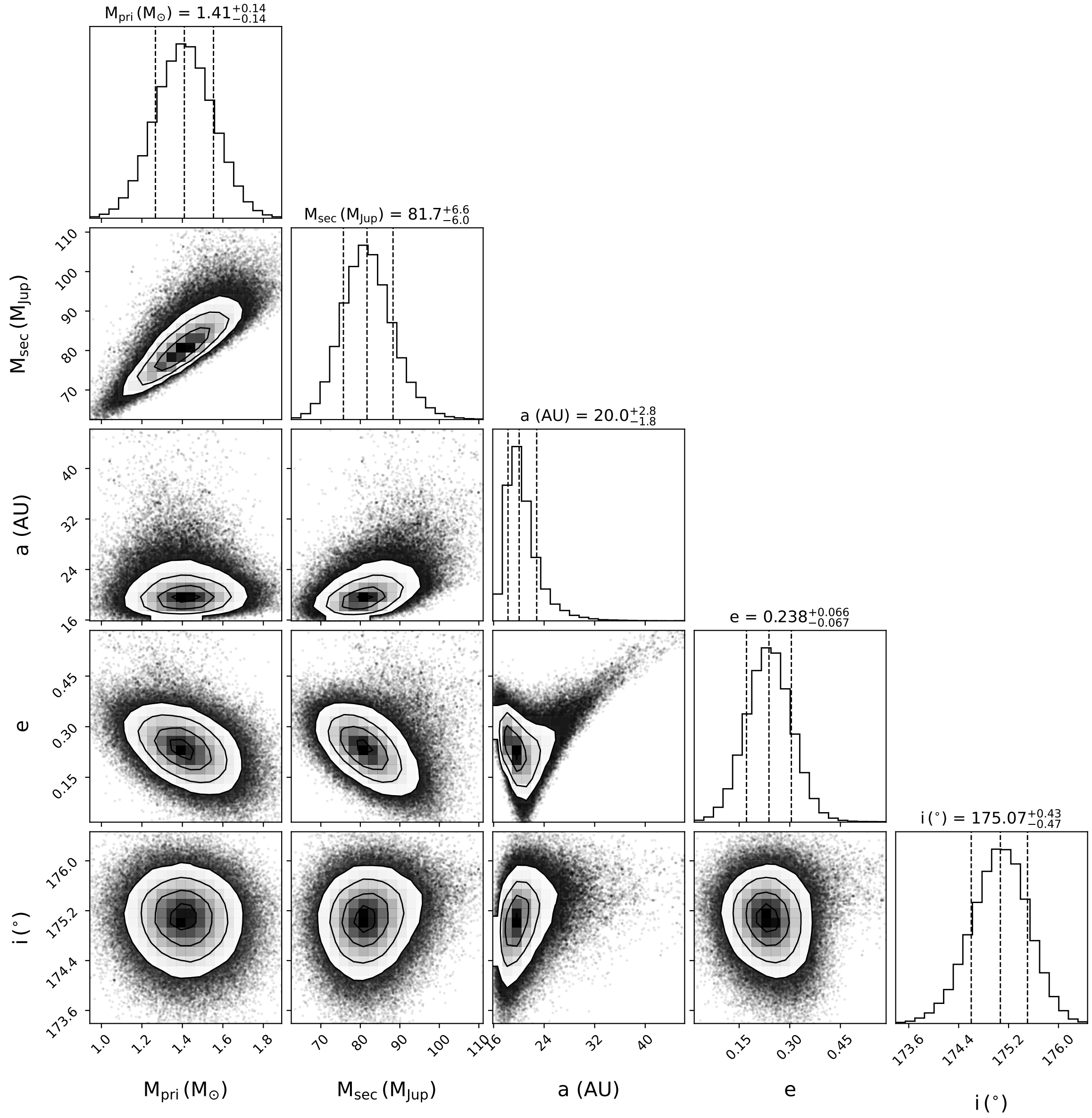

Figure 5.10 Posterior distributions using a wide Gaussian prior of $1.35\pm0.15M$ on the primary mass, both 1D and 2D, are presented for various orbital parameters of HD 63754 B. These distributions are derived from the analysis of radial velocity from HIRES and HARPS, relative astrometry obtained through Keck/NIRC2 direct imaging, and absolute astrometry from Hipparcos and Gaia data using `orvara` (Brandt et al., 2021f). The 1D posterior distributions are accompanied by confidence intervals at 15.85%, 50.0%, and 84.15%, with the median ± 1σ values indicated. Additionally, the 2D posterior distribution is visualized with contour levels corresponding to 1, 2, and 3σ.

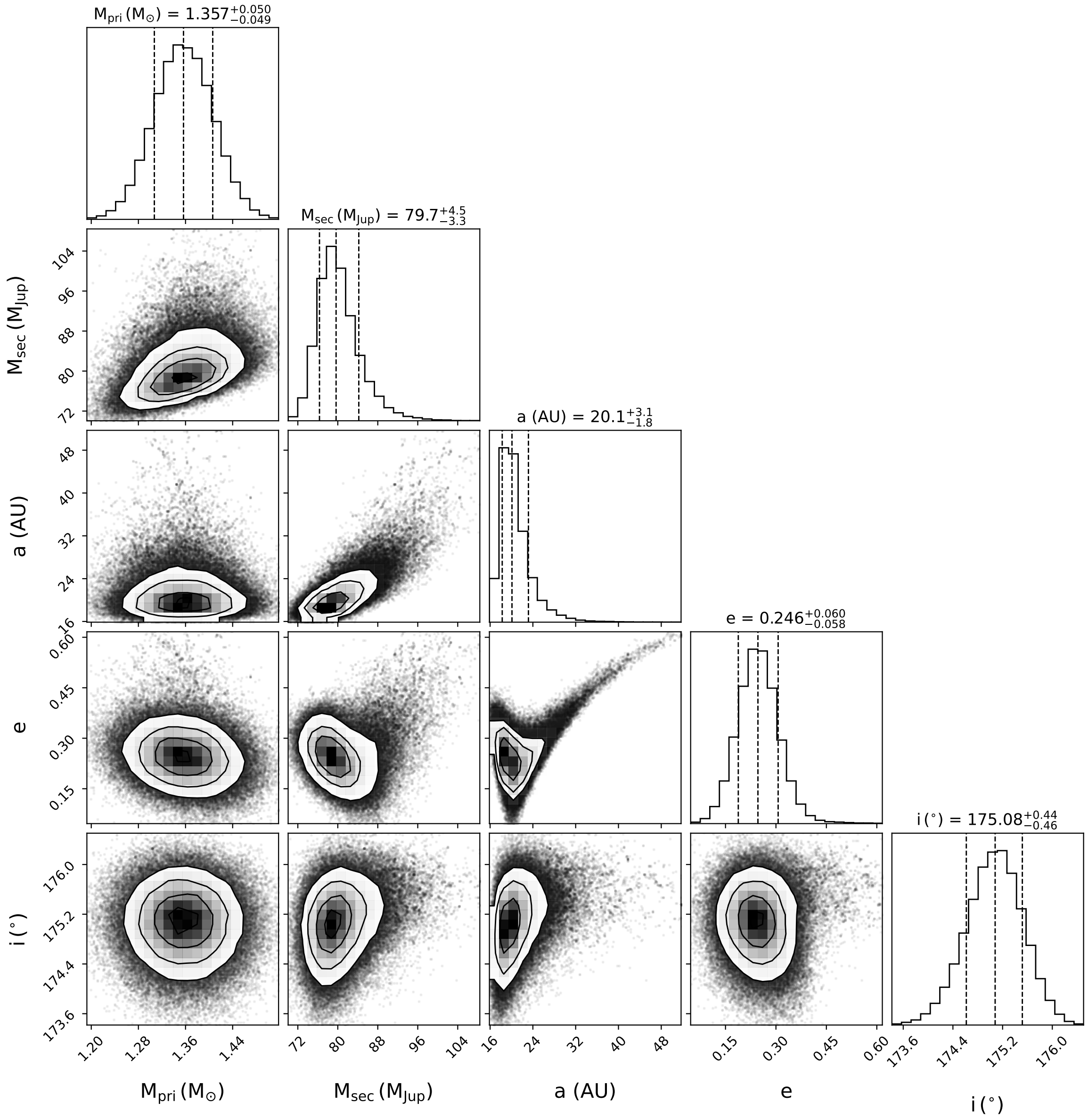

Figure 5.11 Posterior distributions for HD 63754 B using a narrow Gaussian prior of $1.35 \pm 0.05M$ on the primary mass in the `orvara` fit.

Appendix A

Appendix

Figures A1-A20 show the full results from the `orvara` orbital fits to the 11 companions (nine planets and brown dwarfs, plus two stellar companions) in nine systems. Figures A1-A9 show the radial velocity measurements and fitted orbits in the left panels, and the absolute astrometry in the right panels. Figures A10-A20 show corner plots of the astrophysically interesting parameters: masses, semimajor axis, and eccentricity, along with inclination.

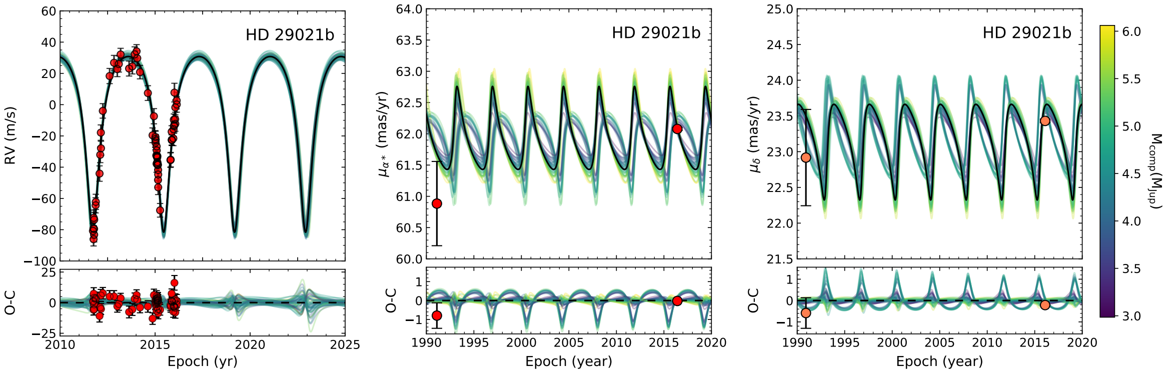

Figure A1 Left panel: Radial Velocity orbit for HD 29021 b. The RV data are from the OHP 1.93m SOPHIE spectrograph. Middle and right panels: astrometric acceleration in right ascension and declination. The red and orange points are proper motion measurements from *Hipparcos* near epoch 1991 and *Gaia* near epoch 2016. The thick black lines indicate the best-fit orbits in the MCMC chain while the colored lines are solutions randomly drawn from the chain, color-coded by the dynamical mass of the companion.

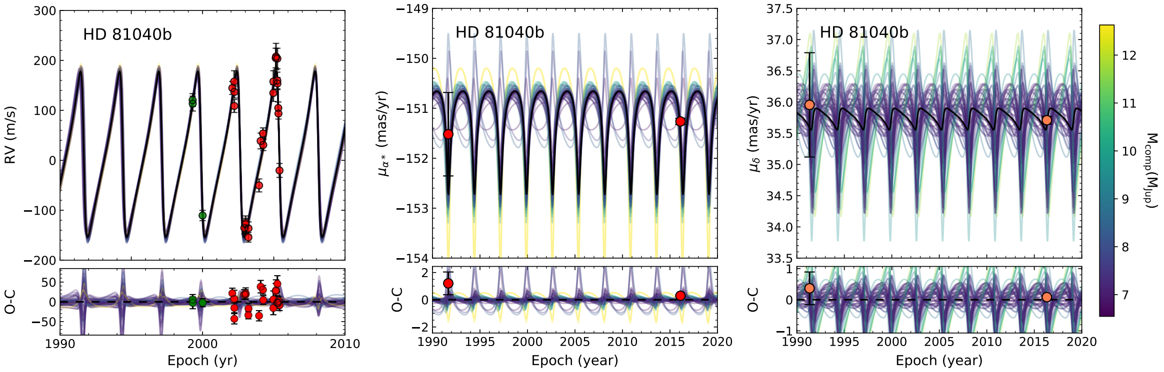

Figure A2 HD 81040 b. Same as Fig. A1. Data for RVs come from HIRES/Keck (green) and ELODIE (red).

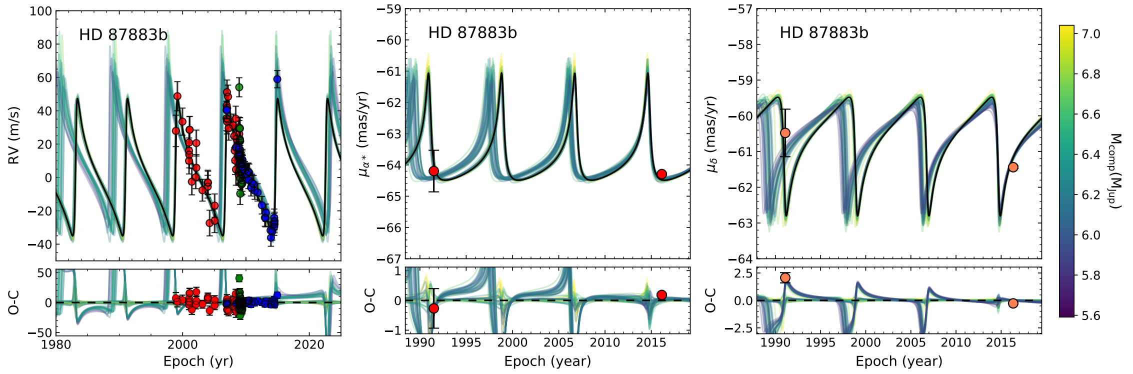

Figure A3 HD 87883 b. Same as Fig. A1. Red and blue points with error bars are RVs from Hamilton/Lick published in 2009 and 2017, respectively, and the green points are velocities from HIRES/Keck.

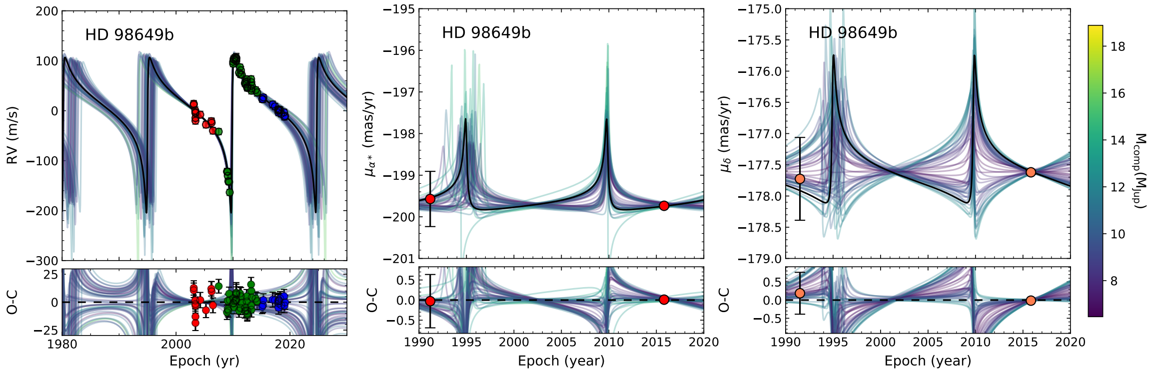

Figure A4 HD 98649 b. Same as Fig. A1. The red and green data points in the left panel are RVs from CORALIE-98 and CORALIE-07, respectively.

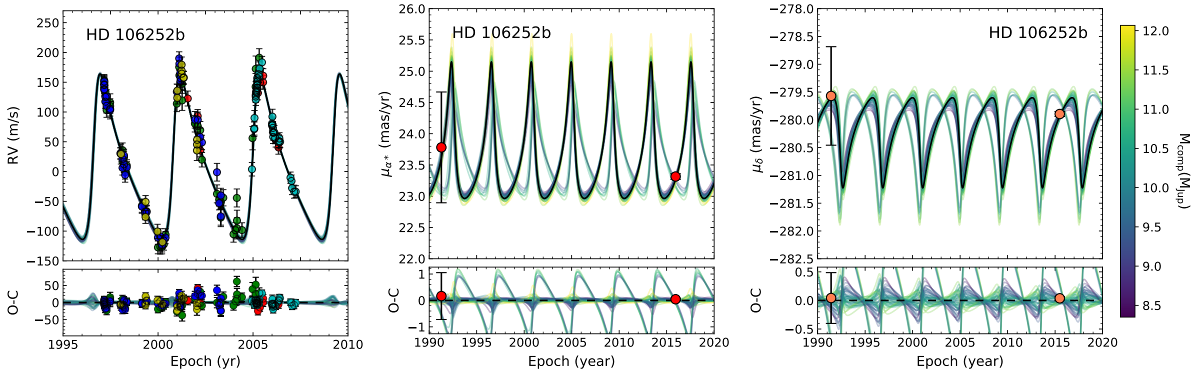

Figure A5 HD 106252 b. Same as Fig. A1. The solid circles and error bars in the left most panel represent RVs from ELODIE (blue), Hamilton/Keck (yellow and green), CDES-TS2 (red), and HRS/HET (cyan).

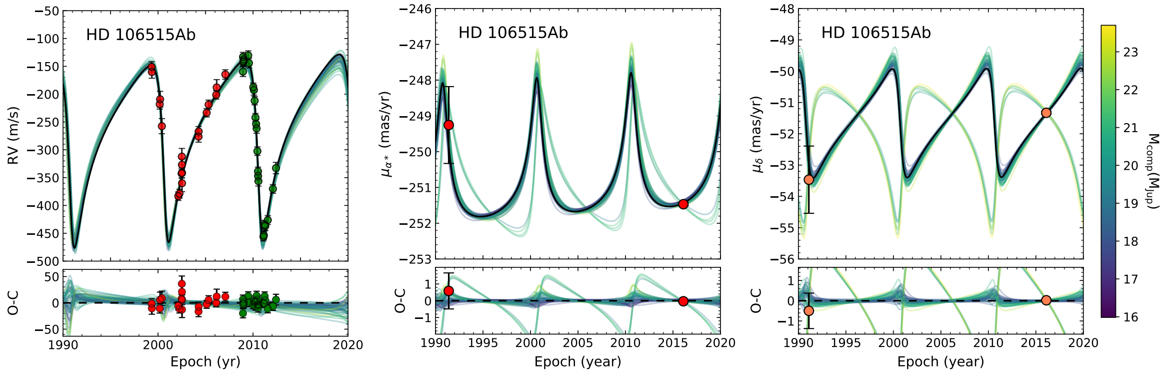

Figure A6 HD 106515 Ab. Same as Fig. A1. Red and green RV data show CORALIE-98 and CORALIE-07 measurements, respectively.

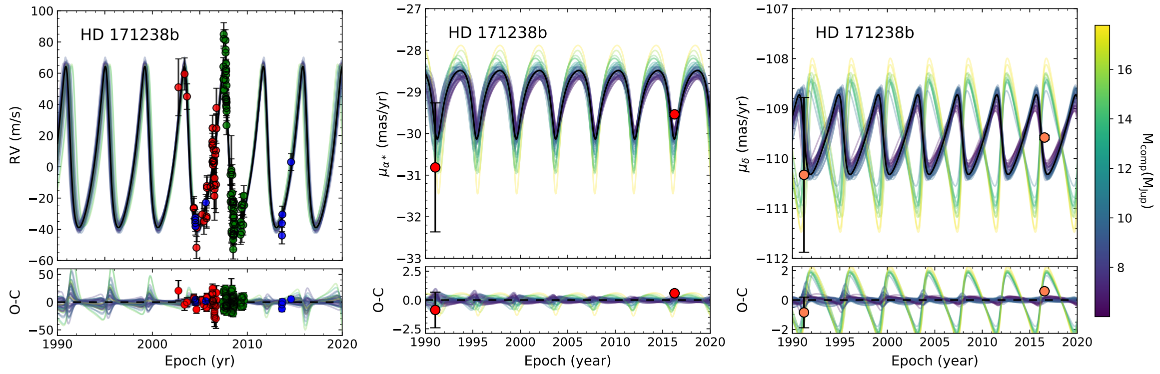

Figure A7 HD 171238 b. Same as Fig. A1. In the left panel, the RVs from CORALIE-98 are in red, the velocities from CORALIE-07 are in green, and the blue data points represent velocities from HIRES/Keck published in 2017.

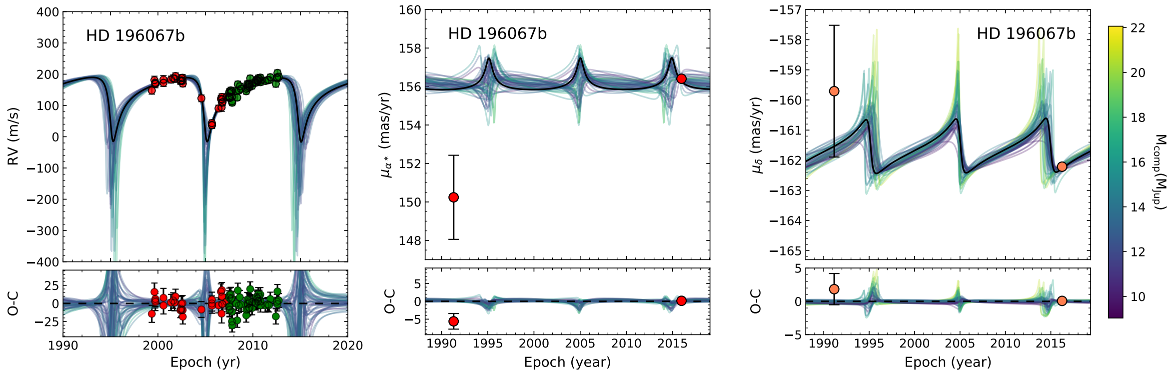

Figure A8 HD 196067 b. Same as Fig. A1. The RV measurements are from CORALIE-98 (red) and CORALIE-07 (green).

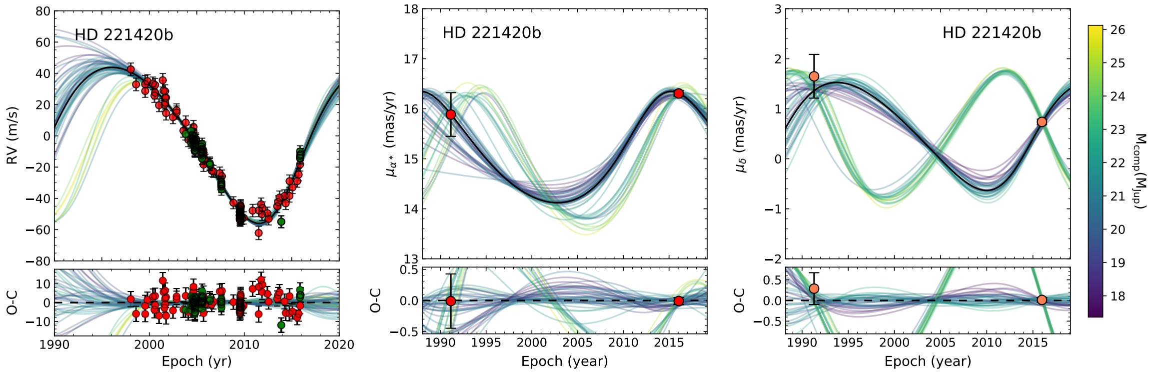

Figure A9 HD 221420 b. Same as Fig. A1. In the left panel, the red data points show RVs from AAT, and the HARPS RVs are showcased by green data points.

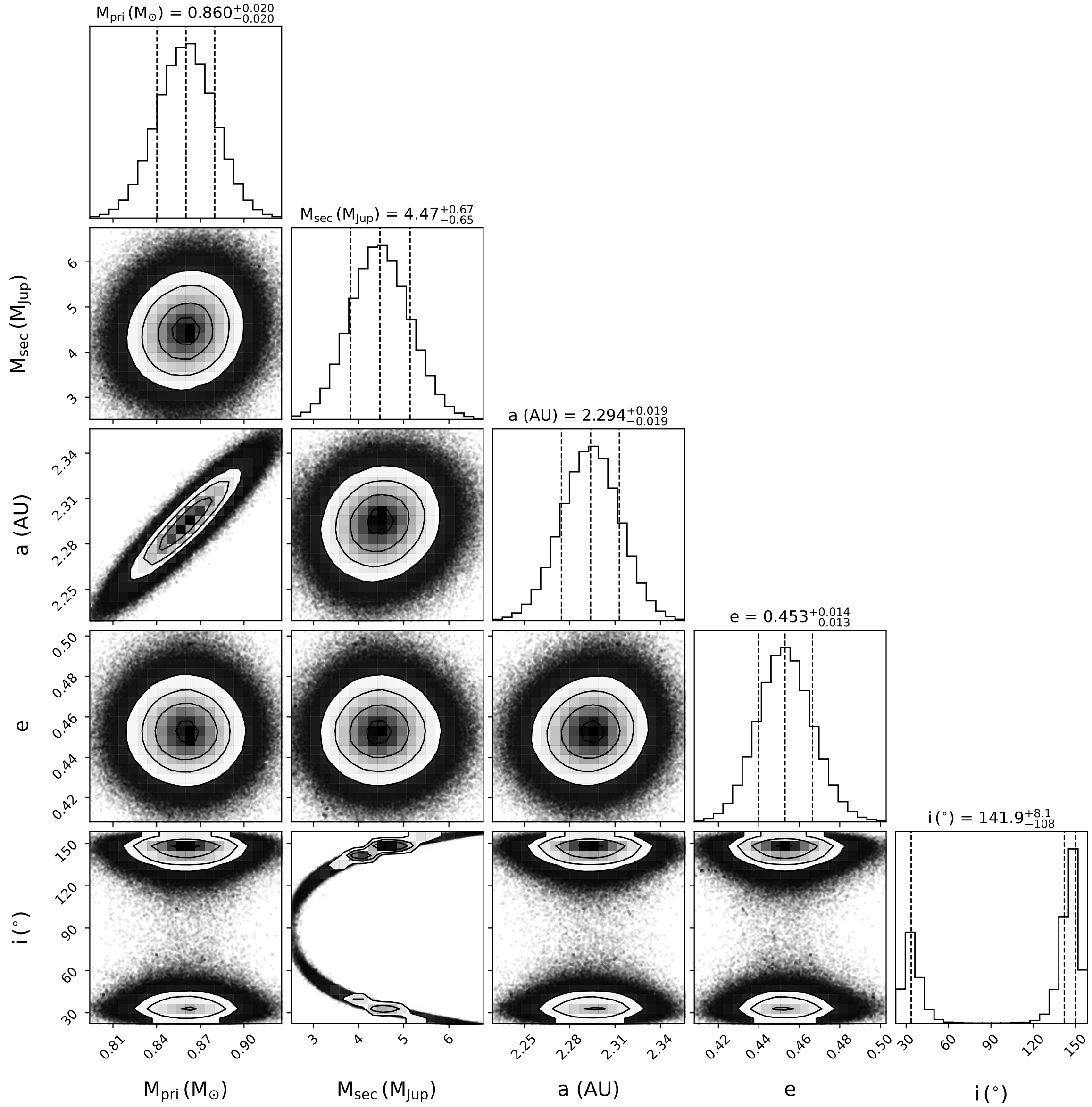

Figure A10 Joint posterior distributions for selected orbital parameters of HD 29021 b. These are the host star's mass (M_{pri}), the companion mass (M_{sec}), the semi-major axis a, the orbital eccentricity e, and the orbital inclination i. The values and histogram distributions of the posteriors of selected parameters are shown, along with 1 σ uncertainties.

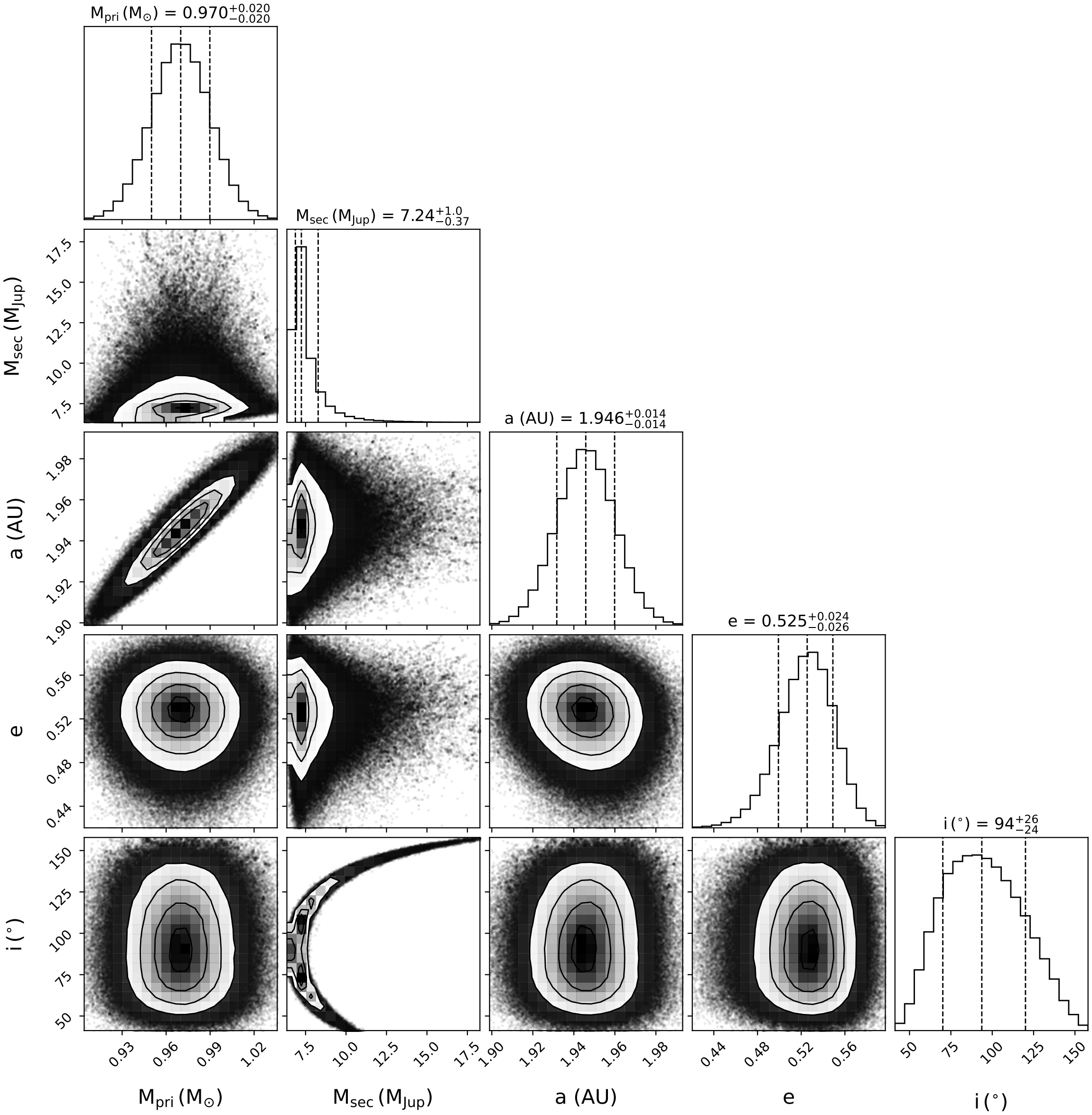

Figure A11 HD 81040 b. Same as Fig. A10.

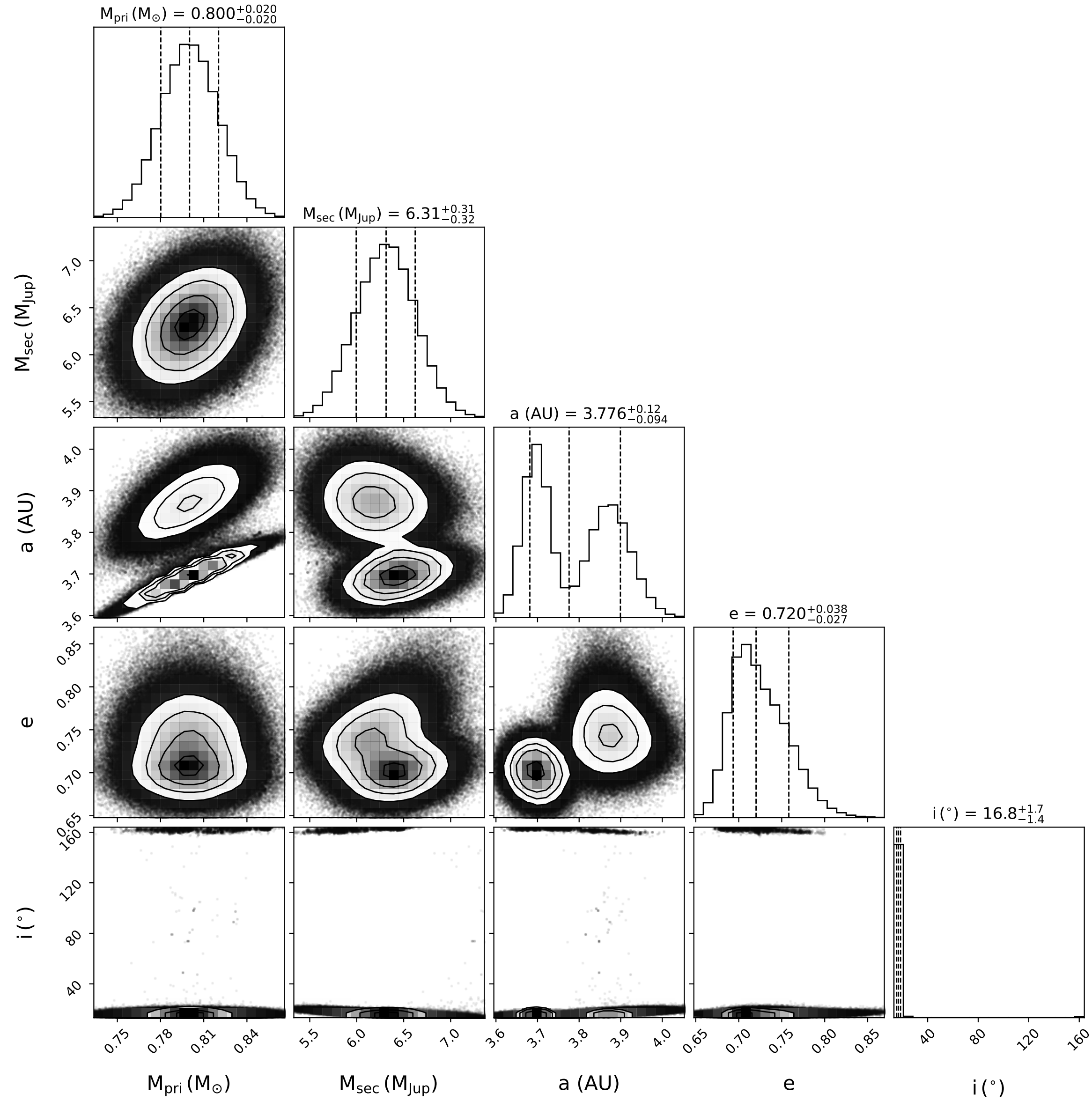

Figure A12 HD 87883 b. Same as Fig. A10.

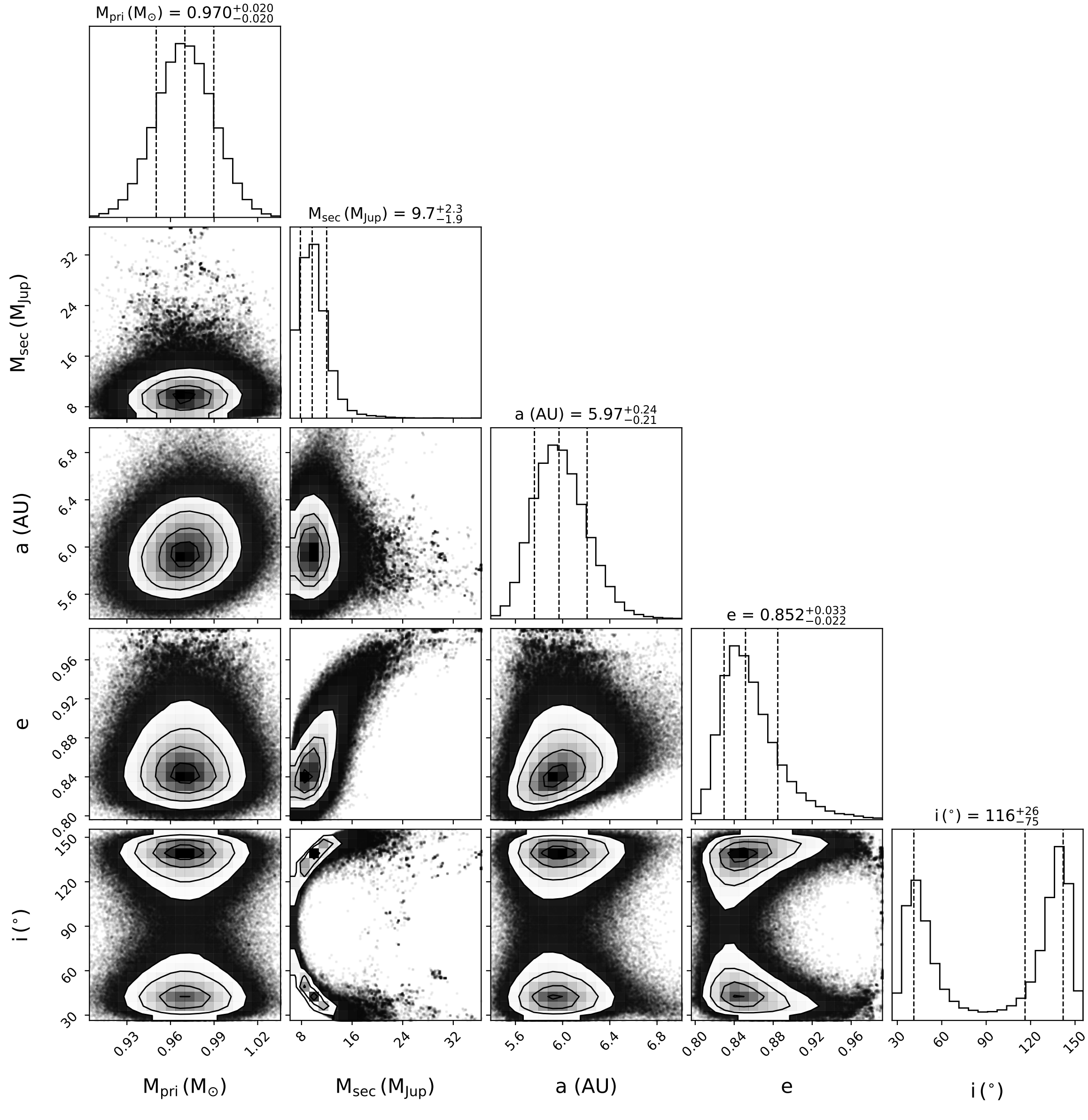

Figure A13 HD 98649 b. Same as Fig. A10.

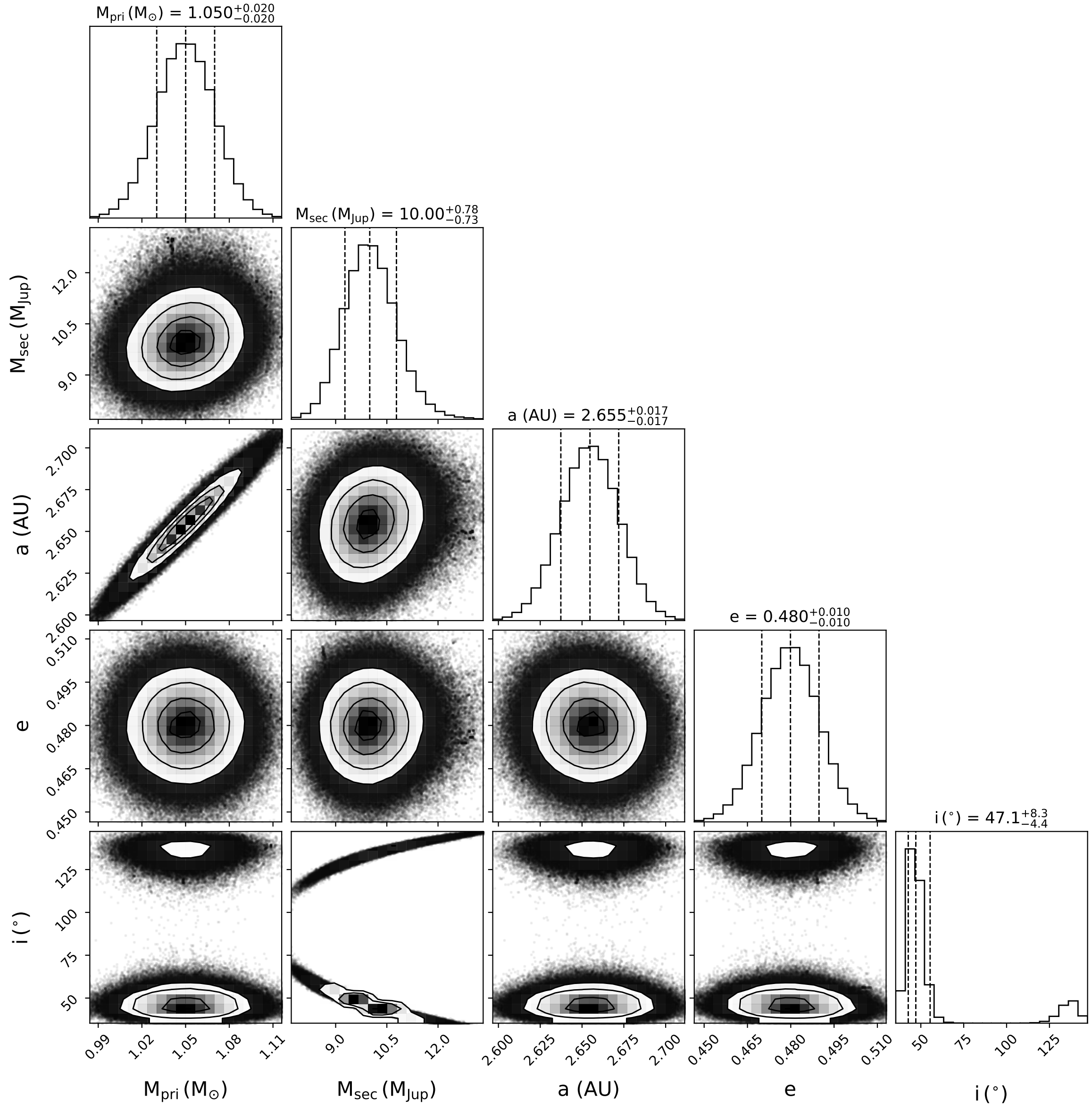

Figure A14 HD 106252 b. Same as Fig. A10.

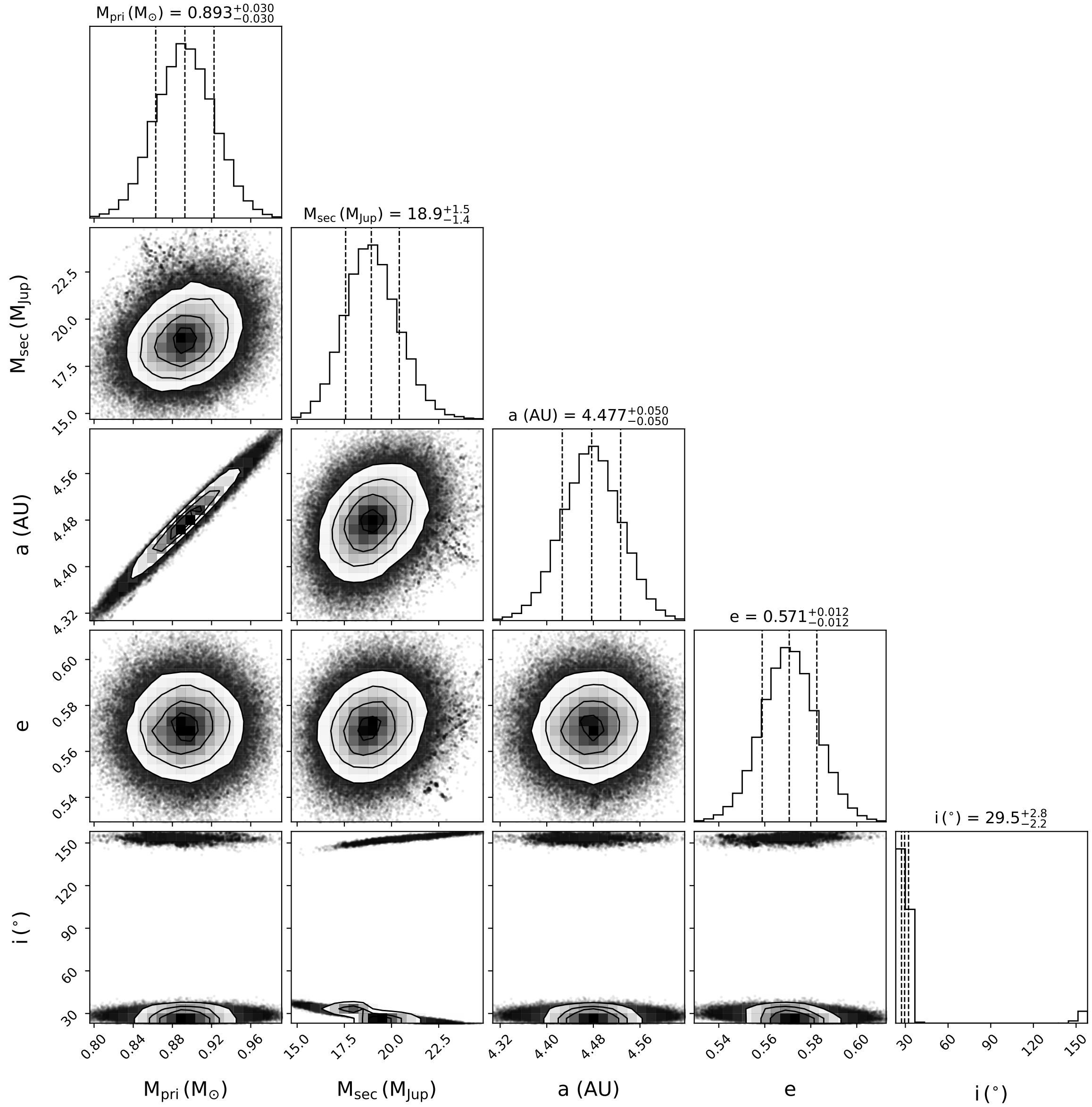

Figure A15 HD 106515 Ab. Same as Fig. A10.

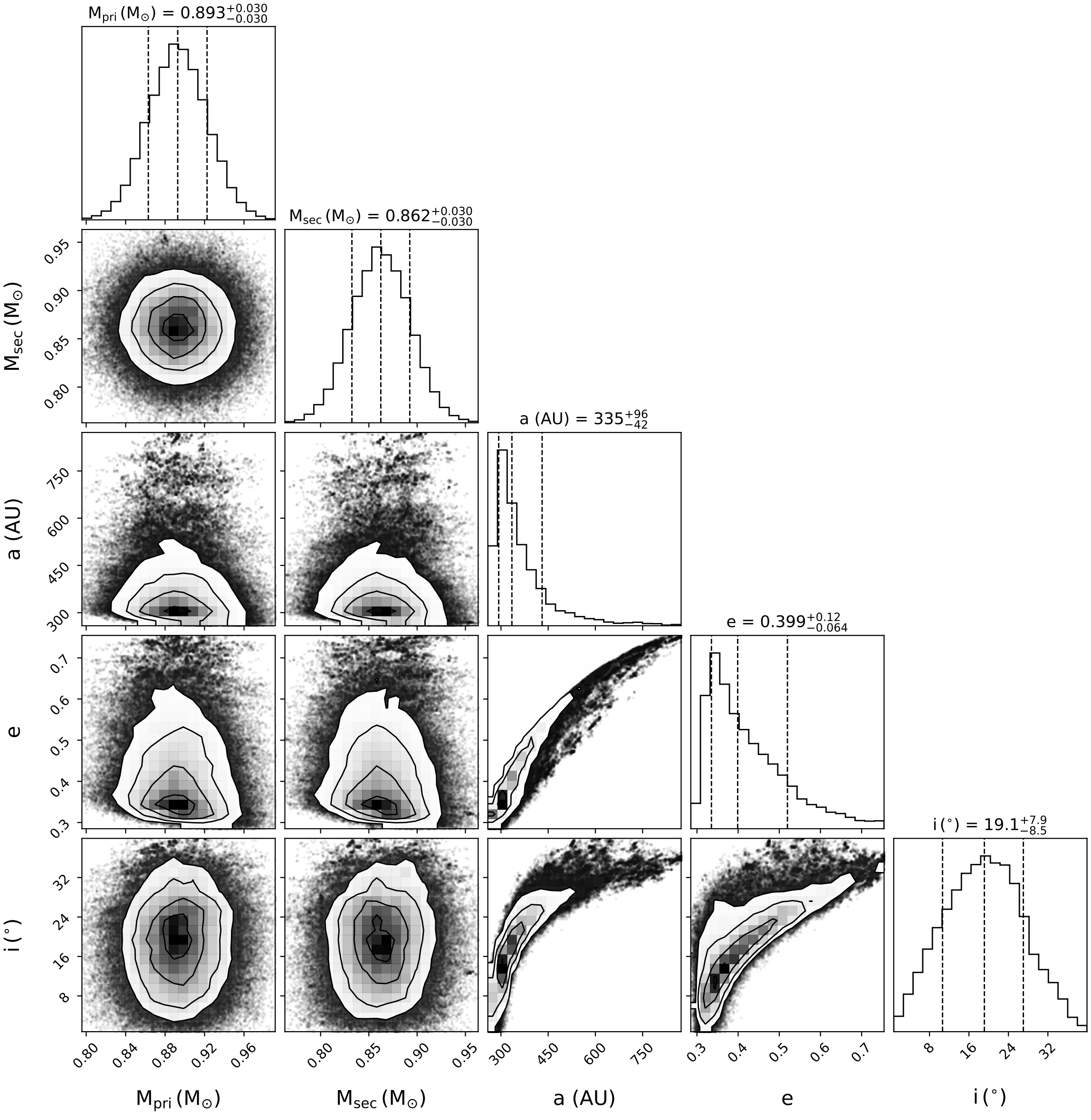

Figure A16 HD 106515 B, the stellar companion to HD 106515 A. Same as Fig. A10.

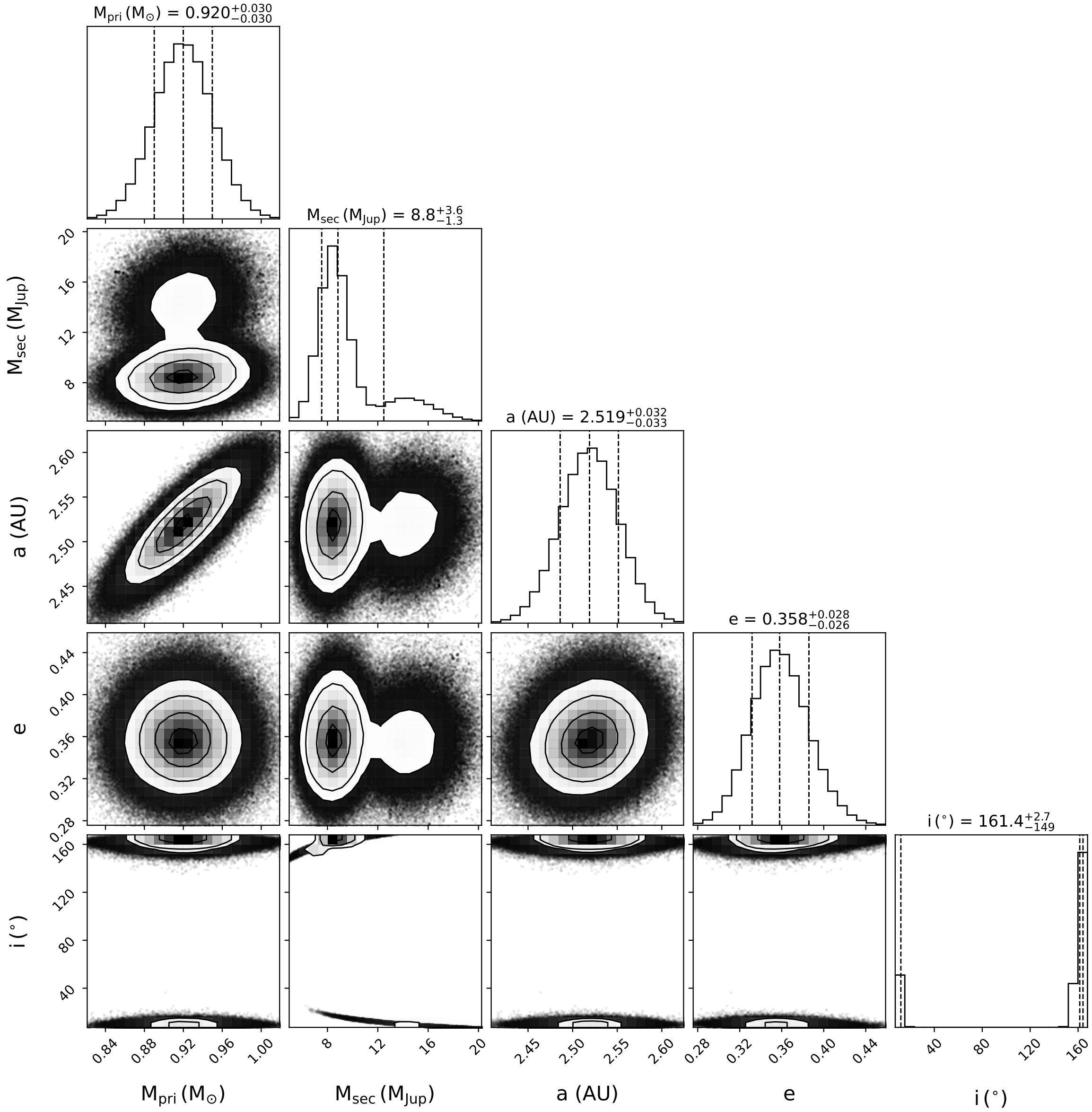

Figure A17 HD 171238 b. Same as Fig. A10.

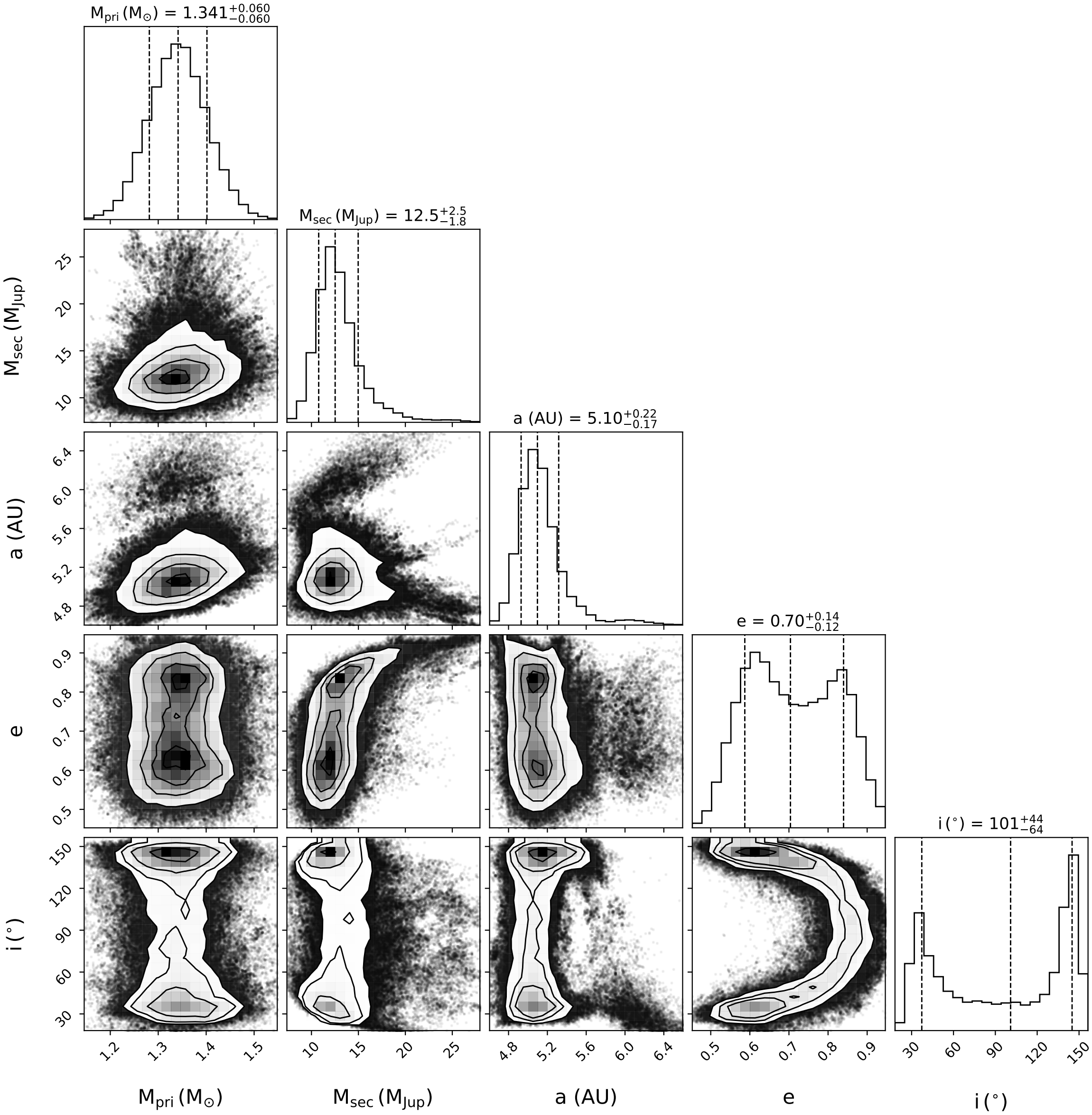

Figure A18 HD 196067 b. Same as Fig. A10.

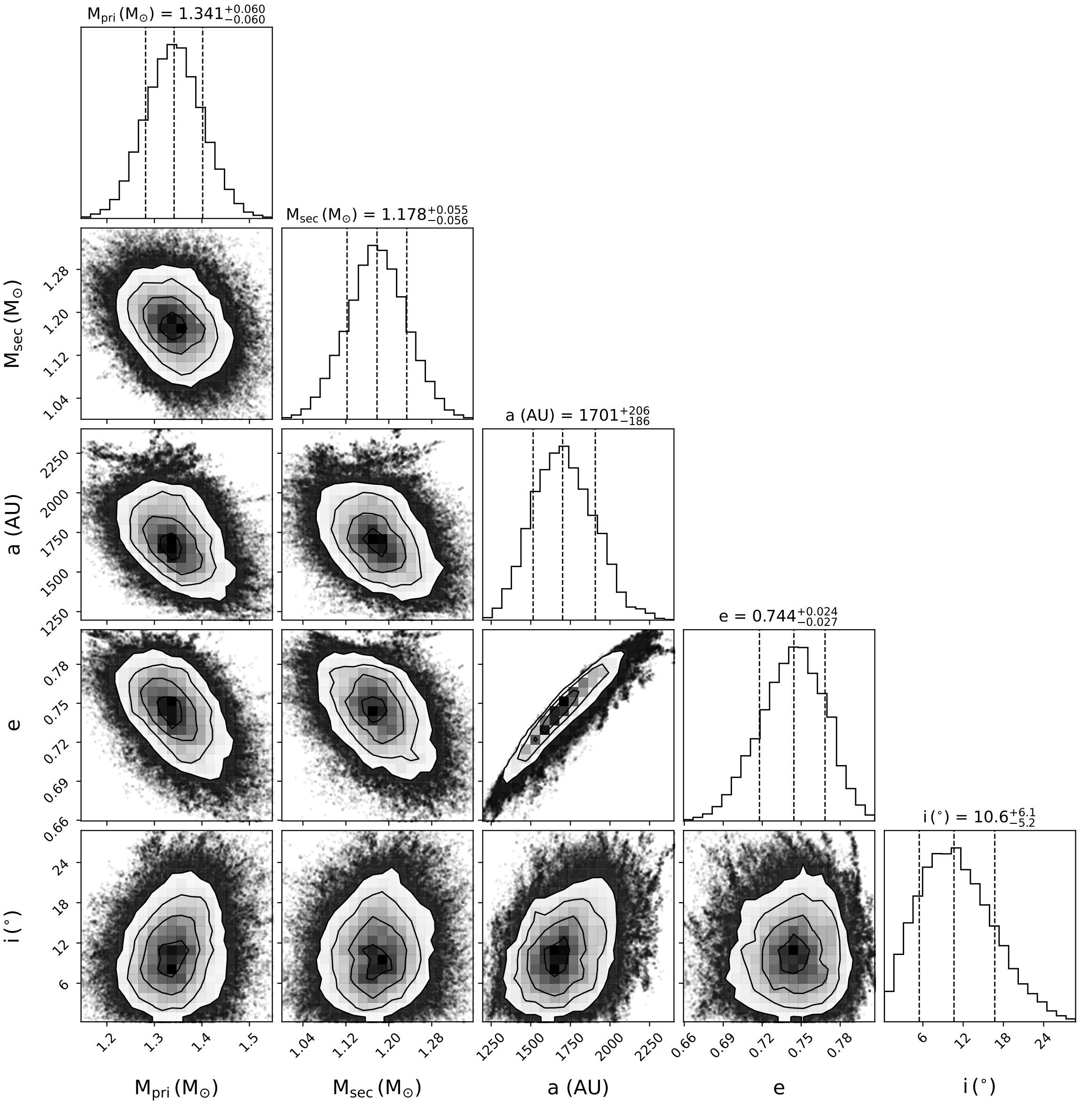

Figure A19 HD 196068. It is bound to HD 196067. Same as Fig. A10.

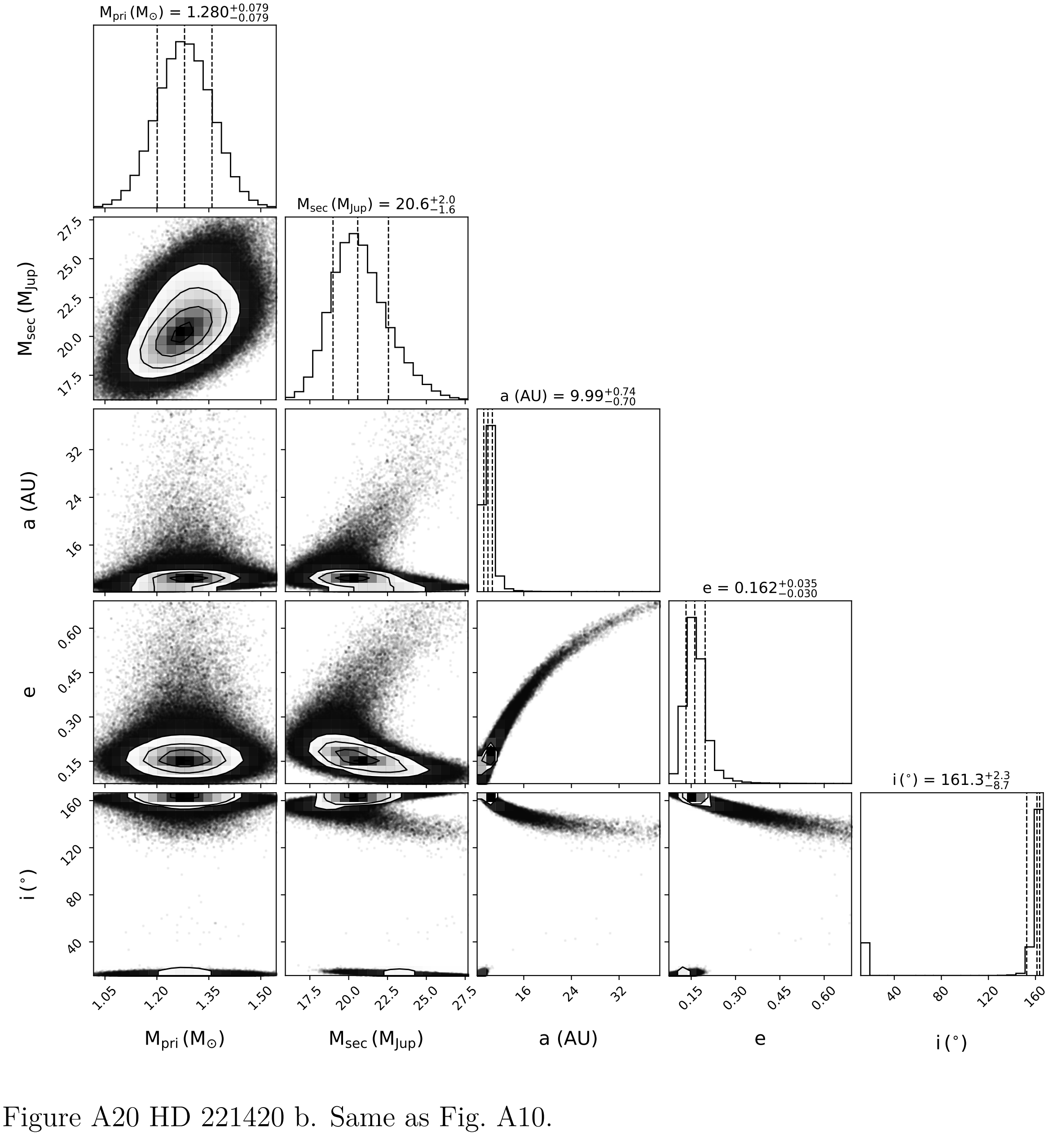

Figure A20 HD 221420 b. Same as Fig. A10.

Bibliography

Abia, C., Rebolo, R., Beckman, J. E., & Crivellari, L. 1988, A&A, 206, 100

Absil, O., Milli, J., Mawet, D., et al. 2013, A&A, 559, L12, doi: 10.1051/0004-6361/201322748

Adams, W. S., Joy, A. H., Humason, M. L., & Brayton, A. M. 1935, ApJ, 81, 187, doi: 10.1086/143628

Adibekyan, V., de Laverny, P., Recio-Blanco, A., et al. 2018, A&A, 619, A130, doi: 10.1051/0004-6361/201834285

Adibekyan, V. Z., Sousa, S. G., Santos, N. C., et al. 2012, A&A, 545, A32, doi: 10.1051/0004-6361/201219401

Adibekyan, V. Z., Figueira, P., Santos, N. C., et al. 2013, A&A, 560, A51, doi: 10.1051/0004-6361/201322551

Aguilera-Gómez, C., Ramírez, I., & Chanamé, J. 2018, A&A, 614, A55, doi: 10.1051/0004-6361/201732209

Akeson, R. L., Chen, X., Ciardi, D., et al. 2013, PASP, 125, 989, doi: 10.1086/672273

Alibert, Y., Ataiee, S., & Venturini, J. 2018, in Handbook of Exoplanets, ed. H. J. Deeg & J. A. Belmonte, 64, doi: 10.1007/978-3-319-55333-7_64

Allard, F., Hauschildt, P. H., Alexander, D. R., Tamanai, A., & Schweitzer, A. 2001, ApJ, 556, 357, doi: 10.1086/321547

Allard, F., Homeier, D., & Freytag, B. 2012, Philosophical Transactions of the Royal Society of London Series A, 370, 2765, doi: 10.1098/rsta.2011.0269

Allende Prieto, C., & Lambert, D. L. 1999, A&A, 352, 555. https://arxiv.org/abs/astro-ph/9911002

Amara, A., & Quanz, S. P. 2012, MNRAS, 427, 948, doi: 10.1111/j.1365-2966.2012.21918.x

Anders, F., Khalatyan, A., Chiappini, C., et al. 2019a, A&A, 628, A94, doi: 10.1051/0004-6361/201935765

—. 2019b, A&A, 628, A94, doi: 10.1051/0004-6361/201935765

Anderson, E., & Francis, C. 2012, Astronomy Letters, 38, 331, doi: 10.1134/S1063773712050015

Angus, R., Aigrain, S., Foreman-Mackey, D., & McQuillan, A. 2015, MNRAS, 450, 1787, doi: 10.1093/mnras/stv423

Apai, D., Reid, I., & Burrows, A. 2010, Spitzer Proposal

Appenzeller, I., Fricke, K., Fürtig, W., et al. 1998, The Messenger, 94, 1

Arriagada, P. 2011, ApJ, 734, 70, doi: 10.1088/0004-637X/734/1/70

Astropy Collaboration, Robitaille, T. P., Tollerud, E. J., et al. 2013, A&A, 558, A33, doi: 10.1051/0004-6361/201322068

Astropy Collaboration, Price-Whelan, A. M., Sipőcz, B. M., et al. 2018, AJ, 156, 123, doi: 10.3847/1538-3881/aabc4f

Avila, G., Rupprecht, G., & Beckers, J. M. 1997, in Society of Photo-Optical Instrumentation Engineers (SPIE) Conference Series, Vol. 2871, Optical Telescopes of Today and Tomorrow, ed. A. L. Ardeberg, 1135–1143, doi: 10.1117/12.269000

Avila, R. J., Hack, W., Cara, M., et al. 2015, in Astronomical Society of the Pacific Conference Series, Vol. 495, Astronomical Data Analysis Software an Systems XXIV (ADASS XXIV), ed. A. R. Taylor & E. Rosolowsky, 281. https://arxiv.org/abs/1411.5605

Baliunas, S. L., Sokoloff, D., Soon, W., et al. 2002, ApJL, 567, L53, doi: 10.1086/339201

Baraffe, I., Chabrier, G., Barman, T. S., Allard, F., & Hauschildt, P. H. 2003, A&A, 402, 701, doi: 10.1051/0004-6361:20030252

Baraffe, I., Homeier, D., Allard, F., & Chabrier, G. 2015, A&A, 577, A42, doi: 10.1051/0004-6361/201425481

Barnes, S. A. 2003, ApJ, 586, 464, doi: 10.1086/367639

—. 2007, ApJ, 669, 1167, doi: 10.1086/519295

Basri, G. 2000, ARA&A, 38, 485, doi: 10.1146/annurev.astro.38.1.485

Basu, S., Chaplin, W. J., Elsworth, Y., et al. 2008, ApJ, 674, 1086, doi: 10.1086/524707

Batalha, N. E., Lewis, T., Fortney, J. J., et al. 2019, ApJL, 885, L25, doi: 10.3847/2041-8213/ab4909

Batista, S. F. A., Adibekyan, V. Z., Sousa, S. G., et al. 2014, A&A, 564, A43, doi: 10.1051/0004-6361/201423645

Bauer, F. F., Zechmeister, M., Kaminski, A., et al. 2020, A&A, 640, A50, doi: 10.1051/0004-6361/202038031

Baumann, P., Ramírez, I., Meléndez, J., Asplund, M., & Lind, K. 2010, A&A, 519, A87, doi: 10.1051/0004-6361/201015137

Beatty, T. G., Morley, C. V., Curtis, J. L., et al. 2018, AJ, 156, 168, doi: 10.3847/1538-3881/aad697

Benedict, G. F., McArthur, B. E., & Bean, J. L. 2008, IAU Symp., 248, 23, doi: 10.1017/S1743921308018577

Benedict, G. F., McArthur, B. E., Fredrick, L. W., et al. 2002, AJ, 124, 1695, doi: 10.1086/342014

Benedict, G. F., McArthur, B. E., Gatewood, G., et al. 2006, The Astronomical Journal, 132, 2206, doi: 10.1086/508323

Bessell, M. S., & Brett, J. M. 1988, PASP, 100, 1134, doi: 10.1086/132281

Beuzit, J.-L., Feldt, M., Dohlen, K., et al. 2008, in Society of Photo-Optical Instrumentation Engineers (SPIE) Conference Series, Vol. 7014, Ground-based and Airborne Instrumentation for Astronomy II, ed. I. S. McLean & M. M. Casali, 701418, doi: 10.1117/12.790120

Bochanski, J. J., Faherty, J. K., Gagné, J., et al. 2018, AJ, 155, 149, doi: 10.3847/1538-3881/aaaebe

Boffin, H. M. J., Rivinius, T., Mérand, A., et al. 2016, A&A, 593, A90, doi: 10.1051/0004-6361/201629127

Bonavita, M., Fontanive, C., Gratton, R., et al. 2022, Monthly Notices of the Royal Astronomical Society, 513, 5588, doi: 10.1093/mnras/stac1250

Bond, C. Z., Cetre, S., Lilley, S., et al. 2020, Journal of Astronomical Telescopes, Instruments, and Systems, 6, 039003, doi: 10.1117/1.JATIS.6.3.039003

Bond, J. C., Tinney, C. G., Butler, R. P., et al. 2006, MNRAS, 370, 163, doi: 10.1111/j.1365-2966.2006.10459.x

Bonfanti, A., Ortolani, S., & Nascimbeni, V. 2016, A&A, 585, A5, doi: 10.1051/0004-6361/201527297

Bonfanti, A., Ortolani, S., Piotto, G., & Nascimbeni, V. 2015, A&A, 575, A18, doi: 10.1051/0004-6361/201424951

Borgniet, S., Lagrange, A. M., Meunier, N., et al. 2019, A&A, 621, A87, doi: 10.1051/0004-6361/201833431

Boss, A. P. 2008, The Astrophysical Journal, 677, 607, doi: 10.1086/533496

Bourgés, L., Lafrasse, S., Mella, G., et al. 2014, in Astronomical Society of the Pacific Conference Series, Vol. 485, Astronomical Data Analysis Software and Systems XXIII, ed. N. Manset & P. Forshay, 223

Bouy, H., Duchêne, G., Köhler, R., et al. 2004, A&A, 423, 341, doi: 10.1051/0004-6361:20040551

Bowler, B. P. 2016, PASP, 128, 102001, doi: 10.1088/1538-3873/128/968/102001

Bowler, B. P., Blunt, S. C., & Nielsen, E. L. 2020, AJ, 159, 63, doi: 10.3847/1538-3881/ab5b11

Bowler, B. P., Liu, M. C., Shkolnik, E. L., et al. 2012, The Astrophysical Journal, 753, 142, doi: 10.1088/0004-637x/753/2/142

Bowler, B. P., & Nielsen, E. L. 2018, in Handbook of Exoplanets, ed. H. J. Deeg & J. A. Belmonte, 155, doi: 10.1007/978-3-319-55333-7_155

Bowler, B. P., Endl, M., Cochran, W. D., et al. 2021, ApJL, 913, L26, doi: 10.3847/2041-8213/abfec8

Bowler, B. P., Cochran, W. D., Endl, M., et al. 2021, The Astronomical Journal, 161, 106, doi: 10.3847/1538-3881/abd243

Bradley, J. 1727, Philosophical Transactions of the Royal Society of London Series I, 35, 637

Bradley, L., Sipőcz, B., Robitaille, T., et al. 2021, astropy/photutils: 1.1.0, 1.1.0, Zenodo, doi: 10.5281/zenodo.4624996

Brandt, G. M., Brandt, T. D., Dupuy, T. J., Li, Y., & Michalik, D. 2021a, AJ, 161, 179, doi: 10.3847/1538-3881/abdc2e

Brandt, G. M., Michalik, D., Brandt, T. D., et al. 2021b, arXiv e-prints, arXiv:2109.06761. https://arxiv.org/abs/2109.06761

—. 2021c, AJ, 162, 230, doi: 10.3847/1538-3881/ac12d0

Brandt, G. M., Dupuy, T. J., Li, Y., et al. 2021d, AJ, 162, 301, doi: 10.3847/1538-3881/ac273e

—. 2021e, arXiv e-prints, arXiv:2109.07525. https://arxiv.org/abs/2109.07525

Brandt, T. D. 2018, ApJS, 239, 31, doi: 10.3847/1538-4365/aaec06

—. 2021a, ApJS, 254, 42, doi: 10.3847/1538-4365/abf93c

—. 2021b, arXiv e-prints, arXiv:2103.07432. https://arxiv.org/abs/2103.07432

Brandt, T. D., Dupuy, T. J., & Bowler, B. P. 2019, The Astronomical Journal, 158, 140, doi: 10.3847/1538-3881/ab04a8

Brandt, T. D., Dupuy, T. J., & Bowler, B. P. 2019, AJ, 158, 140, doi: 10.3847/1538-3881/ab04a8

Brandt, T. D., Dupuy, T. J., Bowler, B. P., et al. 2020, AJ, 160, 196, doi: 10.3847/1538-3881/abb45e

Brandt, T. D., Dupuy, T. J., Li, Y., et al. 2021f, AJ, 162, 186, doi: 10.3847/1538-3881/ac042e

—. 2021g, arXiv e-prints, arXiv:2105.11671. https://arxiv.org/abs/2105.11671

—. 2021h, arXiv e-prints, arXiv:2105.11671. https://arxiv.org/abs/2105.11671

—. 2021i, AJ, 162, 186, doi: 10.3847/1538-3881/ac042e

Brandt, T. D., Kuzuhara, M., McElwain, M. W., et al. 2014, The Astrophysical Journal, 786, 1, doi: 10.1088/0004-637x/786/1/1

Bressan, A., Marigo, P., Girardi, L., et al. 2012, MNRAS, 427, 127, doi: 10.1111/j.1365-2966.2012.21948.x

Brewer, J. M., Fischer, D. A., Valenti, J. A., & Piskunov, N. 2016, ApJS, 225, 32, doi: 10.3847/0067-0049/225/2/32

Brown, R. A. 2011, ApJ, 733, 68, doi: 10.1088/0004-637X/733/1/68

Burrows, A., Hubbard, W. B., & Lunine, J. I. 1989, ApJ, 345, 939, doi: 10.1086/167964

Burrows, A., Marley, M., Hubbard, W. B., et al. 1997, ApJ, 491, 856, doi: 10.1086/305002

Butler, R. P., Wright, J. T., Marcy, G. W., et al. 2006, ApJ, 646, 505, doi: 10.1086/504701

Butler, R. P., Vogt, S. S., Laughlin, G., et al. 2017, AJ, 153, 208, doi: 10.3847/1538-3881/aa66ca

Calamari, E., Faherty, J. K., Burningham, B., et al. 2022, arXiv e-prints, arXiv:2210.13614. https://arxiv.org/abs/2210.13614

Cantat-Gaudin, T., & Brandt, T. D. 2021, arXiv e-prints, arXiv:2103.07432. https://arxiv.org/abs/2103.07432

Cardoso, C. V., McCaughrean, M. J., King, R. R., et al. 2009, in American Institute of Physics Conference Series, Vol. 1094, 15th Cambridge Workshop on Cool Stars, Stellar Systems, and the Sun, ed. E. Stempels, 509–512, doi: 10.1063/1.3099160

Cardoso, C. V. V. 2012, Ph.D. Thesis, Ph.D. Thesis, University of Exeter

Casagrande, L., Ramírez, I., Meléndez, J., Bessell, M., & Asplund, M. 2010, A&A, 512, A54, doi: 10.1051/0004-6361/200913204

Casagrande, L., Schönrich, R., Asplund, M., et al. 2011, A&A, 530, A138, doi: 10.1051/0004-6361/201016276

Chabrier, G., Baraffe, I., Allard, F., & Hauschildt, P. 2000, ApJ, 542, 464, doi: 10.1086/309513

Chabrier, G., & Johansson, P. H. 2023, Astronomy & Astrophysics, 657, A53

Chambers, J. E. 2010, ApJ, 724, 92, doi: 10.1088/0004-637X/724/1/92

Chandler, C. O., McDonald, I., & Kane, S. R. 2016, AJ, 151, 59, doi: 10.3847/0004-6256/151/3/59

Chauvin, G., Lagrange, A. M., Zuckerman, B., et al. 2005, A&A, 438, L29, doi: 10.1051/0004-6361:200500111

Chauvin, G., Lagrange, A. M., Bonavita, M., et al. 2010, A&A, 509, A52, doi: 10.1051/0004-6361/200911716

Chauvin, G., Gratton, R., Bonnefoy, M., et al. 2018, A&A, 617, A76, doi: 10.1051/0004-6361/201732077

Cheetham, A., Ségransan, D., Peretti, S., et al. 2018, A&A, 614, A16, doi: 10.1051/0004-6361/201630136

Chen & Li, M., Li, Y., Brandt, T. D., et al. 2022, arXiv e-prints, arXiv:2205.08077. https://arxiv.org/abs/2205.08077

Chen, M., Li, Y., Brandt, T. D., et al. 2022, AJ, 163, 288, doi: 10.3847/1538-3881/ac66d2

Chilcote, J. K., Bailey, V. P., De Rosa, R., et al. 2018, in Society of Photo-Optical Instrumentation Engineers (SPIE) Conference Series, Vol. 10702, Ground-based and Airborne Instrumentation for Astronomy VII, ed. C. J. Evans, L. Simard, & H. Takami, 1070244, doi: 10.1117/12.2313771

Christiaens, D., Cordero-Grande, L., Pietsch, M., et al. 2021, NeuroImage, 225, 117437, doi: https://doi.org/10.1016/j.neuroimage.2020.117437

Cooper, C. S., & Showman, A. P. 2006, ApJ, 649, 1048, doi: 10.1086/506312

Costa Silva, A. R., Delgado Mena, E., & Tsantaki, M. 2020, A&A, 634, A136, doi: 10.1051/0004-6361/201936523

Crepp, J. R., Gonzales, E. J., Bechter, E. B., et al. 2016, ApJ, 831, 136, doi: 10.3847/0004-637X/831/2/136

Crepp, J. R., & Johnson, J. A. 2014, Research in Astronomy and Astrophysics, 14, 887

Crepp, J. R., Johnson, J. A., Howard, A. W., et al. 2013, ApJ, 771, 46, doi: 10.1088/0004-637X/771/1/46

Crepp, J. R., Johnson, J. A., Howard, A. W., et al. 2014, The Astrophysical Journal, 781, 16

Crepp, J. R., Principe, D. A., Wolff, S., et al. 2018a, ApJ, 853, 192, doi: 10.3847/1538-4357/aaa2fd

—. 2018b, ApJ, 853, 192, doi: 10.3847/1538-4357/aaa2fd

Cumming, A. 2004, Monthly Notices of the Royal Astronomical Society, 354, 1165, doi: 10.1111/j.1365-2966.2004.08275.x

Currie, T., Brandt, T. D., Kuzuhara, M., et al. 2020, ApJL, 904, L25, doi: 10.3847/2041-8213/abc631

Currie, T., Brandt, T. D., Kuzuhara, M., et al. 2021, in Society of Photo-Optical Instrumentation Engineers (SPIE) Conference Series, Vol. 11823, Techniques and Instrumentation for Detection of Exoplanets X, ed. S. B. Shaklan & G. J. Ruane, 1182304, doi: 10.1117/12.2595001

Currie, T., Brandt, G. M., Brandt, T. D., et al. 2022, arXiv e-prints, arXiv:2212.00034. https://arxiv.org/abs/2212.00034

Cutri, R. M., Skrutskie, M. F., van Dyk, S., et al. 2003, VizieR Online Data Catalog, II/246

Datson, J., Flynn, C., & Portinari, L. 2012, MNRAS, 426, 484, doi: 10.1111/j.1365-2966.2012.21730.x

—. 2015, A&A, 574, A124, doi: 10.1051/0004-6361/201425000

David, T. J., & Hillenbrand, L. A. 2015, ApJ, 804, 146, doi: 10.1088/0004-637X/804/2/146

Delgado Mena, E., Bertrán de Lis, S., Adibekyan, V. Z., et al. 2015, A&A, 576, A69, doi: 10.1051/0004-6361/201425433

Delgado Mena, E., Moya, A., Adibekyan, V., et al. 2019, A&A, 624, A78, doi: 10.1051/0004-6361/201834783

Delorme, P., Willott, C. J., Forveille, T., et al. 2008, A&A, 484, 469, doi: 10.1051/0004-6361:20078843

Desidera, S., Gratton, R., Carolo, E., et al. 2012, A&A, 546, A108, doi: 10.1051/0004-6361/201220038

Diego, F., Charalambous, A., Fish, A. C., & Walker, D. D. 1990, in Society of Photo-Optical Instrumentation Engineers (SPIE) Conference Series, Vol. 1235, Instrumentation in Astronomy VII, ed. D. L. Crawford, 562–576, doi: 10.1117/12.19119

Dieterich, S. B., Henry, T. J., Jao, W.-C., et al. 2014, The Astronomical Journal, 147, 94, doi: 10.1088/0004-6256/147/5/94

Dieterich, S. B., Weinberger, A. J., Boss, A. P., et al. 2018, The Astrophysical Journal, 865, 28, doi: 10.3847/1538-4357/aadadc

Dommanget, J., & Nys, O. 2002, VizieR Online Data Catalog, I/274

Dupuy, T. J., & Liu, M. C. 2017a, ApJS, 231, 15, doi: 10.3847/1538-4365/aa5e4c

—. 2017b, ApJS, 231, 15, doi: 10.3847/1538-4365/aa5e4c

Dupuy, T. J., Liu, M. C., Bowler, B. P., et al. 2010, ApJ, 721, 1725, doi: 10.1088/0004-637X/721/2/1725

Dupuy, T. J., Liu, M. C., & Ireland, M. J. 2009, ApJ, 692, 729, doi: 10.1088/0004-637X/692/1/729

—. 2014, ApJ, 790, 133, doi: 10.1088/0004-637X/790/2/133

Dupuy, T. J., Liu, M. C., Leggett, S. K., et al. 2015, ApJ, 805, 56, doi: 10.1088/0004-637X/805/1/56

Dupuy, T. J., Liu, M. C., Best, W. M. J., et al. 2019, AJ, 158, 174, doi: 10.3847/1538-3881/ab3cd1

Eisner, J. A., & Kulkarni, S. R. 2001, ApJ, 550, 871, doi: 10.1086/319801

Endl, M., Kürster, M., Els, S., et al. 2002, A&A, 392, 671, doi: 10.1051/0004-6361:20020937

ESA, ed. 1997, ESA Special Publication, Vol. 1200, The HIPPARCOS and TYCHO catalogues. Astrometric and photometric star catalogues derived from the ESA HIPPARCOS Space Astrometry Mission

Evans, D. S., Menzies, A., & Stoy, R. H. 1957, MNRAS, 117, 534, doi: 10.1093/mnras/117.5.534

Feng, F., Anglada-Escudé, G., Tuomi, M., et al. 2019, MNRAS, 490, 5002, doi: 10.1093/mnras/stz2912

Feng, F., Butler, R. P., Vogt, S. S., et al. 2022, ApJS, 262, 21, doi: 10.3847/1538-4365/ac7e57

Filippazzo, J. C., Rice, E. L., Faherty, J., et al. 2015, ApJ, 810, 158, doi: 10.1088/0004-637X/810/2/158

Fischer, D., Driscoll, P., Isaacson, H., et al. 2009, ApJ, 703, 1545, doi: 10.1088/0004-637X/703/2/1545

Fischer, D. A., Marcy, G. W., Butler, R. P., et al. 2002, PASP, 114, 529, doi: 10.1086/341677

Fischer, D. A., Marcy, G. W., & Spronck, J. F. P. 2013, The Astrophysical Journal Supplement Series, 210, 5, doi: 10.1088/0067-0049/210/1/5

Fischer, D. A., & Valenti, J. 2005, ApJ, 622, 1102, doi: 10.1086/428383

Fischer, D. A., Anglada-Escude, G., Arriagada, P., et al. 2016, PASP, 128, 066001, doi: 10.1088/1538-3873/128/964/066001

Fontanive, C., Mužić, , K., Bonavita, M., & Biller, B. 2019, MNRAS, 490, 1120, doi: 10.1093/mnras/stz2587

Ford, E. B. 2014, Proceedings of the National Academy of Sciences, 111, 12616, doi: 10.1073/pnas.1304219111

Foreman-Mackey, D., Hogg, D. W., Lang, D., & Goodman, J. 2013, PASP, 125, 306, doi: 10.1086/670067

Franson, K., & Bowler, B. P. 2023, AJ, 165, 246, doi: 10.3847/1538-3881/acca18

Franson, K., Bowler, B. P., Brandt, T. D., et al. 2022a, AJ, 163, 50, doi: 10.3847/1538-3881/ac35e8

Franson, K., Bowler, B. P., Bonavita, M., et al. 2022b, arXiv e-prints, arXiv:2211.09840. `https://arxiv.org/abs/2211.09840`

Franson, K., Bowler, B. P., Bonavita, M., et al. 2023, The Astronomical Journal, 165, 39, doi: `10.3847/1538-3881/aca408`

Fuhrmann, K. 2008, MNRAS, 384, 173, doi: `10.1111/j.1365-2966.2007.12671.x`

Gaia Collaboration. 2020, VizieR Online Data Catalog, I/350

—. 2022, VizieR Online Data Catalog, I/355

Gaia Collaboration, Brown, A. G. A., Vallenari, A., et al. 2020, Gaia Early Data Release 3: Summary of the contents and survey properties. `https://arxiv.org/abs/2012.01533`

—. 2018, A&A, 616, A1, doi: `10.1051/0004-6361/201833051`

Gaidos, E., Mann, A. W., Kraus, A. L., & Ireland, M. 2016, MNRAS, 457, 2877, doi: `10.1093/mnras/stw097`

Gáspár, A., Rieke, G. H., & Ballering, N. 2016, ApJ, 826, 171, doi: `10.3847/0004-637X/826/2/171`

Gaudi, B. S. 2021, arXiv e-prints, arXiv:2102.01715. `https://arxiv.org/abs/2102.01715`

Geißler, K., Sterzik, M. R., Chauvin, G., & Pantin, E. 2009, in American Institute of Physics Conference Series, Vol. 1094, 15th Cambridge Workshop on Cool Stars, Stellar Systems, and the Sun, ed. E. Stempels, 521–524, doi: `10.1063/1.3099163`

Gillessen, S., Eisenhauer, F., Trippe, S., et al. 2009, ApJ, 692, 1075, doi: `10.1088/0004-637X/692/2/1075`

Gillessen, S., Plewa, P. M., Eisenhauer, F., et al. 2017, ApJ, 837, 30, doi: `10.3847/1538-4357/aa5c41`

Ginski, C., Mugrauer, M., Seeliger, M., & Eisenbeiss, T. 2012, Monthly Notices of the Royal Astronomical Society, 421, 2498, doi: `10.1111/j.1365-2966.2012.20485.x`

Goda, S., & Matsuo, T. 2019, ApJ, 876, 23, doi: `10.3847/1538-4357/ab0f9c`

Goldman, B., Cushing, M. C., Marley, M. S., et al. 2008, A&A, 487, 277, doi: `10.1051/0004-6361:20065075`

Golub, L. 1996, Ap&SS, 237, 33, doi: `10.1007/BF02424425`

Gomes da Silva, J., Santos, N. C., Adibekyan, V., et al. 2021, A&A, 646, A77, doi: 10.1051/0004-6361/202039765

Gomez Gonzalez, C. A., Absil, O., Absil, P. A., et al. 2016, A&A, 589, A54, doi: 10.1051/0004-6361/201527387

Gomez Gonzalez, C. A., Wertz, O., Absil, O., et al. 2017a, AJ, 154, 7, doi: 10.3847/1538-3881/aa73d7

—. 2017b, AJ, 154, 7, doi: 10.3847/1538-3881/aa73d7

Gondoin, P. 2020, A&A, 641, A110, doi: 10.1051/0004-6361/202038291

Gontcharov, G. A. 2012, Astronomy Letters, 38, 771, doi: 10.1134/S1063773712120031

Gonzales, E. C. 2020, in American Astronomical Society Meeting Abstracts, Vol. 235, American Astronomical Society Meeting Abstracts #235, 132.04

Gonzalez, G., Carlson, M. K., & Tobin, R. W. 2010, MNRAS, 403, 1368, doi: 10.1111/j.1365-2966.2009.16195.x

González Hernández, J. I., Israelian, G., Santos, N. C., et al. 2010, ApJ, 720, 1592, doi: 10.1088/0004-637X/720/2/1592

Gould, A., & Chaname, J. 2004, The Astrophysical Journal Supplement Series, 150, 455, doi: 10.1086/381147

Grandjean, A., Lagrange, A. M., Beust, H., et al. 2019, A&A, 627, L9, doi: 10.1051/0004-6361/201935044

Gravity Collaboration, Abuter, R., Accardo, M., et al. 2017, A&A, 602, A94, doi: 10.1051/0004-6361/201730838

Gray, R. O., Corbally, C. J., Garrison, R. F., et al. 2006, AJ, 132, 161, doi: 10.1086/504637

Gray, R. O., Corbally, C. J., Garrison, R. F., McFadden, M. T., & Robinson, P. E. 2003, AJ, 126, 2048, doi: 10.1086/378365

Grimm, S. L., Deming, D., Knutson, H. A., et al. 2018, The Astronomical Journal, 155, 104, doi: 10.3847/1538-3881/aaab76

Gubler, J., & Tytler, D. 1998, PASP, 110, 738, doi: 10.1086/316172

Güdel, M. 2004, A&A Rv, 12, 71, doi: 10.1007/s00159-004-0023-2

Hall, J. C. 2008, Living Reviews in Solar Physics, 5, 2, doi: 10.12942/lrsp-2008-2

Han, I., Black, D. C., & Gatewood, G. 2001, The Astrophysical Journal, 548, L57, doi: 10.1086/318927

Hatzes, A. P. 2016, The Radial Velocity Method for the Detection of Exoplanets, ed. V. Bozza, L. Mancini, & A. Sozzetti, Vol. 428, 3, doi: 10.1007/978-3-319-27458-4_1

Hayashi, C., & Nakano, T. 1963, Progress of Theoretical Physics, 30, 460, doi: 10.1143/PTP.30.460

He, M. Y., Ford, E. B., & Ragozzine, D. 2020, The Astronomical Journal, 161, 16, doi: 10.3847/1538-3881/abc68b

Heiter, U., & Luck, R. E. 2003, AJ, 126, 2015, doi: 10.1086/378366

Helled, R., Movshovitz, N., & Nettelmann, N. 2022, arXiv e-prints, arXiv:2202.10046, doi: 10.48550/arXiv.2202.10046

Herrero, E., Ribas, I., Jordi, C., Guinan, E. F., & Engle, S. G. 2012, A&A, 537, A147, doi: 10.1051/0004-6361/201117809

Hinkel, N. R., Timothy McElwain, M., Kane, S. R., et al. 2016, ApJS, 226, 4, doi: 10.3847/0067-0049/226/1/4

Høg, E., Fabricius, C., Makarov, V. V., et al. 2000a, A&A, 355, L27

—. 2000b, A&A, 355, L27

Holmberg, J., Nordström, B., & Andersen, J. 2009, A&A, 501, 941, doi: 10.1051/0004-6361/200811191

Howard, A. W., Marcy, G. W., Johnson, J. A., et al. 2010, Science, 330, 653, doi: 10.1126/science.1194854

Howard, A. W., Marcy, G. W., Bryson, S. T., et al. 2012, ApJS, 201, 15, doi: 10.1088/0067-0049/201/2/15

Hsu, D. C., Ford, E. B., Ragozzine, D., & Ashby, K. 2019, The Astronomical Journal, 158, 109, doi: 10.3847/1538-3881/ab31ab

Huang, C., Zhao, G., Zhang, H. W., & Chen, Y. Q. 2005, MNRAS, 363, 71, doi: 10.1111/j.1365-2966.2005.09395.x

Hubbard, A., & Ebel, D. S. 2014, Icarus, 237, 84, doi: 10.1016/j.icarus.2014.04.015

Huby, E., Baudoz, P., Mawet, D., & Absil, O. 2015, A&A, 584, A74, doi: 10.1051/0004-6361/201527102

Huby, E., Bottom, M., Femenia, B., et al. 2017, A&A, 600, A46, doi: 10.1051/0004-6361/201630232

Hunter, J. D. 2007, Computing in Science Engineering, 9, 90, doi: 10.1109/MCSE.2007.55

Ireland, M. J., Kraus, A., Martinache, F., Law, N., & Hillenbrand, L. A. 2010, The Astrophysical Journal, 726, 113, doi: 10.1088/0004-637x/726/2/113

Ireland, M. J., Kraus, A., Martinache, F., Lloyd, J. P., & Tuthill, P. G. 2008, The Astrophysical Journal, 678, 463, doi: 10.1086/529578

Isaacson, H., & Fischer, D. 2010, ApJ, 725, 875, doi: 10.1088/0004-637X/725/1/875

Jardine, M., Wood, K., Collier Cameron, A., Donati, J. ., & Mackay, D. H. 2002, Monthly Notices of the Royal Astronomical Society, 336, 1364, doi: 10.1046/j.1365-8711.2002.05877.x

Jenkins, J. S., Jones, H. R. A., Pavlenko, Y., et al. 2008, A&A, 485, 571, doi: 10.1051/0004-6361:20078611

Jenkins, J. S., Murgas, F., Rojo, P., et al. 2011, A&A, 531, A8, doi: 10.1051/0004-6361/201016333

Jin, S. 2021, arXiv e-prints, arXiv:2102.05808. https://arxiv.org/abs/2102.05808

Jofré, E., Petrucci, R., Saffe, C., et al. 2015, A&A, 574, A50, doi: 10.1051/0004-6361/201424474

Kane, S. R., Dalba, P. A., Li, Z., et al. 2019, AJ, 157, 252, doi: 10.3847/1538-3881/ab1ddf

Kang, W., Lee, S.-G., & Kim, K.-M. 2011, ApJ, 736, 87, doi: 10.1088/0004-637X/736/2/87

Kasdin, N. J., Bailey, V. P., Mennesson, B., et al. 2020, in Society of Photo-Optical Instrumentation Engineers (SPIE) Conference Series, Vol. 11443, Society of Photo-Optical Instrumentation Engineers (SPIE) Conference Series, 114431U, doi: 10.1117/12.2562997

Kenworthy, M., Hofmann, K.-H., Close, L., et al. 2001, ApJL, 554, L67, doi: 10.1086/320934

Kervella, P., Arenou, F., Mignard, F., & Thévenin, F. 2019, A&A, 623, A72, doi: 10.1051/0004-6361/201834371

Kervella, P., Arenou, F., & Schneider, J. 2020, A&A, 635, L14, doi: 10.1051/0004-6361/202037551

Kiefer, F., Hébrard, G., Lecavelier des Etangs, A., et al. 2021, A&A, 645, A7, doi: 10.1051/0004-6361/202039168

King, R. R., McCaughrean, M. J., Homeier, D., et al. 2010, A&A, 510, A99, doi: 10.1051/0004-6361/200912981

Knutson, H. A., Fulton, B. J., Montet, B. T., et al. 2014, The Astrophysical Journal, 785, 126, doi: 10.1088/0004-637x/785/2/126

Koen, C. 2005, MNRAS, 360, 1132, doi: 10.1111/j.1365-2966.2005.09119.x

—. 2013, MNRAS, 428, 2824, doi: 10.1093/mnras/sts208

Koen, C., Tanabé, T., Tamura, M., & Kusakabe, N. 2005, MNRAS, 362, 727, doi: 10.1111/j.1365-2966.2005.09280.x

Kollatschny, W. 1980, A&A, 86, 308

Konopacky, Q. M., Ghez, A. M., Barman, T. S., et al. 2010, ApJ, 711, 1087, doi: 10.1088/0004-637X/711/2/1087

Kotoneva, E., Shi, J. R., Zhao, G., & Liu, Y. J. 2006, A&A, 454, 833, doi: 10.1051/0004-6361:20042498

Kozai, Y. 1962, AJ, 67, 591, doi: 10.1086/108790

Kraft, R. P. 1967, ApJ, 150, 551, doi: 10.1086/149359

Kumar, S. S. 1963, ApJ, 137, 1121, doi: 10.1086/147589

Kuzuhara, M., Currie, T., Takarada, T., et al. 2022, The Astrophysical Journal Letters, 934, L18, doi: 10.3847/2041-8213/ac772f

Lachaume, R., Dominik, C., Lanz, T., & Habing, H. J. 1999, A&A, 348, 897

Lafrenière, D., Jayawardhana, R., & van Kerkwijk, M. H. 2008, ApJL, 689, L153, doi: 10.1086/595870

Lafrenière, D., Marois, C., Doyon, R., Nadeau, D., & Artigau, É. 2007, ApJ, 660, 770, doi: 10.1086/513180

Lagrange, A.-M. 2014, Philosophical transactions. Series A, Mathematical, physical, and engineering sciences, 372, 20130090, doi: 10.1098/rsta.2013.0090

Lagrange, A. M., Bonnefoy, M., Chauvin, G., et al. 2010, Science, 329, 57, doi: 10.1126/science.1187187

Lanza, A. F., Malavolta, L., Benatti, S., et al. 2018, A&A, 616, A155, doi: 10.1051/0004-6361/201731010

Laws, C., Gonzalez, G., Walker, K. M., et al. 2003, AJ, 125, 2664, doi: 10.1086/374626

Leggett, S. K., Allard, F., & Hauschildt, P. H. 1998, ApJ, 509, 836, doi: 10.1086/306517

Lenzen, R., Hartung, M., Brandner, W., et al. 2003, in Society of Photo-Optical Instrumentation Engineers (SPIE) Conference Series, Vol. 4841, Instrument Design and Performance for Optical/Infrared Ground-based Telescopes, ed. M. Iye & A. F. M. Moorwood, 944–952, doi: 10.1117/12.460044

Levine, J. L., Steinhauer, A., Elston, R. J., & Lada, E. A. 2006, ApJ, 646, 1215, doi: 10.1086/504964

Li, Y., Brandt, T. D., Brandt, G. M., et al. 2021a, AJ, 162, 266, doi: 10.3847/1538-3881/ac27ab

—. 2021b, arXiv e-prints, arXiv:2109.10422. https://arxiv.org/abs/2109.10422

Li, Y., Brandt, T. D., Brandt, G. M., et al. 2023, Monthly Notices of the Royal Astronomical Society, 522, 5622, doi: 10.1093/mnras/stad1315

Lidov, M. L. 1962, Planet. Space Sci., 9, 719, doi: 10.1016/0032-0633(62)90129-0

Lindegren, L., & Dravins, D. 2003, A&A, 401, 1185, doi: 10.1051/0004-6361:20030181

Lindegren, L., Klioner, S. A., Hernández, J., et al. 2020, arXiv e-prints, arXiv:2012.03380. https://arxiv.org/abs/2012.03380

Lineweaver, C. H., & Grether, D. 2003, The Astrophysical Journal, 598, 1350, doi: 10.1086/379124

Liu, K., Bi, S.-L., Li, T.-D., et al. 2014, Research in Astronomy and Astrophysics, 14, 1447, doi: 10.1088/1674-4527/14/11/008

Liu, M. C., Dupuy, T. J., & Ireland, M. J. 2008, ApJ, 689, 436, doi: 10.1086/591837

Llorente de Andrés, F., Chavero, C., de la Reza, R., Roca-Fàbrega, S., & Cifuentes, C. 2021, A&A, 654, A137, doi: 10.1051/0004-6361/202141339

Lodders, K., & Fegley, B., J. 2006, in Astrophysics Update 2, ed. J. W. Mason, 1, doi: 10.1007/3-540-30313-8_1

Lorenzo-Oliveira, D., Porto de Mello, G. F., Dutra-Ferreira, L., & Ribas, I. 2016, A&A, 595, A11, doi: 10.1051/0004-6361/201628825

Lovis, C., Mayor, M., Bouchy, F., et al. 2008, A&A, 486, 951, doi: 10.1051/0004-6361:200809426

Luck, R. E. 2017, AJ, 153, 21, doi: 10.3847/1538-3881/153/1/21

Luck, R. E., & Heiter, U. 2006, AJ, 131, 3069, doi: 10.1086/504080

Luhman, K. L. 2008, in Astronomical Society of the Pacific Conference Series, Vol. 398, Extreme Solar Systems, ed. D. Fischer, F. A. Rasio, S. E. Thorsett, & A. Wolszczan, 357

Madhusudhan, N., Burrows, A., & Currie, T. 2011, ApJ, 737, 34, doi: 10.1088/0004-637X/737/1/34

Maire, A. L., Baudino, J. L., Desidera, S., et al. 2020, A&A, 633, L2, doi: 10.1051/0004-6361/201937134

Maldonado, J., Eiroa, C., Villaver, E., Montesinos, B., & Mora, A. 2012, A&A, 541, A40, doi: 10.1051/0004-6361/201218800

Maldonado, J., Martínez-Arnáiz, R., Eiroa, C., Montes, D., & Montesinos, B. 2010, Astronomy & Astrophysics, 521, A12, doi: 10.1051/0004-6361/201014935

Maldonado, J., & Villaver, E. 2016, A&A, 588, A98, doi: 10.1051/0004-6361/201527883

Maldonado, J., Villaver, E., Eiroa, C., & Micela, G. 2019, A&A, 624, A94, doi: 10.1051/0004-6361/201833827

Maldonado, R. F., Chavez, M., Bertone, E., & Cruz-Saenz de Miera, F. 2017, MNRAS, 471, 3419, doi: 10.1093/mnras/stx1766

Mamajek, E. E., & Hillenbrand, L. A. 2008, ApJ, 687, 1264, doi: 10.1086/591785

Marchi, S. 2007, ApJ, 666, 475, doi: 10.1086/519760

Marchwinski, R. C., Mahadevan, S., Robertson, P., Ramsey, L., & Harder, J. 2014, The Astrophysical Journal, 798, 63, doi: 10.1088/0004-637x/798/1/63

Marley, M. S., Saumon, D., Guillot, T., et al. 1996, Science, 272, 1919, doi: 10.1126/science.272.5270.1919

Marmier, M., Ségransan, D., Udry, S., et al. 2013, A&A, 551, A90, doi: 10.1051/0004-6361/201219639

Marois, C., Lafrenière, D., Doyon, R., Macintosh, B., & Nadeau, D. 2006, ApJ, 641, 556, doi: 10.1086/500401

Marois, C., Macintosh, B., Barman, T., et al. 2008, Science, 322, 1348, doi: 10.1126/science.1166585

Marois, C., Macintosh, B., & Véran, J.-P. 2010, in Adaptive Optics Systems II, ed. B. L. Ellerbroek, M. Hart, N. Hubin, & P. L. Wizinowich, Vol. 7736, International Society for Optics and Photonics (SPIE), 77361J, doi: 10.1117/12.857225

Marsakov, V. A., & Shevelev, Y. G. 1995, Bulletin d'Information du Centre de Donnees Stellaires, 47, 13

Mathar, R. J. 2007, Journal of Optics A: Pure and Applied Optics, 9, 470, doi: 10.1088/1464-4258/9/5/008

Mawet, D., Milli, J., Wahhaj, Z., et al. 2014, ApJ, 792, 97, doi: 10.1088/0004-637X/792/2/97

Mayor, M., & Queloz, D. 1995, Nature, 378, 355, doi: 10.1038/378355a0

Mayor, M., Pepe, F., Queloz, D., et al. 2003, The Messenger, 114, 20

McArthur, B. E., Benedict, G. F., Barnes, R., et al. 2010, The Astrophysical Journal, 715, 1203, doi: 10.1088/0004-637x/715/2/1203

McCaughrean, M. J., Close, L. M., Scholz, R. D., et al. 2004, A&A, 413, 1029, doi: 10.1051/0004-6361:20034292

McKinney, W. 2010, in Proceedings of the 9th Python in Science Conference, ed. S. van der Walt & J. Millman, 51–56

Ment, K., Fischer, D. A., Bakos, G., Howard, A. W., & Isaacson, H. 2018, AJ, 156, 213, doi: 10.3847/1538-3881/aae1f5

Metchev, S. A., & Hillenbrand, L. A. 2009, The Astrophysical Journal Supplement Series, 181, 62, doi: 10.1088/0067-0049/181/1/62

Meunier, N., & Lagrange, A. M. 2019, A&A, 628, A125, doi: 10.1051/0004-6361/201935347

Mewe, R. 1996, SoPh, 169, 335, doi: 10.1007/BF00190610

Mints, A., & Hekker, S. 2017, A&A, 604, A108, doi: 10.1051/0004-6361/201630090

Mishenina, T. V., Soubiran, C., Bienaymé, O., et al. 2008, A&A, 489, 923, doi: 10.1051/0004-6361:200810360

Montes, D., López-Santiago, J., Gálvez, M., et al. 2001, Monthly Notices of the Royal Astronomical Society, 328, 45, doi: 10.1046/j.1365-8711.2001.04781.x

Morley, C. V., Kreidberg, L., Rustamkulov, Z., Robinson, T., & Fortney, J. J. 2017, ApJ, 850, 121, doi: 10.3847/1538-4357/aa927b

Mortier, A., Santos, N. C., Sousa, S., et al. 2013, A&A, 551, A112, doi: 10.1051/0004-6361/201220707

Mugrauer, M. 2019, MNRAS, 490, 5088, doi: 10.1093/mnras/stz2673

Murgas, F., Jenkins, J. S., Rojo, P., Jones, H. R. A., & Pinfield, D. J. 2013, A&A, 552, A27, doi: 10.1051/0004-6361/201219483

Nelder, J. A., & Mead, R. 1965, The Computer Journal, 7, 308, doi: 10.1093/comjnl/7.4.308

Nielsen, E. L., De Rosa, R. J., Macintosh, B., et al. 2019, AJ, 158, 13, doi: 10.3847/1538-3881/ab16e9

Nielsen, E. L., De Rosa, R. J., Wang, J. J., et al. 2020, AJ, 159, 71, doi: 10.3847/1538-3881/ab5b92

Noyes, R. W., Hartmann, L. W., Baliunas, S. L., Duncan, D. K., & Vaughan, A. H. 1984, ApJ, 279, 763, doi: 10.1086/161945

Oelkers, R. J., Rodriguez, J. E., Stassun, K. G., et al. 2018, AJ, 155, 39, doi: 10.3847/1538-3881/aa9bf4

Oppenheimer, B. R., Kulkarni, S. R., Matthews, K., & Nakajima, T. 1995, Science, 270, 1478, doi: 10.1126/science.270.5241.1478

Pace, G. 2013, A&A, 551, L8, doi: 10.1051/0004-6361/201220364

Pägert, M., Mugrauer, M., Riffeser, A., et al. 2021, Astronomy & Astrophysics, 652, a58, doi: 10.1051/0004-6361/202140805

Pairet, B., Cantalloube, F., Gomez Gonzalez, C. A., Absil, O., & Jacques, L. 2019, MNRAS, 487, 2262, doi: 10.1093/mnras/stz1350

Palla, M., Santos-Peral, P., Recio-Blanco, A., & Matteucci, F. 2022, A&A, 663, A125, doi: 10.1051/0004-6361/202142645

Parker, E. N. 1955, ApJ, 122, 293, doi: 10.1086/146087

—. 1979, Cosmical magnetic fields. Their origin and their activity, Oxford: Clarendon Press, 1979.

Paunzen, E., Iliev, I. K., Kamp, I., et al. 2002, A&A, 392, 671, doi: 10.1051/0004-6361:20020941

Perdigon, J., de Laverny, P., Recio-Blanco, A., et al. 2021, A&A, 647, A162, doi: 10.1051/0004-6361/202040147

Perrier, C., Sivan, J. P., Naef, D., et al. 2003, A&A, 410, 1039, doi: 10.1051/0004-6361:20031340

Phillips, M. W., Tremblin, P., Baraffe, I., et al. 2020a, A&A, 637, A38, doi: 10.1051/0004-6361/201937381

—. 2020b, A&A, 637, A38, doi: 10.1051/0004-6361/201937381

Phipps, T. E. 1989, American Journal of Physics, 57, 549, doi: 10.1119/1.15969

Pinheiro, F. J. G., Fernandes, J. M., Cunha, M. S., et al. 2014, MNRAS, 445, 2223, doi: 10.1093/mnras/stu1812

Plavchan, P., Latham, D., Gaudi, S., et al. 2015, Radial Velocity Prospects Current and Future: A White Paper Report prepared by the Study Analysis Group 8 for the Exoplanet Program Analysis Group (ExoPAG). https://arxiv.org/abs/1503.01770

Plewa, P. M. 2018, Ph.D. Thesis, Ph.D. Thesis, Ludwig–Maximilians–Universität, München

Plewa, P. M., Gillessen, S., Eisenhauer, F., et al. 2015, MNRAS, 453, 3234, doi: 10.1093/mnras/stv1910

Plewa, P. M., Gillessen, S., Bauböck, M., et al. 2018, Research Notes of the AAS, 2, 35, doi: 10.3847/2515-5172/aab3df

Porto de Mello, G. F., da Silva, R., da Silva, L., & de Nader, R. V. 2014, A&A, 563, A52, doi: 10.1051/0004-6361/201322277

Queiroz, A. B. A., Anders, F., Chiappini, C., et al. 2020, A&A, 638, A76, doi: 10.1051/0004-6361/201937364

Rajan, A., Patience, J., Wilson, P. A., et al. 2015, Monthly Notices of the Royal Astronomical Society, 448, 3775

Rameau, J., Chauvin, G., Lagrange, A.-M., et al. 2013, The Astrophysical Journal Letters, doi: 10.1088/2041-8205/772/2/L15

Ramírez, I., Meléndez, J., Bean, J., et al. 2014, A&A, 572, A48, doi: 10.1051/0004-6361/201424244

Reffert, S., & Quirrenbach, A. 2011, A&A, 527, A140, doi: 10.1051/0004-6361/201015861

Reiners, A., & Zechmeister, M. 2020, ApJS, 247, 11, doi: 10.3847/1538-4365/ab609f

Reinhold, T., & Hekker, S. 2020, A&A, 635, A43, doi: 10.1051/0004-6361/201936887

Ren, B., Pueyo, L., Zhu, G. B., Debes, J., & Duchêne, G. 2018, ApJ, 852, 104, doi: 10.3847/1538-4357/aaa1f2

Rey, J., Hébrard, G., Bouchy, F., et al. 2017, A&A, 601, A9, doi: 10.1051/0004-6361/201630089

Rica, F. M., Barrena, R., Henríquez, J. A., Pérez, F. M., & Vargas, P. 2017, Publications of the Astronomical Society of Australia, 34, e004, doi: 10.1017/pasa.2016.59

Rice, K. 2014, Challenges, 5, 296, doi: 10.3390/challe5020296

Rich, E. A., Wisniewski, J. P., McElwain, M. W., et al. 2017, MNRAS, 472, 1736, doi: 10.1093/mnras/stx2051

Rickman, E. L., Ségransan, D., Hagelberg, J., et al. 2020, A&A, 635, A203, doi: 10.1051/0004-6361/202037524

Rickman, E. L., Möller-Nilsson, O., Rice, E. L., et al. 2016, The Astronomical Journal, 152, 147

Rickman, E. L., Ségransan, D., Marmier, M., et al. 2019, A&A, 625, A71, doi: 10.1051/0004-6361/201935356

Rickman, E. L., Matthews, E., Ceva, W., et al. 2022, A&A, 668, A140, doi: 10.1051/0004-6361/202244633

Rousset, G., Lacombe, F., Puget, P., et al. 2003, in Society of Photo-Optical Instrumentation Engineers (SPIE) Conference Series, Vol. 4839, Adaptive Optical System Technologies II, ed. P. L. Wizinowich & D. Bonaccini, 140–149, doi: 10.1117/12.459332

Sadakane, K., Ohkubo, M., Takeda, Y., et al. 2002, PASJ, 54, 911, doi: 10.1093/pasj/54.6.911

Saffe, C., Jofré, E., Miquelarena, P., et al. 2019, A&A, 625, A39, doi: 10.1051/0004-6361/201935352

Sahlmann, J., Ségransan, D., Queloz, D., et al. 2011, A&A, 525, A95, doi: 10.1051/0004-6361/201015427

Santos, N. C., Israelian, G., & Mayor, M. 2004, A&A, 415, 1153, doi: 10.1051/0004-6361:20034469

Santos, N. C., Israelian, G., Mayor, M., et al. 2005, A&A, 437, 1127, doi: 10.1051/0004-6361:20052895

Santos, N. C., Israelian, G., Mayor, M., Rebolo, R., & Udry, S. 2003, A&A, 398, 363, doi: 10.1051/0004-6361:20021637

Santos, N. C., Sousa, S. G., Mortier, A., et al. 2013, A&A, 556, A150, doi: 10.1051/0004-6361/201321286

Santos, N. C., Adibekyan, V., Figueira, P., et al. 2017, A&A, 603, A30, doi: 10.1051/0004-6361/201730761

Saumon, D., Chabrier, G., & van Horn, H. M. 1995, ApJS, 99, 713, doi: 10.1086/192204

Saumon, D., & Marley, M. S. 2008, ApJ, 689, 1327, doi: 10.1086/592734

Schatzman, E. 1962, Annales d'Astrophysique, 25, 18

Schatzman, E. 1990, International Astronomical Union Colloquium, 121, 5–17, doi: 10.1017/S0252921100067786

Schlaufman, K. C. 2018, ApJ, 853, 37, doi: 10.3847/1538-4357/aa961c

Scholz, R. D., McCaughrean, M. J., Lodieu, N., & Kuhlbrodt, B. 2003, A&A, 398, L29, doi: 10.1051/0004-6361:20021847

Schröder, C., Reiners, A., & Schmitt, J. H. M. M. 2009, A&A, 493, 1099, doi: 10.1051/0004-6361:200810377

Ségransan, D., Udry, S., Mayor, M., et al. 2010, A&A, 511, A45, doi: 10.1051/0004-6361/200912136

Serabyn, E., Huby, E., Matthews, K., et al. 2017, AJ, 153, 43, doi: 10.3847/1538-3881/153/1/43

Service, M., Lu, J. R., Campbell, R., et al. 2016, PASP, 128, 095004, doi: 10.1088/1538-3873/128/967/095004

Skiff, B. A. 2014, VizieR Online Data Catalog, B/mk

Skrutskie, M. F., Cutri, R. M., Stiening, R., et al. 2006, AJ, 131, 1163, doi: 10.1086/498708

Skumanich, A. 1972, ApJ, 171, 565, doi: 10.1086/151310

Smart, W. M. 1977, Textbook on Spherical Astronomy (Cambridge University Press), doi: 10.1017/CBO9781139167574

Snellen, I. A. G., & Brown, A. G. A. 2018, Nature Astronomy, 2, 883, doi: 10.1038/s41550-018-0561-6

Soderblom, D. R. 2010, ARA&A, 48, 581, doi: 10.1146/annurev-astro-081309-130806

Soderblom, D. R., Duncan, D. K., & Johnson, D. R. H. 1991, ApJ, 375, 722, doi: 10.1086/170238

Soto, M. G., & Jenkins, J. S. 2018a, A&A, 615, A76, doi: 10.1051/0004-6361/201731533

—. 2018b, A&A, 615, A76, doi: 10.1051/0004-6361/201731533

Soubiran, C., Brouillet, N., & Casamiquela, L. 2022, A&A, 663, A4, doi: 10.1051/0004-6361/202142409

Soubiran, C., Le Campion, J.-F., Brouillet, N., & Chemin, L. 2016, A&A, 591, A118, doi: 10.1051/0004-6361/201628497

Soubiran, C., Jasniewicz, G., Chemin, L., et al. 2018, A&A, 616, A7, doi: 10.1051/0004-6361/201832795

Soummer, R., Pueyo, L., & Larkin, J. 2012, The Astrophysical Journal, 755, L28, doi: 10.1088/2041-8205/755/2/l28

Sousa, S. G., Santos, N. C., Israelian, G., Mayor, M., & Monteiro, M. J. P. F. G. 2006, A&A, 458, 873, doi: 10.1051/0004-6361:20065658

Sousa, S. G., Santos, N. C., Israelian, G., Mayor, M., & Udry, S. 2011, A&A, 533, A141, doi: 10.1051/0004-6361/201117699

Sousa, S. G., Santos, N. C., Mayor, M., et al. 2008, A&A, 487, 373, doi: 10.1051/0004-6361:200809698

Sousa, S. G., Adibekyan, V., Delgado-Mena, E., et al. 2018, A&A, 620, A58, doi: 10.1051/0004-6361/201833350

Sozzetti, A., & Desidera, S. 2010, A&A, 509, A103, doi: 10.1051/0004-6361/200912717

Sozzetti, A., Udry, S., Zucker, S., et al. 2006, A&A, 449, 417, doi: 10.1051/0004-6361:20054303

Spiegel, D. S., Burrows, A., & Milsom, J. A. 2011, ApJ, 727, 57, doi: 10.1088/0004-637X/727/1/57

Spina, L., Meléndez, J., & Ramírez, I. 2016, A&A, 585, A152, doi: 10.1051/0004-6361/201527429

Stamatellos, D., Hubber, D. A., & Whitworth, A. P. 2007, MNRAS, 382, L30, doi: 10.1111/j.1745-3933.2007.00383.x

Stamatellos, D., & Whitworth, A. P. 2008, A&A, 480, 879, doi: 10.1051/0004-6361:20078628

Stassun, K. G., Collins, K. A., & Gaudi, B. S. 2017, AJ, 153, 136, doi: 10.3847/1538-3881/aa5df3

Stassun, K. G., & Torres, G. 2021, ApJL, 907, L33, doi: 10.3847/2041-8213/abdaad

Stassun, K. G., Oelkers, R. J., Paegert, M., et al. 2019, AJ, 158, 138, doi: 10.3847/1538-3881/ab3467

Stetson, P. B. 1987, PASP, 99, 191, doi: 10.1086/131977

Strassmeier, K., Washuettl, A., Granzer, T., Scheck, M., & Weber, M. 2000, A&AS, 142, 275, doi: 10.1051/aas:2000328

Suárez-Andrés, L., Israelian, G., González Hernández, J. I., et al. 2017, A&A, 599, A96, doi: 10.1051/0004-6361/201629434

Swimmer, N., Currie, T., Steiger, S., et al. 2022, AJ, 164, 152, doi: 10.3847/1538-3881/ac85a8

Takeda, G., Ford, E. B., Sills, A., et al. 2007, ApJS, 168, 297, doi: 10.1086/509763

Tal-Or, L., Trifonov, T., Zucker, S., Mazeh, T., & Zechmeister, M. 2018, Monthly Notices of the Royal Astronomical Society: Letters, 484, L8, doi: 10.1093/mnrasl/sly227

Testa, P., Saar, S., & Drake, J. 2015, Philosophical transactions. Series A, Mathematical, physical, and engineering sciences, 373, doi: 10.1098/rsta.2014.0259

Trifonov, T., Tal-Or, L., Zechmeister, M., et al. 2020, A&A, 636, A74, doi: 10.1051/0004-6361/201936686

Trippe, S., Gillessen, S., Gerhard, O. E., et al. 2008, A&A, 492, 419, doi: 10.1051/0004-6361:200810191

Tsantaki, M., Sousa, S. G., Adibekyan, V. Z., et al. 2013, A&A, 555, A150, doi: 10.1051/0004-6361/201321103

Udry, S., Fischer, D., & Queloz, D. 2007, Protostars and Planets V

Valenti, J. A., & Fischer, D. A. 2005, ApJS, 159, 141, doi: 10.1086/430500

—. 2007, ApJ, 669, 1167, doi: 10.1086/519295

van Belle, G. T., Ciardi, D. R., Thompson, R. R., Akeson, R. L., & Lada, E. A. 2007, A&A, 474, 653, doi: 10.1051/0004-6361:20078357

van der Walt, S., Colbert, S. C., & Varoquaux, G. 2011, Computing in Science and Engineering, 13, 22, doi: 10.1109/MCSE.2011.37

van Dokkum, P. G. 2001, PASP, 113, 1420, doi: 10.1086/323894

van Leeuwen, F. 2007, A&A, 474, 653, doi: 10.1051/0004-6361:20078357 van Saders, J. L., Ceillier, T., Metcalfe, T. S., et al. 2016, Nature, 529, 181, doi: 10.1038/nature16168

VanderPlas, J. T. 2018, The Astrophysical Journal Supplement Series, 236, 16, doi: 10.3847/1538-4365/aab766

Venner, A., Vanderburg, A., & Pearce, L. A. 2021, arXiv e-prints, arXiv:2104.13941. https://arxiv.org/abs/2104.13941

Virtanen, P., Gommers, R., Oliphant, T. E., et al. 2020, Nature Methods, 17, 261, doi: 10.1038/s41592-019-0686-2

Virtanen, P., Gommers, R., Oliphant, T. E., et al. 2020, Nature Methods, 17, 261, doi: 10.1038/s41592-019-0686-2

Voges, W., Aschenbach, B., Boller, T., et al. 1999, A&A, 349, 389. https://arxiv.org/abs/astro-ph/9909315

—. 2000, IAUC, 7432, 3

Vousden, W. D., Farr, W. M., & Mandel, I. 2016a, MNRAS, 455, 1919, doi: 10.1093/mnras/stv2422

—. 2016b, MNRAS, 455, 1919, doi: 10.1093/mnras/stv2422

Walker, G. A. 2012, New Astronomy Reviews, 56, 9, doi: https://doi.org/10.1016/j.newar.2011.06.001

Wei, J. 2018, arXiv e-prints, arXiv:1805.02771. https://arxiv.org/abs/1805.02771

Wertz, O., Absil, O., Gómez González, C. A., et al. 2017, A&A, 598, A83, doi: 10.1051/0004-6361/201628730

White, R. J., Gabor, J. M., & Hillenbrand, L. A. 2007, AJ, 133, 2524, doi: 10.1086/514336

Whitworth, A. P., & Zinnecker, H. 2004, A&A, 427, 299, doi: 10.1051/0004-6361:20041131

Wilson, O. C. 1968, ApJ, 153, 221, doi: 10.1086/149652

Winter, A. J., Kruijssen, J. M. D., Longmore, S. N., & Chevance, M. 2020, Nature, 586, 528, doi: 10.1038/s41586-020-2800-0

Wittenmyer, R. A., Endl, M., Cochran, W. D., Levison, H. F., & Henry, G. W. 2009, ApJS, 182, 97, doi: 10.1088/0067-0049/182/1/97

Wittenmyer, R. A., Butler, R. P., Tinney, C. G., et al. 2016, ApJ, 819, 28, doi: 10.3847/0004-637X/819/1/28

Wizinowich, P. 2013, PASP, 125, 798, doi: 10.1086/671425

Wright, C. O., Egan, M. P., Kraemer, K. E., & Price, S. D. 2003, AJ, 125, 359, doi: 10.1086/345511

Wright, J. T. 2018, Handbook of Exoplanets, 619–631, doi: 10.1007/978-3-319-55333-7_4

Wright, J. T., Marcy, G. W., Butler, R. P., & Vogt, S. S. 2004, ApJS, 152, 261, doi: 10.1086/386283

Xuan, W. J., Mawet, D., Ngo, H., et al. 2018, AJ, 156, 156, doi: 10.3847/1538-3881/aadae6

Yee, S. W., Petigura, E. A., & von Braun, K. 2017, ApJ, 836, 77, doi: 10.3847/1538-4357/836/1/77

Yelda, S., Lu, J. R., Ghez, A. M., et al. 2010, The Astrophysical Journal, 725, 331, doi: 10.1088/0004-637x/725/1/331

Zapatero Osorio, M. R., Lane, B. F., Pavlenko, Y., et al. 2004, ApJ, 615, 958, doi: 10.1086/424507

Zechmeister, M., & Kürster, M. 2009, A&A, 496, 577, doi: 10.1051/0004-6361:200811296

Zechmeister, M., Kürster, M., Endl, M., et al. 2013, A&A, 552, A78, doi: 10.1051/0004-6361/201116551

Zhang, Z. 2021, in The 20.5th Cambridge Workshop on Cool Stars, Stellar Systems, and the Sun (CS20.5), Cambridge Workshop on Cool Stars, Stellar Systems, and the Sun, 159, doi: 10.5281/zenodo.4565071

Zhuleku, J., Warnecke, J., & Peter, H. 2020, A&A, 640, A119, doi: 10.1051/0004-6361/202038022